

3. DYNAMIC LOAD ANALYSIS FOR NEW FUEL RACKS IN THE BUFFER POOL

3.1 INTRODUCTION

3.1.1 Purpose

The purpose of this section is to present the structural analysis of New Fuel Storage Racks (FSR) for the Buffer Pool located in the Reactor Building (RB) of the ESBWR.

The FSR are structures fabricated from stainless steel plates, forming 7x2 cells to house the new fuel assemblies. Each two FSR are joined and installed together forming a 14x2 cell assembly (ID 6). Therefore the calculation presented in this report is based on a 14x2 configuration. The FSR are anchored to the floor of the Buffer Pool at elevation 27000.

3.1.2 Scope

The scope of this analysis covers the design principles, load analysis and justification of the structural configuration of the FSR.

The boundaries of the analysis include all the sections of the structure, including plate and weld stress evaluations. Maximum displacements at the top of the FSR are checked. Reactions at the bottom of FSR are obtained to validate the anchor bolt section.

The maximum lateral forces between the fuel assemblies and the top of the FSR cell, along with the maximum vertical forces between fuel assemblies and the FSR base plate are determined.

The calculation of the embedment for the anchor bolts is not within the scope of this document analysis. The structural evaluation of the new fuel assemblies enclosed in the FSR is not covered in this analysis, but their masses have been taken into account. The structural evaluation of the FSR against accidental equipment drop, the fatigue analysis, and the functionality of the mechanical components are not within the scope of this analysis.

3.2 INPUT DATA

Table 3-1
List of Document Input Data (ID)

| No. | Source Document | | | Requirement/Data | Status |
|-----|-----------------|-------|----------------------------------------------------------------------------------------|-------------------------------------------------------------------------------------------------------------------------------------------------------------------------------------|----------------|
| | No. | Issue | Title | | |
| 1 | 5926.D500 | 01 | New Fuel Rack Assembly Drawing | Geometry. Materials. | V |
| 2 | 5926.D510 | 01 | New Fuel Rack Base Plate | Geometry | V |
| 3 | 5926.D520 | 01 | New Fuel Rack Miscellaneous Detail | Geometry | V |
| 4 | 26A7032 | 3 | Fuel Storage Rack Design Specification | Design Codes. Design Requirements. Fuel assembly weight. Fuel handling loads. Applicable Response Spectra . Loading Combinations. Spent Fuel Pool Water Temperatures | V |
| 5 | 26A6558 | 4 | General Civil Design Criteria | Stress free temperature | V |
| 6 | 5926.D110 | 01 | Rack Layout at Reactor Building | Rack layout. Distance between racks and distance to the walls. | V |
| 7 | 105E3908 | 03 | General Arrangement, ESBWR Nuclear Island | Plant axes | V |
| 8 | 55926ATN04 | 00 | ESBWR Reactor Pool Bottom (elevation +27m) Synthesized SSE Acceleration Time Histories | SSE acceleration time histories | V ⁺ |

3.3 SUMMARY OF RESULTS

Table 3-2 summarizes the most critical results obtained from the analysis of the FSR and the comparison with the allowable values in accordance with the design code (Reference 3).

**Table 3-2
FSR Main Analysis Results**

| Steel Plates | Calculated Stress (MPa) | Stress Limit (MPa) | Ratio |
|-------------------------------------|--------------------------------|---------------------------|--------------|
| 8 mm thick channel plate | 267 | 292.8 | 0.91 |
| Channel to support-base welds | 182 | 198.6 | 0.92 |
| 12 mm thick door plates | 123 | 195.2 | 0.63 |
| Assembly grid plate | 52.5 | 195.2 | 0.27 |
| Axis and hinge | 130 | 195.2 | 0.67 |
| 15 mm thick support-base stiffeners | 138 | 195.2 | 0.71 |
| 15 mm thick folded base plate | 266 | 292.8 | 0.91 |
| 30 mm thick bolted support plates | 124 | 292.8 | 0.42 |
| M24x2 anchor bolts | 0.91 (*) | 1 (*) | 0.91 |

(*) This is a stress ratio, not a stress value (see Sections 3.4.9 and 3.5.3).

3.4 ANALYSIS SUMMARY

Section 3.4.1 presents a brief description of the FSR.

Section 3.4.2 presents the properties of the FSR materials.

Section 3.4.3 indicates the applicable design code for analysis of the FSR.

Section 3.4.4 presents the assumptions used in the analysis of the FSR.

Section 3.4.5 gives a detailed description of the FSR model. A detail Finite Element Model (FEM) is developed for the FSR in order to analyze stresses, reactions and displacements.

Section 3.4.6 describes the different load cases which apply to the FSR analysis.

Section 3.4.7 presents the load combinations applied for the FSR analysis.

Section 3.4.8 presents the analysis procedure description for the FSR.

Section 3.4.9 gives the allowable stress limits used in the FSR analysis.

3.4.1 New Fuel Storage Rack Description

The FSR support and protect stored new fuel assemblies. The FSR are structures made of stainless steel plates, forming a 14x2 array of storage cells. The FSR are located in the Buffer Pool within the Reactor Building and are anchored to the pool floor at elevation 27000.

A detailed description of FSR is shown in the assembly and detail drawings of the FSR (ID 1, 2, 3 and 6). As described in ID 6 each pair of 7x2 FSR are laterally joined forming a 14x2 FSR. The rest of the document describes and analyzes the behavior of the 14x2 FSR.

The rack is formed by the assembly of a matrix of cells. The typical cell is a U-section of plain SS 8 mm thick (see ID 3, section "D-D").

The assembly of individual cells to conform a stiff structure is accomplished by the joining the grids to the base plate. The grids are formed from plain SS plates jointed by slot insertion that later, are welded to increase the strength (see the typical 6 mm x 50-100 vertical corner weld in ID 1, view "A"). The individual cells are then welded to the grids (see ID 1).

Each channel is welded to the support-base plate, which is stiffened underneath with plates. The base plate is anchored to the pool with sixteen (16) M24x2 anchor bolts embedded in the pool floor.

The main dimensions of the FSR are 3672x650 mm and 3697 mm in height. Different thicknesses of plates are used in the FSR: 8 mm for the main plates that form each channel, 12 mm for the two (2) plates per channel that form the doors, 10 mm for the plates of the two (2) grid assemblies that stiffen the channels at two different elevations, and 15 mm for the support-base plate that supports the 28 channels, including the stiffener plates.

Each channel has two doors that remain open at the lateral entrance for the fuel assembly. When the fuel assembly is positioned within the channel and rests on the support-base plate hole, the doors close remain blocked. The axis is a cylinder of 48 mm outside diameter and 33 mm inside diameter. The axis is guided by three hinges and a hole located in the support plate. Each hinge is a cylinder of 70 mm outside diameter and 50 mm inside diameter welded to the corresponding channel.

3.4.2 Materials

The FSR are manufactured using stainless steel SA-240 Type 304L. Material SA-564 Type 630 H1075 is used for anchor bolts.

The mechanical properties of type 304L stainless steel are greater than those of type 304, so the mechanical properties of the latter are used.

Table 3-3 shows the material properties in accordance with Section II, Part D of the ASME Code (Reference 2). Material properties at 121.1°C (250°F) are assumed based on ID 4.

Table 3-3
Material Properties at 250°F (121.1°C)

| Material | E (MPa) | ρ (kg/m ³) | α (1/°C) | S _y (MPa) | S _u (MPa) | S (MPa) |
|-----------------------|----------------------|--------------------------------|-----------------------|-------------------------|-------------------------|------------|
| SA-240 Type 304L (*) | 1.90·10 ⁵ | 7850 | 16.4·10 ⁻⁶ | 162.7 | 472.9 | 134.1 |
| SA-564 Type 630 H1075 | 1.91·10 ⁵ | 7850 | 11.3·10 ⁻⁶ | 797.0 | 999.7 | 285.4 |

(*) Properties shown are those corresponding to type 304 stainless steel

- ρ ≡ Density (Reference 1)
- E ≡ Modulus of elasticity (Reference 2, Table TM-1)
- α ≡ Coefficient of thermal expansion (Reference 2, Table TE-1)
- S_y ≡ Yield strength (Reference 2, Table Y-1)
- S_u ≡ Ultimate strength (Reference 2, Table U)
- S ≡ Maximum – allowable Stress (Reference 2, Table 1A)

3.4.3 Design Code

Stresses in the structural components of the FSR shall not exceed the allowable stress levels given in the ASME B&PV Code, Section III, Division I, Subsection NF (Reference 3).

3.4.4 Assumptions

The calculation procedure used for the analysis has been performed based on the following assumptions of FSR behavior:

- It is assumed that the material of the structure (stainless steel) has a linear elastic behavior within the field of the small displacement/deformations.
- An assumption of FSRs with a 100% fuel load shall be considered. Since the FSRs are anchored to the pool floor and the fuel elements have a large mass but do not provide any stiffness to the assembly, it is reasonable to expect that this case will present the maximum deformations and stresses.
- For the fuel assembly the dry weight is assumed to be 540 lbs (245 kg) and the net immersed weight to be 474 lbs (215 kg) (ID 4).
- The fuel assembly shall be conservatively rigid enough that it is only supported on the top part of the upper doors, in addition to the support-base plate.

- The water mass acting in the vertical direction is not considered because the water could flow inside each one of the cells in the vertical direction.
- Prior experience in the study of the dynamic behavior of the freestanding FSRs shows a significant reduction in the lateral displacements of the FSR when the hydrodynamic coupling between the FSRs and between the FSRs and the walls through the water around them is considered. It is reasonable to assume that the coupling effect shall be lower for FSRs anchored to the bottom of the pool, as in the case under study. Therefore, in order to simplify the calculations, a conservative assumption has been made to disregard the positive effect of the hydrodynamic coupling towards the FSR design. Another conservative assumption shall take into account the added mass to be included in the models, without considering neighboring FSRs or walls.

3.4.5 FSR Analysis Model

A finite element model (FEM) for the analysis of the FSR is built with ANSYS 10.0 (Reference 7). A description of the FEM (see Figures E1 and E2 in Appendix E) follows:

- The channel plates of the FSR (see Figure E3) are modeled with an 8 mm thick stainless steel plate (Reference 7, SHELL 63 ANSYS elements). These channel plates are welded in their entire bottom end to the support plate and are connected by the grid assemblies at two elevations.
- The channel plates in contact with the grid assembly plates (see Figure E4) are modeled with (8+10) mm thick stainless steel plate (Reference 7, SHELL 63 ANSYS elements). The grid assembly plates not in contact with the channels are modeled with 10 mm stainless steel plates (Reference 7, SHELL 63 ANSYS elements).
- The door plates (see Figure E5) are modeled with 12 mm thick stainless steel plates (Reference 7, SHELL 63 ANSYS elements). These plates are welded to the rotation axis, which is modeled with 7.5 mm thick stainless steel plates (Reference 7, SHELL 63 ANSYS elements). The hinges are modeled with 10 mm thick stainless steel plates (Reference 7, SHELL 63 ANSYS elements). The connections between the axis and the hinges and between the axis and the support-base plate are represented by coupling in the radial direction between nodes of the two connected plates. The nodes located at the bottom elevation of the middle hinge are also coupled in the tangential direction to represent the lock-out device. The bottom end axis nodes are also coupled in vertical direction with the corresponding nodes on the support-base plate.
- The support-base plate (see Figure E6) of the FSR is modeled with stainless steel plates (Reference 7, SHELL 63 ANSYS elements). This support includes the 15 mm thick folded plate with 98 mm diameter holes for each one of the 28 channels and with 68 mm diameter holes for each one of the 28 axes, the 15 mm thick rectangular stiffeners welded under the folded plate, the 15 mm thick triangular stiffeners welded on the folded plate near the bolt holes, and the (15+15) mm thick reinforced anchor plates. The 30 mm diameter hole centered in the plate is not modeled. Due to this fact and in order to achieve a more realistic boundary condition, as well as fixing the three displacements at the central point, the two horizontal rotations are also fixed.

- 50% of the fuel mass ($245 \cdot 28 \cdot 0.5 = 3430$ kg) acting in the horizontal X direction is distributed in the central top node of the upper doors. The same 3430 kg acting in the horizontal Y direction is distributed in the channels upper end, and the other 50% (3430 kg) is distributed in the nodes of the model located in the support-base plate holes in both horizontal directions. 100% of the mass (6860 kg) shall apply vertically in the nodes of the model located in the support-base plate. These fuel assembly masses are included as lumped masses (Reference 7, MASS 21 ANSYS elements) in the model.
- The internal water mass acting in the two horizontal directions is distributed in the inner nodes of the model. The node mass distribution is proportional to the volume associated with each inner node. The internal water mass is obtained from the total FSR internal volume where the fuel volume and metal volume is subtracted. Metal mass is ANSYS calculated. Each fuel assembly has a volume of 0.03 m^3 . The internal water masses are included as lumped masses (MASS 21 ANSYS (Reference 7) elements) in the model.
- The external water added mass has been obtained from Reference 6, where the added mass of a rigid rectangular plate is calculated using the equation $m_w = (\pi \cdot a^2 \cdot b \cdot \phi / 4)$ (where (a) and (b) are the short and long lengths, respectively, of the FSR channel plate, and (ϕ) is the water density). The added mass of the FSR is approximately 2420 kg. This added mass corresponds to the following assumptions: (a) infinitely stiff plate, (b) moving as a stiff solid body (c) in an infinite mass of water. The FSR (a) is elastically deformable, (b) is anchored to the ground, i.e. it moves like a cantilever and (c) has a finite layer of water around it, so the motion of each FSR shall be coupled through water to the motion of neighboring FSRs. Therefore, the actual added mass and the actual horizontal displacements of the top part of the FSR shall be lower than those obtained in the analysis. Introducing 2420 kg of added mass is a conservative estimate but it is verified that this added mass does not significantly impact in the final results of the FSR analysis (stresses and bolt reactions). The external water added masses are included in the model multiplying the internal water masses by a factor.
- The mass of the SS plates is accounted for by means of its density.
- The coordinate system adopted in the FEM is the right hand Cartesian coordinate system. The X-direction represents the North-South direction, the Y-direction represents the East-West direction, and the Z-direction is vertical (ID 7).
- The units used in the FSR FEM are kilograms for mass, meters for length, and seconds for time.

The FSR mass considered in the analysis model is presented in Table 3-4:

Table 3-4
Mass Breakdown

| Component | Horizontal mass (kg) | Vertical mass (kg) |
|-------------------------------|----------------------|--------------------|
| Stainless Steel | 5863 | 5863 |
| Fuel Assemblies (28 elements) | 6860 | 6860 |
| Internal Water | 4110 | - |
| External Added Water | 2420 | - |
| Total Mass | 19253 | 12723 |

3.4.6 Analysis Loads

The following loads are considered in the analysis of the FSR:

| | |
|----------------|---------------------------------------------------------------------|
| D | Dead Weight + Buoyancy |
| P _f | Upward force by postulated stuck fuel assembly |
| T _o | Differential temperature induced loads (normal or upset conditions) |
| T _a | Differential temperature induced loads (abnormal design condition) |
| SSE | Safe Shutdown Earthquake |
| SRVD | Safety Relief Valve Discharge |
| LOCA | Loss of Coolant Accident |
| L _R | Lifting FSR during installation |

3.4.6.1 Dead Weight + Buoyancy (D)

In addition to the dead weight of the FSR and fuel assemblies, it is necessary to consider the buoyancy, that is, the thrust that the water applies on the FSR and the immersed fuel. This effect is taken into account in the analysis by reducing the gravity acceleration by a reducing factor calculated as follows:

| | |
|-------------------------|------------------------------------------------------|
| FSR steel mass: | $M_s = 5830 \text{ kg}$ (see Table 3-4) |
| Steel volume: | $V_s = M_s / \rho = 5830 / 7850 = 0.743 \text{ m}^3$ |
| Fuel assemblies mass: | $M_f = 245 * 28 = 6860 \text{ kg}$ |
| Fuel assemblies volume: | $V_f = 0.03 * 28 = 0.84 \text{ m}^3$ |
| Total mass: | $M_T = 5830 + 6860 = 12690 \text{ kg}$ |

Total volume: $V_T = 0.743 + 0.84 = 1.583 \text{ m}^3$

That means 1583 kg of water mass moved. Then, the reducing factor is:

$$F = (12690 - 1583) / 12690 = 0.876$$

And the reduced gravity acceleration is obtained from

$$g' = 0.876 \cdot g = 8.6 \text{ m/s}^2$$

3.4.6.2 Fuel Handling Loads (P_f)

The FSR shall be designed to withstand a pull-up force of 17.79 kN, which is necessary in the event of a fuel assembly or grapple device hanging up during removal and a horizontal force of 4.45 kN being applied at the top of the FSR (ID 4).

3.4.6.3 Differential Temperature Induced Loads (T_o , T_a)

The maximum Buffer Pool water temperatures are 48.9°C (120°F) in normal conditions and 60°C (140°F) in abnormal conditions (ID 4).

The stress-free temperature is assumed to be 15.5°C (ID.5).

The only restrictions on the FSR are the sixteen anchor bolts to the pool floor.

The maximum distance between bolts is $((2 \cdot (1506 + 165))^2 + (2 \cdot 295)^2)^{0.5} = 3394 \text{ mm}$ (ID 2).

The maximum expansion projected between these two most separated anchor points, conservatively assuming a maximum temperature of 121.1°C (250°F)(ID 4), is calculated to be:

$$\alpha \cdot L \cdot \Delta T = 16.4 \text{ E-6} \cdot 3394 \cdot (121.1 - 15.5) = 5.9 \text{ mm}$$

The M24 anchor bolts are placed in the 30 mm diameter hole located in the 15 mm thick folded plate of the FSR. Under these conditions the tolerance between the anchor bolt diameter and the diameter of hole is enough to absorb the maximum expansion estimated. Therefore, no thermal induced stresses are calculated in this analysis. The racks are submerged in water and can expand in both the vertical and horizontal directions without significant restrictions. The temperature gradient in the vertical direction is considered negligible for structural analysis.

3.4.6.4 Safe Shutdown Earthquake (SSE)

The FSR shall be designed to withstand the SSE loads specified in ID 4 Appendix A30. A structural damping value of 4% for SSE conditions is used (Reference 12). Of the two applicable response spectra (nodes 108 and 208) for each direction, the enveloping one is chosen and conservatively applied. Figures E-7a, E-7b, and E-8 in Appendix A show the spectra applied in both horizontal and vertical directions.

3.4.6.5 Safety Relief Valve Discharge (SRVD)

The FSR shall be designed to withstand the SRVD loads specified in ID 4 Appendix A30. A structural damping value of 4% for SRVD conditions is used (Reference 12). Figures E-9 and E10 in Appendix E show the spectra applied in both horizontal and vertical directions.

3.4.6.6 Loss of Coolant Accident (LOCA)

The FSR shall be designed to withstand the LOCA loads specified in ID 4 Appendix A30. A structural damping value of 4% for LOCA conditions is used (Reference 12). Figures E-11 and E12 in Appendix E show the spectra applied in both horizontal and vertical directions in.

3.4.6.7 Lifting FSR During Installation (L_R)

The FSR is verified to withstand the lifting load during installation. The FSR is supported in the four upper holes of the tow grid upper plates (ID 1 and ID 2, item 53.001).

3.4.7 Load Combinations

The load combinations and acceptance criteria shall be per Appendix D of SRP 3.8.4. Table 3-5 shows the envelope load combinations that will be conservatively used for the design of the FSR, based on the aforementioned load combinations.

**Table 3-5
Load Combinations**

| | |
|-----------------|-------------------------------|
| Level A: | $D + P_f$ |
| Level D: | $D + SSE + SRVD + LOCA + T_a$ |

$D + P_f$ is a Level B load combination, but it is conservatively assumed as a Level A load combination.

3.4.8 Analysis Methodology Description

Static and dynamic loads are considered in the analysis. The response spectrum analysis method is used to analyze the dynamic loads.

The static load case (D) is resolved by structural static analysis applying the reduced gravity acceleration g' (see Section 3.4.6.1).

The fuel handling load case (P_f) is analyzed by applying the forces prescribed in Section 3.4.6.2 in a central channel (see Figure E-13).

The lifting load during installation case (L_R) is analyzed by applying the gravity acceleration, g , and supporting the FSR in the appropriate four grid points.

The dynamic load cases are resolved by response spectrum analysis. Before the response spectrum analysis is performed, a modal analysis is performed to determine the natural frequencies and mode shapes of the FSR. The subspace method is used for mode extraction in modal analysis. One hundred fifty (150) eigenfrequencies are requested in the modal analysis.

Once the eigenfrequencies of the model have been determined with the modal analysis, a response spectra analysis for each dynamic event (SSE, SRVD and LOCA) is evaluated for each of the three directions, X, Y and Z.

The input response spectra are represented by no more than twenty (20) points (ANSYS limitation), beginning at a frequency lower than the lowest obtained in the FSR modal analysis.

Once the response spectrum analysis has been performed for each direction, the modal responses are combined in accordance with the grouping method established in Regulatory Guide 1.92 (Reference 5).

That the modes used for the modal combinations are not enough to reach the required 90% of the mass in each direction (see Section 3.5). Therefore the missing mass in each direction will be computed as the difference between the total mass of the model and the sum of the effective masses of the low frequency modes taken into account in the response spectrum analysis. In short, an additional static analysis is performed for each direction with the highest response spectrum acceleration corresponding to any frequency higher than the highest one considered in the modal combination (acceleration greater than ZPA, therefore conservative). Such acceleration will be applied to the fraction of mass not included in the modal combination. The total combined response to high-frequency modes is combined by the Square-Root-Sum-of-Squares (SRSS) method with the total combined response from lower-frequency modes to determine the overall responses.

Finally, as the load combination includes multiple dynamic loads, these loads are combined by the SRSS method.

3.4.9 Stress Limits

The stress limits are taken from ASME Code (3), Subsection NF an Appendix F corresponding to the Design by Analysis for Class 3 Plate and Sheet Type Supports.

Base metal SA-240 Type 304L (with mechanical characteristics of SA-240 Type 304)

Level A Conditions (NF-3251.1 and Table NF-3552(b)-1)

$$P_m \leq S = 134.1 \text{ MPa}$$

$$P_m + P_b \leq 1.5 \cdot S = 201.1 \text{ MPa}$$

$$\tau \leq 0.6 \cdot S = 80.4 \text{ MPa}$$

Level D Conditions (Appendix F.F-1332)

$$P_m \leq \text{Minimum of } 1.2 S_y \text{ or } 0.7 S_u = 195.2 \text{ MPa}$$

$$P_m + P_b \leq 1.5 \cdot P_m \text{ (limit)} = 292.8 \text{ MPa}$$

$$\tau \leq 0.42 \cdot S_u = 198.6 \text{ MPa}$$

Bolting Material SA-564 Type 630 H1075

Level A Conditions (NF-3324.6 for austenitic steel)

$$\text{Average normal stress} = f_t \leq F_{tb} = S_u/3.33 = 300.2 \text{ Mpa}$$

$$\text{Shear stress} = f_v \leq F_{vb} = 0.62 \cdot S_u/5 = 123.9 \text{ MPa}$$

$$\text{Combined tensile and shear stress: } f_t^2 / F_{tb}^2 + f_v^2 / F_{vb}^2 \leq 1$$

Level D Conditions (Appendix F.F-1335)

$$\text{Average normal stress} = f_t \leq F_{tb} = \text{Minimum of } S_y \text{ or } 0.7 S_u = 699.8 \text{ Mpa}$$

$$\text{Shear stress} = f_v \leq F_{vb} = \text{Minimum of } 0.42 \cdot S_u \text{ or } 0.6 S_y = 419.8 \text{ MPa}$$

$$\text{Combined tensile and shear stress: } f_t^2 / F_{tb}^2 + f_v^2 / F_{vb}^2 \leq 1$$

Welds

Level A Conditions (NF-3324.5 and Table NF-3324.5(a)-1)

Fillet welds:

$$\text{Shear Stress on effective throat} \leq 0.3 \cdot S_u^{(1)} = 165.4 \text{ MPa}$$

$$\text{Shear Stress on base metal} \leq 0.4 \cdot S_y = 65.1 \text{ MPa}$$

Tension or compression parallel to axis of weld \leq Same as base metal

⁽¹⁾ Base metal tensile strength range between 472.9 MPa and 551.5 MPa (68.6 and 80 ksi), minimum weld metal tensile strength, 551.5 MPa (80 ksi).

Level D Conditions (Appendix F.F-1332)

$$\text{Shear Stress} \leq 0.42 S_u = 198.6 \text{ MPa}$$

Tension or compression parallel to axis of weld \leq Same as base metal

3.5 RESULTS OF THE ANALYSIS

The ANSYS output for static, modal and spectrum analyses, including the modal combination, is included in Appendix F.

Table 3-6 presents the main eigenfrequencies, obtained from the modal analysis, with the associated effective mass. Additionally, some lower frequency modes (modes 2 and 5) are included as examples of typical mode shapes that do not contribute to the solution response.

Figures E-14 through E-23 in Appendix E show the deformed shapes of these eigenmodes.

Table 3-6
Main Eigenfrequencies

| Mode | Frequency (Hz) | Effective Mass (kg) | Description | Figure in Appendix E |
|------|----------------|---------------------|-------------------------|----------------------|
| 1 | 7.0 | 11034 | Y Bending | E14 |
| 2 | 7.2 | - | Z Torsion | E15 |
| 3 | 9.6 | - | YZ plane Bending | E16 |
| 4 | 14.5 | - | YZ plane double Bending | E17 |
| 5 | 16.8 | 12844 | X Bending | E18 |
| 31 | 33.2 | 1164(X), 17(Y) | Bending Axes | E19 |
| 61 | 48.5 | 89(X), 71(Y) | Bending Axes | E20 |
| 63 | 51.0 | 624(X), 355(Y) | Bending Axes | E21 |
| 69 | 54.2 | 254(X), 66(Y) | Bending Axes | E22 |
| 71 | 54.4 | 182(X), 41(Y) | Bending Axes | E23 |

Table 3-7a indicates the amount of mass considered in the modal combination and the corresponding percentage with respect to the total mass.

Table 3-7a
Combined Effective Masses

| Event | X direction | | Y direction | | Z direction | |
|-------|---------------|-----|---------------|-----|-------------|-----|
| | Mass (kg) | (%) | Mass (kg) | (%) | Mass (kg) | (%) |
| SSE | 13931 (72.3%) | | 14415 (74.8%) | | 6 (0%) | |
| LOCA | 13260 (68.8%) | | 15546 (80.7%) | | 6 (0%) | |
| SRVD | 13260 (68.8%) | | 14406 (74.8%) | | 6 (0%) | |

Table 3-7b indicates the acceleration considered to account for the high-frequency modes, with the corresponding percentage of missing mass.

**Table 3-7b
Acceleration for Missing Masses**

| Event | X direction | | Y direction | | Z direction | |
|-------|------------------|------|------------------|------|------------------|-----|
| | Acceleration (g) | (%) | Acceleration (g) | (%) | Acceleration (g) | (%) |
| SSE | 1.27 | 27.7 | 1.25 | 25.2 | 1.74 | 100 |
| LOCA | 0.05 | 31.2 | 0.029 | 19.3 | 0.225 | 100 |
| SRVD | 0.067 | 31.2 | 0.067 | 25.2 | 0.143 | 100 |

3.5.1 Displacements Results

The maximum horizontal displacement obtained at the top of the FSR for the most unfavorable load combination is 18.0 mm and occurs in the X-direction (see Figure A-24, in Appendix A).

One half of the expansion due to thermal expansion (Section 3.4.6.3) is applied to each rack in opposing horizontal directions. If the abnormal pool temperature were to occur simultaneously with a seismic event, the resulting total displacement is calculated as:

$$18.0 \text{ mm} + 5.9 \text{ mm}/2 = 21.0 \text{ mm}$$

The minimum distance between adjacent FSR at the top level or between FSR and pool wall is 100 mm (ID 6). Therefore, no contact occurs between adjacent FSR or between the FSR and the pool walls.

3.5.2 Plate Stress results

The stress results obtained for the different load combinations are checked in the most critical sections of the different plates of the FSR. Figures E-25 to E-28 in Appendix E show the results.

3.5.2.1 8 mm Thick Channel Plate

The maximum stresses obtained for the 8mm thick channel plate compared with the corresponding allowable stresses are given in Table 3-8, where:

- $S_z \equiv$ Vertical direction (Z) membrane stress
- $S_H \equiv$ Horizontal direction (X or Y) membrane stress
- $S_{HZ} \equiv$ Shear membrane stresses on the plane of the plate.

- Bending stresses across the plate thickness are negligible and are classified as secondary stresses; however, other directions of the plate contain primary bending stresses that are included in the stress analysis results.

Table 3-8
8mm Thick Channel Plate Stress Results

| Stress Category | Calculated Stress (MPa) | Allowable Stress (MPa) |
|-------------------------------------------------|----------------------------|------------------------|
| Level A Conditions Maximum Membrane Stresses | $S_z = 35.8$ (Figure E-25) | 134.1 |
| | $S_H = 6.7$ | 134.1 |
| | $S_{HZ} = 3.9$ | 80.4 |
| Level D Conditions Maximum Membrane Stresses | $S_z = 267$ (Figure E-26) | 292.8 |
| | $S_H = 57.4$ | 292.8 |
| | $S_{HZ} = 41.5$ | 198.6 |

The maximum stresses obtained for the channel to support-base, compared with the corresponding allowable stresses are given in Table 3-9.

Table 3-9
Channel to Support-Base Weld Stress Results

| Stress Category | Calculated Stress (MPa) | Allowable Stress (MPa) |
|-----------------------------------------|-------------------------------|------------------------|
| 6 mm double fillet welds (end channels) | $(267) \times (8/12) = 178.0$ | 198.6 |
| 6 mm fillet welds (all channels) | $(137) \times (8/6) = 182.6$ | 198.6 |

3.5.2.2 12 mm Thick Door Plates

The maximum stress obtained for the 12 mm thick door plates compared with the corresponding allowable stresses are given in Table 3-10, where:

- $S_z \equiv$ Vertical direction (Z) membrane stress

- S_H \equiv Horizontal direction (X or Y) membrane stress
- S_{HZ} \equiv Shear membrane stresses on the plane of the plate.
- Bending stresses across the plate thickness are negligible and are classified as secondary stresses; however, other directions of the plate contain primary bending stresses that are included in the stress analysis results.

Table 3-10
12 mm Thick Door Plates Stress Results

| Stress Category | Calculated Stress (MPa) | Allowable Stress (MPa) |
|-------------------------------------------------|---------------------------|------------------------|
| Level A Conditions Maximum Membrane Stresses | $S_Z = 0.1$ | 134.1 |
| | $S_H = 0.08$ | 134.1 |
| | $S_{HZ} = 0.2$ | 80.4 |
| Level D Conditions Maximum Membrane Stresses | $S_Z = 40.3$ | 195.2 |
| | $S_H = 123$ (Figure E-27) | 195.2 |
| | $S_{HZ} = 44.2$ | 198.6 |

3.5.2.3 10 mm and (10+8) mm Assembly Grid Plates

The maximum stress obtained for the assembly grid plates compared with the corresponding allowable stresses are given in Table 3-11, where:

- S_Z \equiv Vertical direction (Z) membrane stress
- S_H \equiv Horizontal direction (X or Y) membrane stress
- S_{HZ} \equiv Shear membrane stresses on the plane of the plate.
- Bending stresses across the plate thickness are negligible and are classified as secondary stresses; however, other directions of the plate contain primary bending stresses that are included in the stress analysis results.

Table 3-11
10 mm and (10+8) mm Thickness Assembly Grid Stress Results

| Stress Category | Calculated Stress (MPa) | Allowable Stress (MPa) |
|-------------------------------------------------|-----------------------------|------------------------|
| Level A Conditions Maximum Membrane Stresses | $S_Z = 11$ | 134.1 |
| | $S_H = 14$ | 134.1 |
| | $S_{HZ} = 3$ | 80.4 |
| Lifting Load | $S_{HZ} = 47$ (Figure E-29) | 80.4 |
| Level D Conditions Maximum Membrane Stresses | $S_Z = 37.4$ | 195.2 |
| | $S_H = 52.5$ (Figure E-28) | 195.2 |
| | $S_{HZ} = 7$ | 198.6 |

Welds in these plates are judged to have enough margin in view of the low stress results in plates.

3.5.2.4 Axis and Hinge Plates

The maximum stress obtained for the axis and hinges compared with the corresponding allowable stresses are given in Table 3-12, where:

- $S_Z \equiv$ Vertical direction (Z) membrane stress
- $S_H \equiv$ Horizontal direction (X or Y) membrane stress
- $S_{HZ} \equiv$ Shear membrane stresses on the plane of the plate.
- Bending stresses across the plate thickness are negligible and are classified as secondary stresses; however, other directions of the plate contain primary bending stresses that are included in the stress analysis results.

Table 3-12
Axis and Hinge Stress Results

| Stress Category | Calculated Stress (MPa) | Allowable Stress (MPa) |
|-------------------------------------------------|-------------------------|------------------------|
| Level A Conditions Maximum Membrane Stresses | $S_Z = 3.8$ | 134.1 |
| | $S_H = 1.6$ | 134.1 |
| | $S_{HZ} = 1.1$ | 80.4 |
| Level D Conditions Maximum Membrane Stresses | $S_Z = 106$ | 195.2 |
| | $S_H = 130$ | 195.2 |
| | $S_{HZ} = 31.3$ | 198.6 |

3.5.2.5 15 mm Thick Support-Base Stiffener Plates

The maximum stress obtained for the 15 mm thick stiffener plates and welds compared with the corresponding allowable stresses are given in Table 3-13, where:

- $S_Z \equiv$ Vertical direction (Z) membrane stress
- $S_H \equiv$ Horizontal direction (X or Y) membrane stress
- $S_{HZ} \equiv$ Shear membrane stresses on the plane of the plate
- Bending stresses across the plate thickness are negligible and are classified as secondary stresses; however, other directions of the plate contain primary bending stresses that are included in the stress analysis results.

Table 3-13
15mm Thick Stiffener Plates Stress Results

| Stress Category | Calculated Stress (MPa) | Allowable Stress (MPa) |
|-------------------------------------------------|-------------------------|------------------------|
| Level A Conditions Maximum Membrane Stresses | $S_Z = 2.6$ | 134.1 |
| | $S_H = 8.9$ | 134.1 |
| | $S_{HZ} = 3.2$ | 80.4 |
| Level D Conditions Maximum Membrane Stresses | $S_Z = 127$ | 195.2 |
| | $S_H = 138$ | 195.2 |
| | $S_{HZ} = 54$ | 198.6 |

The stress results in stiffeners welds (7 mm double fillet) are enveloped by the above stress results in plates.

3.5.2.6 15 mm Thick Folded Base Plate and (15+15) mm Thick Bolted Support Plates

The maximum stress obtained for the 15 mm thick folded base plate and in (15+15) mm thick bolted support plates compared with the corresponding allowable stresses are indicated in Table 3-14. Stress values for the bolted support plates are based on the following formula from (Reference 9):

$$\sigma = 0.511 \cdot W / t^2, \text{ where } W \text{ is bolt tensile force (see next Table 5.10) and } t = 30 \text{ mm}$$

Table 3-14
15 mm Thick Folded Base Plate and (15+15) mm Thick Bolted Support Plates Stress Results

| Stress Category | Calculated Stress (MPa) | Allowable Stress (MPa) |
|------------------------------------------|-------------------------|------------------------|
| Level A Conditions. Folded Base plate | 6 | 201.1 |
| Level D Conditions. Folded Base plate | 266 | 292.8 |
| Level A Conditions. Bolted support plate | 1.3 | 201.1 |
| Level D Conditions. Bolted support plate | 124 | 292.8 |

3.5.3 Bolt Stress Results

The actual stress area available for M24x2 bolts is 374.4 mm², based on the minor diameter of the bolt root of 21.835 mm (Reference 8). The maximum reaction forces obtained at the bolt location and the calculated stresses compared with the corresponding allowable stresses are presented in Table 3-15.

Table 3-15
Bolt Stress Results

| Stress Category | Reaction Force (N) | Calculated Stress (MPa) | Allowable Stress (MPa) |
|-----------------------------|--------------------|-------------------------|------------------------|
| Level A Conditions. Shear | 5390 | 14.4 | 123.9 |
| Level A Conditions. Tensile | 2239 | 6.0 | 300.2 |
| Level D Conditions. Shear | 93701 | 250.2 | 419.8 |
| Level D Conditions. Tensile | 218410 | 583.3 | 699.8 |

In addition, the condition for combined shear and tensile stress $f_t^2 / F_{tb}^2 + f_v^2 / F_{vb}^2 \leq 1$ is met:

- For the Level A Condition using the above enveloping reactions:

$$f_t^2 / F_{tb}^2 + f_v^2 / F_{vb}^2 = 0.01 \leq 1$$

- Level the D Condition, the equation has to be checked for each bolt:

| Node# | Rx (N) | Ry (N) | Rz (N) | Shear (N) | Tensile (N) | Tensile stress (MPa) | Shear Stress (MPa) | $f_t^2 / F_{tb}^2 + f_v^2 / F_{vb}^2$ |
|-------|--------|--------|--------|-----------|-------------|----------------------|--------------------|---------------------------------------|
| 1038 | 89212 | 26741 | 194960 | 93134 | 194960 | 520.7 | 248.7 | 0.90 |
| 3164 | 48239 | 21506 | 218390 | 52816 | 218390 | 583.2 | 141.0 | 0.81 |
| 5290 | 29986 | 25363 | 215010 | 39274 | 215010 | 574.2 | 104.9 | 0.74 |
| 7416 | 26379 | 24320 | 170220 | 35879 | 170220 | 454.6 | 95.8 | 0.47 |
| 8479 | 26785 | 24359 | 170490 | 36205 | 170490 | 455.3 | 96.7 | 0.48 |
| 10605 | 29922 | 25807 | 215190 | 39514 | 215190 | 574.7 | 105.5 | 0.74 |
| 12731 | 47734 | 22698 | 218380 | 52856 | 218380 | 583.2 | 141.2 | 0.81 |
| 14857 | 89600 | 27417 | 194450 | 93701 | 194450 | 519.3 | 250.2 | 0.91 |
| 15972 | 89230 | 26730 | 194980 | 93148 | 194980 | 520.7 | 248.8 | 0.90 |
| 18055 | 48239 | 21517 | 218410 | 52820 | 218410 | 583.3 | 141.1 | 0.81 |
| 20137 | 29986 | 25369 | 215020 | 39278 | 215020 | 574.2 | 104.9 | 0.74 |
| 22224 | 26375 | 24315 | 170220 | 35873 | 170220 | 454.6 | 95.8 | 0.47 |
| 23265 | 26786 | 24361 | 170490 | 36207 | 170490 | 455.3 | 96.7 | 0.48 |
| 25344 | 29921 | 25802 | 215180 | 39510 | 215180 | 574.7 | 105.5 | 0.74 |
| 27422 | 47733 | 22686 | 218370 | 52850 | 218370 | 583.2 | 141.1 | 0.81 |
| 29493 | 89582 | 27429 | 194430 | 93687 | 194430 | 519.2 | 250.2 | 0.91 |

and it is verified that:

$$\max (f_t^2 / F_{tb}^2 + f_v^2 / F_{vb}^2) = 0.91 \leq 1$$

3.5.4 Fuel Impact Forces Analysis

In order to obtain the maximum fuel impact forces, a simplified finite element model for the FSR is built with ANSYS 10.0 (Reference 7), one model for the North-South direction and one for the East-West direction.

Each simplified model is composed of 2-D elastic beam BEAM3 elements, and concentrated mass MASS21 elements.

A vertical line of beam elements represents the enveloping plate of the FSR cells, and another vertical line of beam elements represents the fuel elements assembly.

The area properties and inertias of the cell beams have been adequately adjusted so that the model will have the same eigenfrequencies as the detail model in Section 3.4.5. The structural characteristics of the fuel assembly beams are adjusted based on their first axial frequency (ID 4), their axial area, and their moment of inertia.

The coupling between FSR cell and fuel beam immersed in water, are modeled through MATRIX27 elements applied by node pairs (see Reference 10 for details).

Mass elements reproducing the mass of internal water are considered on the connection nodes of the beam elements simulating the FSR cells.

The fuel beam is coupled in the horizontal direction with the FSR beam at the bottom node. One vertical contact element is located at this same location to evaluate whether the fuel uplifts then impacts with a vertical load when it falls and strikes the base plate.

Between the FSR beam top node and fuel beam top node, two horizontal contact elements (one for each direction of movement) are located to evaluate any potential lateral impacts that may be produced against the FSR cells. The stiffness of these contacts has been estimated by a local analysis made with the detail analysis model, applying local loads at the top cell level.

Based on the acceleration time-histories corresponding to the SSE (ID 8), double integration is used to generate the displacement histories to be applied at the node of the model that represent the pool. Intervals of 0.005 s were used, which means 3200 load steps for a 16-s transient.

The dead weight and the buoyancy effects are considered during the process by application of a constant vertical downward acceleration value of 8.6 g (reduced gravity acceleration, see Section 3.4.6.1).

The maximum impact loads obtained from the this local analysis are:

$$\text{Maximum top fuel horizontal force} \Rightarrow \text{FHT} \approx 1.2 \text{ E}+4 / 28 = 429 \text{ N}$$

$$\text{Maximum bottom fuel horizontal force} \Rightarrow \text{FHB} \approx 5.3 \text{ E}+4 / 28 = 1893 \text{ N}$$

$$\text{Maximum bottom fuel vertical force} \Rightarrow \text{FHT} \approx 150 \text{ E}+4 / 28 = 53571 \text{ N}$$

The stresses produced by these impact forces are analyzed using the detailed FSR model defined in Section 3.4.5. The analysis is only focused on the stress produced for the FSR fuel base plate, since the top fuel impact forces obtained are low and therefore judged to be insignificant.

The impact forces are applied in the three directions by nodal forces on the circular holes of the fuel support base plate.

The vertical fuel impact forces have high values. For this reason a plastic material analysis is considered for the FSR fuel base plate. The plastic stress-strain material curve is obtained from Reference 11.

The stress distribution on the base plate is show in Figure E-30. The maximum stress is $S_{\max} = 180 \text{ MPa}$.

This maximum stress is lower than the maximum membrane plus bending admissible stress from Appendix F, F-1341.2 Reference 4, $S_{\text{adm}} = 0.9 \times S_U = 436 \text{ MPa}$.

3.6 CONCLUSIONS

The analyses performed for the FSRs with the geometry of drawings ID 1, 2, 3 and 6 demonstrate the integrity of these structures when subjected to the applicable loads and load combinations as described in the report.

The analyses presented herein demonstrate that the FSR satisfy the structural requirements of ASME B&PV Code, Section III, Subsection NF (Reference 3) for all proposed loading condition specified in FSR Design Specification (ID 4).

The geometry analyzed corresponds to a continuous 2x14 cell rack, formed by joining two 2x7 cell racks per drawing ID 6, because:

- The racks response is dependant on bending in the out of plane direction (or short, dimension), rather than the long dimension.
- Since the forces at rack junctions are assumed to be low, the joining pieces will be simple as designed.
- Additionally, the base plate is a “very rigid” structure that is bolted to the pool floor and there are no internal forces in the longitudinal direction to connect cells. In other words, the connection of racks is through the concrete at the pool floor. Therefore, it is not necessary to utilize a steel base plate connection.

Table 3.2 summarizes results obtained from the analysis of the FSR components: plate thickness, welds, and anchor bolts. Included in the table are the ratios of the actual results with their allowable values.

3.7 REFERENCES

1. ASME Boiler & Pressure Vessel Code, Section II Materials, Part A Ferrous Material Specifications, 2001 Edition with Add. 2003
2. ASME Boiler & Pressure Vessel Code, Section II Materials, Part D Properties (Customary), 2001 Edition with Add. 2003
3. ASME Boiler & Pressure Vessel Code, Section III Rules for Construction of Nuclear Facility Components, Division 1, Subsection NF, Supports, 2001 Edition with Add. 2003
4. ASME Boiler & Pressure Vessel Code, Section III Rules for Construction of Nuclear Facility Components, Division 1, Appendices, 2001 Edition with Add. 2003
5. Regulatory Guide 1.92, Rev. 1. Combining Modal Responses and Spatial Components in Seismic Response Analysis
6. Sarpkaya: Mechanics of Wave Forces on Off-Shore Structures
7. ANSYS 10.0 Documentation (User Manual, Theoretical Manual)
8. ASME B1.13M-2001 Metric Screw Threads: M Profile
9. ROARK'S Formulas for Stress & Strain, 6th Edition
10. 092-175-F-M-00001, Issue 2, Spent High Density Fuel Storage Racks Design Report

11. NUREG/CR-0481, "An Assessment of Stress-Strain Data Suitable for Finite-Element Elastic-Plastic Analysis of Shipping Containers", H.J. Rack y G.A. Knorovsky, Syia Laboratories, SY77-1872, September 1978
12. Regulatory Guide 1.61, Rev.1. Damping Values for Seismic Design of Nuclear Power Plants

APPENDIX E - FIGURES

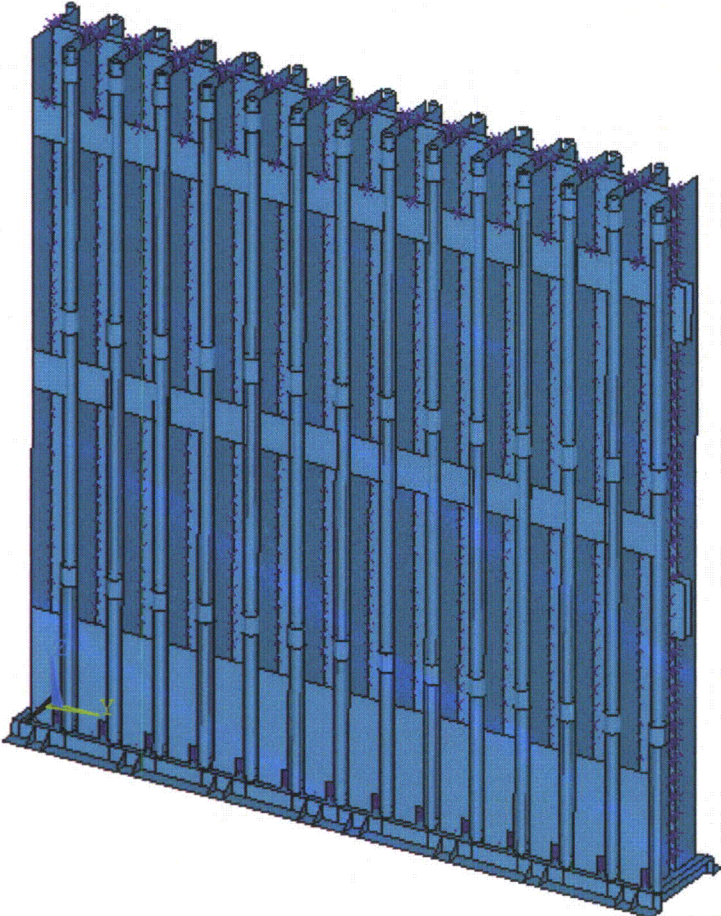


Figure E-1. FSR FEM

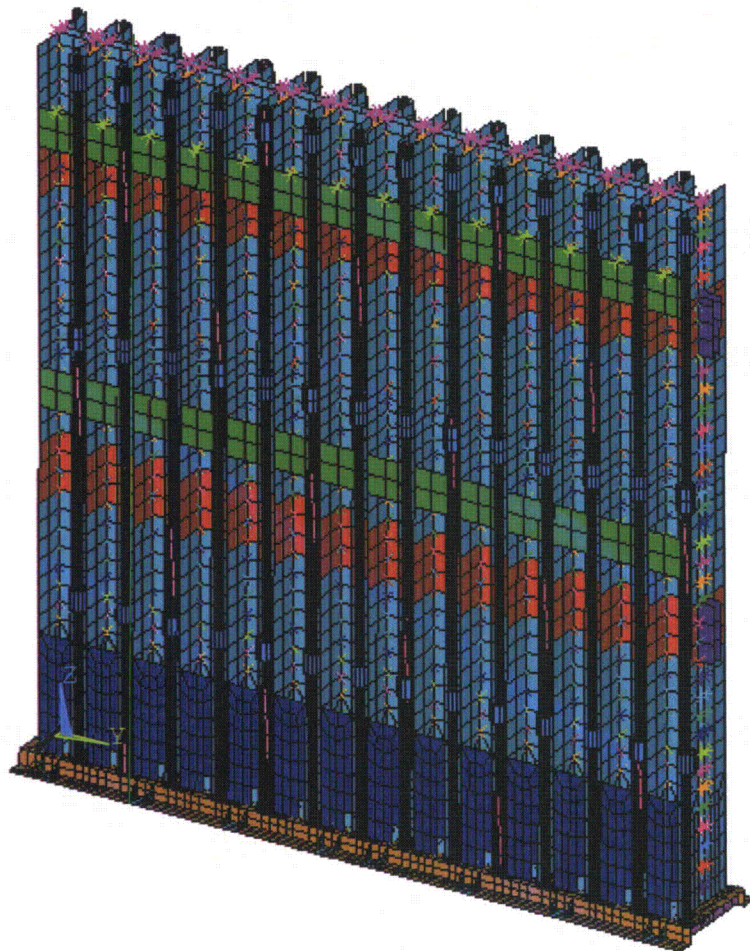


Figure E-2. FSR FEM

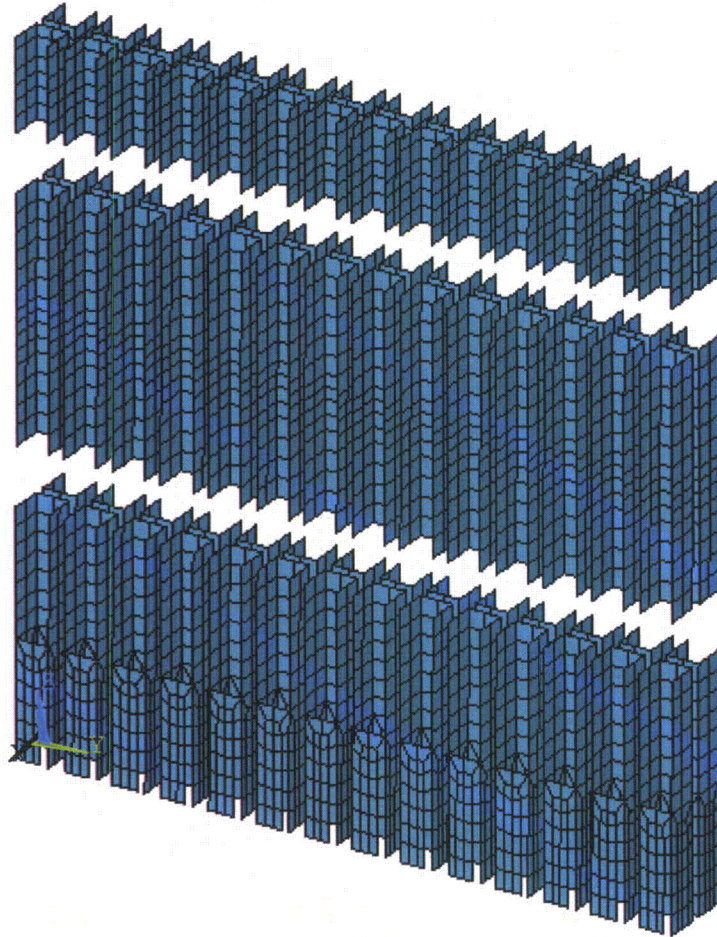
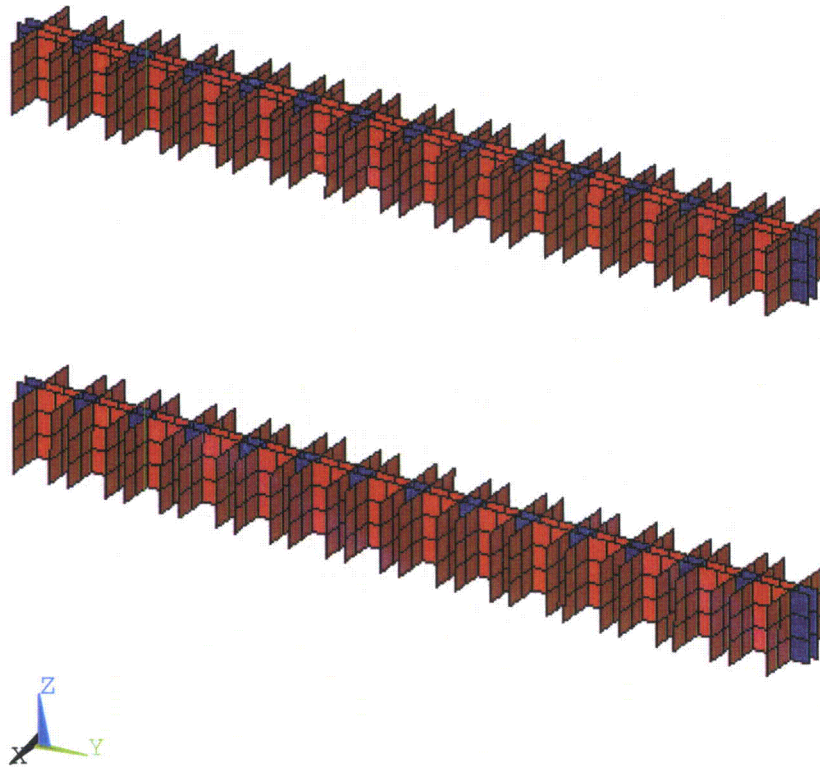


Figure E-3. FSR FEM 8 mm Thick Channel Plates



**Figure E-4. FSR FEM (10+8) mm Thick (Grid+Channel) Plates in Red, and
10 mm Thick Grid Plates in Purple**

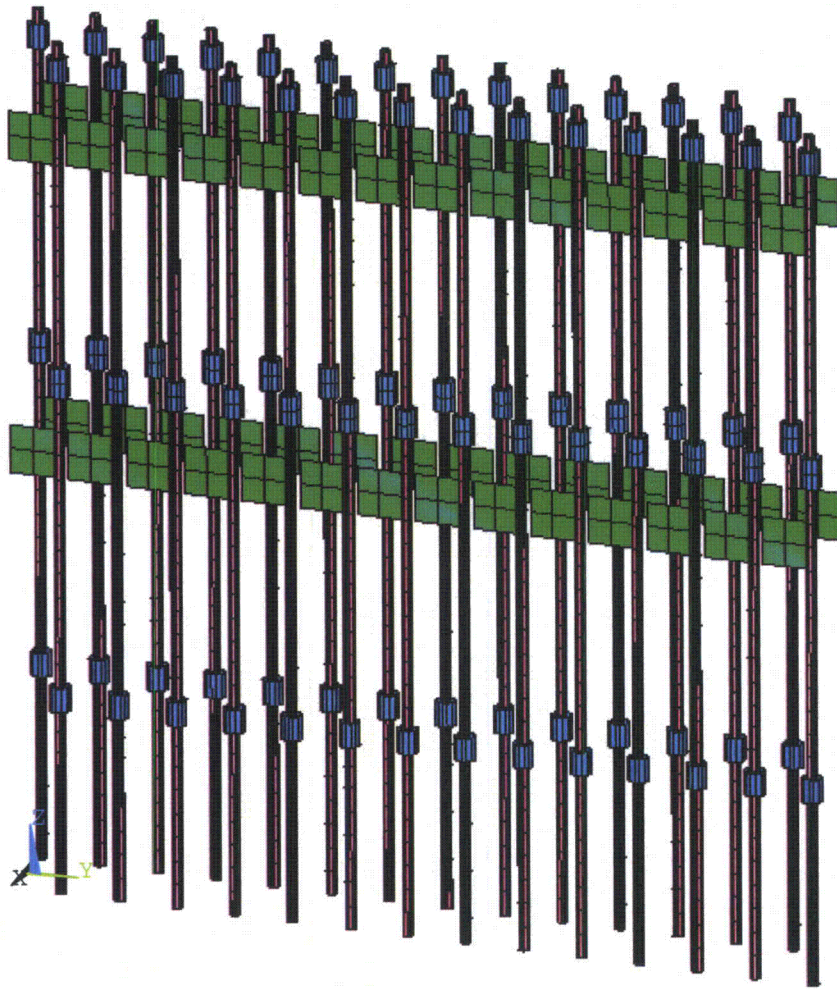


Figure E-5. FSR FEM 12 mm Thick Door Plates, 7.5 mm Thick Door Axis Plate and 10 mm Thick Hinge Plates

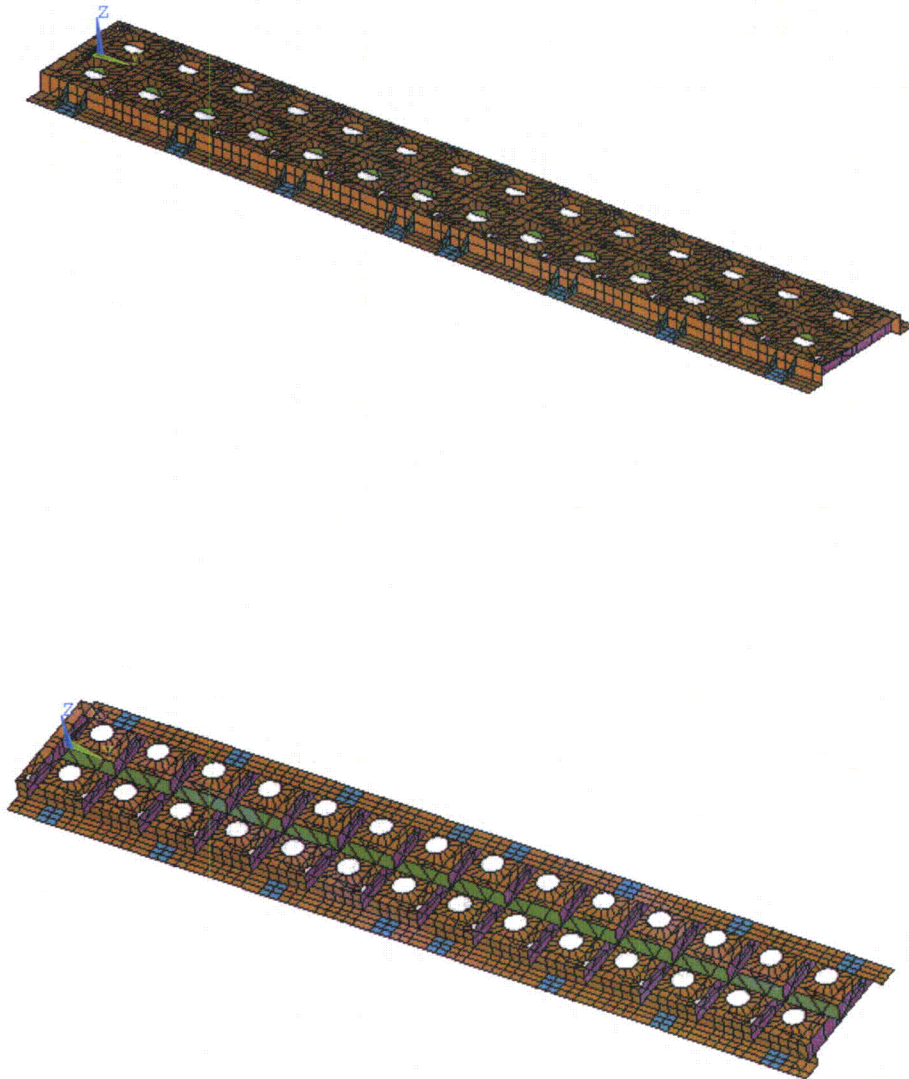


Figure E-6. FSR FEM 15 mm Thick Support-Base Plate and Stiffener Plates, and (15+15) mm Reinforced Bolted Plate in Llu

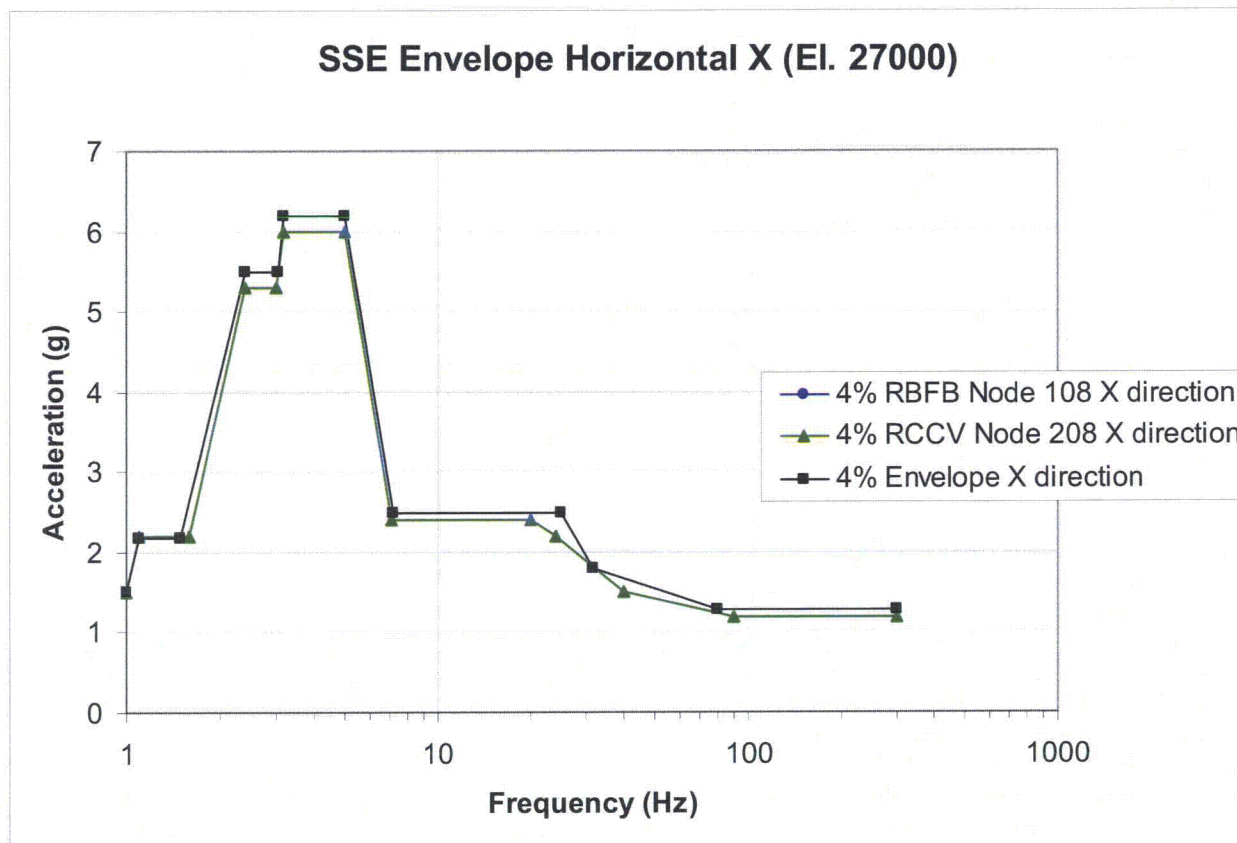


Figure E-7a. SSE Horizontal X Enveloping Floor Response Spectra

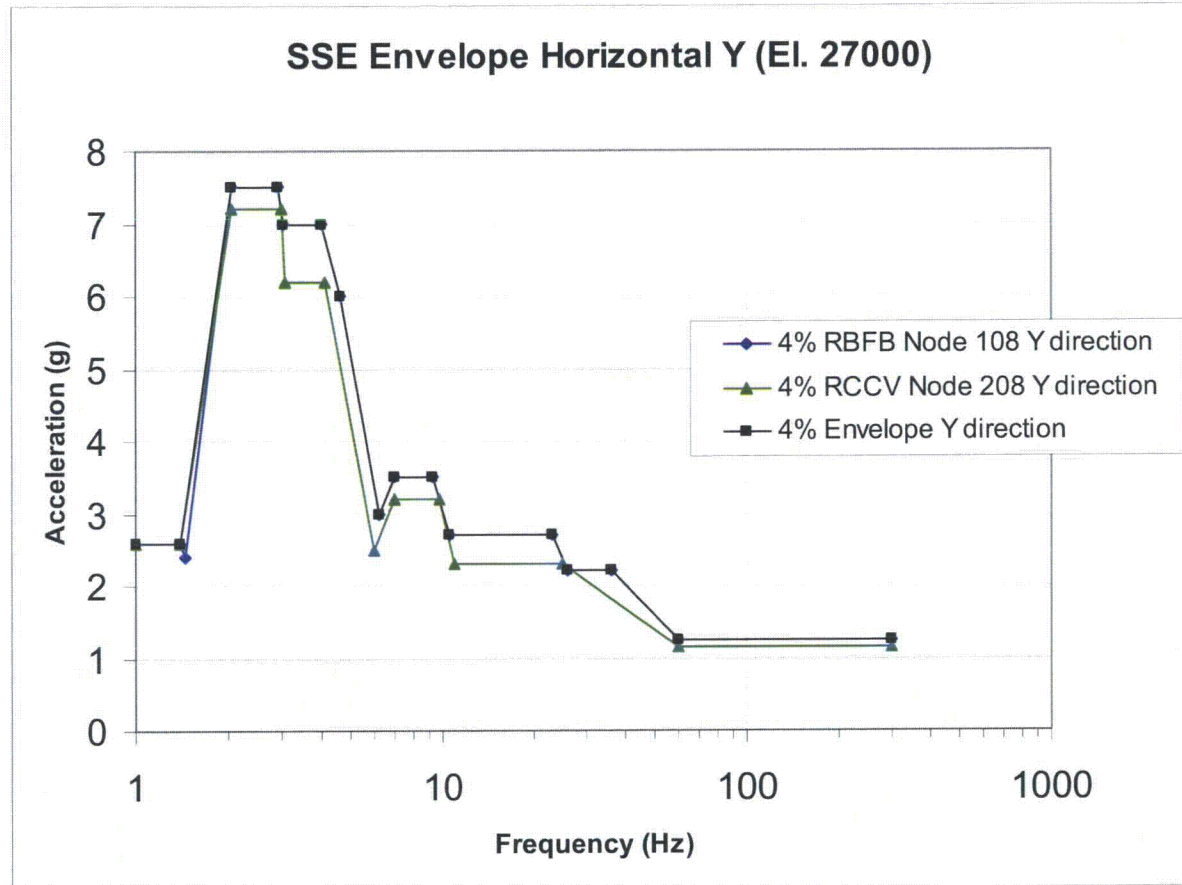


Figure E-7b. SSE Horizontal Y Enveloping Floor Response Spectra

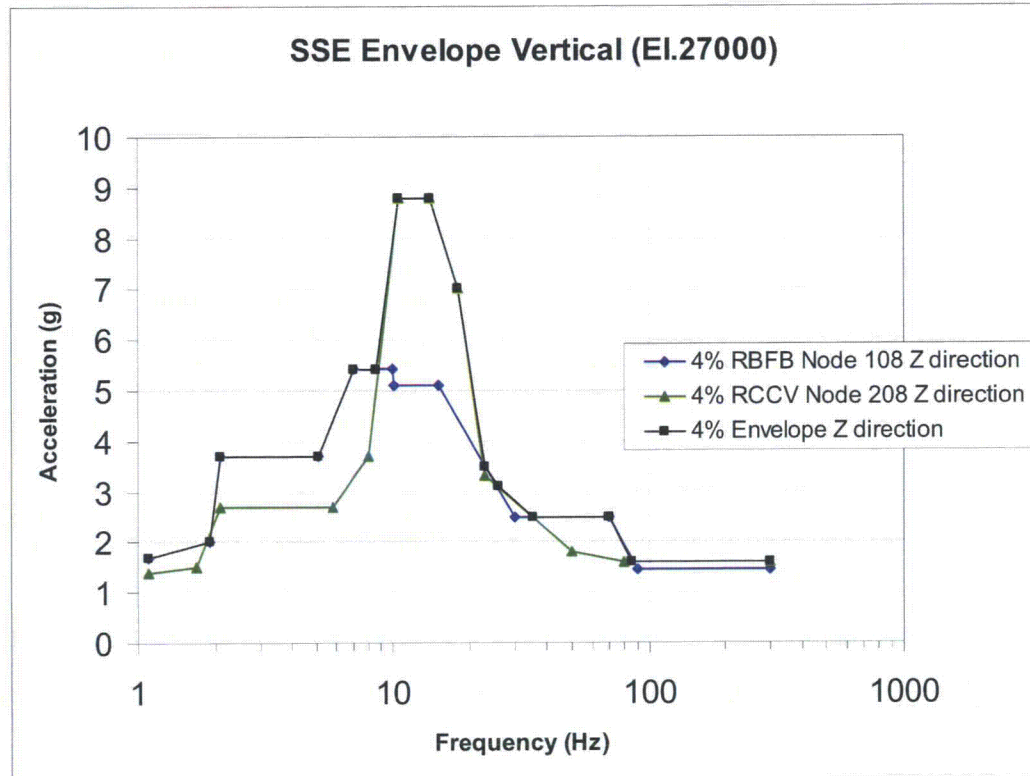


Figure E-8. SSE Vertical Enveloping Floor Response Spectra

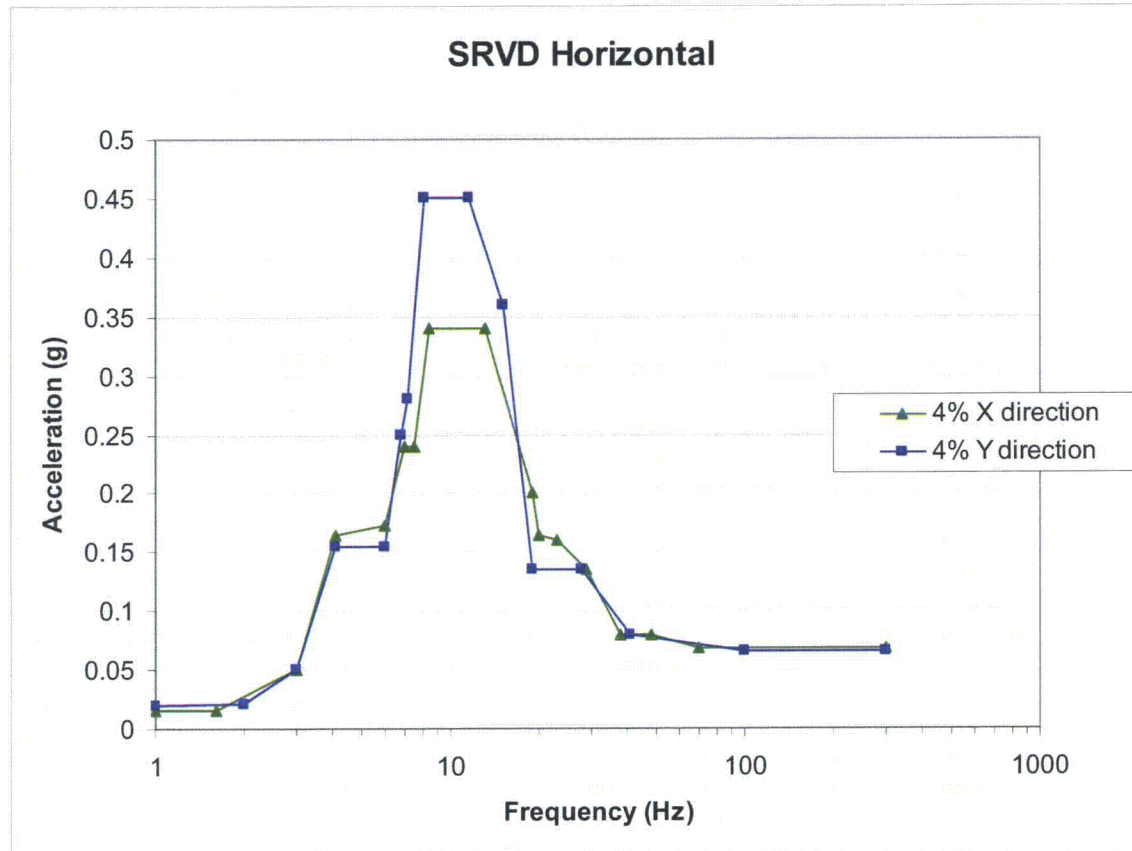


Figure E-9. SRVD Horizontal Enveloping Floor Response Spectra

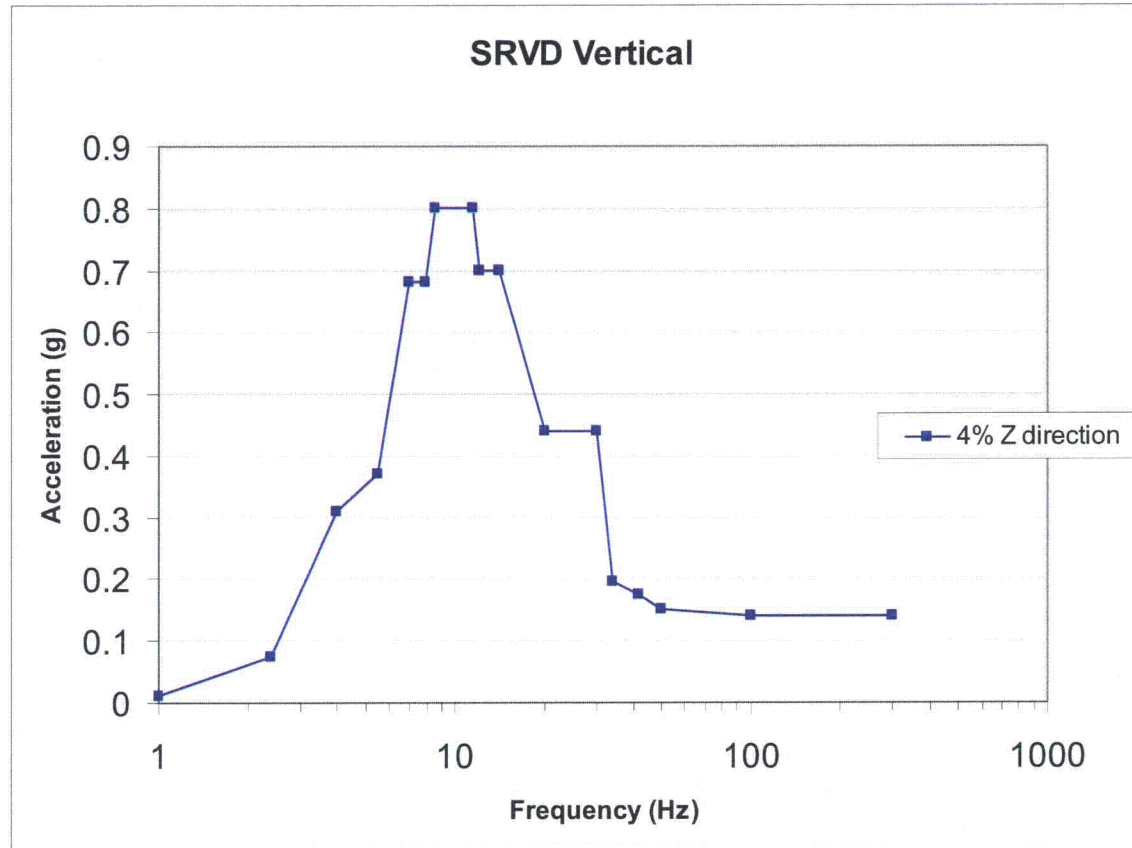


Figure E-10. SRVD Vertical Enveloping Floor Response Spectra

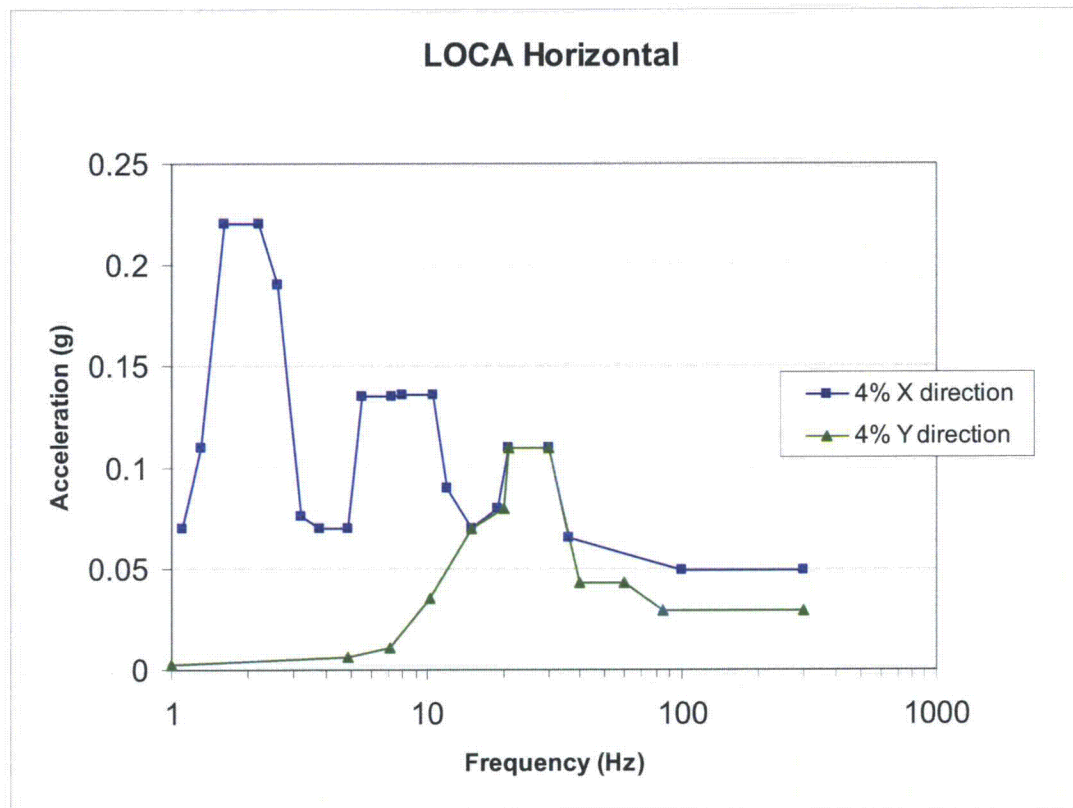


Figure E-11. LOCA Horizontal Enveloping Floor Response Spectra

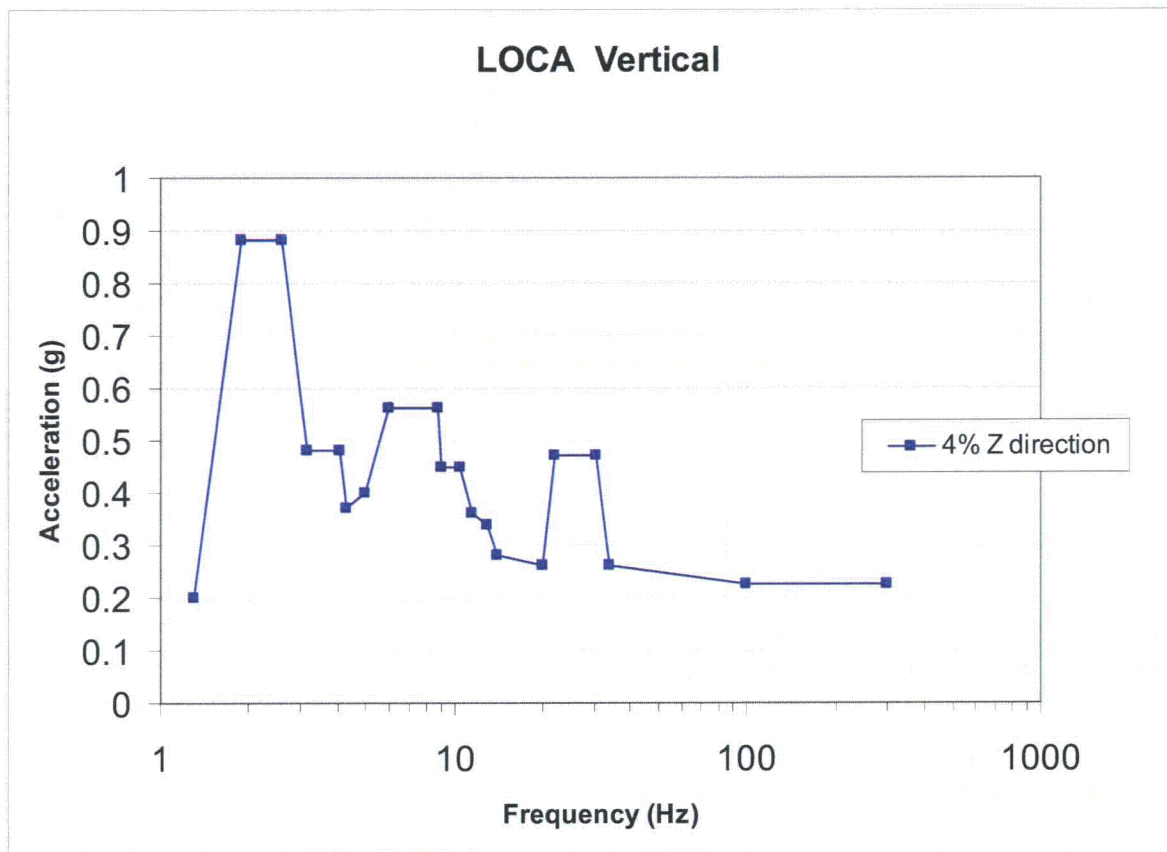


Figure E-12. LOCA Horizontal Enveloping Floor Response Spectra

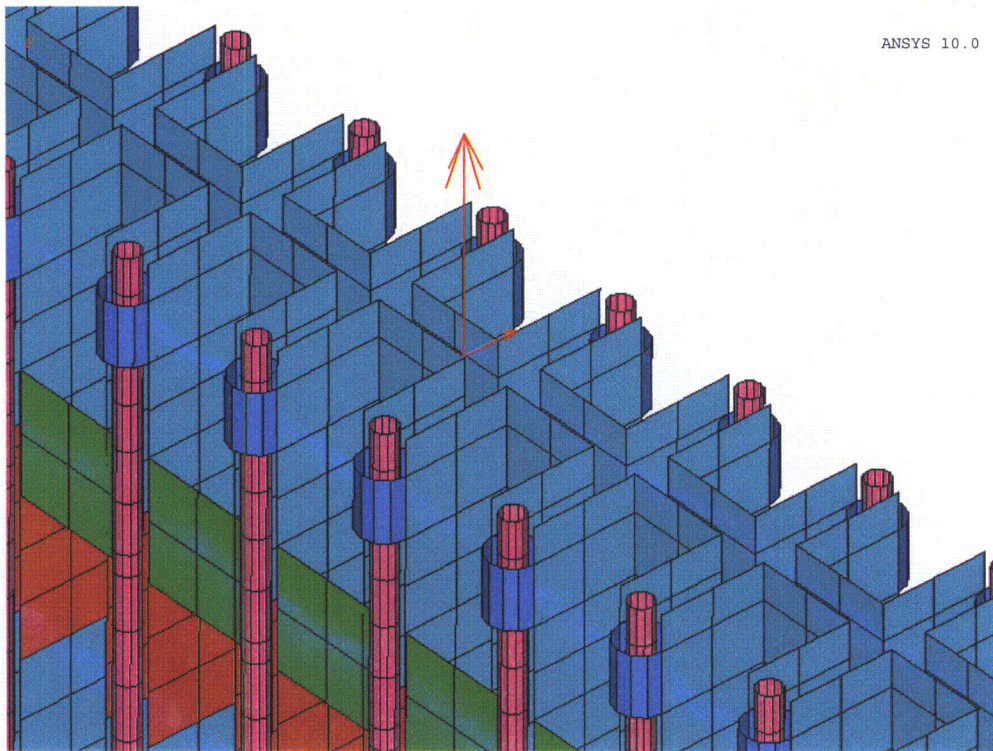


Figure E-13. FSR Fuel Handling Loads

STEP=1
SUB =1
FREQ=7.058
RSYS=0
DMX =.012838

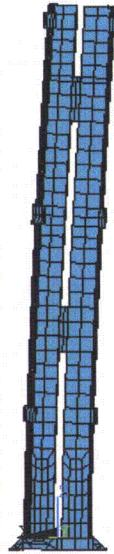


Figure E-14. FSR Deformed Shape Eigenmode 1

STEP=1
SUB =2
FREQ=7.215
RSYS=0
DMX =.021728



Figure E-15. FSR Deformed Shape Eigenmode 2

STEP=1
SUB =3
FREQ=9.572
RSYS=0
DMX =.025428

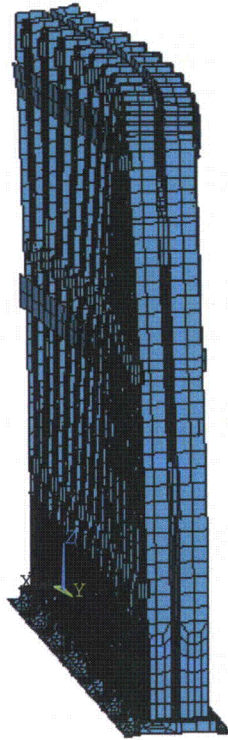


Figure E-16. FSR Deformed Shape Eigenmode 3

STEP=1
SUB =4
FREQ=14.474
RSYS=0
DMX =.026132

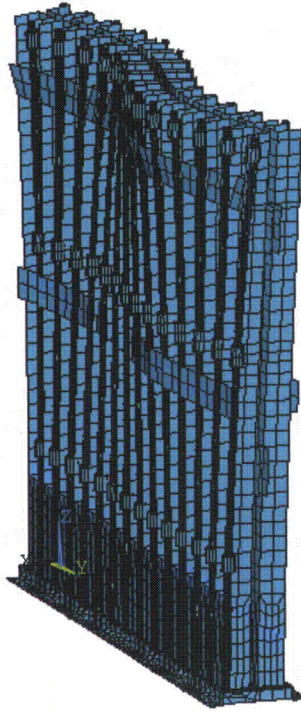


Figure E-17. FSR Deformed Shape Eigenmode 4

STEP=1
SUB =5
FREQ=16.797
RSYS=0
DMX =.013647

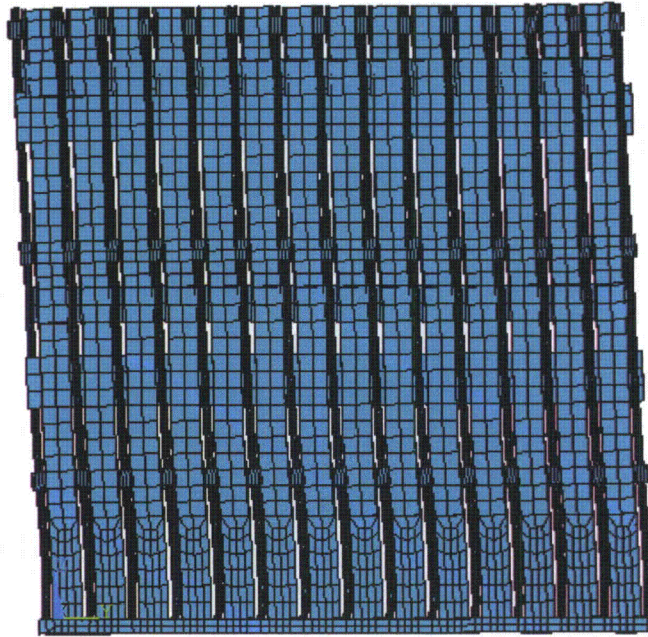


Figure E-18. FSR Deformed Shape Eigenmode 5

STEP=1
SUB =31
FREQ=33.17
RSYS=0
DMX =.02189

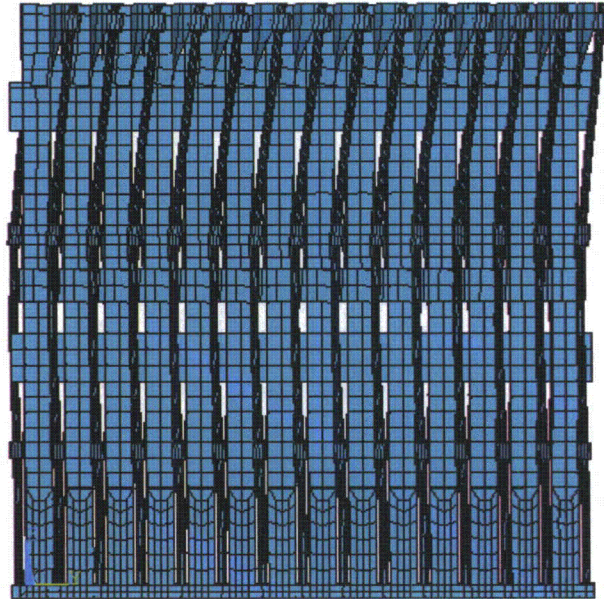


Figure E-19. FSR Deformed Shape Eigenmode 31

STEP=1
SUB =31
FREQ=33.17
RSYS=0
DMX =.02189

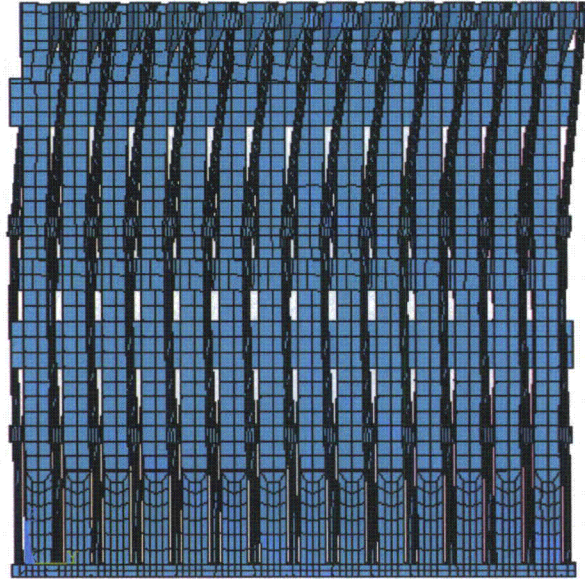


Figure E-20. FSR Deformed Shape Eigenmode 61

STEP=1
SUB =63
FREQ=51.019
RSYS=0
DMX =.069377

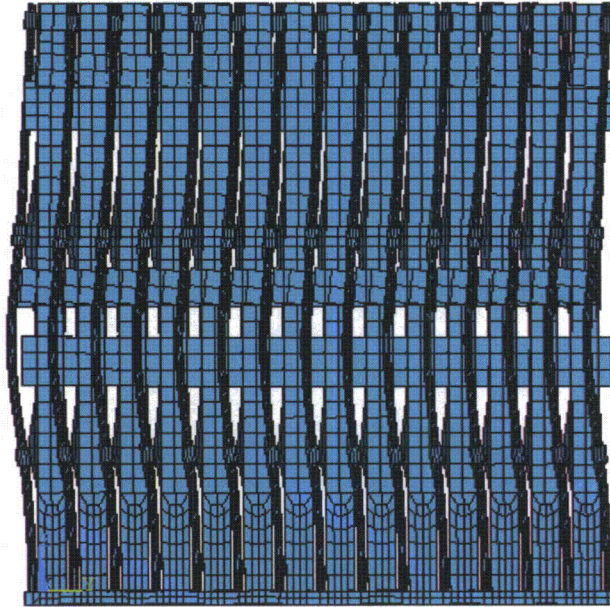


Figure E-21. FSR Deformed Shape Eigenmode 63

STEP=1
SUB =69
FREQ=54.236
RSYS=0
DMX =.108781



Figure E-22. FSR Deformed Shape Eigenmode 69

STEP=1
SUB =71
FREQ=54.423
RSYS=0
DMX =.116733

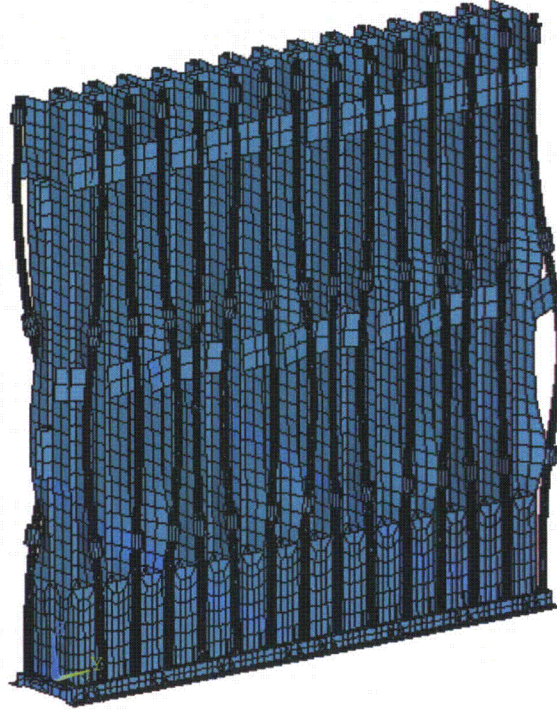


Figure E-23. FSR Deformed Shape Eigenmode 71

UX
TOP
RSYS=0
DMX = .018213
SMN = -.018165
SMX = .018039

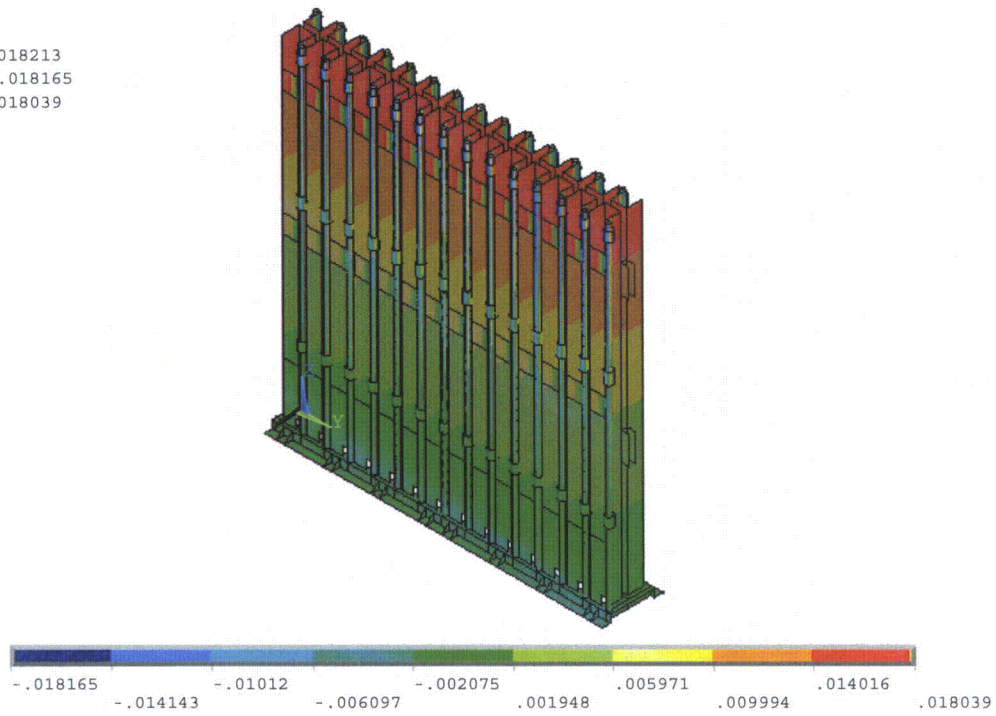


Figure E-24. FSR Horizontal Displacement X (m)

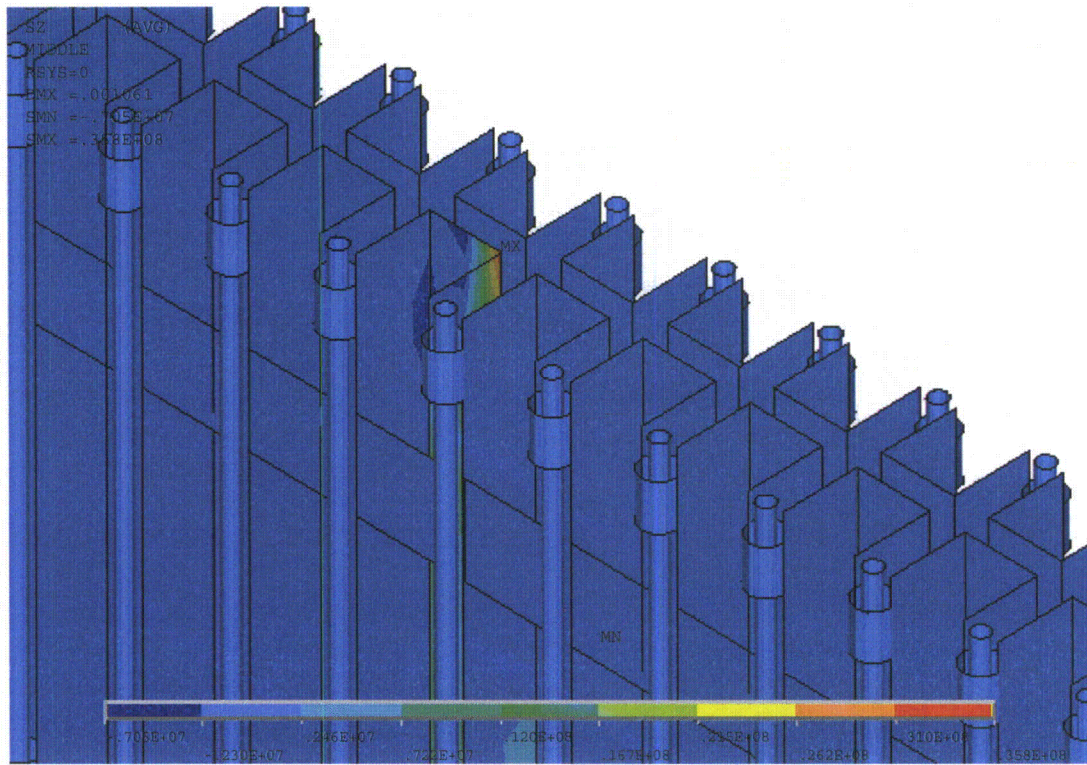


Figure E-25. FSR 8 mm Channel Plates. Level A Vertical Stress (N/m²)

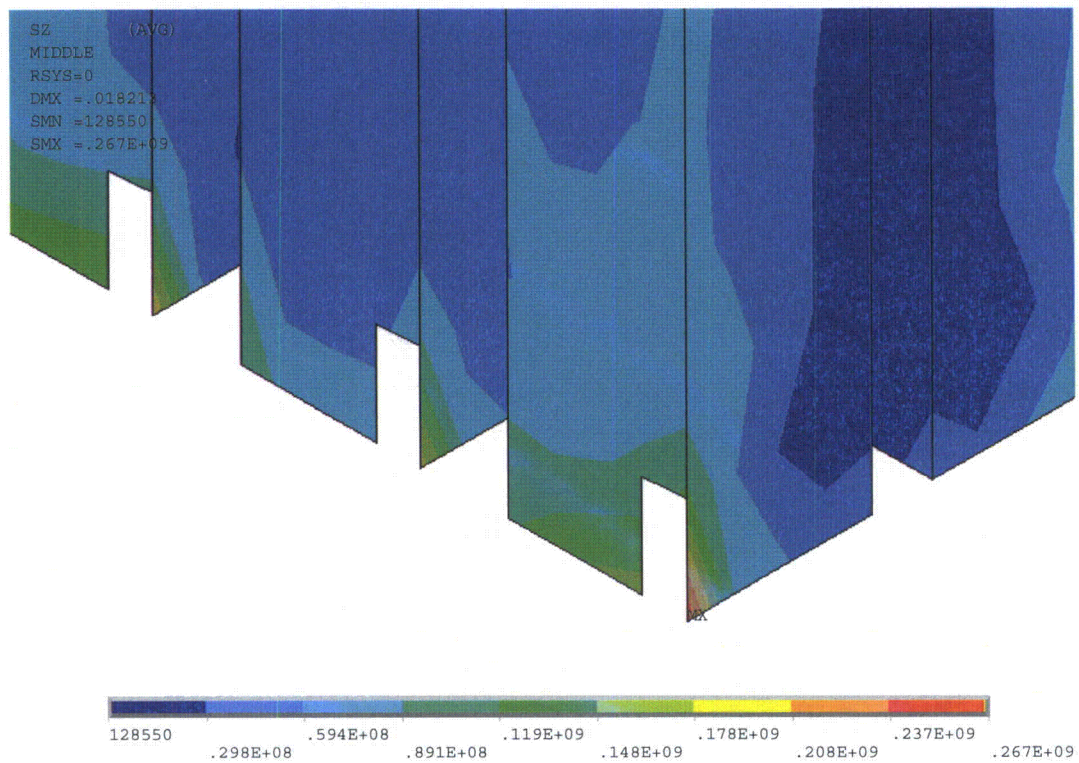


Figure E-26. FSR 8 mm Channel Plates. Level D Vertical Stress (N/m²)

SUB =1
SY (AVG)
MIDDLE
RSYS=0
DMX =.017416
SMN =109050
SMX =.123E+09

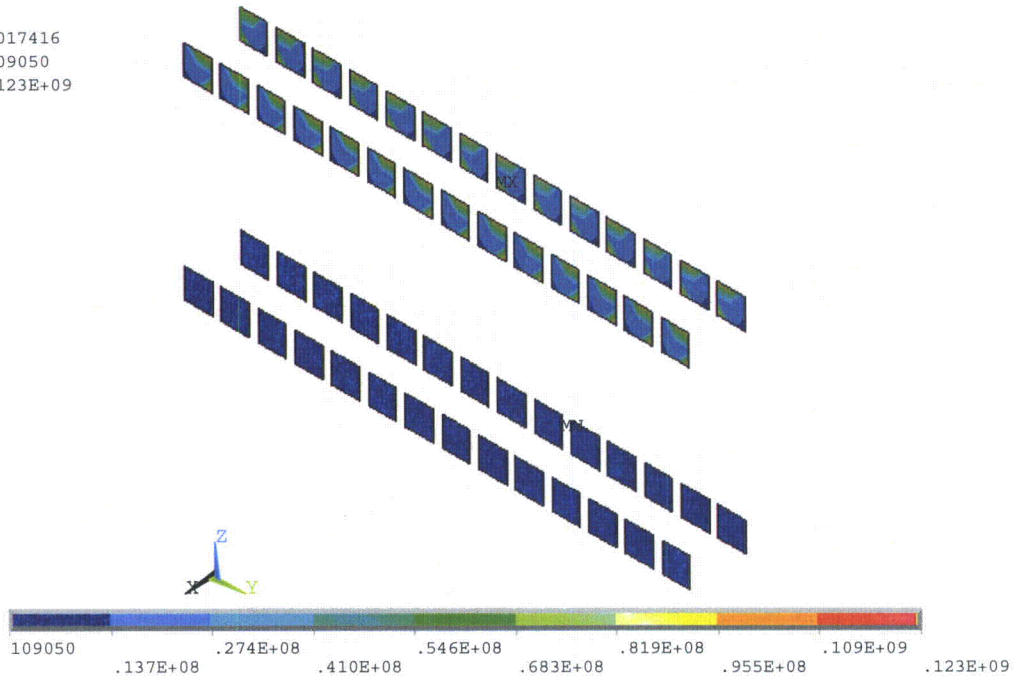


Figure E-27. FSR 12 mm Door Plates. Level D Horizontal Stress (N/m²)

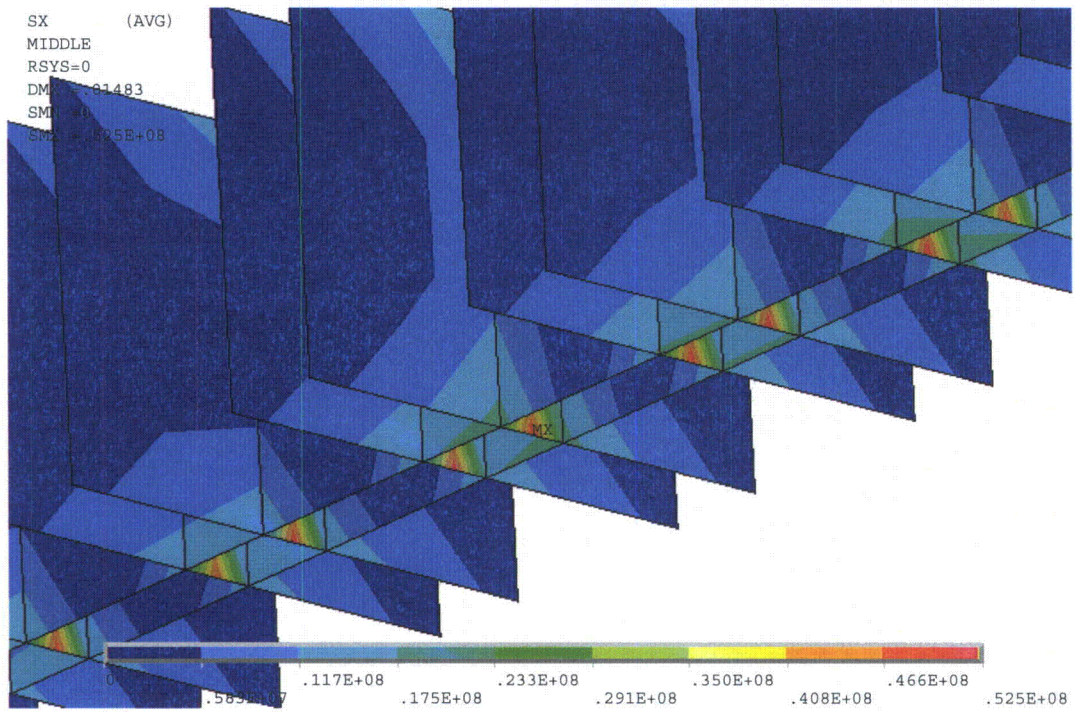


Figure E-28. FSR Assembly Grid Plate. Level D Horizontal Stress (N/m²)

SZ (AVG)
MIDDLE
RSYS=0
DMX = .369E-03
SMN = -.741E+07
SMX = .473E+08

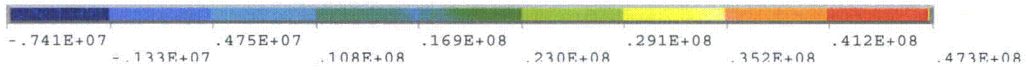


Figure E-29. Lifting Load Stresses (N/m²)

SINT (AVG)
TOP
DMX = .425E-03
SMN = .215E+07
SMX = .180E+09

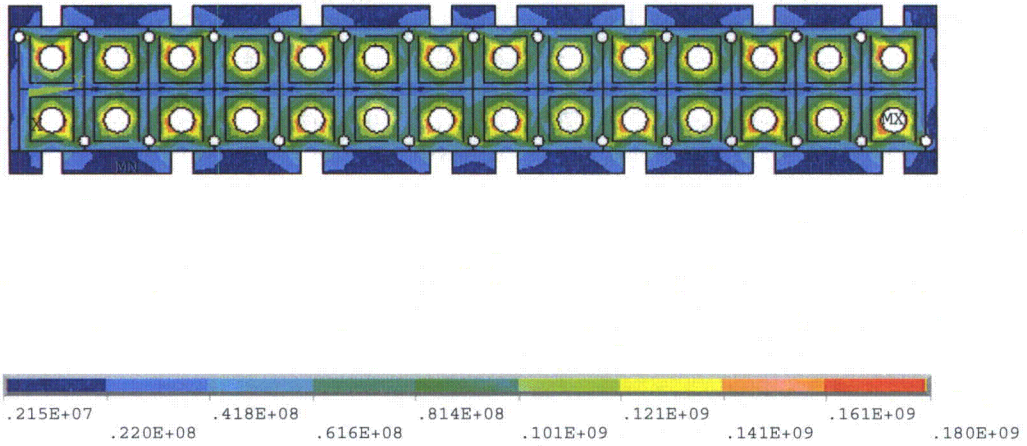


Figure E-30. Fuel Impact Forces. Base Plate Stresses (N/m²)

APPENDIX F - (DELETED)

4. LOAD-DROP (IMPACT) ANALYSIS

4.1 INTRODUCTION

Load drop analysis is required in the design of fuel storage racks for new and spent fuel elements. All the racks have to withstand a number of operational and accidental loads. This section is concerned with the effects of postulated impacts arising from the accidental drop of fuel elements onto the various racks during operations at the plant.

4.1.1 Object

The object of the work consists of evaluating the performance of the ESBWR racks when they are subjected to postulated accidental impacts from fuel elements. There are two types of racks to be considered: racks for spent fuel and racks for fresh fuel.

In the case of the spent fuel racks, the dropped mass may impact the upper part of the rack, in which case the distortions caused should not affect criticality (i.e. should not reach the active zones of the elements stored in adjoining cells); also, fuel cells other than those directly involved in the impact should not be affected by the accident. Alternatively, the dropped mass may not interact with the upper part of the rack, but enter a cell and proceed all the way to the bottom plate, which should then be capable of successfully arresting the falling mass.

In the case of the fresh fuel racks, the dropped mass may impact the upper part of the short wall of the cell, an accident that should not affect the walls separating contiguous elements. Alternatively, it could continue to impact the bottom plate, which should be capable of successfully arresting the falling mass.

4.1.2 Scope

In order to carry out the evaluations mentioned, the necessary data was first acquired and critically assessed. When the value of a parameter could vary over a range, conservative assumptions have been incorporated to evaluate the postulated accidents.

The evaluations have been performed using a combination of computer calculations, hand calculations and engineering judgment, depending on the specific characteristics of the case of interest. The computer calculations are all finite element analyses based on explicit integration in the time domain using Lagrangian formulations. The code Abaqus/Explicit (SIMULIA, 2008) has been used for this task.

As mentioned earlier in relation with spent fuel racks, a dropped element may fall through to the bottom of a cell and impact the base plate of the rack; alternatively, it may be arrested at the top of the storage cells by impact against the upper part of the cell walls. Both possible alternatives have been considered in the present work. For the spent fuel racks, the impacts on the upper part of the cells are supposed to correspond to 6.4 m drops. However, for the impacts on the base plate, the drops are assumed to take place from an elevation of 1.8 m above the top of the racks.

For the fresh fuel racks, the element drops from 1 m above the base plate, thus prescribing the drops heights for impacts against the top of the wall and against the base plate.

It has been assumed that a 201 kg handling tool may or may not accompany the dropped fuel element in all cases; hence the analyses have been repeated with and without the handling tool. Since no specific details are currently known about the handling tool, it has been represented simply as a point mass fixed to the top of the fuel element.

For the spent fuel racks, in which the impacts involve considerable drop heights, the interaction of the falling element with the surrounding water has been taken into account; this removes part of the energy of the dropped element. However, for the impacts against the fresh fuel racks, in which the drop heights are rather small, the effects of this interaction have been conservatively neglected.

4.1.3 Layout of Report

The report is organized as follows:

Section 4.2 describes the problems under consideration, including the geometry and behavior of the falling fuel element and the two types of storage racks, as well as the accident conditions.

The next two sections are dedicated to studying the impacts on spent fuel racks. Section 4.3 is concerned with impacts against the base plate, while Section 4.4 deals with the impacts taking place against the upper part of the rack.

Section 4.5 discusses the impacts against fresh fuel racks, including both the case in which the dropped element impacts the top of the wall and that in which it continues falling through the interior of one of the storage cells to reach the bottom plate.

The conclusions and recommendations derived from the work conducted are presented in Section 4.6.

The appendix contains the list of bibliographic references mentioned in the text of the report.

4.2 DESCRIPTION OF THE PROBLEM

4.2.1 The Fuel Element and Handling Tool

The ESBWR fuel element under consideration is a 10x10 BWR fuel element (GE14E), which is slightly shorter than the traditional fuel elements.

From the viewpoint of the present analyses, the basic mechanical properties of the ESBWR fuel element are the following:

- global mass of the element: $m = 244$ kg
- length of the element: $l = 3.671$ m
- first longitudinal frequency: $f_1 = 124$ Hz

The geometrical shape of the nose at the bottom of the element must be reproduced fairly precisely in the models in order to achieve realistic results during the interaction, but it only involves a comparatively small mass. Apart from that mass, the rest of the fuel element is assumed to behave as a uniform elastic bar with the properties listed above; this assumption is conservative in that it maximizes the forces and damage caused to the rack, which would obviously be smaller if the element were assumed to collapse.

Together with the fuel element, the fuel handling tool is assumed to fall. The only known characteristics about the fuel handling tool are its mass of 201 kg and the fact that its cross section would allow it to follow an element entering a cell without interacting with the cell walls. For lack of more detailed information about the tool, it will be represented here as a point mass, rigidly fixed to the top of the fuel element; again this is considered to be a conservative assumption, as the exchange of momentum would be slower with a more deformable tool or connection with the fuel element.

It has been assumed that the falling fuel element will not collapse or undergo plastic deformations. This is always conservative because all the impact energy has to be dissipated in deformations of the impacted rack or kept as kinetic energy (rebound velocity and internal vibrations)

4.2.2 Spent Fuel Racks

4.2.2.1 Description

The rack is described in ENSA drawing no. 5926.D200 rev. 02. It is designed to house 15 x 12 fuel elements within a rectangular arrangement measuring 2.541 m x 2.037 m. The height of the storage cells is 3.587 m, with the top of their base plate located at 0.289 m above the bottom of the pool. The thickness of the uppermost plates of the rack is 7 mm. An elevation view of the rack can be seen in Figure 4-1.

The rack rests on four symmetrically arranged supports, located under the four corner cells. The base plate is 20 mm thick and is provided with a partially tapered orifice for engaging the nose of the fuel element. It is reinforced by several stiffeners, as can be seen in Figure 4-2 and is described in ENSA drawing no. 5926.D210 rev. 02.

The storage cells provide a square inner space, 168 mm per side, and their geometry is described in ENSA drawing no. 5926.D220 rev. 00.

Most of the rack is made with borated steel plates with 3.4 mm thickness. However, the base plate of the rack and the uppermost plates of the cells provide greater structural integrity and are free from isolation requirements; as a consequence, these parts are made using SA-240 Tp.304L steel.

The two steels mentioned have been characterised with a Young's modulus of 210 GPa and a yield stress of 206 Mpa (ASME, 2003). The stress-strain curves are similar in both cases except in respect of the ductility, which attains 0.4 for the structural steel but is limited to only 0.09 for the borated steel. The stress-strain curve mentioned is shown in Figure 4-3.

4.2.2.2 Postulated Accidents

The accidents considered involve drops of a fuel element from various heights above the top of the storage cells. The dropped fuel element may impact the upper part of the walls of the storage cells or, alternatively, it may enter one of the cells and, if the cell is empty, continue falling until it is finally arrested by the base plate.

Following the specifications, the impacts against the upper part of the rack are taken to correspond to 6.4 m drops. By contrast, impacts against the base plate are assumed to take place from an elevation 1.8 m above the top of the rack.

The fall of the fuel element takes place through water, which removes some of the energy from the drop. Following GE's practice (GE, 1978), it will be assumed that the interaction with water removes 20% of the energy of an element falling freely in 1.8 m of water. In the case of the element continuing its fall through one of the storage cells, velocities increase and the lateral confinement of the water by the cell walls provides a more effective brake: the interaction with water would remove then 70% of the energy of the falling element prior to its impact with the base plate. For 6.4 m drops onto the top of the rack, the energy dissipation has been calculated so as to maintain consistency with the 20% dissipation occurring over 1.8 m of unrestrained water.

The above considerations entail an impact velocity of 7.82 m/s for the impacts against the top of the storage cells and 5.68 m/s for the impacts against the base plate.

It is important to consider the reasons why the postulated impacts are potentially significant:

1. Damage to the Rack Cells

The distortions caused by the impacts on the upper part of the cells should be limited; in particular the damage should not reach the active part of other elements stored in adjacent cells. Also, cells other than that directly involved in the impact should not be affected by the accident.

2. Damage to the Base Plate

The base plate should be able to successfully arrest the dropped element, thus preventing its progress towards the pool liner.

3. Survival of the Supports

Excessive loads on the supports of the rack could lead to a failure. Conservative analyses must therefore be carried out to determine the forces developed at the supports in order to allow carrying out the necessary verifications.

4.2.3 Fresh Fuel Racks

4.2.3.1 Description

The fresh fuel racks are described in ENSA drawings no. 5926.D500 rev. 00 and 5926.D510 rev. 00. They are designed to house 2x7 fuel elements within a rectangular arrangement measuring

1.836 m x 0.650 m. The total height of the rack is 3.697 m, with the top of the base plate located at 0.110 m above the bottom of the pool. An elevation view of the rack can be seen in Figure 4-4.

The walls of the cells extend all the way from the base plate to the top except for the outer faces. In those faces the wall is only 0.600 m high in order to allow entry of the element, although there is also an operable door at the top in order to restrain a stored element from leaving the cell accidentally.

The base plate is made with 15 mm structural steel plate and has a number of stiffening members. Figure 4-5 presents a view of the base plate of the fresh fuel racks.

The material used for constructing the fresh fuel racks is the same structural steel SA-240 Tp.304L also employed in the spent fuel racks. Its basic mechanical characteristics were already given in Section 4.2.2.1.

4.2.3.2 Postulated Accidents

The accidents considered here involve drops of a fuel element from a height 1.000 m above the base plate of the rack. The dropped fuel element may impact the upper part of the short wall at the bottom of the storage cells or, alternatively, it may continue falling until it is finally arrested by the base plate. Hence impacts against the wall correspond to 0.400 m drops and impacts against the base plate are associated with 1.000 m drops.

The fall of the fuel element takes place through water, which removes some of the energy from the drop. However, since the drop heights are relatively small and so would be the amount of energy dissipation, this effect has been conservatively neglected. These considerations entail an impact velocity of 2.80 m/s for the impacts against the top of the short wall, which increases to 4.43 m/s for impacts against the base plate.

The reasons why the postulated impacts are potentially significant in the context of the fresh fuel racks are the following:

1. Damage to the rack cells

The distortions caused by the impacts on the upper part of the short wall of the cell should be limited; in particular the double wall separating contiguous elements should remain in place in spite of the accident.

2. Damage to the base plate

The base plate should be able to successfully arrest the dropped element, thus preventing its progress towards the pool liner.

3. Survival of the supports

Excessive loads on the supports of the rack could lead to a failure. Conservative analyses must therefore be carried out to determine the forces developed at the supports in order to allow carrying out the necessary verifications.

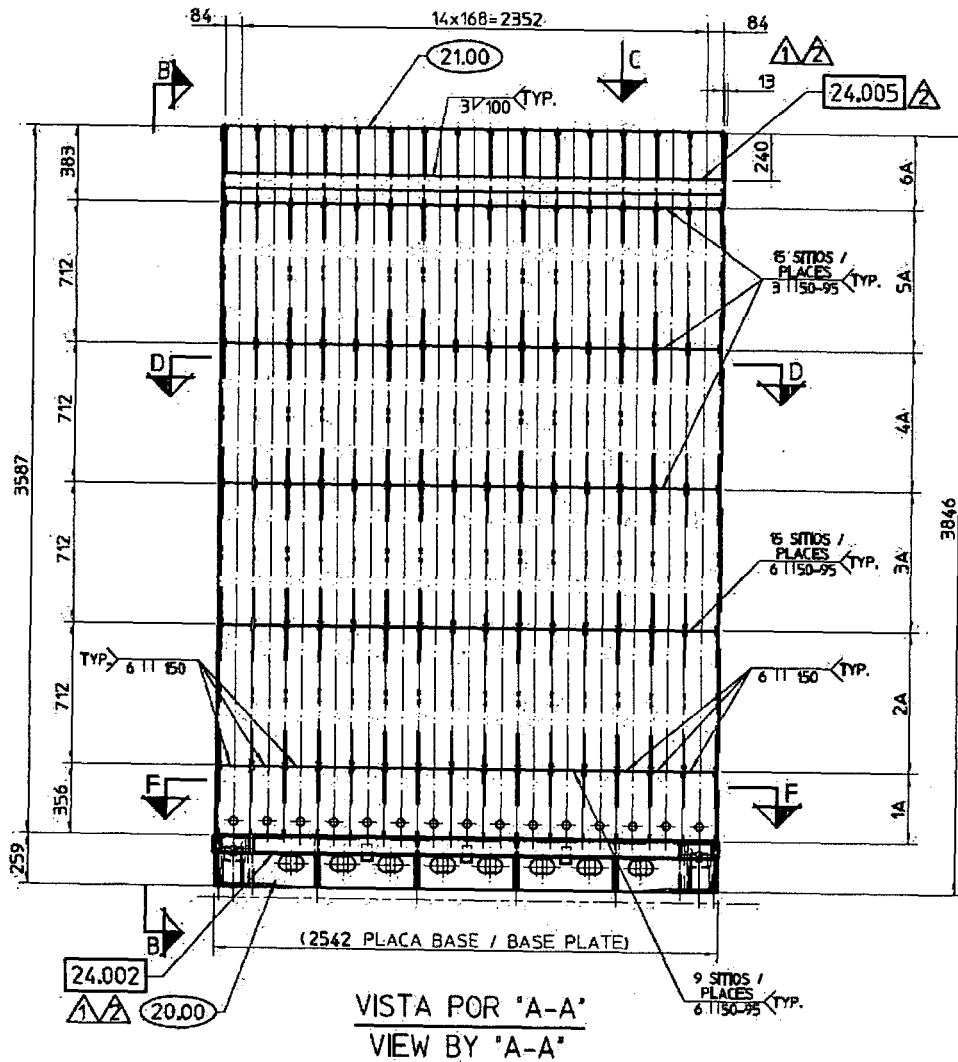


Figure 4-1. Elevation View of the Spent Fuel Rack

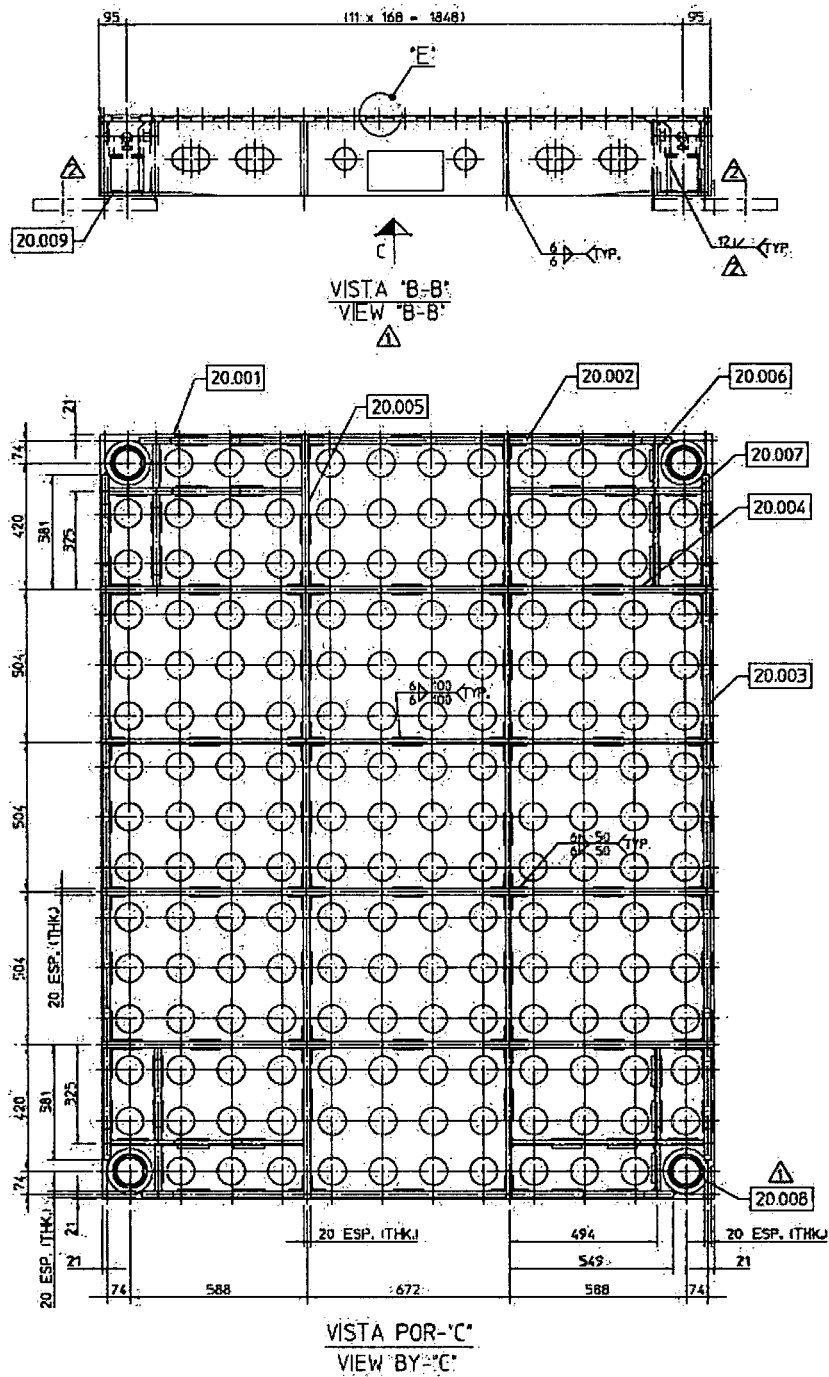


Figure 4-2. Base Plate of the Spent Fuel Rack

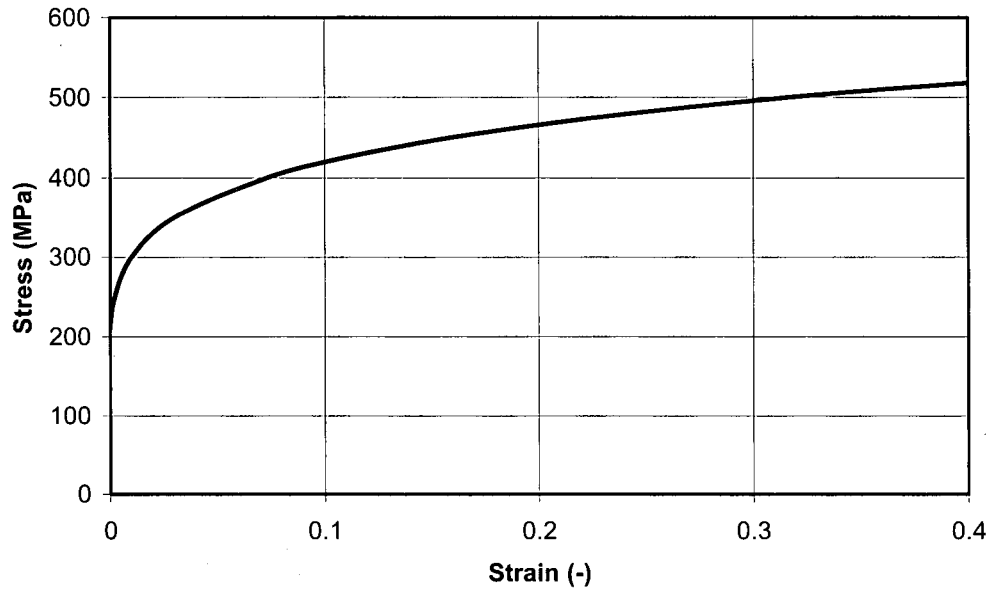


Figure 4-3. Stress-Strain Curve for Structural Steel

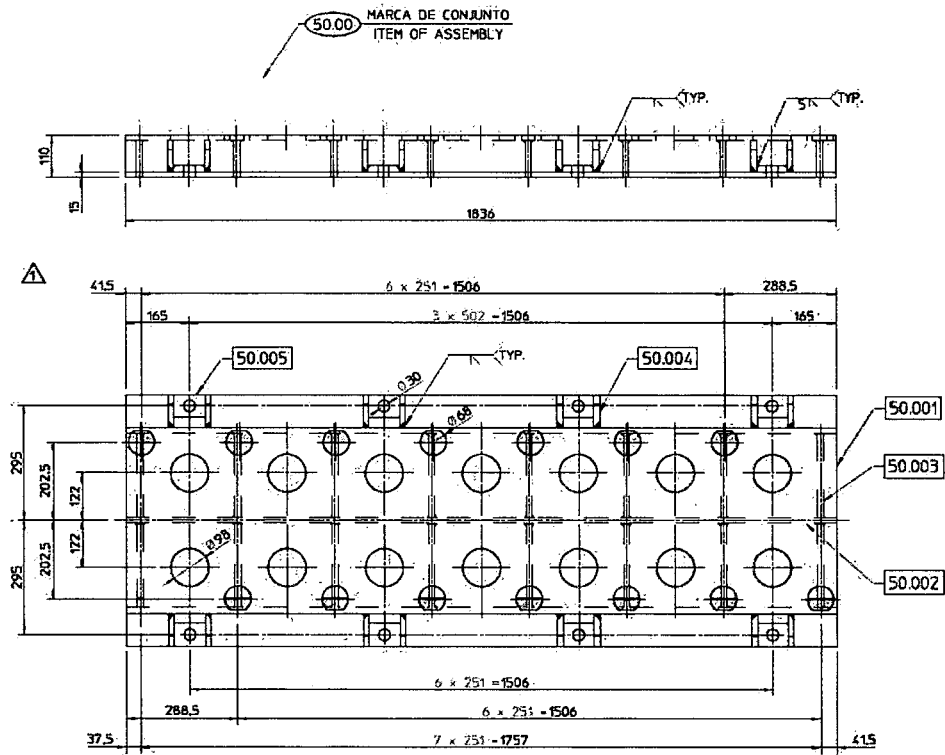


Figure 4-5. Base Plate of the Fresh Fuel Rack

4.3 SPENT FUEL RACKS: IMPACTS ON THE BASE PLATE

4.3.1 Introduction

This chapter is dedicated to the numerical analyses of the expected impacts between a dropped fuel element and the base plate of a spent fuel rack. Such impacts would occur if the dropped element managed to enter the storage cell without any direct interaction with its walls.

In all cases, the base plate has been considered to be rigidly fixed at the locations of the supports of the rack. Since the main effect of interest is the load imposed on the support, it is conservative to assume a greater rigidity than the actual case.

The analyses described in this chapter include the cases in which the cell undergoing the impact is located directly above one of the supports and that it is at the maximum distance from all the supports.

The finite element code Abaqus/Explicit (SIMULIA, 2008) has been used for all the numerical calculations.

As mentioned in Section 4.2, it is assumed that both the element and the fuel handling tool fall in water from a height of 1.8 m and that the impact with the base plate takes place with a velocity of 5.68 m/s.

4.3.2 Impact Above a Leg

A finite element model was developed for studying the impacts directly above one of the supports. The model represents the geometry of the base plate and the part of the fuel element which will interact with the base plate. The rest of the fuel element is modelled with bar elements followed by the point mass representing the fuel handling tool. The overall arrangement is presented in Figure 4-6.

For an impact velocity of 5.68 m/s, the resulting history of impact forces appears in Figure 4-7. The initial sustained value is approximately 0.34 MN. The second hump in the force history is associated with the deceleration of the mass of the fuel handling tool, reaches about 0.67 MN.

The plastic deformations of the base plate are considerable, reaching slightly over 0.36, but they remain highly localised as can be seen in Figure 4-8. In any case, this level of plastic strain is well below 0.40, which is the ductility of the material, therefore this interaction is acceptable.

Figure 4-9 shows the velocity histories of the nose, an intermediate point in the element and the fuel handling tool. Both the force and the velocity histories indicate that the impact has finished in about 12 ms.

The same analysis has been repeated without the handling tool. Figure 4-10 shows the history of impact forces, which is similar to that presented in Figure 4-7, except that the hump associated with the arrival of the handling tool is obviously missing.

The plastic deformations that appear in Figure 4-11 are not too different from those caused by the impact with the handling tool. Finally, the velocities of various points along the fuel element are shown in Figure 4-12.

4.3.3 Impact Between Legs

A similar model to that of the previous section was used here to analyse impacts between the supports of the rack. The new model includes more details of the base plate. The mesh appears in Figure 4-13.

The history of impact forces can be seen in Figure 4-14. The flexibility of the base plate (small but finite) leads to a smoother response than when the base of the cell is rigidly supported. The peak forces are approximately 0.30 MN.

The distribution of the plastic deformations caused by the impact is shown in Figure 4-15. The strains are strongly localised around the orifice and their peak value barely exceeds 0.13, well below the ductility of the material.

Finally, the evolution of the velocities of selected points along the dropped object is presented in Figure 4-16.

The analysis was repeated on the assumption that the element drops without the handling tool. The initial peak impact force is still about 0.30 MN (Figure 4-17), although the force levels at later times are now lower than with the handling tool. The local plastic deformations are limited to 0.11 as can be seen in Figure 4-18. The velocity histories at points of the fuel element appear in Figure 4-19.

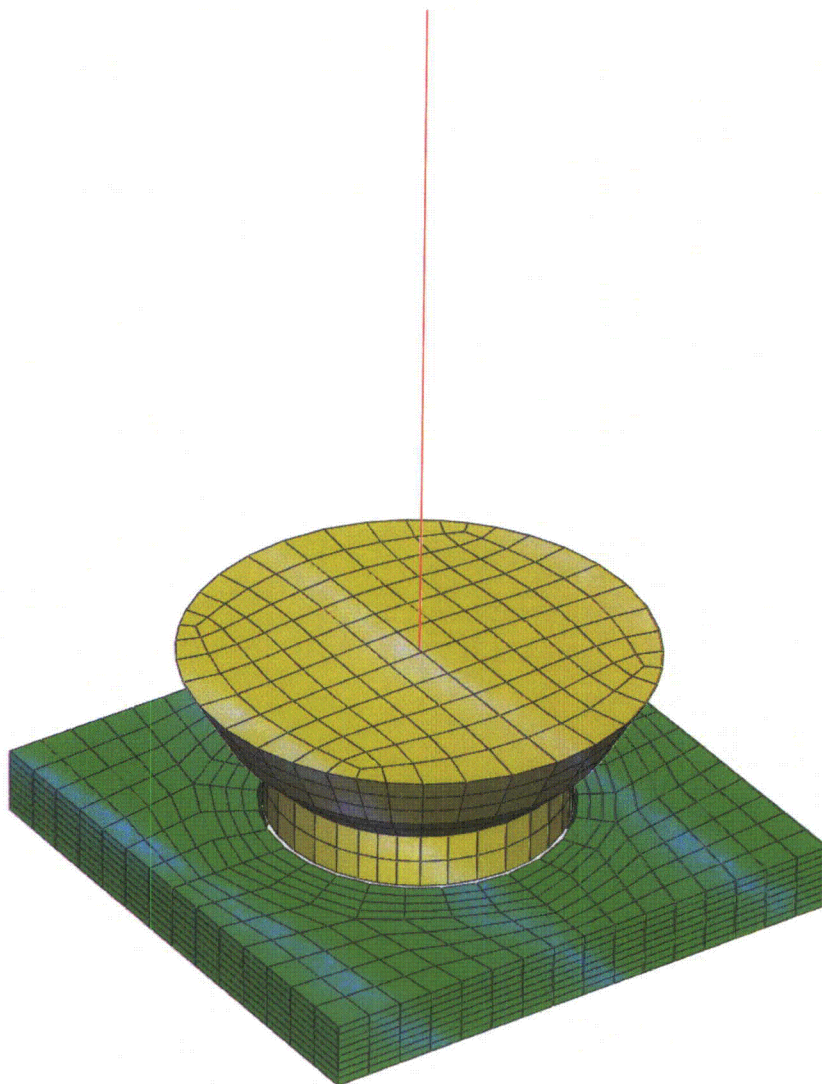


Figure 4-6. Spent Fuel, Above Leg. View of the Mesh

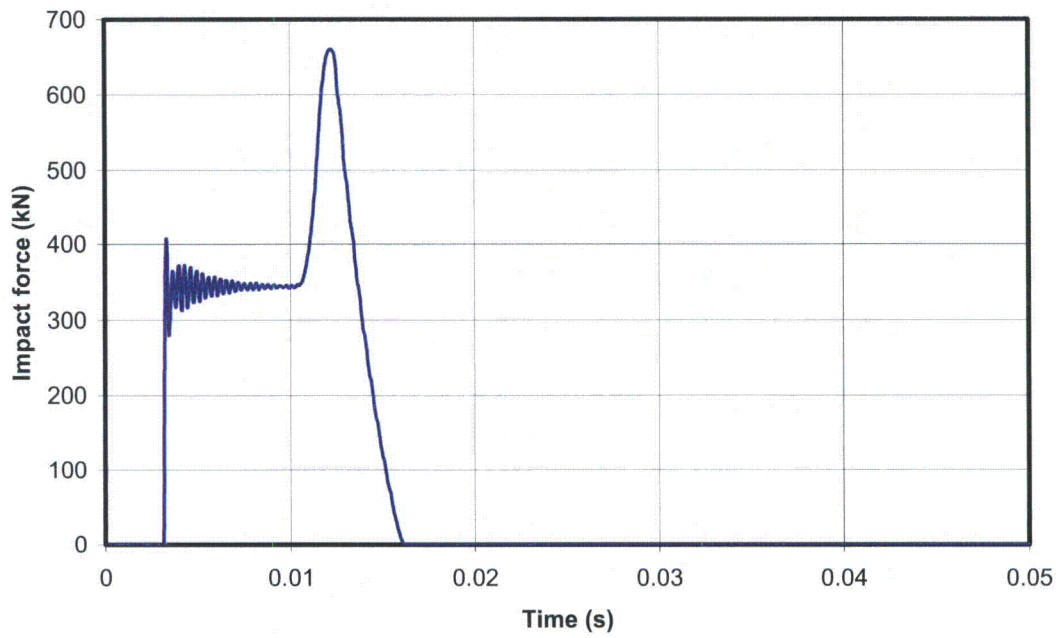


Figure 4-7. Spent Fuel, Above Leg with Tool. Impact Forces

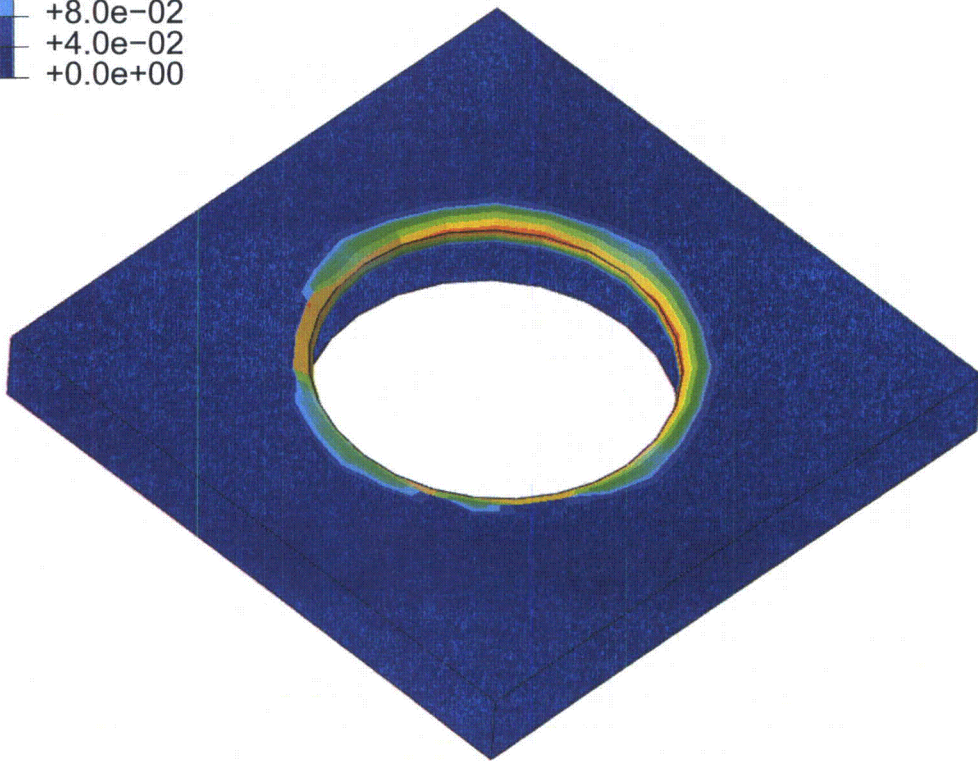
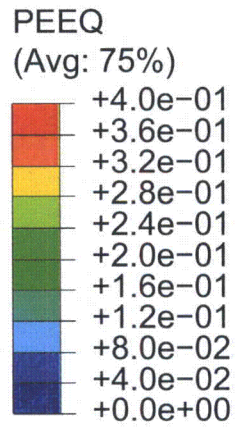


Figure 4-8. Spent Fuel, Above Leg, with Tool. Plastic Deformations

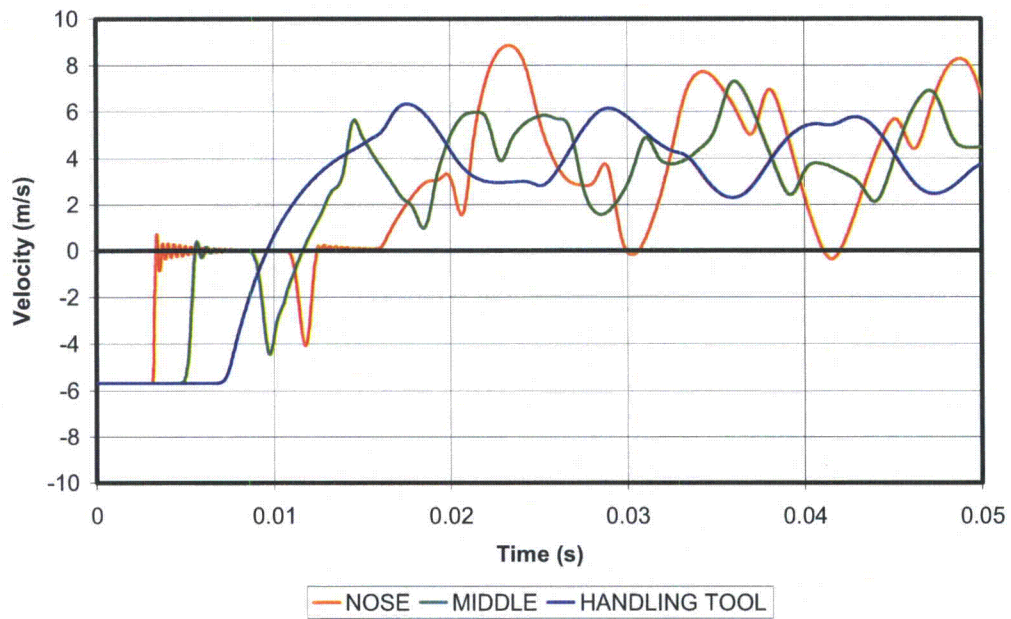


Figure 4-9. Spent Fuel, Above Leg, with Tool. Fuel Velocities

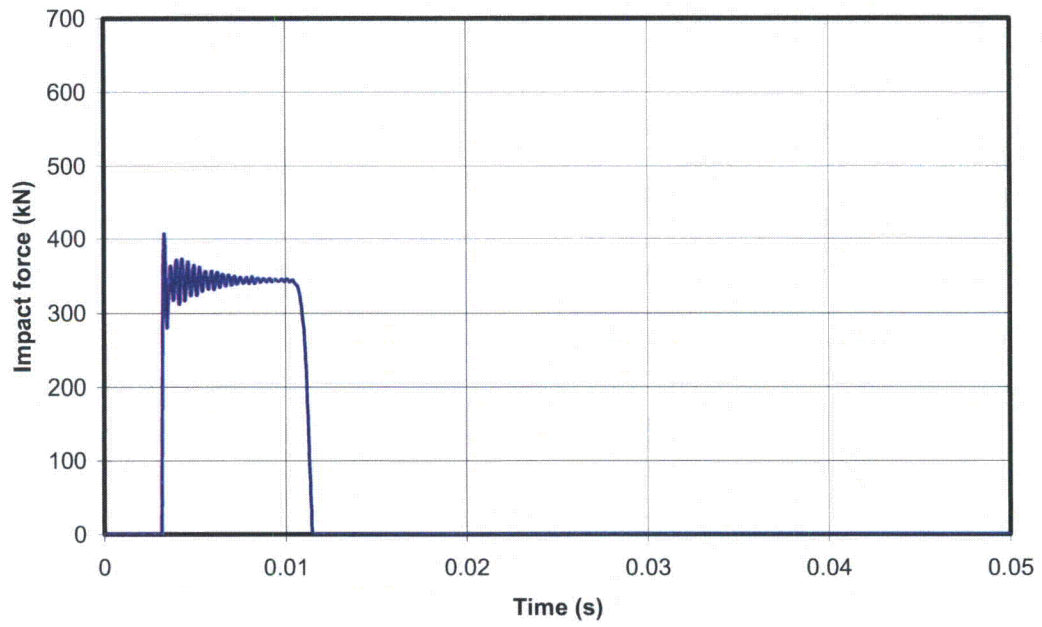


Figure 4-10. Spent Fuel, Above Leg, without Tool. Impact Forces

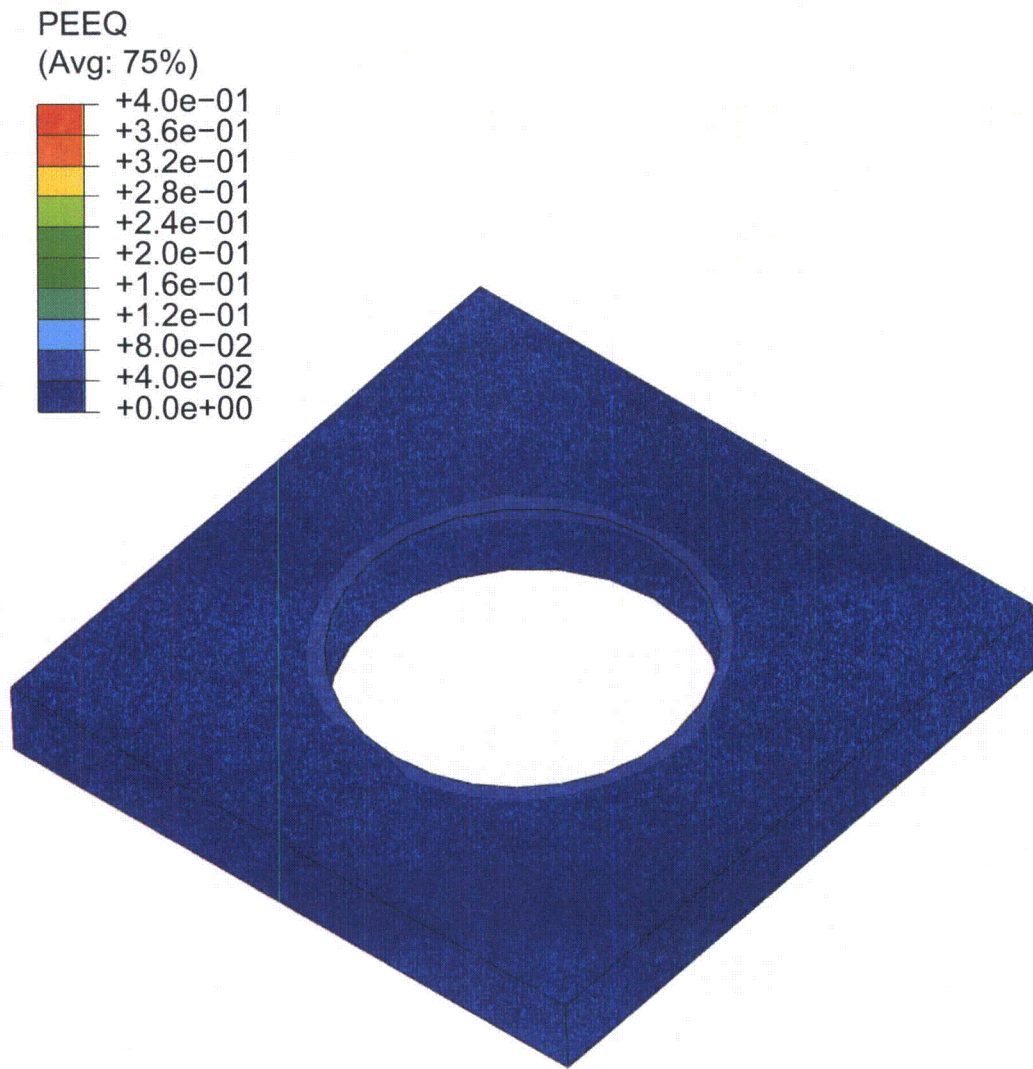


Figure 4-11. Spent Fuel, Above Leg, without Tool. Plastic Deformations

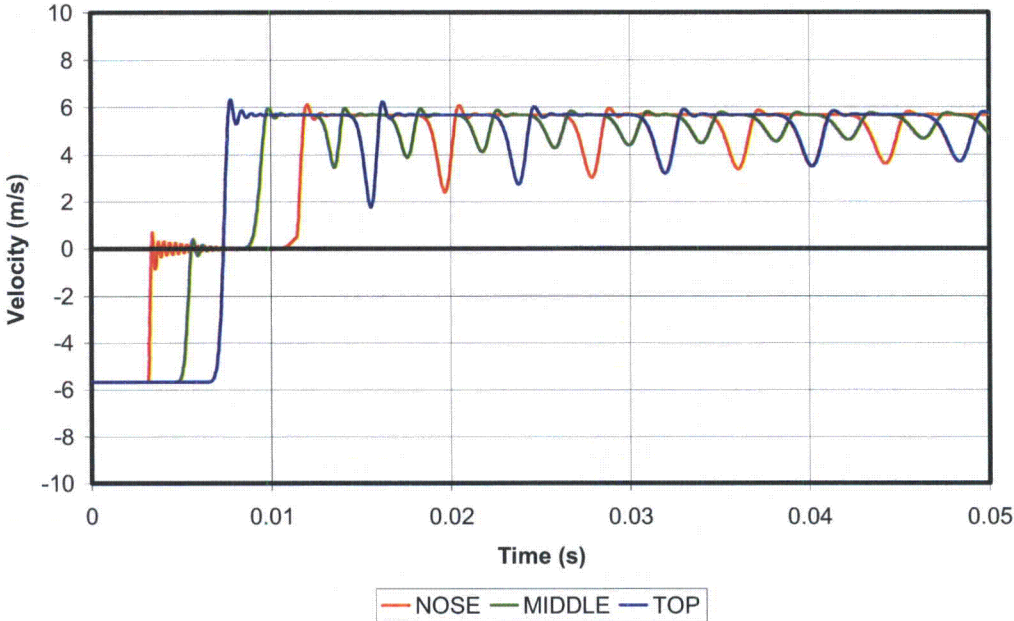


Figure 4-12. Spent Fuel, Above Leg, without Tool. Fuel Velocities

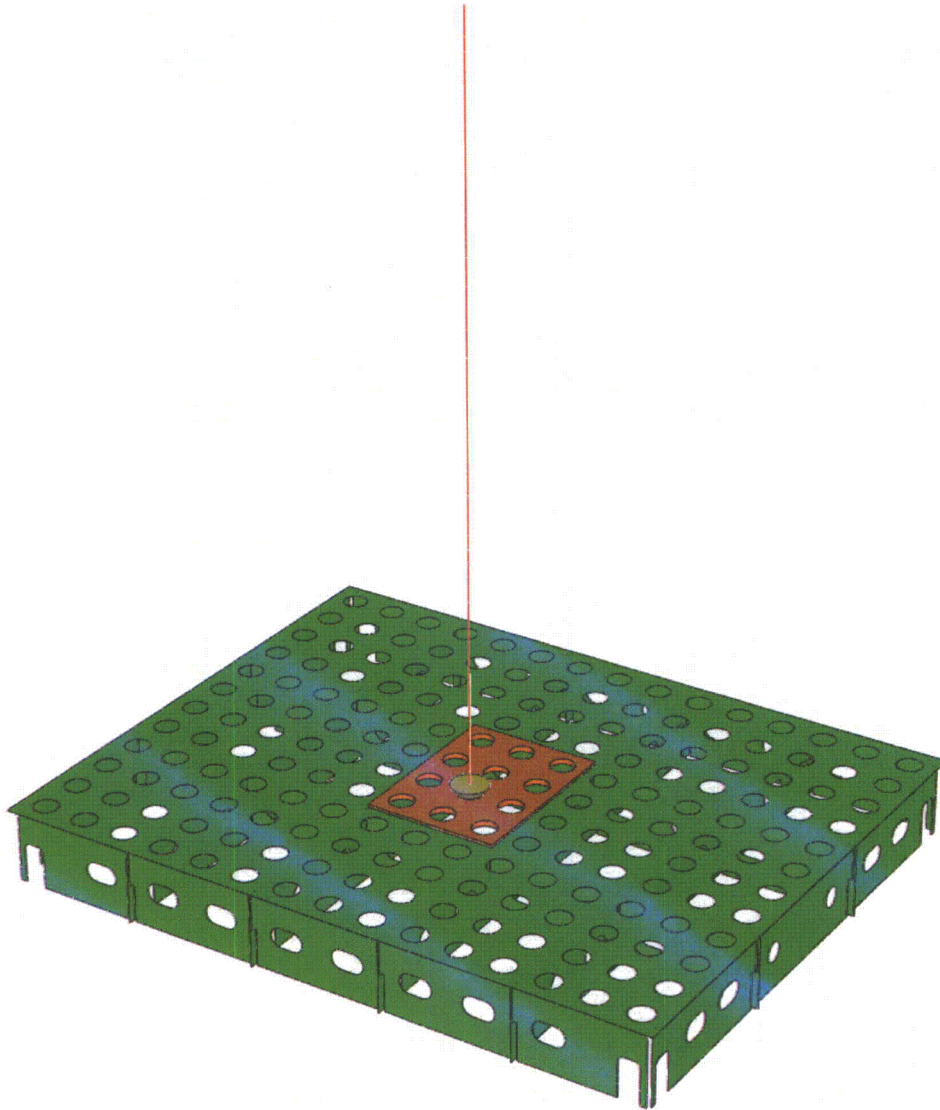


Figure 4–13. Spent Fuel, Between Legs. View of the Mesh

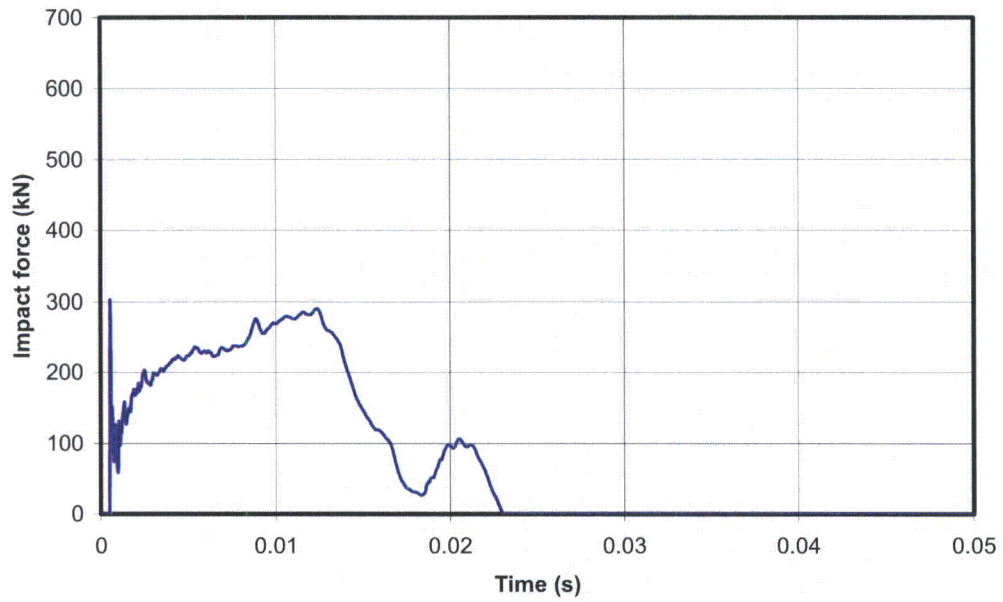


Figure 4-14. Spent Fuel, Between Legs, with Tool. Impact Forces

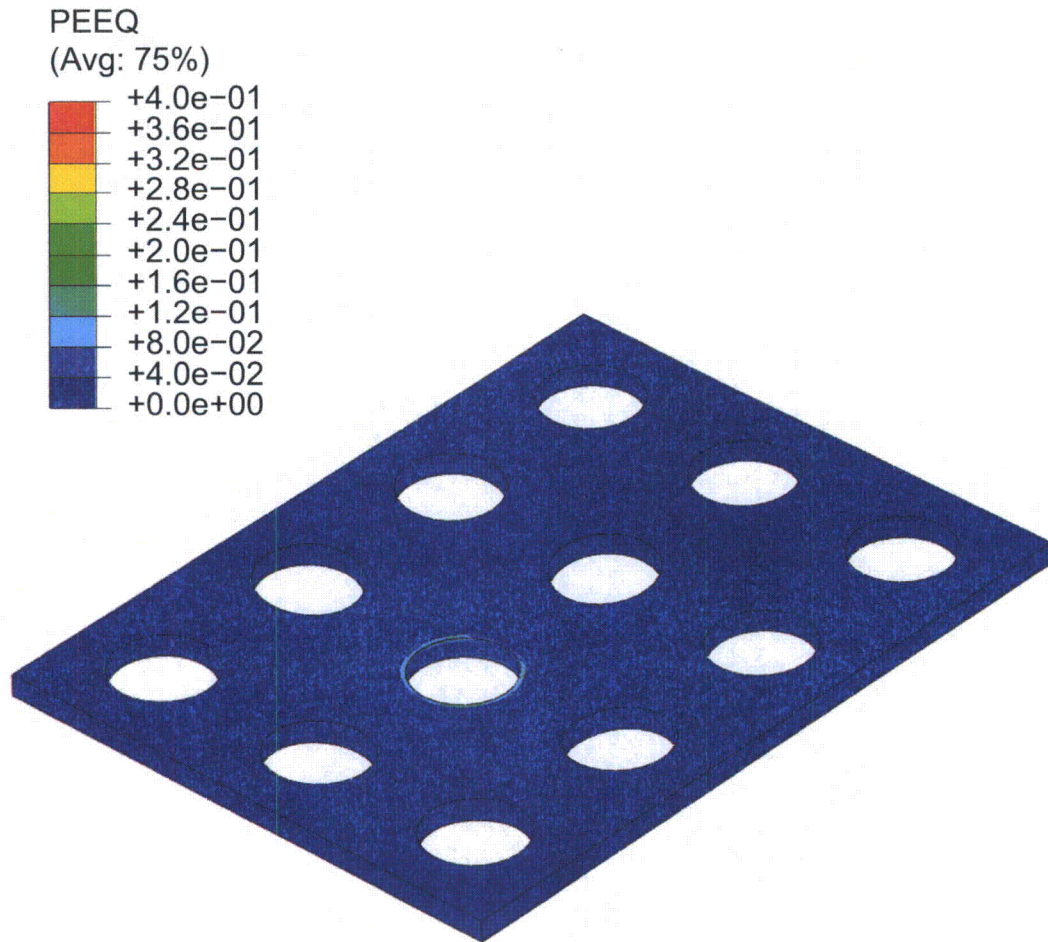


Figure 4-15. Spent Fuel, Between Legs, with Tool. Plastic Deformations

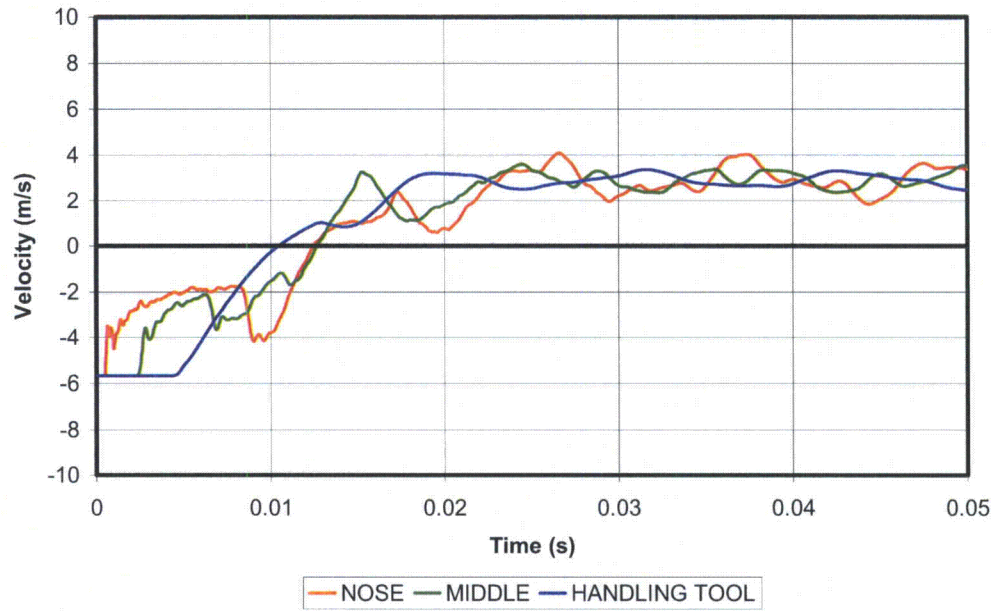


Figure 4-16. Spent Fuel, Between Legs, with Tool. Fuel Velocities

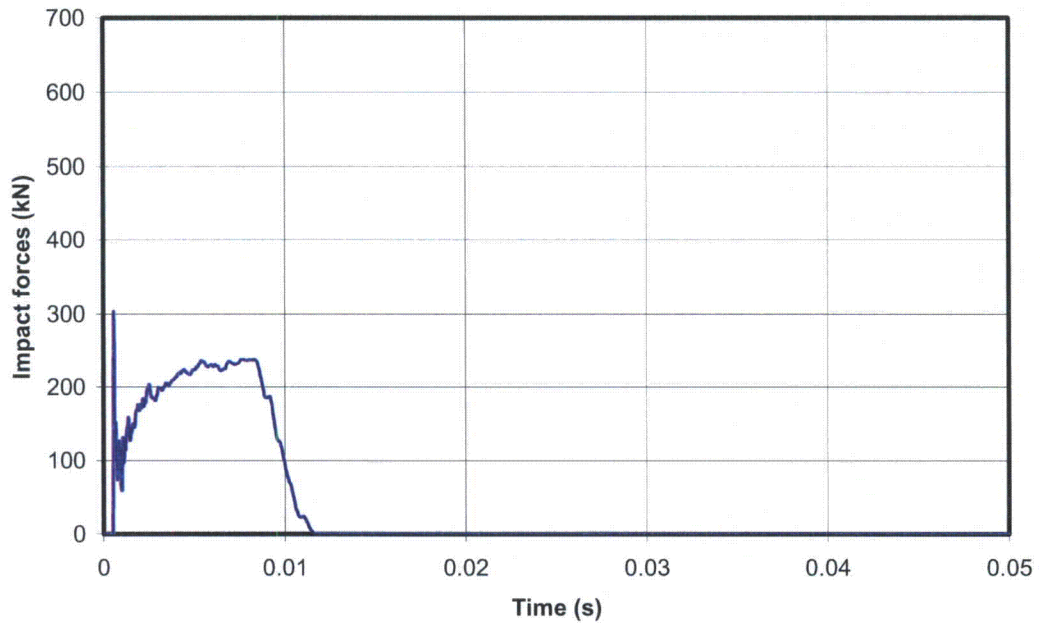


Figure 4-17. Spent Fuel, Between Legs, without Tool. Impact Forces

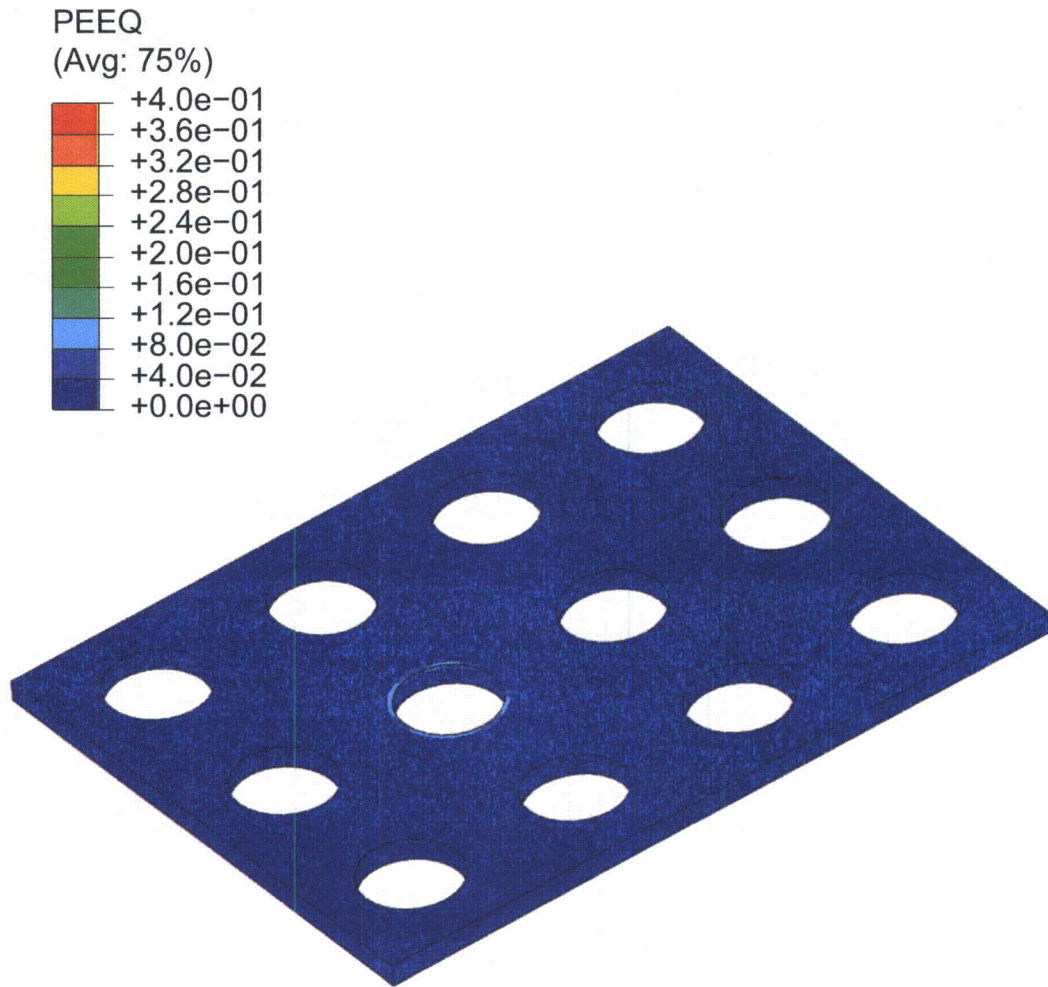


Figure 4-18. Spent Fuel, Between Legs, without Tool. Plastic Deformations

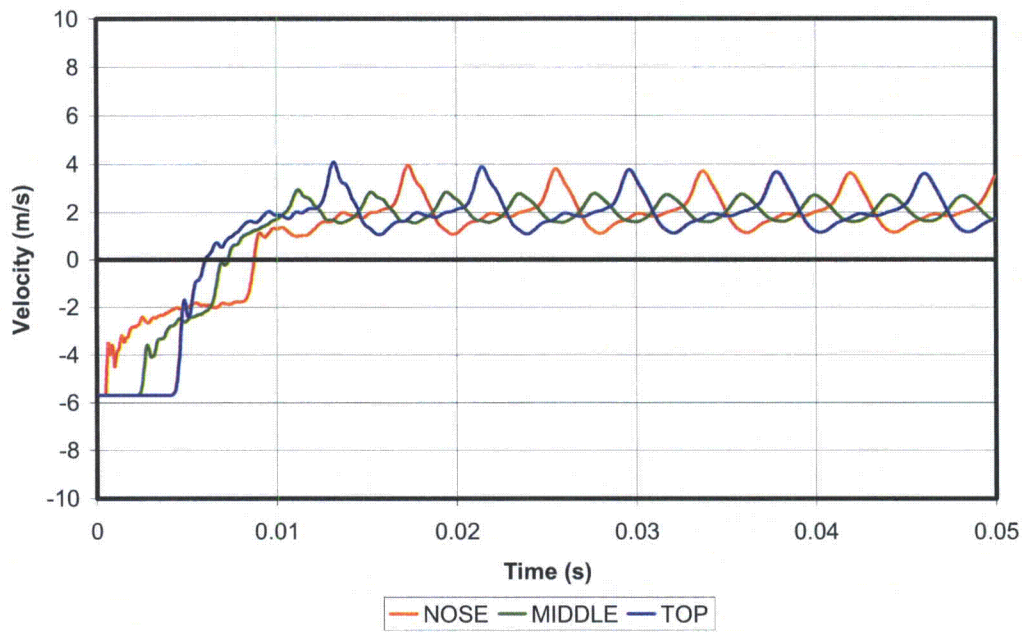


Figure 4-19. Spent Fuel, Between Legs, without Tool. Fuel Velocities

4.4 SPENT FUEL RACKS: IMPACTS AT THE TOP OF THE CELLS

4.4.1 Introduction

This chapter studies the cases in which the dropped fuel element impacts the top of the cell walls rather than entering the cell. At the point of impacting the upper edge of the walls, the falling element has a velocity of 7.82 m/s, following the drop from 6.4 m in water.

Both vertical and inclined attitudes of the dropped fuel element should be considered. Nevertheless, it should be noticed that the kinetic energy which is effective for inducing deformations in the missile or target is maximised when the centre of gravity of the missile and the centre of the contact area are aligned with the missile velocity. Otherwise, the impact results in part of the translational kinetic energy of the missile being converted into rotational kinetic energy; that part of the kinetic energy is preserved and not used for producing deformations.

In the present case, the center of gravity of the fuel element will be aligned with the impact point only when the fuel element falls with a vertical attitude or when the fuel element has a very small inclination (less than 2°) with respect to the vertical. The deviation from verticality in the latter case is so small as to make it unnecessary to repeat the analyses with that inclination. Any other angle of inclination would result in a reduction of the kinetic energy available for producing deformations.

As a consequence, it is concluded that only the vertical attitude should be considered for the study of dropped fuel elements impacting the top of the cell walls.

Three different impacts must be studied, which will be the object of the following sections. In each case, it will be considered that the fuel element may drop with or without the handling tool. The three impacts are:

- Impact on a wall slotted in its upper part
- Impact on a wall slotted in its lower part
- Impact at the intersection between two walls

4.4.2 Impacts on Cell Walls

The first impact considered is that in which the dropped element falls on the center of one of the cell walls. This impact against the cell wall is softer than against the base plate, because the impact is now more energetic and the structure is more susceptible to damage at the top of the rack. Hence, the impact duration can be expected to lengthen and the forces developed will be correspondingly smaller.

The present impacts are negligible from the viewpoint of the demands imposed on the supports. The reason for conducting the analyses is to assess the damage caused on the cell structure.

4.4.2.1 Walls Slotted Below

The upper structural steel plates are slotted, some in their upper region and some in their lower region. This creates two different types of impacts on cell walls, depending on whether the impacted wall is slotted above or below. Impacts on walls slotted below will be considered first.

A considerable portion of the rack, spanning 4 x 4 cells, has been modelled using shell elements (see Figure 4-20). This type of representation is adequate for any deformation mechanisms that trigger primarily local effects. Lateral boundaries are sufficiently spaced that they do not influence the analysis of local effects. The nodes at the bottom of the model are considered to be fixed.

Assuming that the fuel element falls together with the handling tool, Figure 4-21 presents the history of forces developed between the fuel element and the cell wall. There is an initial peak at approximately 0.35 MN, after which the impact force averages approximately 0.20 MN. The dropped fuel element and handling tool are arrested in about 25 ms; over that time, the element has crushed slightly over 7 cm of the upper region of the cell wall, as indicated by the history of displacements of the nose of the fuel element (Figure 4-22).

The deformations caused by the impact can be seen in Figure 4-23, which confirms the very local character of the effects of the impact and the fact that neighboring cells remain unaffected in spite of the severe distortions and minor tearing caused on the impacted wall.

If the fuel element drops without the handling tool, the first part of the history of forces changes little but the second part, which previously corresponded to the arrival of the handling tool, is now considerably reduced (Figure 4-24). This reduction is also reflected by the displacements shown in Figure 4-25, which indicate that only the upper 4 cm at the top of the wall are now crushed. The deformations caused are presented in Figure 4-26.

A difference between the impacts on walls slotted above and below is that, if the wall was slotted below, the impacted plate must displace with it all the structural steel plates located immediately below and running transversely to it. This provides for a fairly wide distribution of the forces transmitted to the weaker and thinner borated steel located at lower levels. The analysis is therefore conservative with respect to those effects, which are not of a purely local nature and which would span 12 or 15 cells rather than the 4 represented in the model.

4.4.2.2 Walls Slotted Above

As in the previous case, a mesh was generated to support the analyses; the numerical model can be seen in Figure 4-27.

Again on the assumption that the handling tool drops with the fuel element, the history of impact forces (Figure 4-28) is now longer than that obtained in the previous section, even though the initial peak changes little. About 50 ms are now necessary to arrest the element and the handling tool.

The displacements achieved by the dropped element grow to approximately 20 cm as can be observed in Figure 4-29. Figure 4-30 presents the deformations induced and the plastic strains induced by the impact, which provide the explanation for the previous observations: the

impacted wall, slotted in its upper part, bends out of the way, thus giving rise to a much softer response on the target.

Similar results are produced when the fuel element drops without the handling tool. The first peak in the force history (Figure 4-31) remains unchanged, although the second part of the history reflects the absence of the handling tool. The peak displacements decrease to about 10 cm (Figure 4-32), but the response mechanism is still that of wall bending, as shown by the deformations presented in Figure 4-33.

4.4.3 Impacts on Cell Contacts

Impacts on the intersection of the walls of neighboring cells have also been analyzed for the sake of completeness. In this case, the fuel element is dropped with its axis coinciding with the contact between the intersecting walls of the cells.

The mesh for studying the problem was constructed as in the previous analyses and is presented in Figure 4-34.

For an element dropped together with the handling tool, the history of impact forces is shown in Figure 4-35. The displacements caused appear in Figure 4-36, peaking at about 3 cm, and the deformations are presented in Figure 4-37. The response of the rack is much stiffer than during impacts on single walls.

When the analysis is repeated without the handling tool, the target is sufficiently strong to generate an essentially elastic response. This is particularly clear in the force and displacement histories (Figures 4-38 and 4-39). Consistently with this, the plastic deformations induced are practically negligible, as evinced in Figure 4-40.

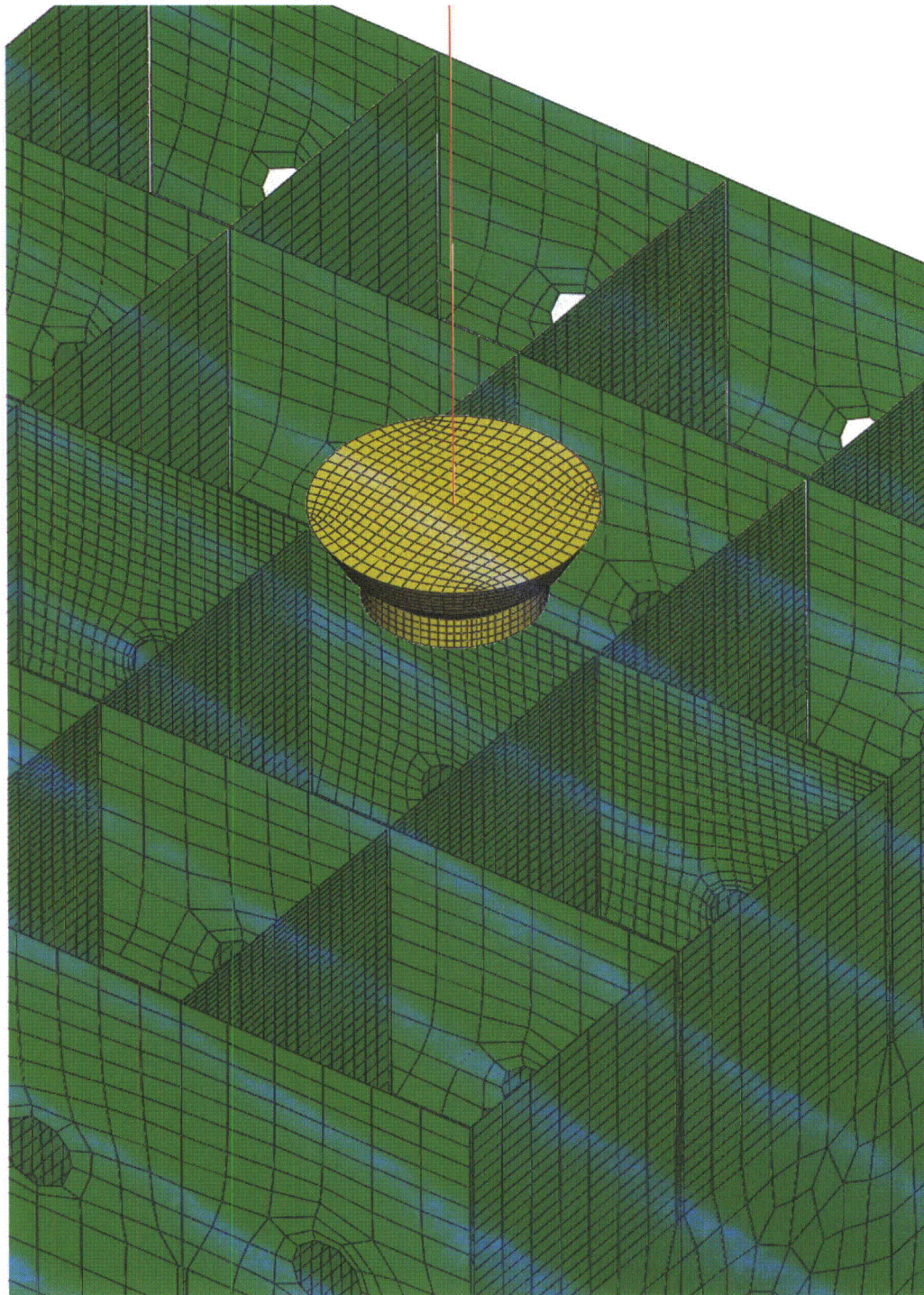


Figure 4–20. Spent Fuel, Slots Below. View of the Mesh

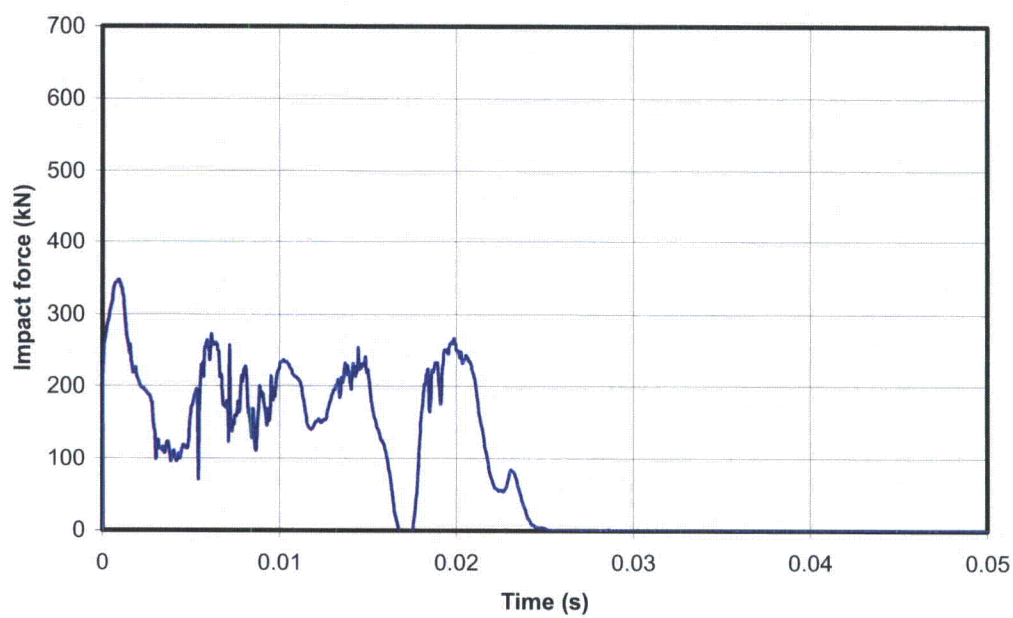


Figure 4-21. Spent Fuel, Slots Below, with Tool. Impact Forces

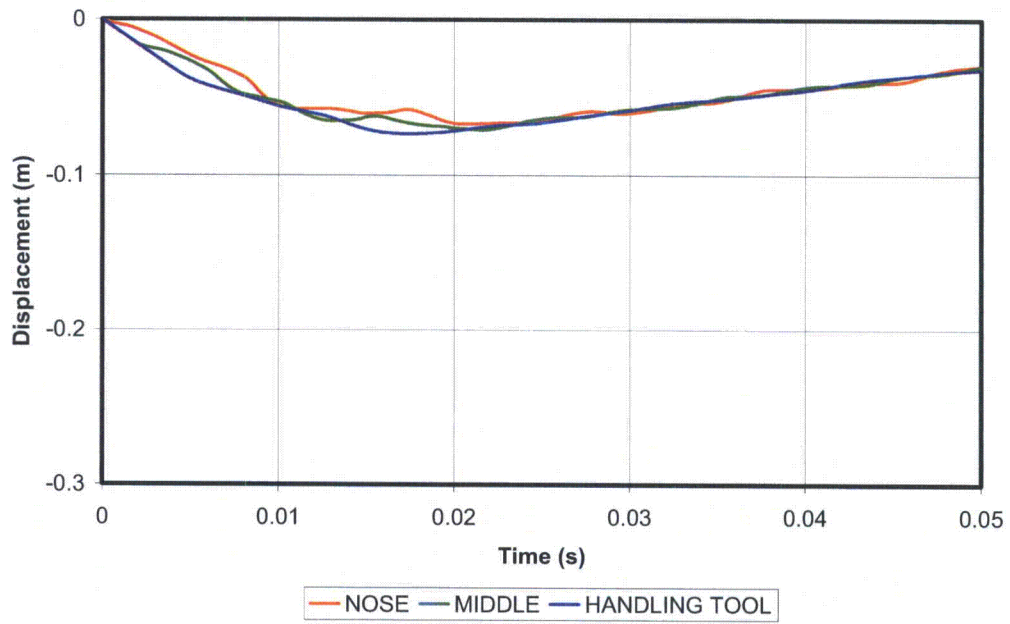


Figure 4-22. Spent Fuel, Slots Below, with Tool. Fuel Displacements

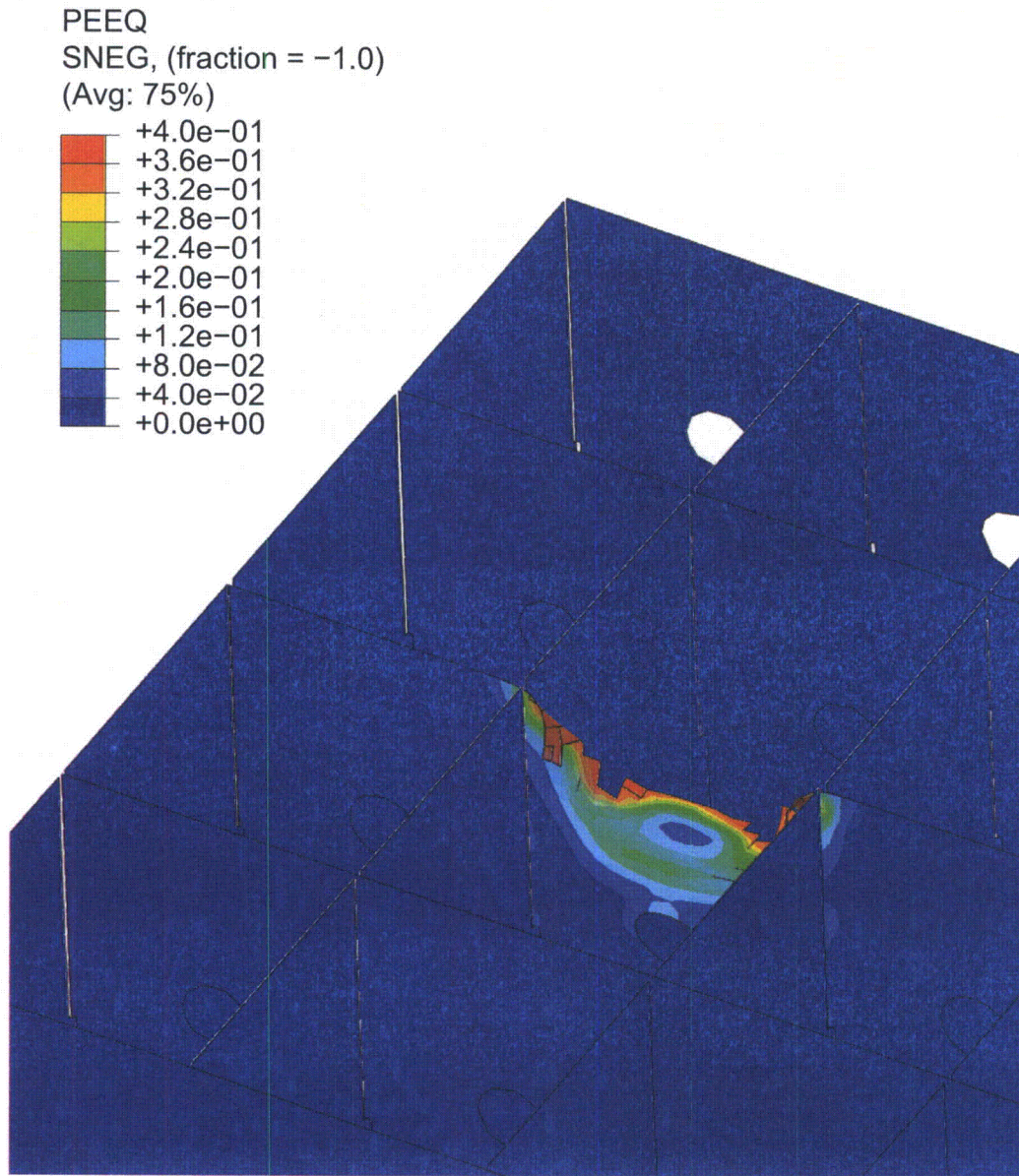


Figure 4-23. Spent Fuel, Slots Below, with Tool. Plastic Deformations

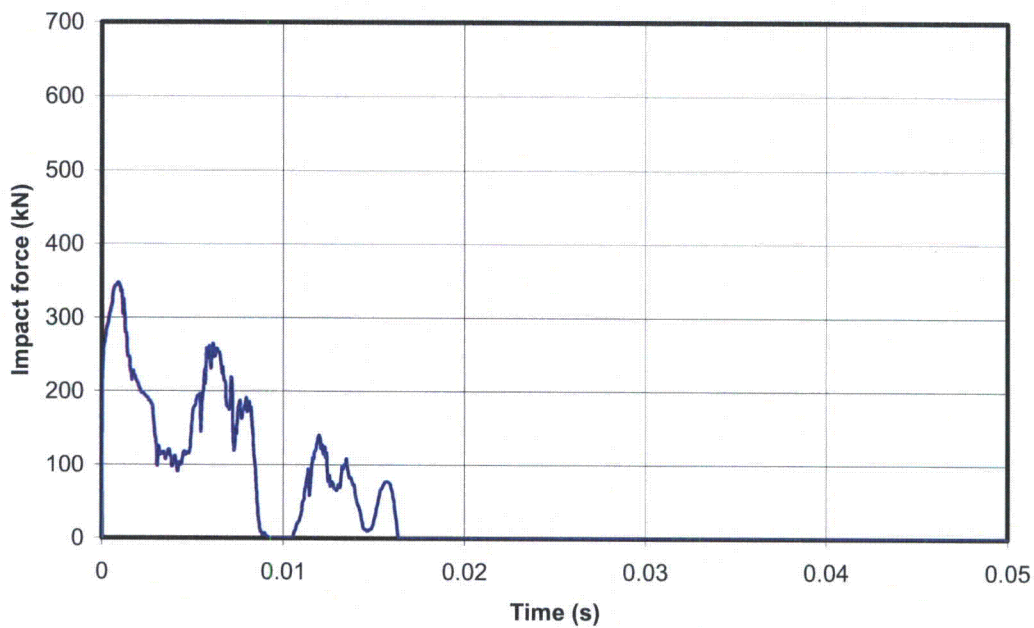


Figure 4-24. Spent Fuel, Slots Below, without Tool. Impact Forces

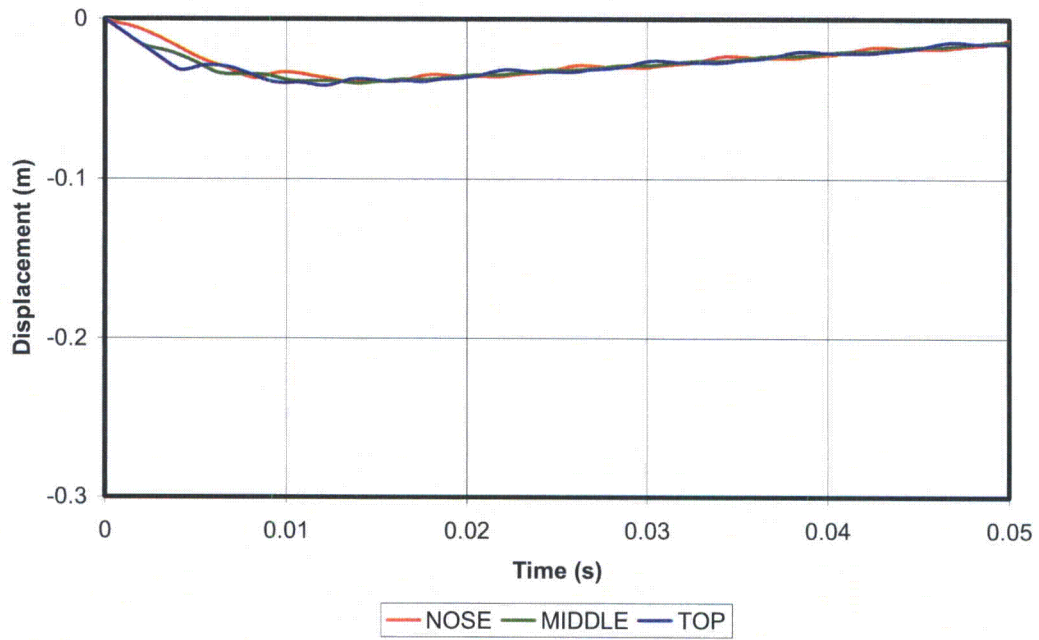


Figure 4-25. Spent Fuel, Slots Below, without Tool. Fuel Displacements

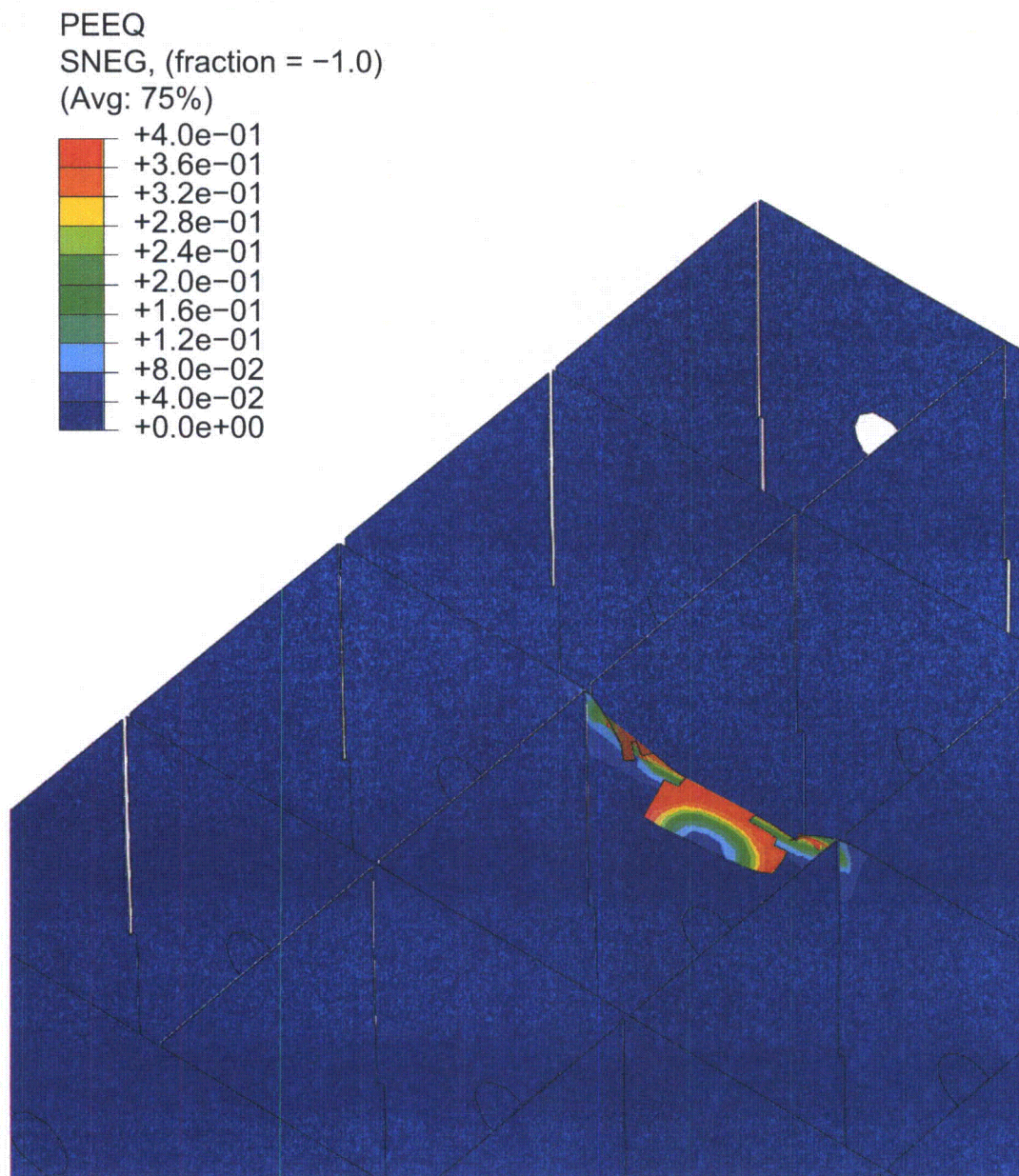


Figure 4-26. Spent Fuel, Slots Below, without Tool. Plastic Deformations

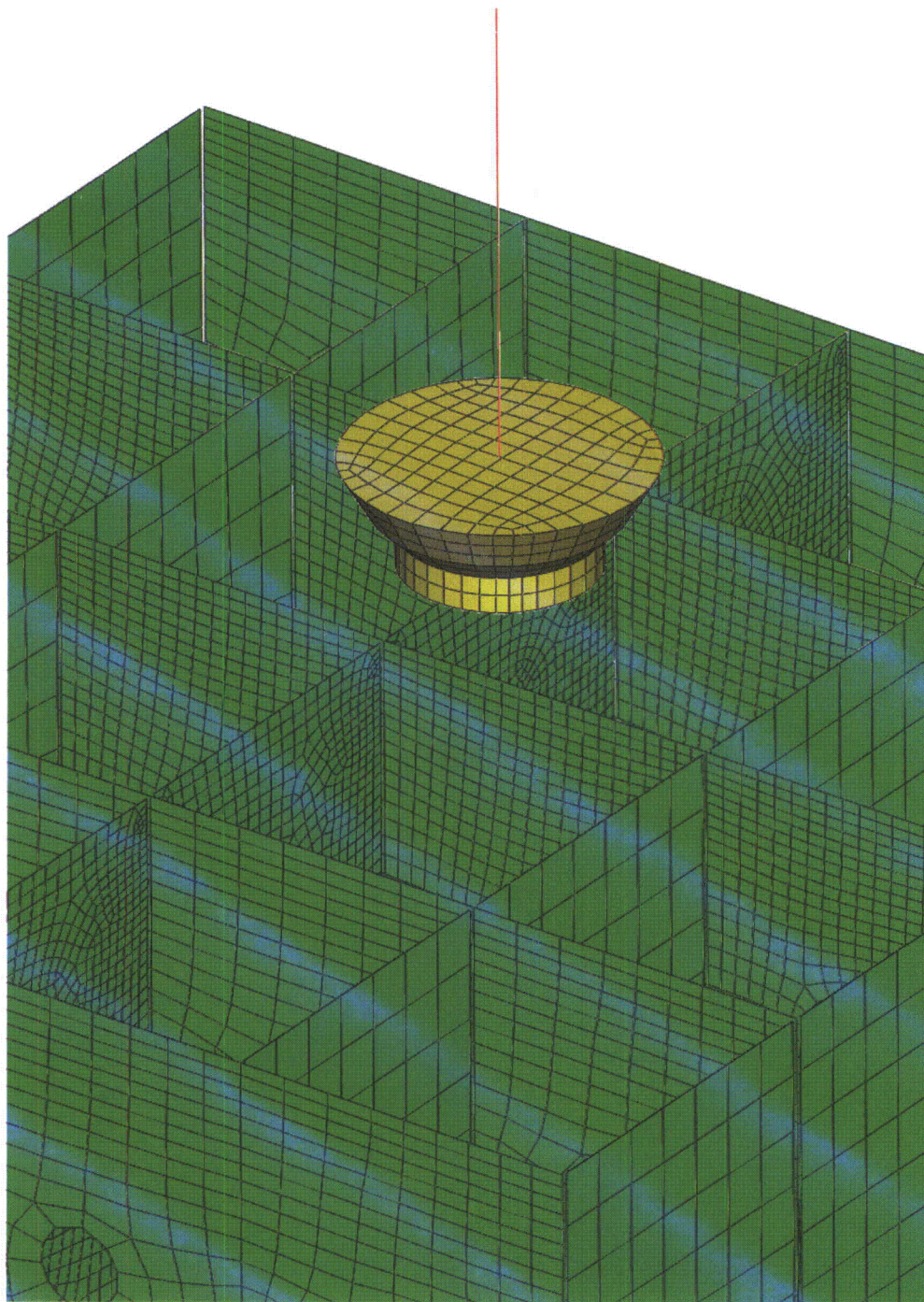


Figure 4-27. Spent Fuel, Slots Above. View of the Mesh

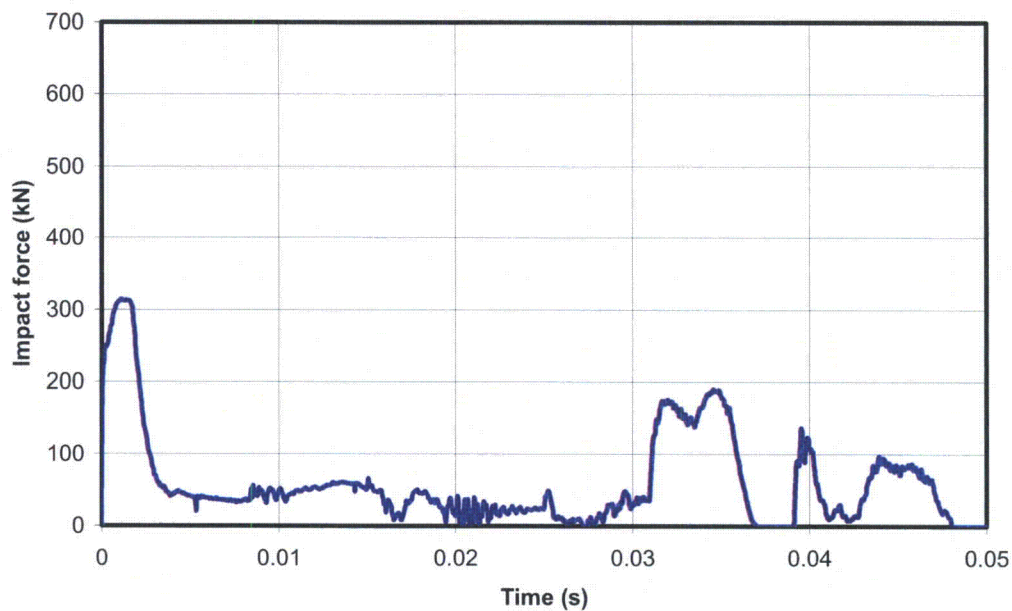


Figure 4-28. Spent Fuel, Slots Above, with Tool. Impact Forces

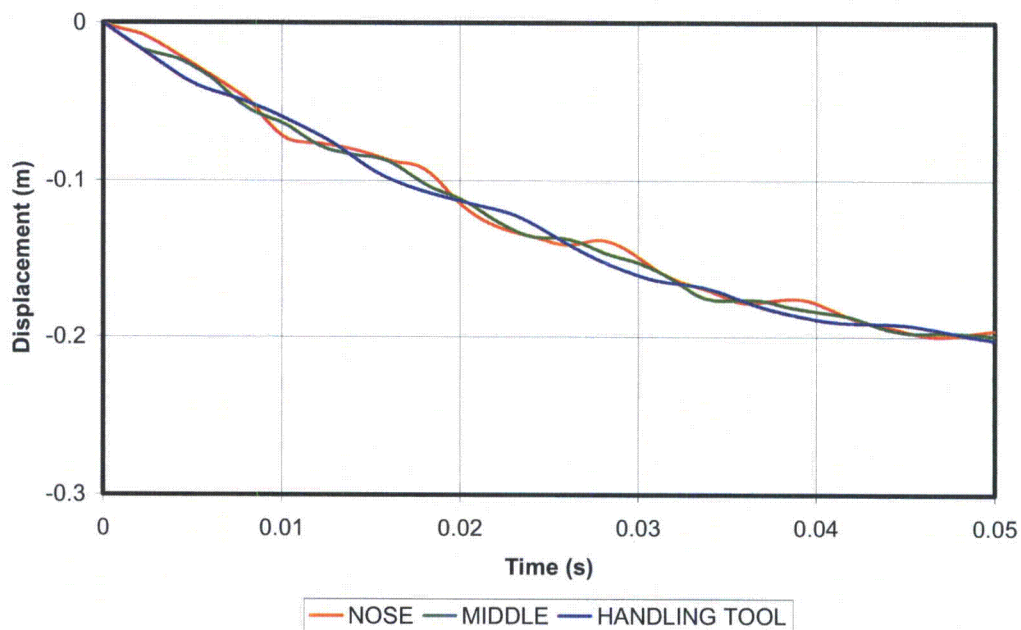


Figure 4-29. Spent Fuel, Slots Above, with Tool. Fuel Displacements

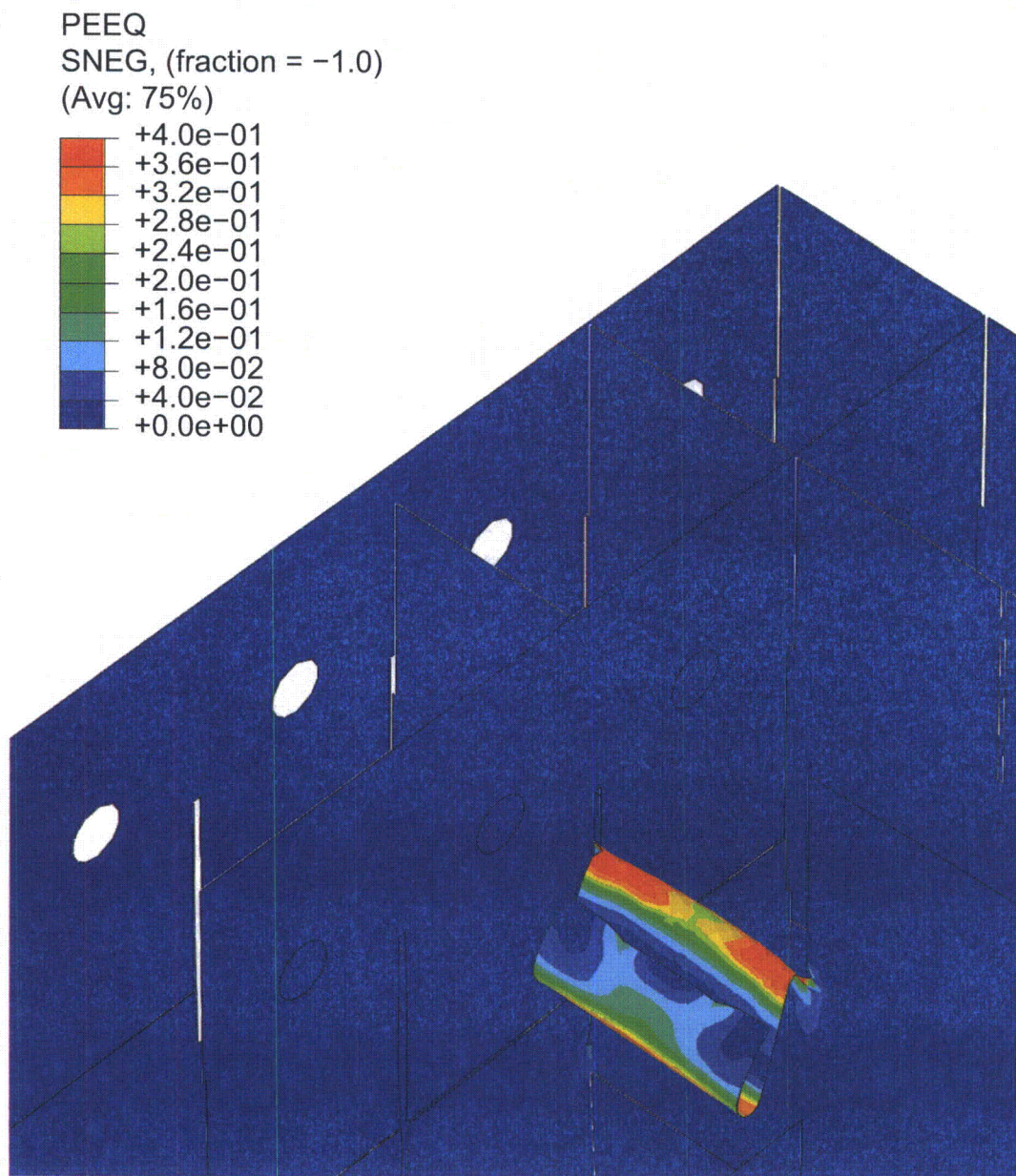


Figure 4-30. Spent Fuel, Slots Above, with Tool. Plastic Deformations

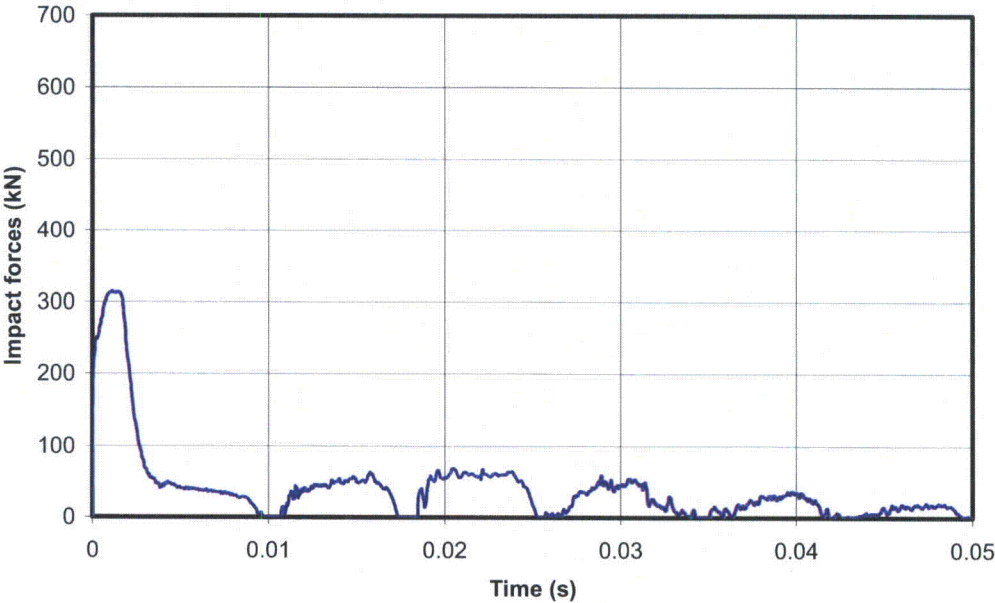


Figure 4-31. Spent Fuel Slots Above, without Tool. Impact Forces

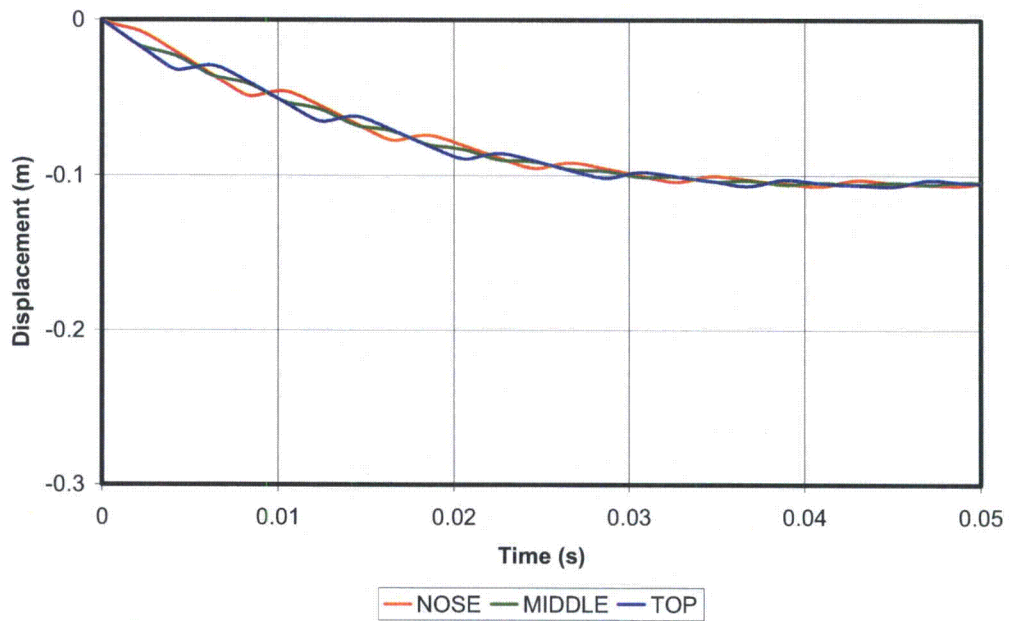


Figure 4-32. Spent Fuel, Slots Above, without Tool. Fuel Displacements

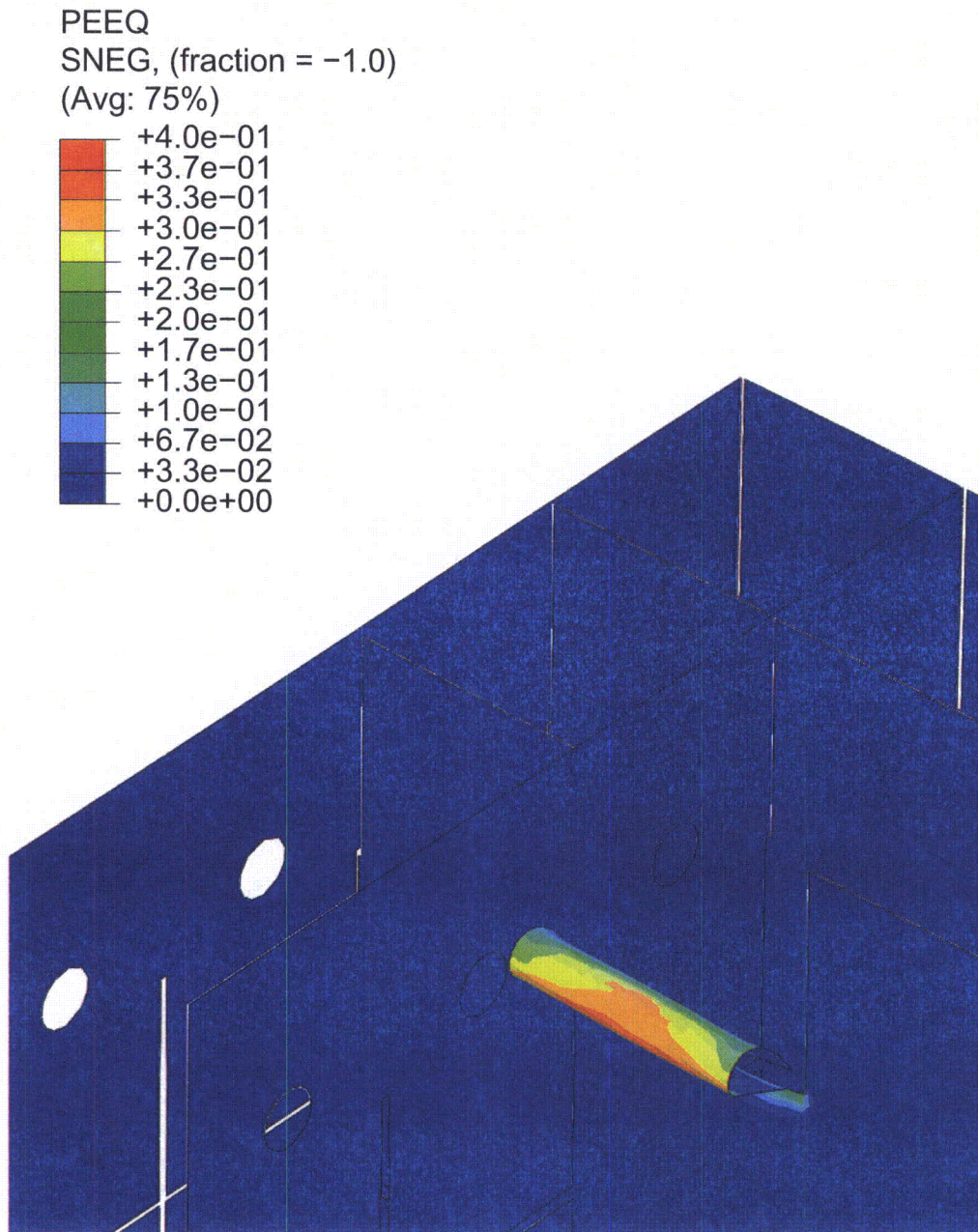


Figure 4-33. Spent Fuel, Slots Above, without Tool. Plastic Deformations

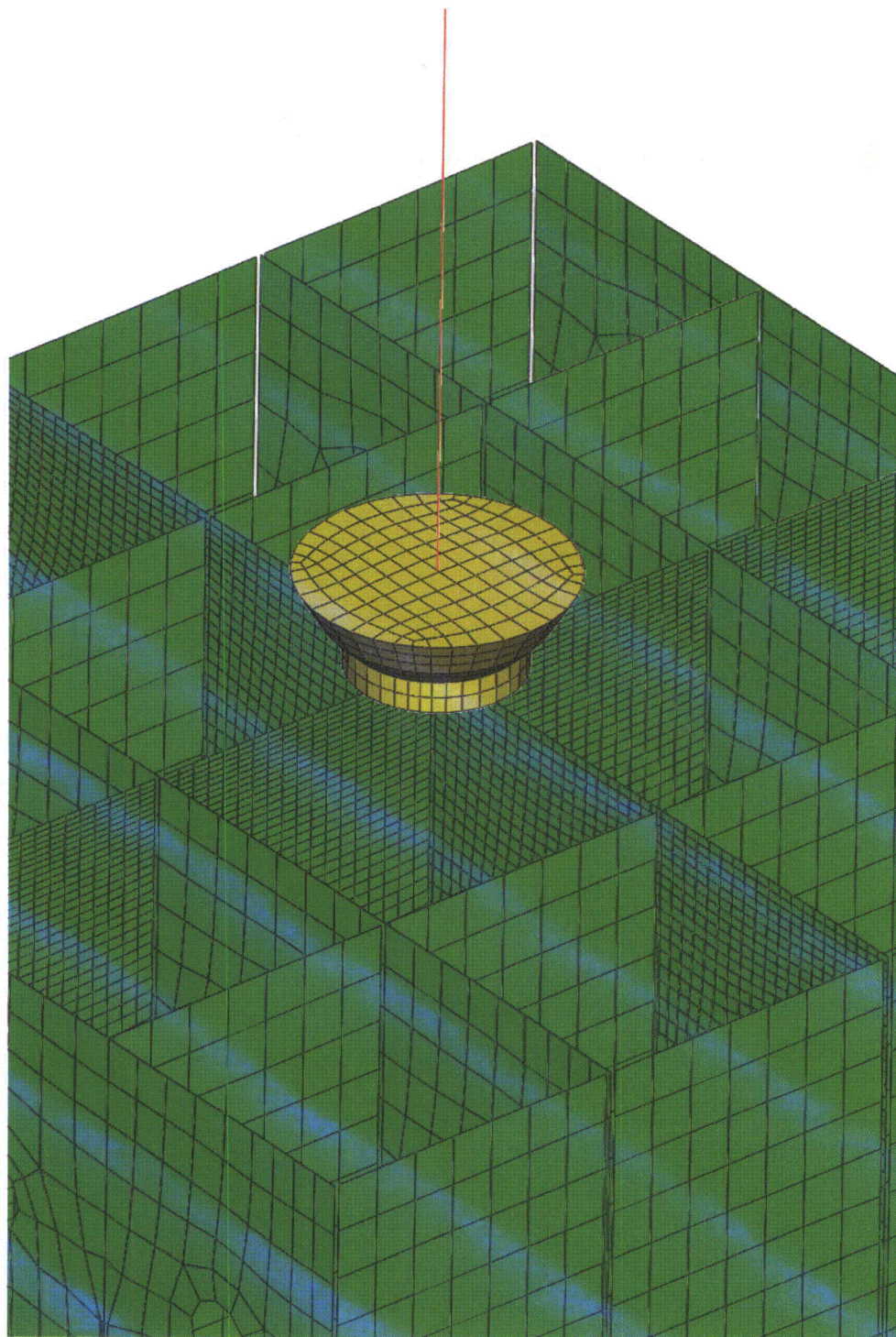


Figure 4-34. Spent Fuel, Intersection. View of the Mesh

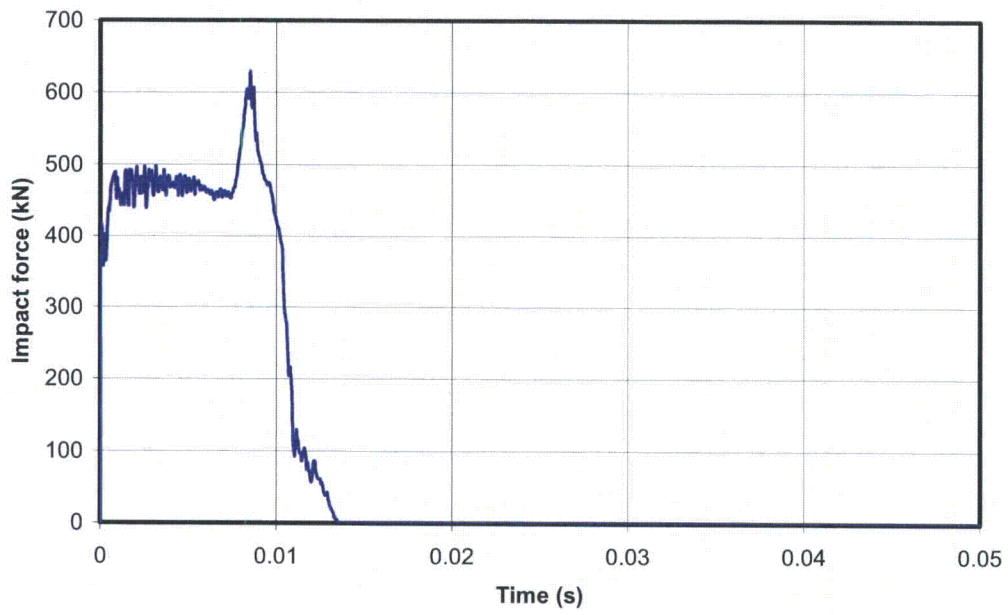


Figure 4-35. Spent Fuel, Intersection. Impact Force

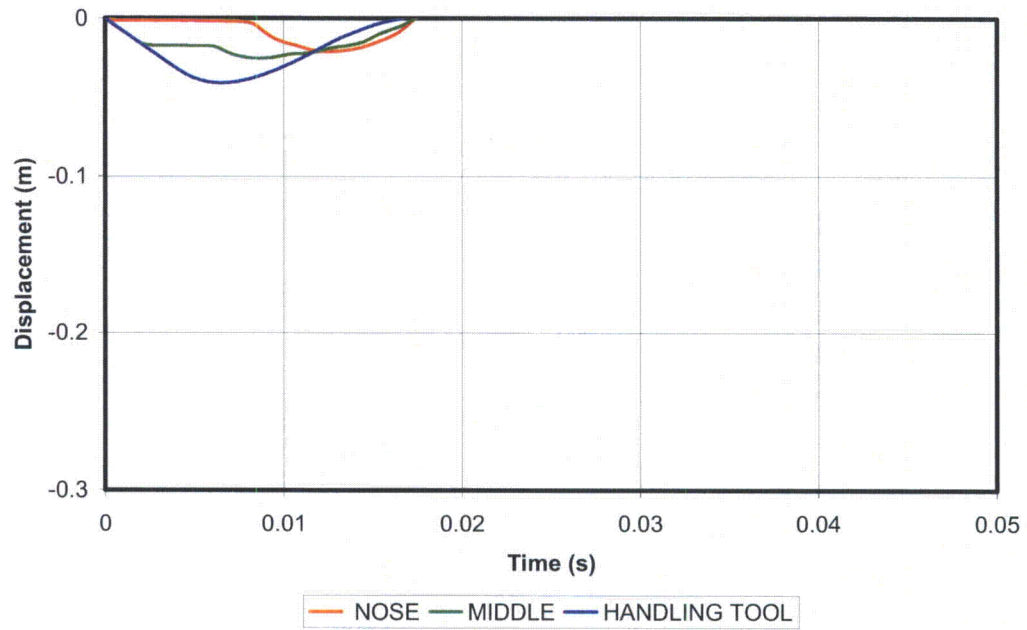


Figure 4-36. Spent Fuel, Intersection, with Tool. Fuel Displacements

PEEQ
SNEG, (fraction = -1.0)
(Avg: 75%)

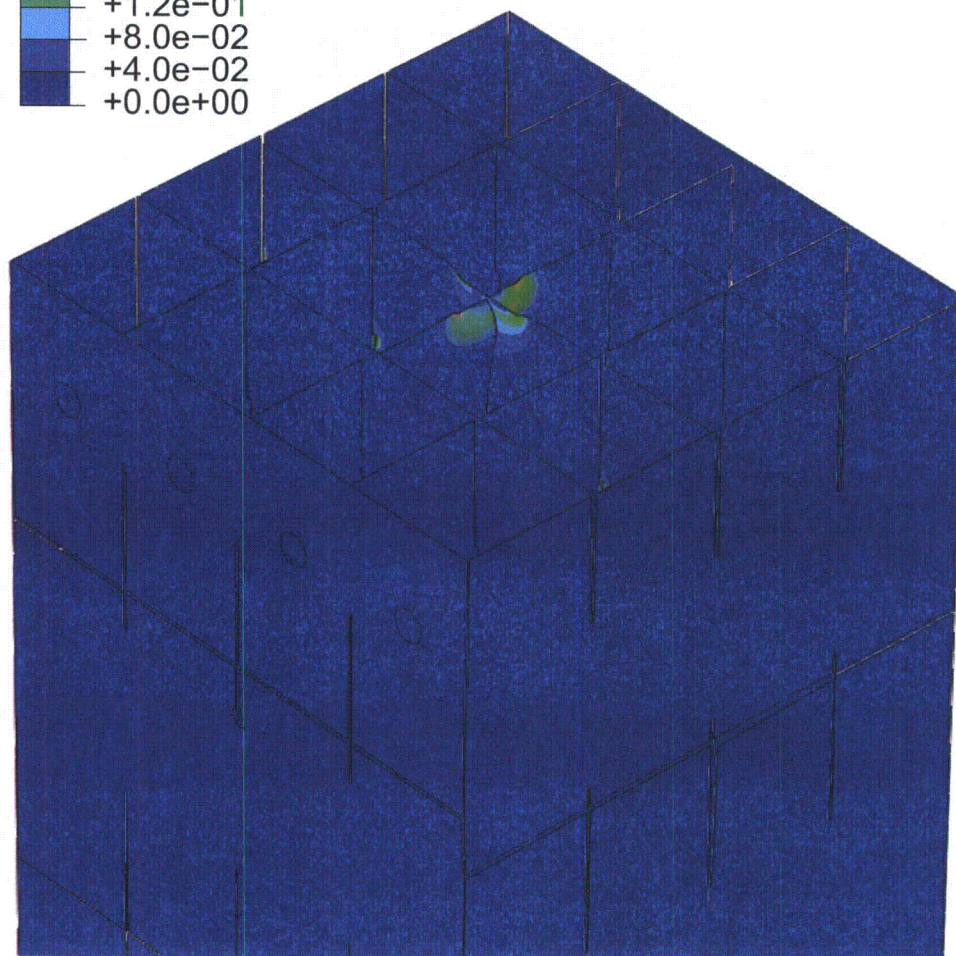
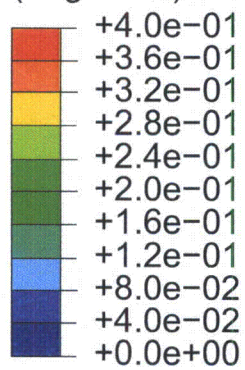


Figure 4-37. Spent Fuel, Intersection, with Tool. Plastic Deformations

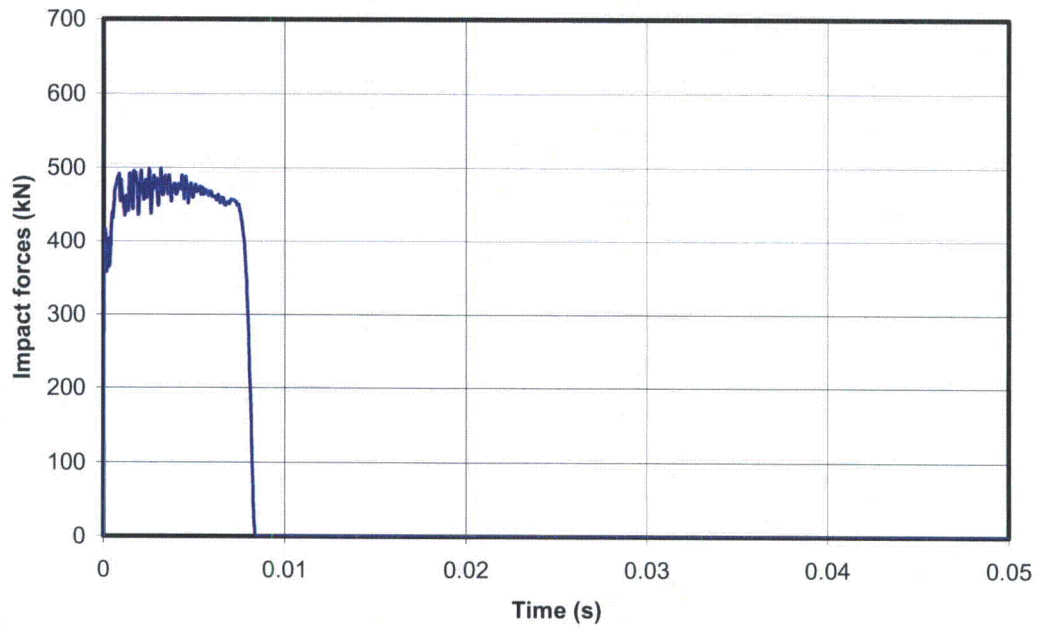


Figure 4-38. Spent Fuel, Intersection, without Tool. Impact Forces

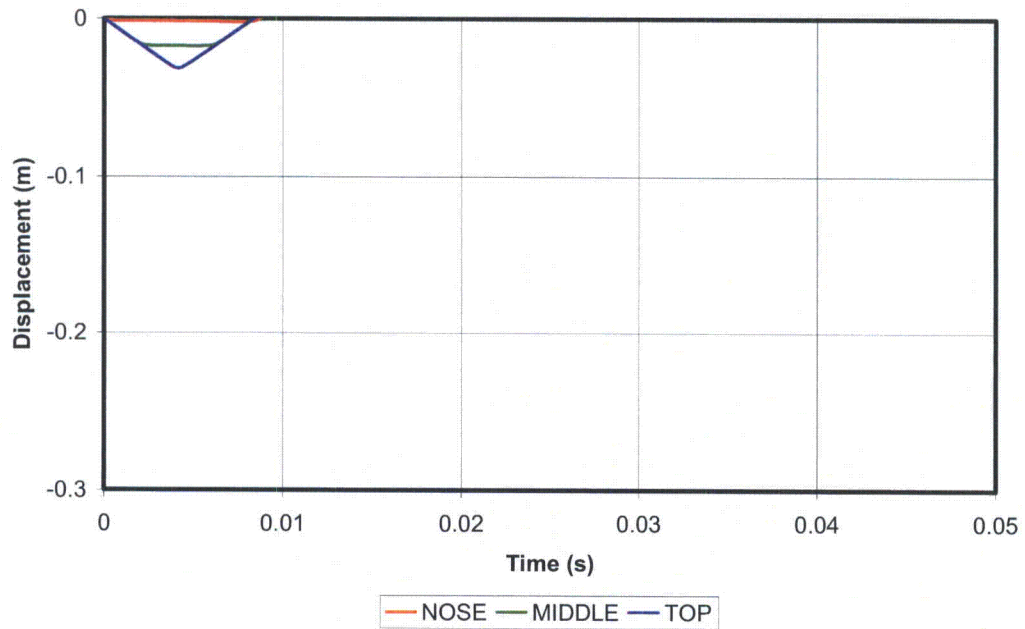


Figure 4-39. Spent Fuel, Intersection, without Tool. Fuel Displacements

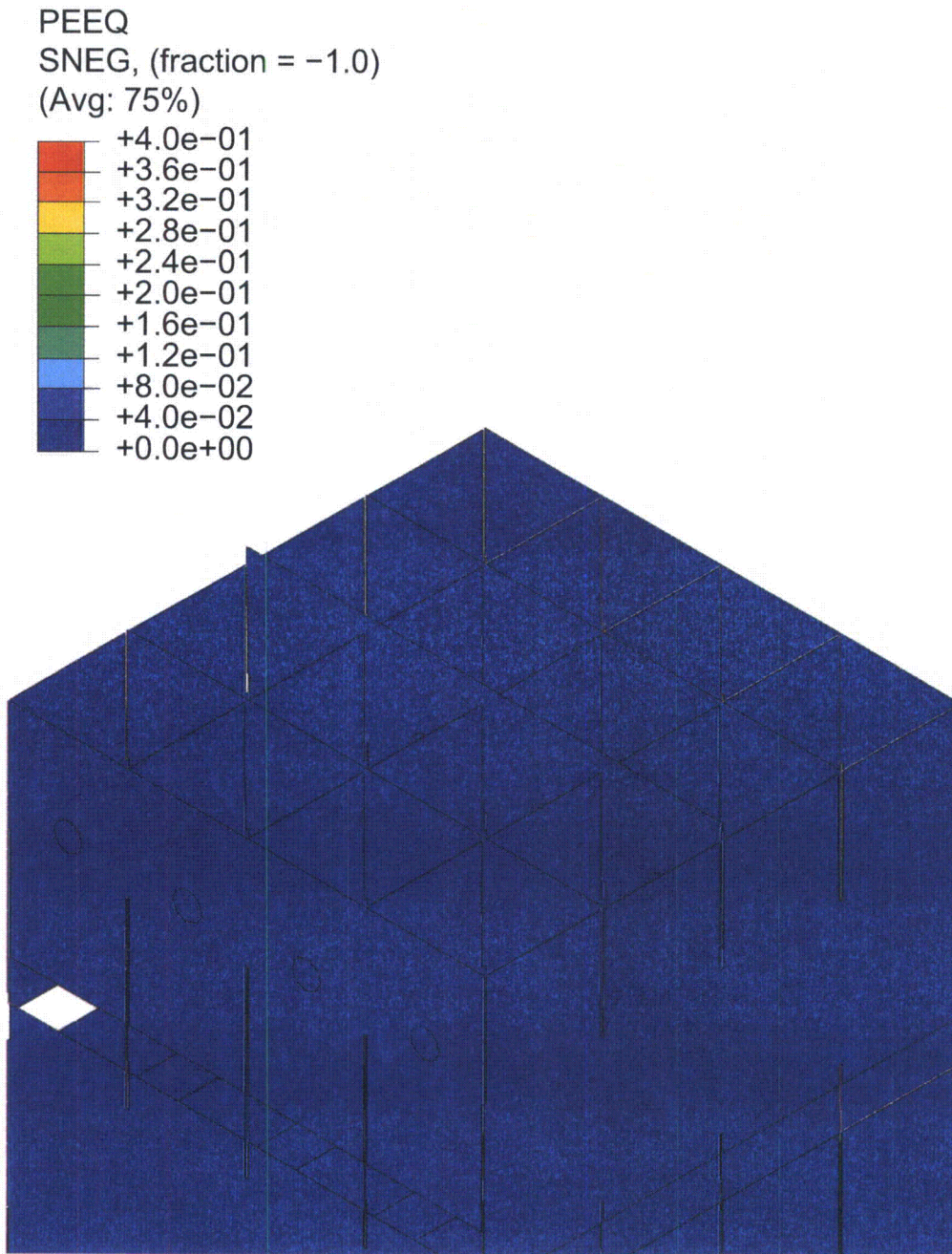


Figure 4-40. Spent Fuel, Intersection, without Tool. Plastic Deformations

4.5 FRESH FUEL RACKS

This section is dedicated to analyzing the postulated impacts on the racks for fresh fuel. These impacts are all assumed to occur when the fuel element is accidentally released from an elevation 1 m above the bottom plate of the rack. The fuel element may or may not be accompanied by the handling tool in the drop. Because of the smaller drop height, the present impacts are far less energetic than those studied in previous sections.

After being released, the element may impact the top of the short wall of the cell or proceed to impact the bottom plate. Both of these problems are analyzed in the present section.

4.5.1 *Impact on the Base Plate*

The impact velocity for 1 m drops onto the base plate, disregarding energy losses by interaction with the water, is 4.43 m/s.

The mesh used for analysing the impact in a cell next to a stiffener is shown in Figure 4-41. For a fuel element falling together with the handling tool, the resulting history of impact forces can be seen in Figure 4-42 and the deformations generated appear in Figure 4-43.

The timing along the history of forces is similar to that characterising the impacts on the base plate of the spent fuel racks. Timing is essentially prescribed by the vibrational characteristics of the fuel element together with the handling tool. What is different is the level of forces developed, which is now smaller as a consequence of the smaller impact velocity. The first part of the history, with sustained forces around 0.24 MN, approximately coincides with the theoretical expectations for impact of an elastic bar; the second part reflects the deceleration of the fuel handling tool.

The plastic deformations are of an essentially local nature and remain below 0.04, hence much lower than ductility of the material, which is 0.4.

When the analysis is repeated without the handling tool, the force history (Figure 4-44) is not very different, except that the hump associated with the handling tool is no longer present. The deformations induced are now very small, as indicated in Figure 4-45.

4.5.2 *Impact on the Wall*

The other possible impact against a fresh fuel rack is the one that could take place against the upper edge of the short outer wall of the cell. The drop height is only 0.400 m and the impact velocity, neglecting any water interaction effects, is 2.80 m/s.

Such an impact has little significance from the viewpoint of the forces generated. The information being sought is the magnitude of the distortions caused on the short wall and the possible transmission of the effects to the side walls.

Figure 4-46 presents the mesh used and Figure 4-47 shows the effects of the postulated impact when the fuel element drops together with the handling tool. Given the relatively small energy of the drop, the distortions-caused are only moderate and the plastic deformations do not reach

the ductility of the material, thus no tearing of the wall would take place. Finally, no deleterious effects occur on the side walls.

The effects are even smaller if the fuel element drops without the handling tool. Figure 4-48 shows that the plastic strains induced are indeed negligible.

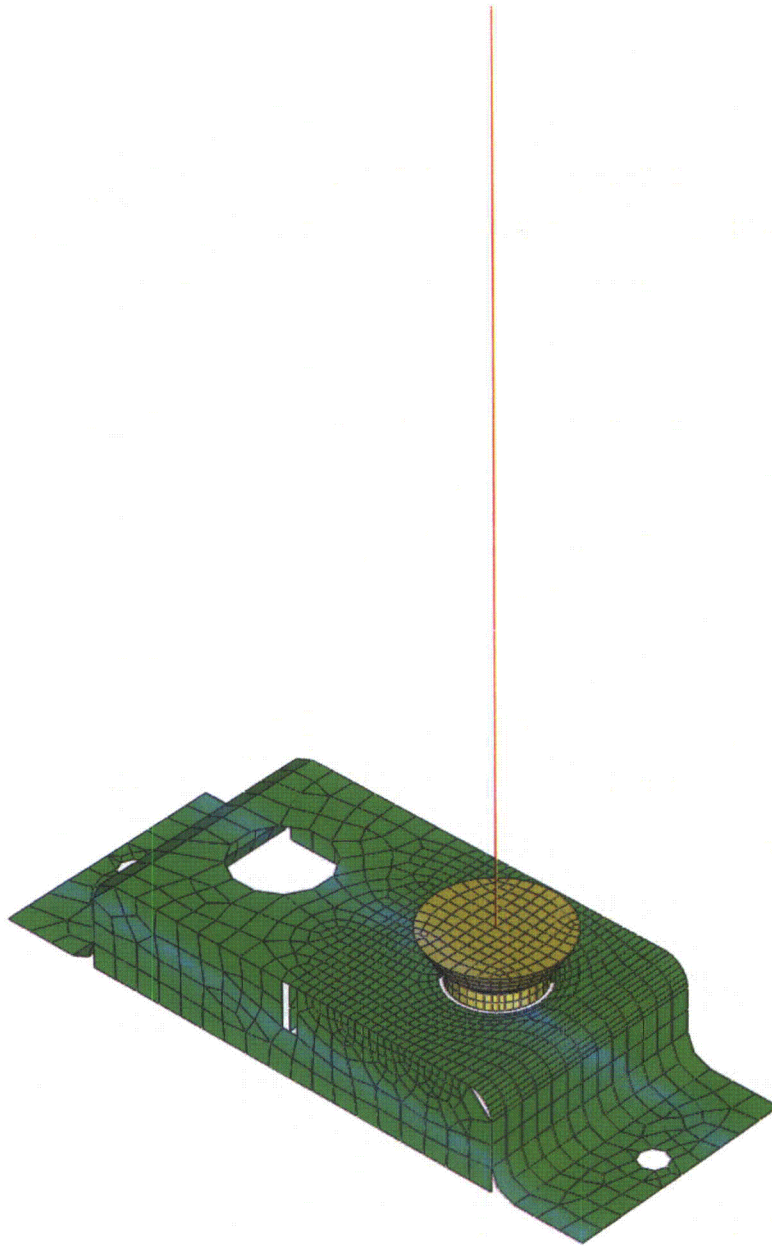


Figure 4-41. Fresh Fuel, Bottom Plate. View of the Mesh

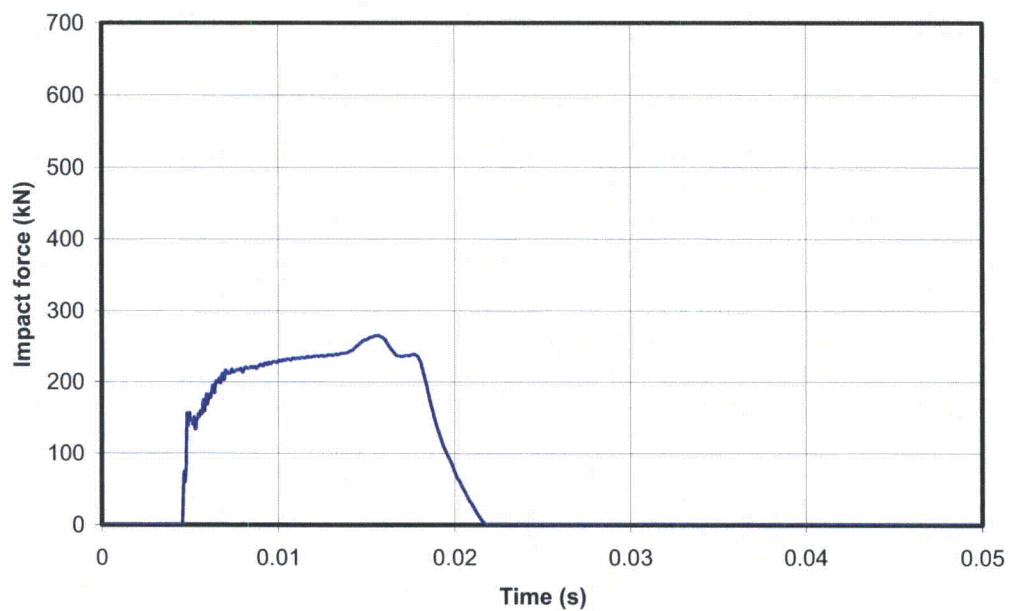


Figure 4-42. Fresh Fuel, Bottom Plate, with Tool. Impact Forces

PEEQ
SNEG, (fraction = -1.0)
(Avg: 75%)

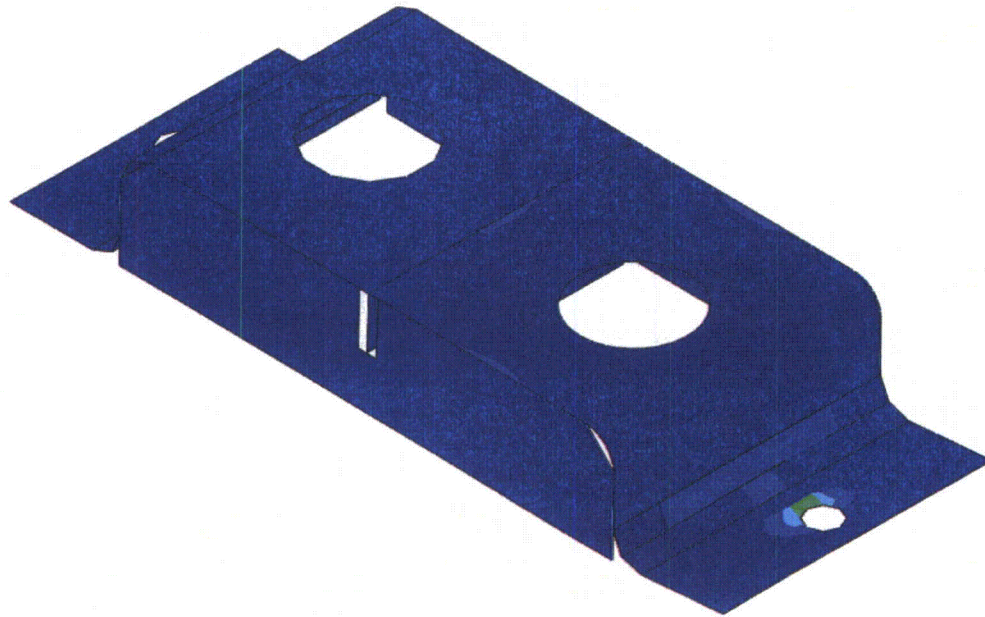
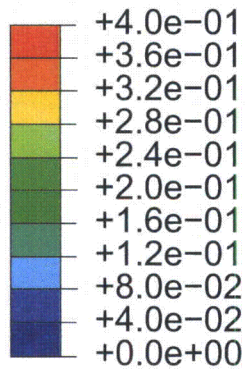


Figure 4-43. Fresh Fuel, Bottom Plate, with Tool. Plastic Deformations

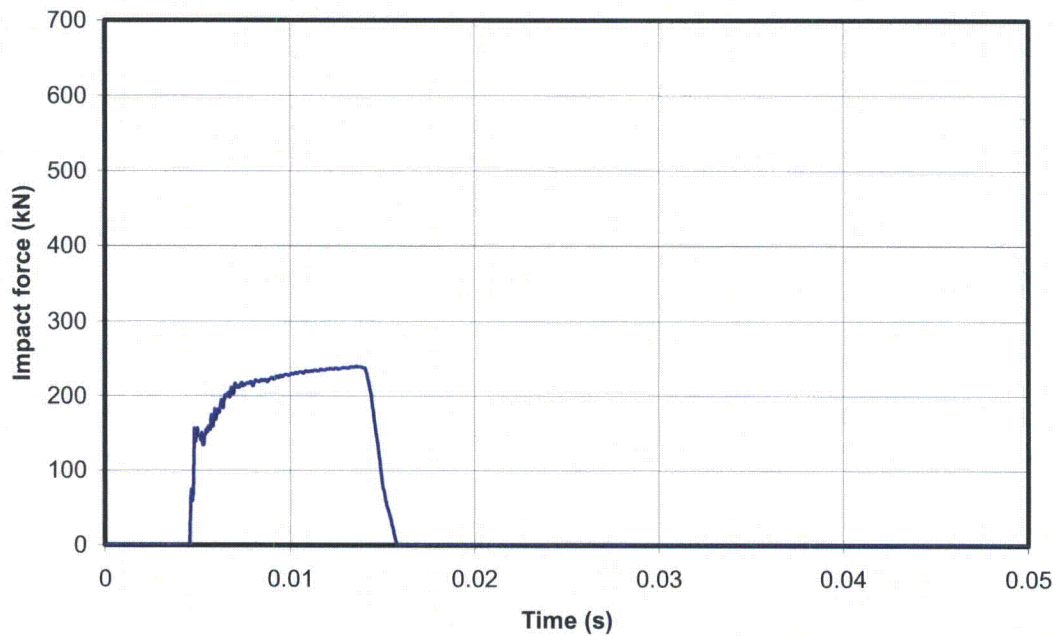


Figure 4-44. Fresh Fuel, Bottom Plate, without Tool. Impact Forces

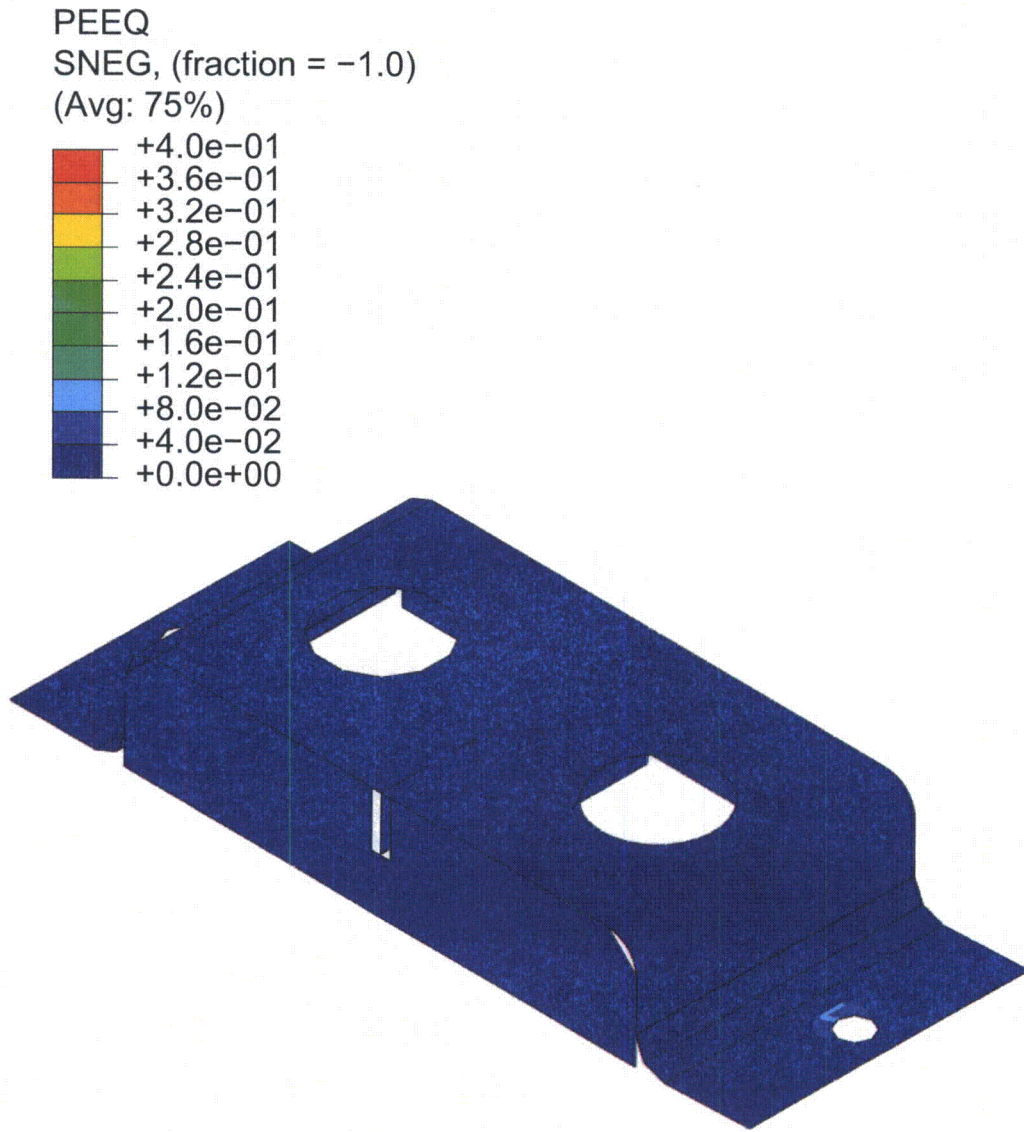


Figure 4-45. Fresh Fuel Bottom Plate, without Tool. Plastic Deformations

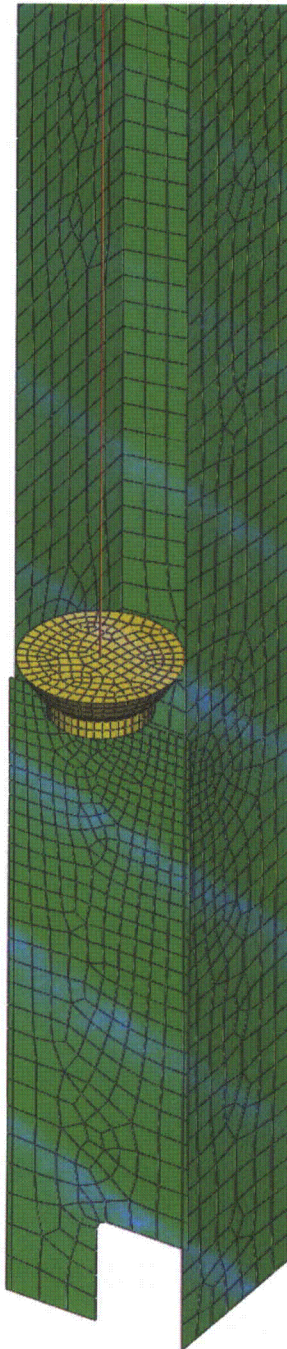


Figure 4-46. Fresh Fuel, Wall. View of the Mesh

PEEQ
SNEG, (fraction = -1.0)
(Avg: 75%)

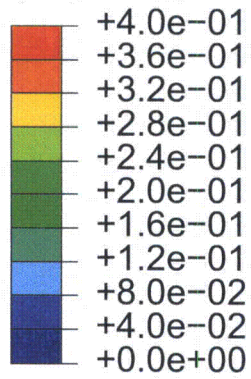


Figure 4-47. Fresh Fuel, Wall with Tool. Plastic Deformations

PEEQ
SNEG, (fraction = -1.0)
(Avg: 75%)

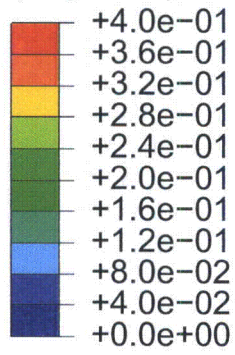


Figure 4-48. Fresh Fuel, Wall, without Tool. Plastic Deformations

4.6 CONCLUSIONS

Analyses have been conducted of the consequences of the impacts arising from postulated drops of fuel elements onto the ESBWR fuel storage racks, including both the racks for spent fuel and for fresh fuel. The analyses have considered both the cases in which the element is arrested by impacts against the upper part of cell walls and those in which the dropped element continues falling through a storage cell until it impacts the base plate. Also, all analyses have been performed twice, taking into account that the handling tool may or may not accompany the fuel element in the drop.

As a result of the analyses conducted, the following conclusions can be offered:

Spent Fuel Racks

1. From the viewpoint of possible damage to the walls, the most demanding impacts are those taking place against the top of the spent fuel racks, which occur after 6.4 m drops with a velocity of 7.82 m/s.
2. When these impacts affect a single wall with the slots in the lower part of the plate, considerable local damage is caused on the upper part of the wall, extending to a depth of about 7 cm if the fuel element falls with the handling tool and about 4 cm otherwise. Such effects are acceptable because they do not reach the active zones of the elements. Impact forces are always moderate and do not exceed 0.35 MN.
3. When the impacts affect a single wall with the slots in the upper part of the plate, the impacted wall can easily bend away, thus generating a fairly soft response. As a consequence, the dropped element is able to advance about 20 cm into the rack if it falls together with the handling tool and about 10 cm without it. Such effects are again acceptable because the 10 cm drop is insufficient to reach the active zones of the elements. It should also be noticed that a greater penetration is not possible by wall bending, but would require tearing through the wall material; this implies that the 20 cm mentioned will not be exceeded.
4. When the impacts take place at the intersection of cell walls, the target is more competent than in impacts against wall single walls. The deformations are therefore considerably smaller and the indentation caused in the rack does not go beyond 3 cm.
5. Impacts against the base plate of the spent fuel racks are due to drops 1.8 m above the rack and result in impact velocities of 5.68 m/s. After an initial peak of 0.41 MN, the impact force quickly stabilizes at about 0.34 MN, a plateau that will eventually be followed by a 0.67 MN hump if the handling tool accompanies the fuel drop in its fall. In all cases the plastic strains remain below the ductility of the material.

New Fuel Racks

6. The impacts postulated against the fresh fuel racks have very moderate effects because the drops occur from only 1 m above the base plate. If the handling tool falls with the fuel element, irrespective of the location in relation with the stiffeners, peak impact forces do not exceed 0.27 MN, a figure that decreases to 0.24 MN without the handling tool. In all cases plastic strains remain covered by the ductility of the material.

7. Finally, impacts on the short front wall of the cell correspond to only 0.4 m drops. The deformations produced are very limited and local and they do not extend to the side walls separating the element from the surrounding ones.

In summary, as a general conclusion, it can be stated that both racks are capable of sustaining the postulated impacts within the bounds imposed by the specifications.

4.7 REFERENCES

1. ASME - American Society of Mechanical Engineers (2003) "ASME Section III. Boiler and Pressure Vessel Code".
2. GE - General Electric (1978) "6' Fuel Drop Analysis", Report EC-07 Rev. 0.
3. GE Hitachi Nuclear Energy (2008) "Fuel Storage Rack Design Specification", Document No. 26A7032 Rev.2,
4. SIMULIA (2008) "Abaqus/Explicit Users' Manual", Version 6.8, Providence, Rhode Island.

5. THERMAL-HYDRAULIC ANALYSIS (17.3 MW CASE)

The analysis in this section assumes an abnormal heat load input of 17.3 MW. However, this heat load was determined not to be a bounding condition. An updated abnormal condition heat load of 19.0 MW (Reference 11) is bounding and shall be considered in addition to the analyses performed at 17.3 MW and 29.0 MW. See Appendix G for the evaluation of the 19.0 MW case.

5.1 INTRODUCTION

The purpose of this analysis is to determine the maximum peak temperatures that will be reached at the exit of the spent fuel racks in the spent fuel pool and the buffer pool in the ESBWR nuclear power station. Also, analysis shall demonstrate that these fuel storage racks are designed such that nucleate boiling is prevented.

A Computational Fluid Dynamics (CFD) based method will be used for the spent fuel pool analysis. This will allow analysis of the behavior of the water within the pool and the temperatures that the water will reach.

Cooling water flow provided to the Buffer Pool is equal to cooling water flow provided to the SFP. Since the heat loads in the Buffer Pool are significantly less than the heat loads in the SFP, the analysis for the Buffer Pool is bounded by the analysis of the SFP (See Section 5.4).

5.1.1 Inputs / Assumptions

1. There are two postulated scenarios to be evaluated for the spent fuel pool (SFP):

a. Normal Conditions

- Heat Load = 10-Year spent fuel accumulation
= 7.626 MW (Reference 1)
- Maximum Pool Bulk Temp = 48.9°C (Reference 1)
- Pool Cooling Rated Flow Rate = 545.1 m³/hr = 150.96 Kg/s
(Reference 1)

b. Abnormal Conditions

- Heat Load = 10-Year spent fuel accumulation + full core offload
= 17.3 MW (Reference 1)
- Maximum Pool Bulk Temp = 60°C (Reference 1)
- Pool Cooling Rated Flow Rate = 1090.2 m³/hr = 301.92 Kg/s
(Reference 1)

2. For the purpose of this analysis, it is assumed that the FAPCS maintains the pool at a steady bulk temperature and always removes heat at the rate it is produced. This assumption simplifies the model into a steady-state analysis by avoiding bulk temperature transients.

5.1.2 Acceptance Criteria

The design of the racks shall allow adequate natural circulation to prevent nucleate boiling within the stored fuel assemblies.

The local coolant temperature of the fluid exiting the top of the spent fuel storage rack shall not exceed the temperature limit for stress properties of the various fuel rack materials, which is 121°C (250°F).

5.2 CALCULATION METHODOLOGY

5.2.1 General Description

The calculation methodology for this analysis consists of two phases.

5.2.1.1 Pool Inlet Temperature Determination

In order to model the fluid dynamics of the pool, it is necessary to determine the temperature of the cooled water being returned to the pool from the FAPCS. The pool inlet temperature will be back-calculated from the assumptions described in 5.1.1. Because this analysis assumes a steady-state condition where the pool bulk temperature is “locked in” at its maximum value, the temperature of the pool inlet water does not necessarily reflect the realistic capabilities of the FAPCS. To determine the maximum inlet temperature of the water in each of the cases, the following values are used: the maximum bulk temperature (also equivalent to the pool outlet temperature), the heat generated by the fuel elements, and the flow rate provided by the FAPCS. Although the calculated pool inlet temperature is not a realistic design parameter, it is conservative in the context of this analysis due to the higher-than-normal bulk pool temperature.

5.2.1.2 Calculation of the Velocities and Temperatures within the Spent Fuel Pool (SFP)

Once the model inputs have been determined, the calculation of the velocities and temperatures are performed using a CFD based method, in order to evaluate the bounding temperature profile within the SFP.

5.2.2 Pool Inlet Temperature Determination

In this section, the maximum pool inlet temperatures are calculated for the normal and abnormal conditions.

The normal condition is defined as the spent fuel from 10 years of plant operation, which is limited by the capacity of the initial configuration of fuel racks in the spent fuel pool. The abnormal condition is defined as the spent fuel from 10 years of plant operation plus a full core offload, which is also limited by the capacity of the initial configuration of fuel racks in the spent fuel pool.

5.2.2.1 Normal Conditions Case

The heat generated under normal conditions is 7.626 MW (Reference 1).

In the normal conditions case, the flow rate is $545.1\text{m}^3/\text{h}=150.96\text{Kg/s}$ (Reference 1).

The normal maximum pool bulk temperature is 48.9°C (Reference 1).

$$\Delta T = \frac{\text{Heat}}{C_p \cdot \text{Flow}} = \frac{7.626 \cdot 10^6 \text{ W}}{4182 \frac{\text{J}}{\text{Kg} \cdot \text{K}} \cdot 150.96 \frac{\text{Kg}}{\text{s}}} = 12.08 \text{ K}$$

Maximum Inlet Temperature

$$T_{in} = 48.9 - 12.08 = 36.8^\circ \text{C}$$

Therefore, the maximum inlet temperature is 36.8°C for the normal conditions case.

5.2.2.2 Abnormal Conditions Case

The heat generated under abnormal conditions is 17.3 MW (Reference 1). In the abnormal conditions case, the flow rate is $1090.2\text{m}^3/\text{h}=301.92\text{Kg/s}$ (Reference 1).

$$\Delta T = \frac{\text{Heat}}{C_p \cdot \text{Flow}} = \frac{17.3 \cdot 10^6 \text{ W}}{4182 \frac{\text{J}}{\text{Kg} \cdot \text{K}} \cdot 301.92 \frac{\text{Kg}}{\text{s}}} = 13.7 \text{ K}$$

Maximum Inlet Temperature

$$T_{in} = 60 - 13.7 = 46.3^\circ \text{C}$$

Therefore, the maximum inlet temperature is 46.3°C for the abnormal conditions case.

5.2.3 Calculation of the Velocities and Temperatures within the Spent Fuel Pool (SFP)

The calculation of the velocities and temperatures are performed using a CFD (Computational Fluid Dynamics) based method, ANSYS CFX 11.0 (Reference 2).

The Spent Fuel Pool (SFP) water has been modeled and the racks located in the SFP have been modeled as subdomains. In these subdomains a volumetric heat generation and a directional loss coefficient have been imposed (the heat generation for each rack is calculated in Sections 5.2.3.2 and 5.2.3.3 the directional loss coefficient is calculated in Section 5.2.3.1).

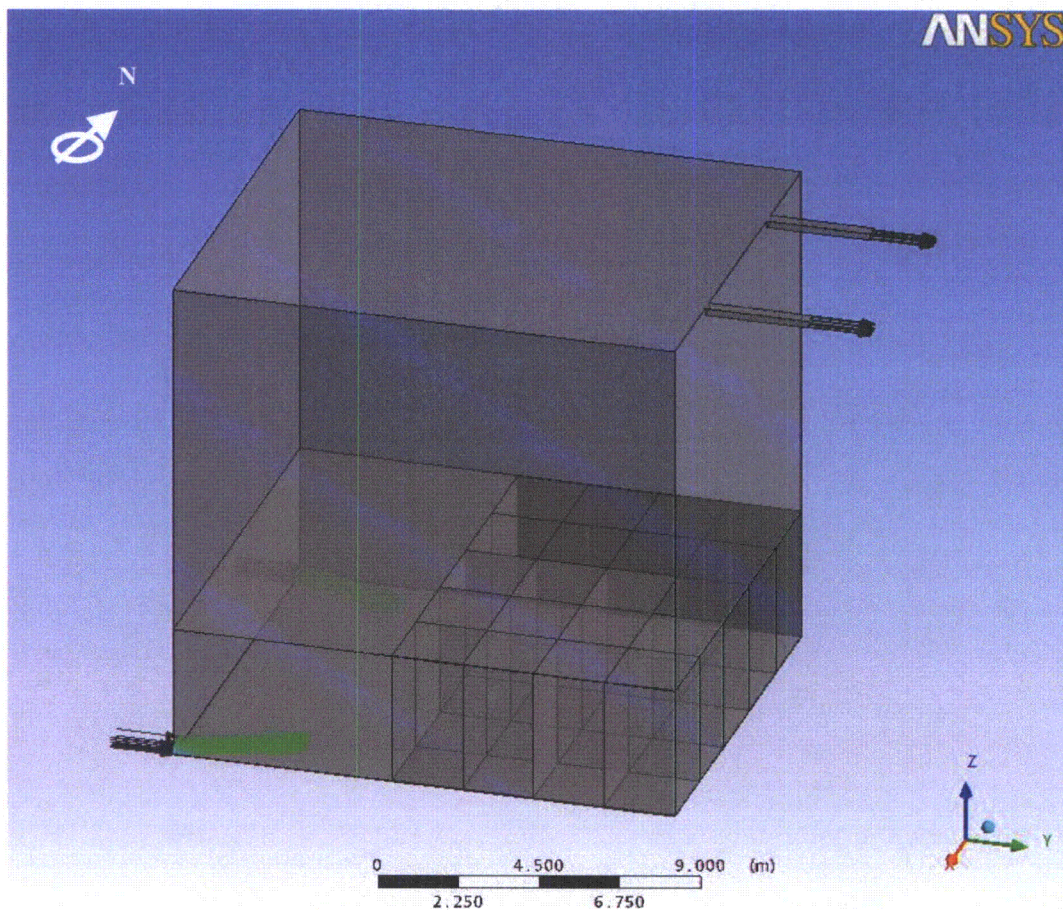


Figure 5-1. SFP Model

The rack layout modeled in Figure 5-1 represents the 10-year configuration (Reference 5). The racks in the three northern rows have an array of 15 x 12. The racks in the two southern rows have an array of 14 x 12. This layout provides a total of 3504 fuel storage spaces.

Two outlets have been modeled at the top of the SFP. Two inlet areas have been modeled at the bottom of the SFP in the corners opposite the racks, including the effect of the diffuser, driving the flow in an angle of 20° measured from the inlet normal direction. The actual inlet locations are inboard from the corners, equally spaced between the pool walls. As this difference from the modelled locations is considered to have negligible impact on results, the model was not modified to reflect the actual inlet locations.

A 42 mm gap between the racks and the northern and southern pool walls has been included in the model. No gap has been considered between the racks and the eastern pool wall. Nor was any gap considered between racks. The gaps used in the model are conservative relative to actual design values.

5.2.3.1 Loss Coefficient Calculation

Figure 5-2 (Reference 8) shows the loss coefficient in the vertical direction inside the racks. This curve is mathematically fit using the following parabolic expression:

$$y = ax^2 + bx + c$$

Where:

y is the pressure drop (PSI)

x is the mass flow rate (LBM/hr)

Since there is no pressure drop when the mass flow rate is zero, $c = 0$. From the parabolic fitting, the coefficients values are:

$$b = 0$$

$$a = 6.2 \cdot 10^{-10} \text{ PSI} \frac{\text{hr}^2}{\text{LBM}^2} = 269.55 \frac{1}{\text{kg} \cdot \text{m}}$$

Thus, pressure loss can be represented by the following formula:

$$\Delta P = K \cdot (m)^2$$

Where:

$$K = 269.55 \text{ Kg}^{-1} \cdot \text{m}^{-1}$$

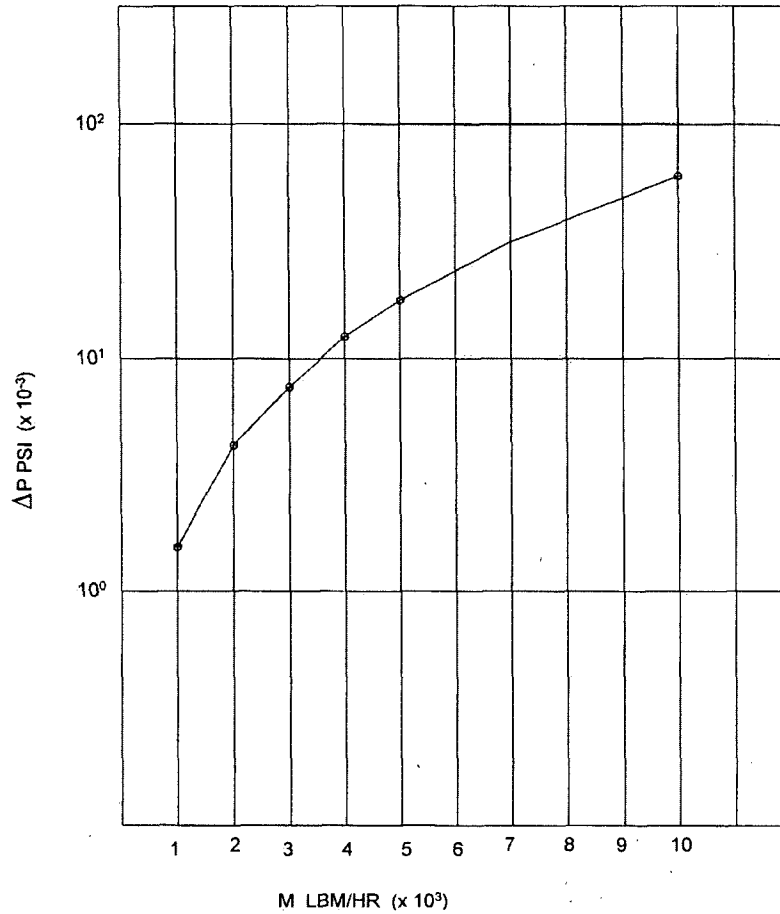


Figure 5-2. Loss coefficient in Racks

The CFD code requires that this loss coefficient be input as a function of velocity. Therefore, an additional calculation using the following formula must be performed. An 8% safety factor has been applied to the loss coefficient obtained previously ($K=269.55\text{Kg}^{-1}\cdot\text{m}^{-1}$).

$$K_N \cdot \rho \cdot L \cdot V^2 = K \cdot (m)$$

$$m = \rho \cdot V \cdot A$$

$$K_N = K \cdot \rho \cdot \frac{A^2}{L} = 269.55 \cdot 1.08 \cdot 1000 \cdot \frac{(0.168^2)^2}{3.856} = 60.13 \text{m}^{-1}$$

This is the value used for all the racks in the model. To model vertical-only water movement inside the racks, the loss coefficient applied in the two horizontal directions (x, y) is assumed to be 10^6 times greater than in the vertical direction.

To simulate the heat generation produced by the Fuel Assemblies (FA) inside the racks, a volumetric heat generation has been applied to the subdomains. For conservatism, it has been assumed that the most recently discharged FA (the most active FA) are located together. The temperature reached with this configuration is greater than the temperature that would be reached if the discharged FA were distributed uniformly between all the racks in the SFP.

5.2.3.2 Heat Generation Calculation in Each Rack Under the Normal Conditions Case

The heat generated by the FA under the normal conditions case is = 7.626MW. For conservatism, it is assumed that all the heat is generated by the discharged FA.

$$\frac{7.626 \cdot 10^6 W}{476 FA_{new}} = 16021 \frac{W}{FA_{new}}$$

In reference to the FA distribution between the racks, the worst-case configuration has the discharged FA located in the racks farthest from the SFP inlet. The discharged FA will be located in the racks 5, 9 and 13.

$$\text{Heat generated in rack 5: } 180 FA_{New} \cdot 16021 \frac{W}{FA_{New}} = 2883780W$$

$$\text{Heat generated in rack 9: } 180 FA_{New} \cdot 16021 \frac{W}{FA_{New}} = 2883780W$$

$$\text{Heat generated in rack 13: } 7.626 \cdot 10^6 W - 2883780W - 2883780W = 1858440W$$

The rest of the racks do not have any heat generation applied.

5.2.3.3 Heat Generation Calculation in Each Rack Under the Abnormal Conditions Case

The heat generated by the FA under the abnormal conditions case is = 17.3MW. Of the 17.3MW considered, 7.626MW is attributed to the accumulation of 10-years of spent fuel. The remainder is attributed to a full core offload.

$$\frac{(17.3 - 7.626) \cdot 10^6 W}{1132 FA_{new}} = 8545.93 \frac{W}{FA_{new}}$$

Fuel from a full core offload requires 6 complete racks and 76 storage spaces in a 7th rack. The heat generated by the accumulation of 10 years of spent fuel is divided among the remainder of storage capacity.

The hottest fuel assemblies are conservatively assumed to be located in the area receiving the least amount of cooling. These racks are 5, 6, 9, 10, 13, and 14.

$$\text{Heat generated in rack 5, 6, 9 and 10: } 180FA_{New} \cdot 8545.93 \frac{W}{FA_{New}} = 1538267.4W$$

$$\text{Heat generated in rack 13 and 14: } 168FA_{New} \cdot 8545.93 \frac{W}{FA_{New}} = 1435716.2W$$

Heat generated in rack 11:

$$(17.3-7.626) \cdot 10^6 W - 4 \cdot 1538267.4W - 2 \cdot 1435716.2W = 649498W \rightarrow FA_{New} \text{ in rack 11} = \frac{649498W}{8545.93 \frac{W}{FA_{New}}} = 76FA_{New}$$

$$\text{Number and generation of old FA: } 8 \cdot (15 \cdot 12) + 6 \cdot (14 \cdot 12) + (15 \cdot 12 - 76) = 2552FA \rightarrow \frac{7.62610^6 W}{2552FA} = 2988.24 \frac{W}{FA}$$

$$\text{so, heat generated in rack 11: } 76FA_{New} \cdot 8545.93 \frac{W}{FA_{New}} + (15 \cdot 12 - 76)FA \cdot 2988.24 \frac{W}{FA} = 960267.6W$$

Heat generated in racks not completed by new FA:

$$15 \times 12 \text{ Type: } 180FA \cdot 2988.24 \frac{W}{FA} = 537883.2W$$

$$14 \times 12 \text{ Type: } 168FA \cdot 2988.24 \frac{W}{FA} = 502024.32W$$

5.2.4 Summary Tables

The following tables show a summary of the model characteristics and the modeled fluid properties used.

Model Characteristics

| | |
|---------------------------|----------------------------------------------|
| Solver | CFX Serial Standard |
| Solver Advection Scheme | High Resolution |
| Simulation Type | Steady State |
| Buoyancy Option | Buoyant |
| Gravity direction | <0, 0, -9.81m/s ² > |
| Buoyancy Ref. Temperature | 60°C |
| Heat Transfer Option | Total Energy |
| Turbulence Option | k-Epsilon |
| Fluid | Liquid Water |
| | Density = 997 Kg/m ³ |
| | Dynamic Viscosity = 0.0008899 Kg/m s |
| | Specific Heat Capacity Cp = 4181.7 J/Kg°C |
| | Thermal Conductivity = 0.6069 W/m K |
| | Linear Variation of Density with Temperature |

Boundary Conditions

| Normal Conditions | Abnormal Conditions |
|------------------------------------------------------------------------------|------------------------------------------------------------------------------|
| In Flow Rate = 150.96 Kg/s 75.48 Kg/s (each inlet) | In Flow Rate = 301.92 Kg/s 150.96 Kg/s (each inlet) |
| Inlet Flow Direction = 20° Offset Diffuser, Offset towards center of pool | Inlet Flow Direction = 20° Offset Diffuser, Offset towards center of pool |
| Turbulence Intensity = 1% | Turbulence Intensity = 1% |
| Inlet Temperature = 36.8°C | Inlet Temperature = 46.3°C |
| Adiabatic Walls | Adiabatic Walls |
| Outlet Flow Rate 150.96 Kg/s (total of both outlets) | Outlet Flow Rate 301.92 Kg/s (total of both outlets) |
| Loss coeff = 60.13/m | Loss coeff = 60.13/m |
| Transverse Loss Coeff. Multiplier = 1000000 | Transverse Loss Coeff. Multiplier = 1000000 |
| Heat Generation per Section 5.2.3.2 | Heat Generation perSection 5.2.3.3 |

5.2.5 CFD Model Sensitivity

CFD analysis methodology has been used in the past for other spent fuel pool thermal-hydraulic studies. The effect of hypothesis and assumptions, and also the modelling methodology (turbulence model selection, buoyancy treatment or mesh density) has been evaluated by sensitivity studies, according to the best practice guidelines for the use of CFD in nuclear reactor safety applications.

The sensitivity studies are presented in two parts: sensitivity to the numerical method and sensitivity to the mesh density.

Considering the numerical method, many parameters have been evaluated as shown below:

- Inlet mass flow rate increased by 10%
- Inlet temperature reduced by 10%
- Loss coefficient increased by 20%
- Turbulence model validated by a different model (k- ϵ model vs. SST-k- ω model)
- Reference temperature for buoyancy model reduced by 10%
- Turbulence intensity at the inlets increased by 9% (maximum allowed by the code)

The shape of the temperature distribution throughout the pool remains constant, with temperature variations (peak and bulk) of $\approx 1.5\%$. For variations of inlet mass flow rate, loss coefficient, and inlet temperature, the temperature variations (peak and bulk) are $\approx 4\%$ to 6% . Inlet temperature refers to the maximum allowable pool inlet temperature. This value is dependent on the heat load in the pool, as the abnormal flow rate (301.92 Kg/s) and maximum bulk pool temperature (60°C) are analyzed as constant. As the heat load in the pool is increased, the corresponding rack exit temperature increases and the maximum allowable pool inlet temperature must decrease to maintain the bulk pool temperature. Conversely, as the heat load in the pool is decreased, the corresponding rack exit temperature decreases and the maximum allowable pool inlet temperature can increase to maintain the bulk pool temperature.

With regard to the sensitivity of mesh density, typically three cases are used for comparison: the original mesh density, a 50% increase over the original mesh density, and a 100% increase over the original mesh density. Specific examples from a specific thermal-hydraulic analysis of an operating BWR are presented below.

The temperature profiles and values of horizontal slices through the spent fuel pool are analyzed at various elevations for comparison purposes. In comparing the three models, the temperature distributions within the pools were constant and the bulk temperature variance for different locations was less than 2°C .

For the peak temperature value, the original mesh density model produced a result of 101.1°C . The 50% mesh density increase case produced a maximum peak temperature of 105.9°C . The doubled mesh density case produced a maximum peak temperature of 107.0°C . The maximum variation for peak temperature was 5.9°C .

Also a thermal-hydraulic analysis of a representative spent fuel pool has been modelled and solved by two different CFD codes. The shape of the temperature distribution throughout the pool is similar for both models.

The results of these sensitivity studies show that the hypothesis and numerical model to be valid.

5.3 RESULTS

Solving the two cases described previously, the results shown in the following sections are obtained.

5.3.1 Temperature Distribution Under Normal Conditions Case

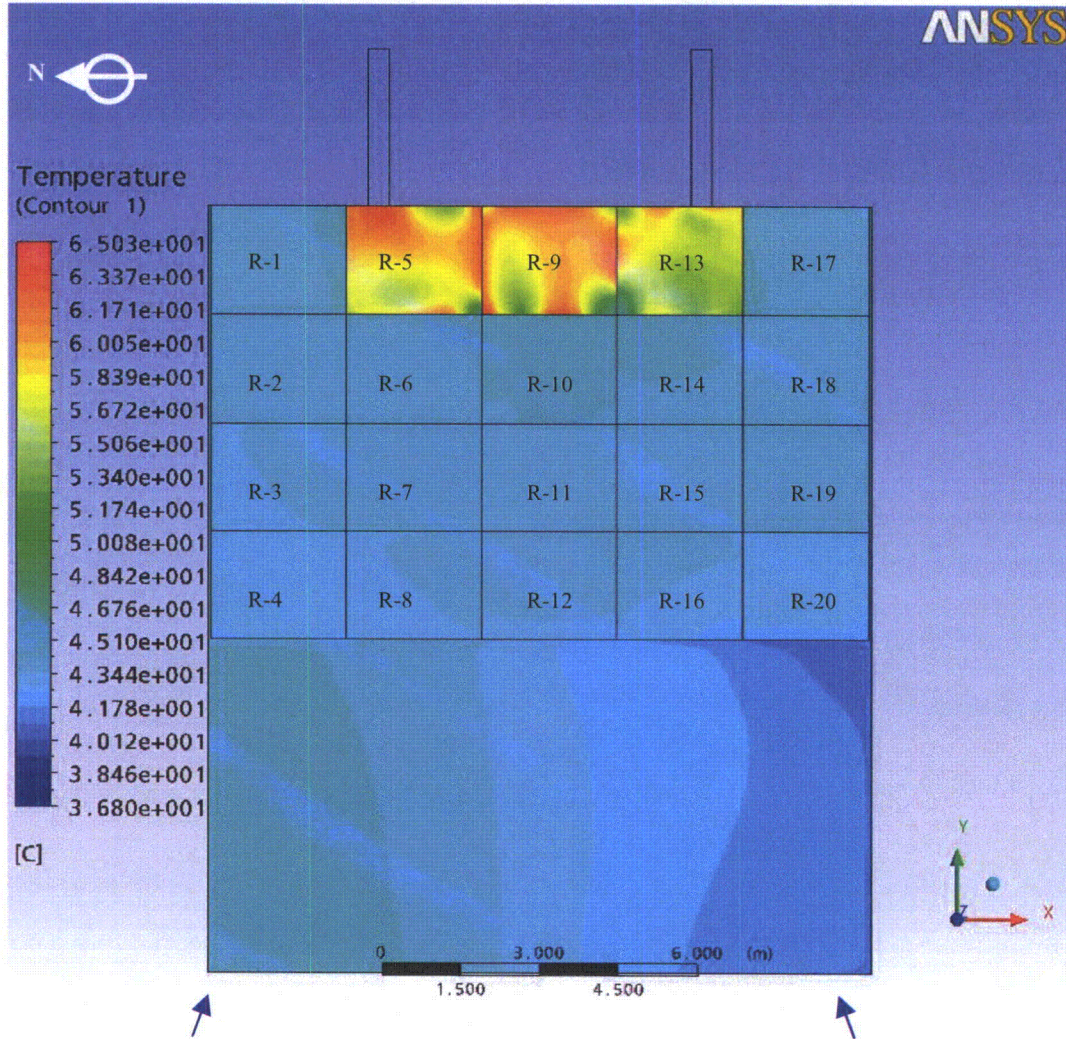


Figure 5-3. Temperature Distribution under the Normal Conditions Case (x,y)

Figure 5-3 shows the temperature distribution in the racks under the normal conditions case. The maximum peak temperature reached in this case is 65.03°C and is reached in the racks where the discharged FA are located. The maximum is reached at the top of the rack and is significantly less than the maximum allowable temperature of 121°C.

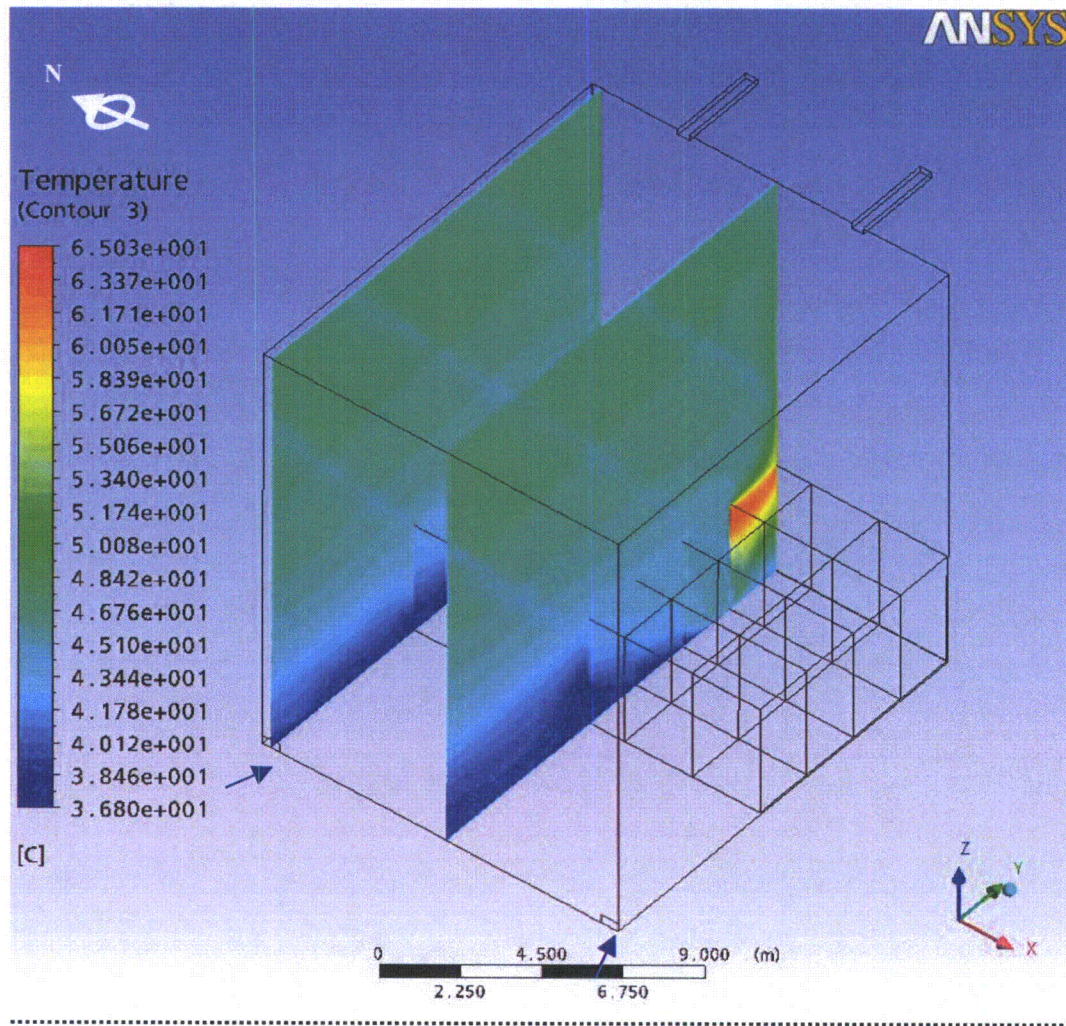


Figure 5-4. Temperature Distribution under the Normal Conditions Case (y,z)

Figure 5-4 shows the temperature distribution in the SFP under the normal conditions case. The temperature scale on the left ranges from the minimum to the maximum temperature on the SFP global. Given the outlet temperature of 48.9°C presented in Section 5.1.1, the maximum inlet temperature (as calculated in Section 5.2.2.1) is determined to be 36.8°C.

5.3.2 Temperature Distribution Under Abnormal Conditions Case

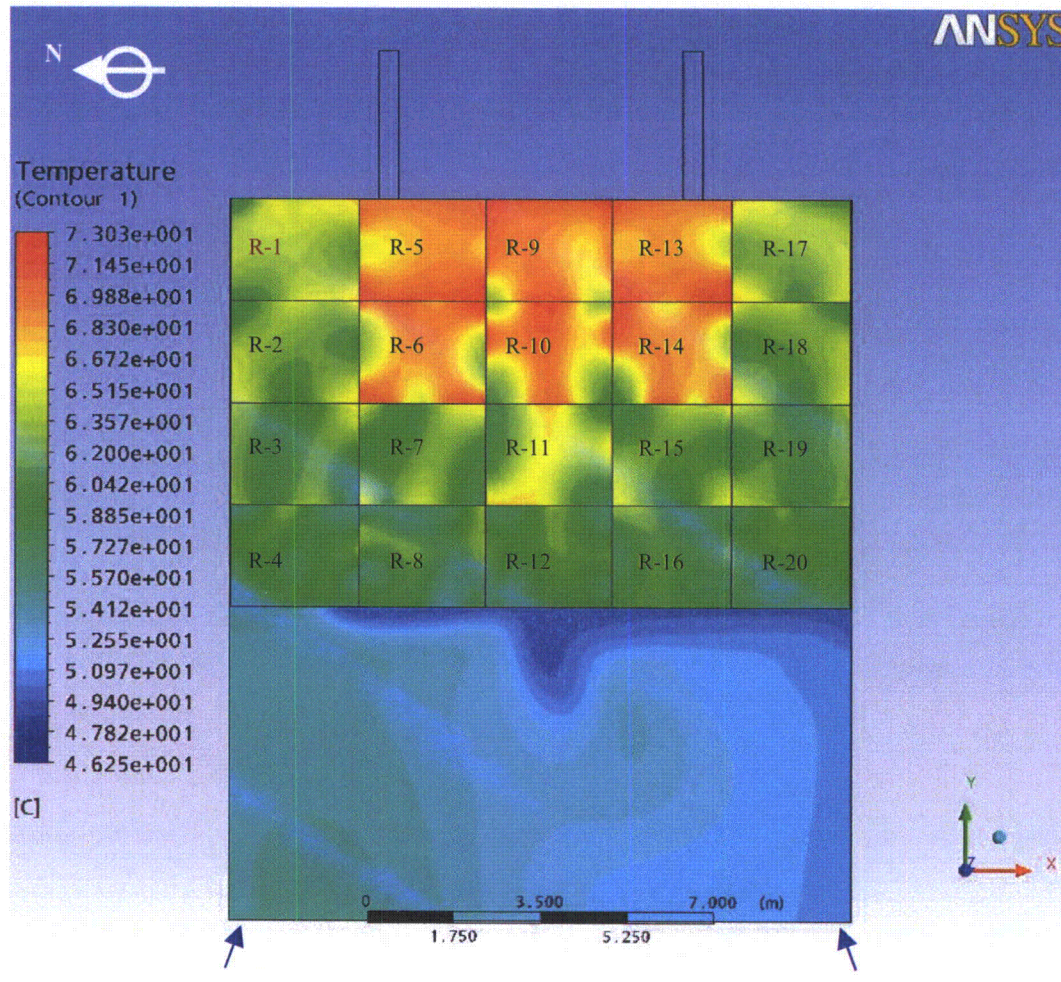


Figure 5-5. Temperature Distribution under the Abnormal Conditions Case (x,y)

Figure 5-5 shows the temperature distribution in the racks under the abnormal conditions case. The maximum peak temperature reached in this case is 73.03°C and is reached in the racks where the discharged FA are located. The maximum is reached at the top of the rack and is significantly less than the maximum allowable temperature of 121°C.

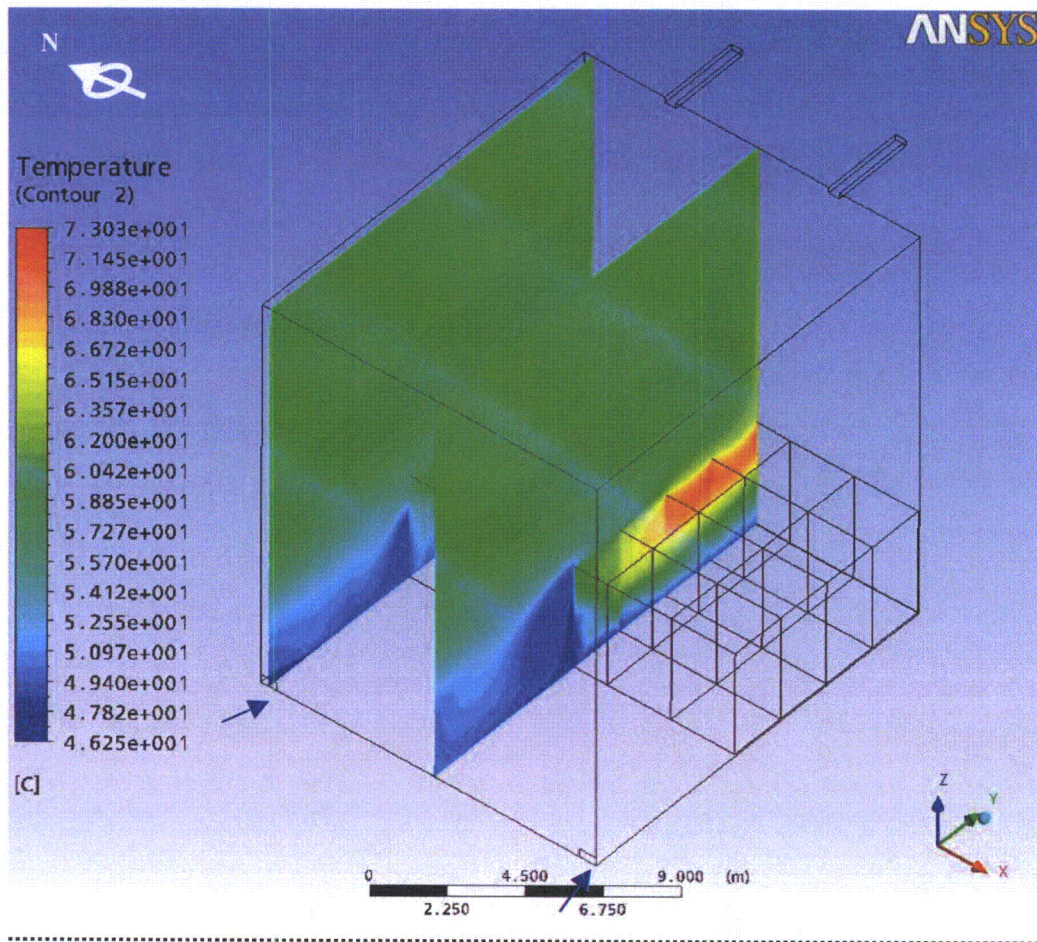


Figure 5-6. Temperature Distribution under the Abnormal Conditions Case (y,z)

Figure 5-6 shows the temperature distribution in the SFP under the abnormal conditions case. The temperature scale on the left ranges from the minimum to the maximum temperature on the SFP global. Given the outlet temperature of 60°C presented in Section 5.1.1, the inlet temperature (as calculated in Section 5.2.2) is 46.3°C.

5.3.3 Velocity Distribution Under Normal Conditions Case

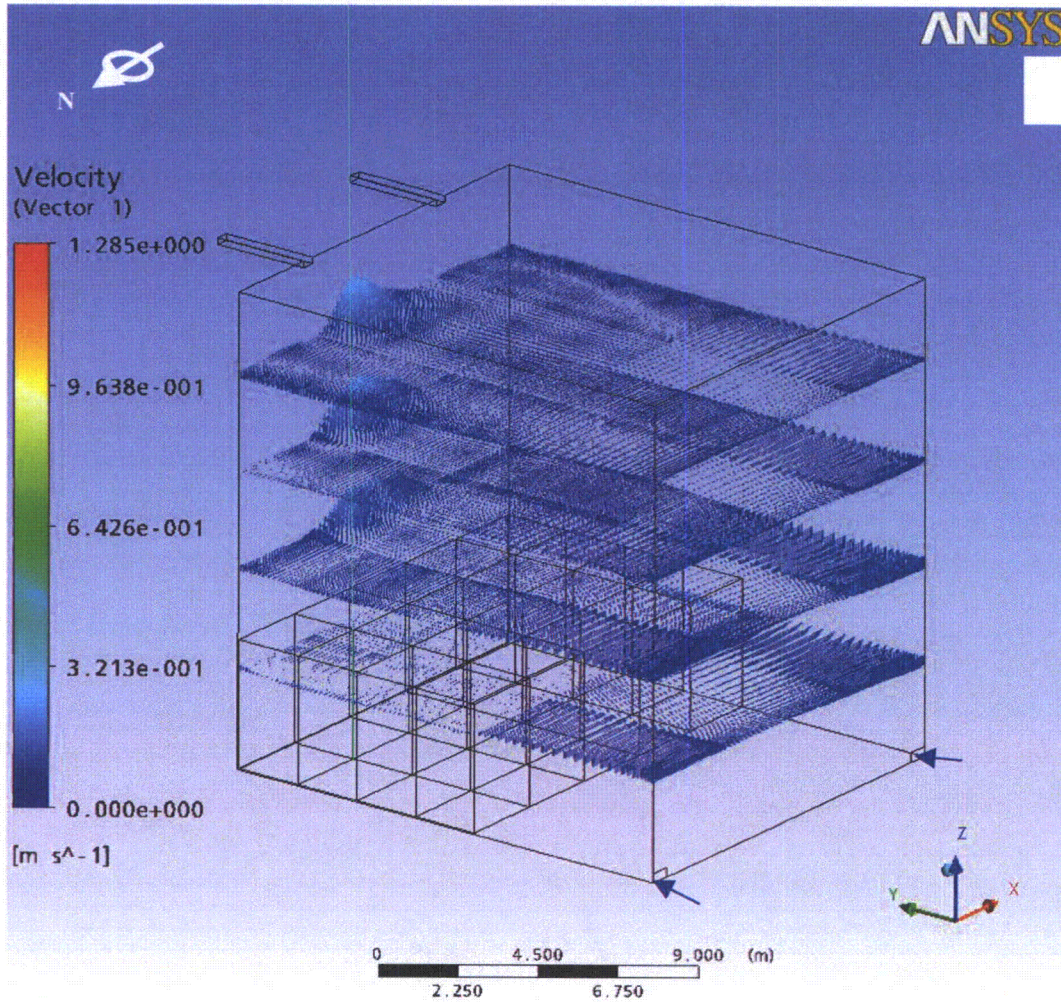


Figure 5-7. Velocity under the Normal Conditions Case (y,z)

Figure 5-7 shows the velocity distribution in the SFP under the normal conditions case. Velocities for horizontal planes at 3, 6, 9, & 12 metres high are shown. Natural convection is forcing a vertical flow from the racks with the highest heat load.

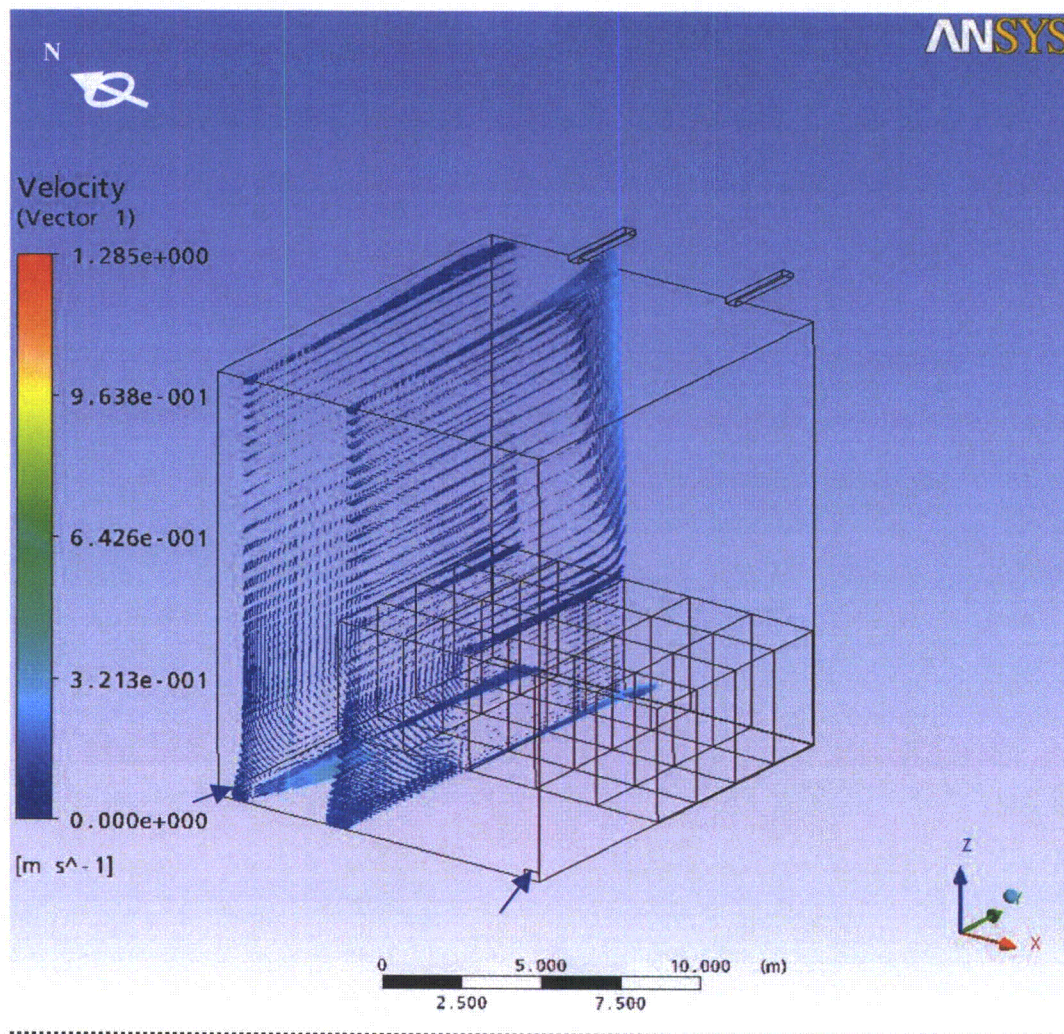


Figure 5–8. Velocity under the Normal Conditions Case (y,z)

Figure 5-8 shows the velocity distribution in the SFP under the normal conditions case. For this figure vertical planes (y,z) have been selected.

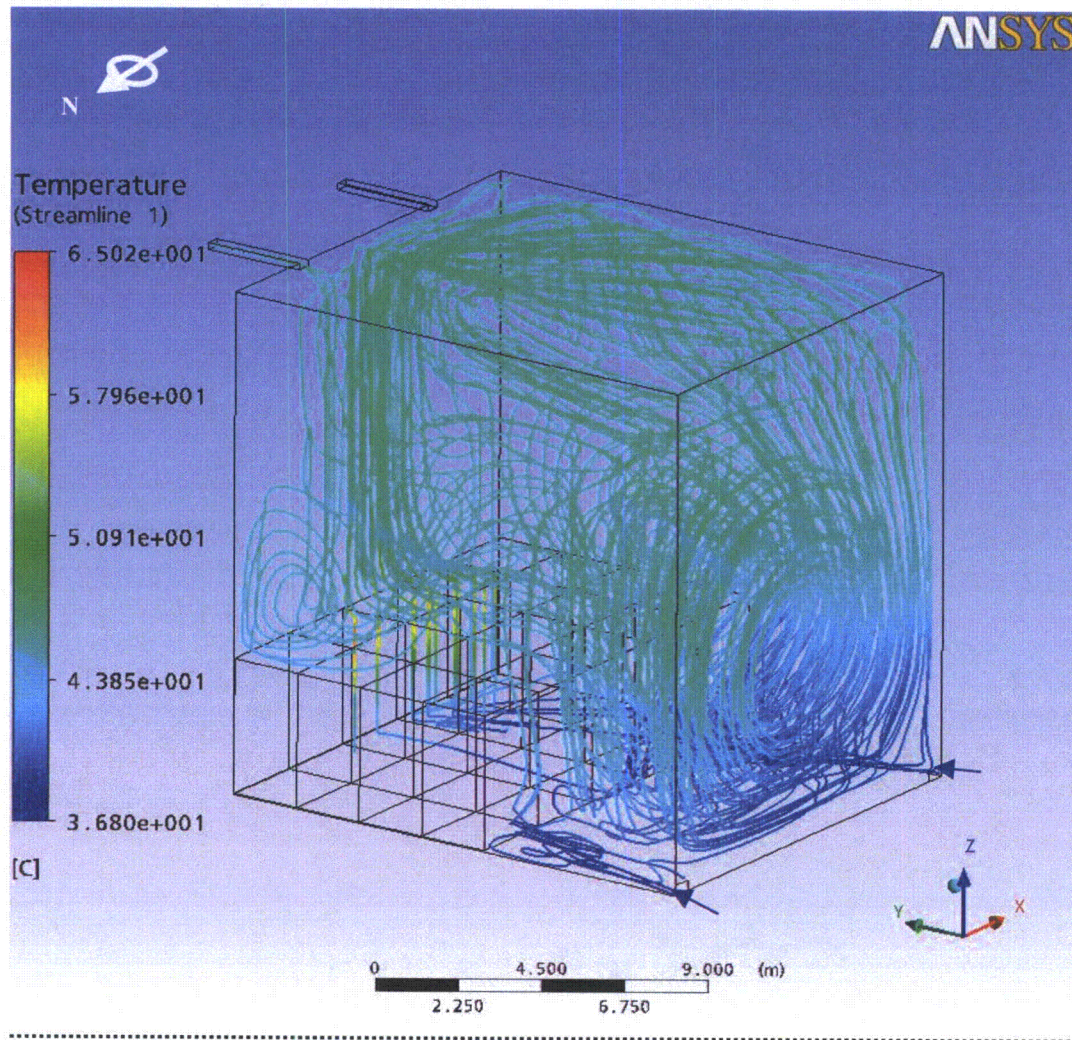


Figure 5-9. Streamlines from Inlets to Outlets under the Normal Conditions Case

Figure 5-9 shows streamlines from the inlets and streamlines to the outlets in the SFP under the normal conditions case. The color of the streamline represents the temperature for each point. As each rack is modeled as an individual domain, and is independent of the fluid domain that is in the pool, flow through the rack is obscured from view in this streamline diagram. Evidence of water temperature increasing as it flows through the rack, from bottom to top, is seen in Figure 5-4.

5.3.4 Velocity Distribution Under Abnormal Conditions Case

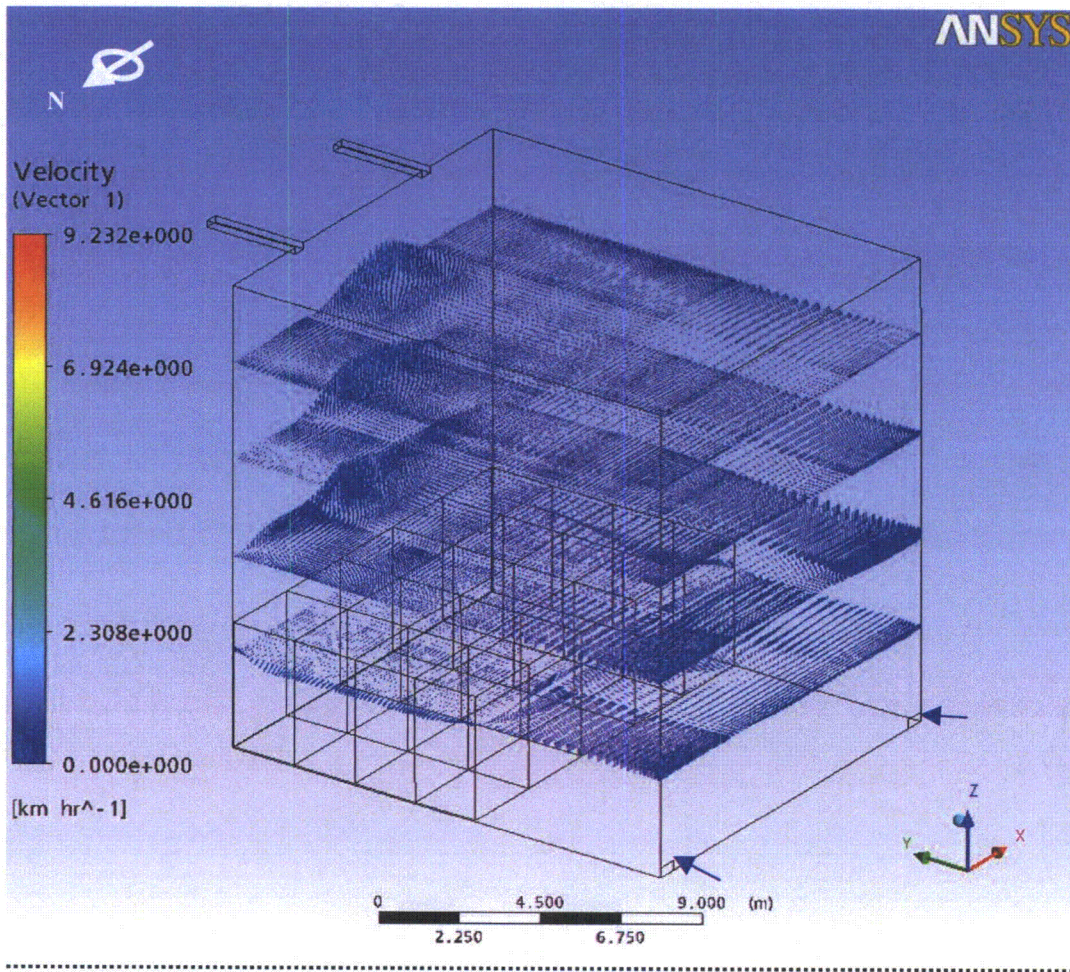


Figure 5–10. Velocity under the Abnormal Conditions Case (y,z)

Figure 5-10 shows the velocity distribution in the SFP under the abnormal conditions case. Velocities for horizontal planes at 3, 6, 9, & 12 metres high are shown. Natural convection is forcing a vertical flow from the racks with the highest heat load.

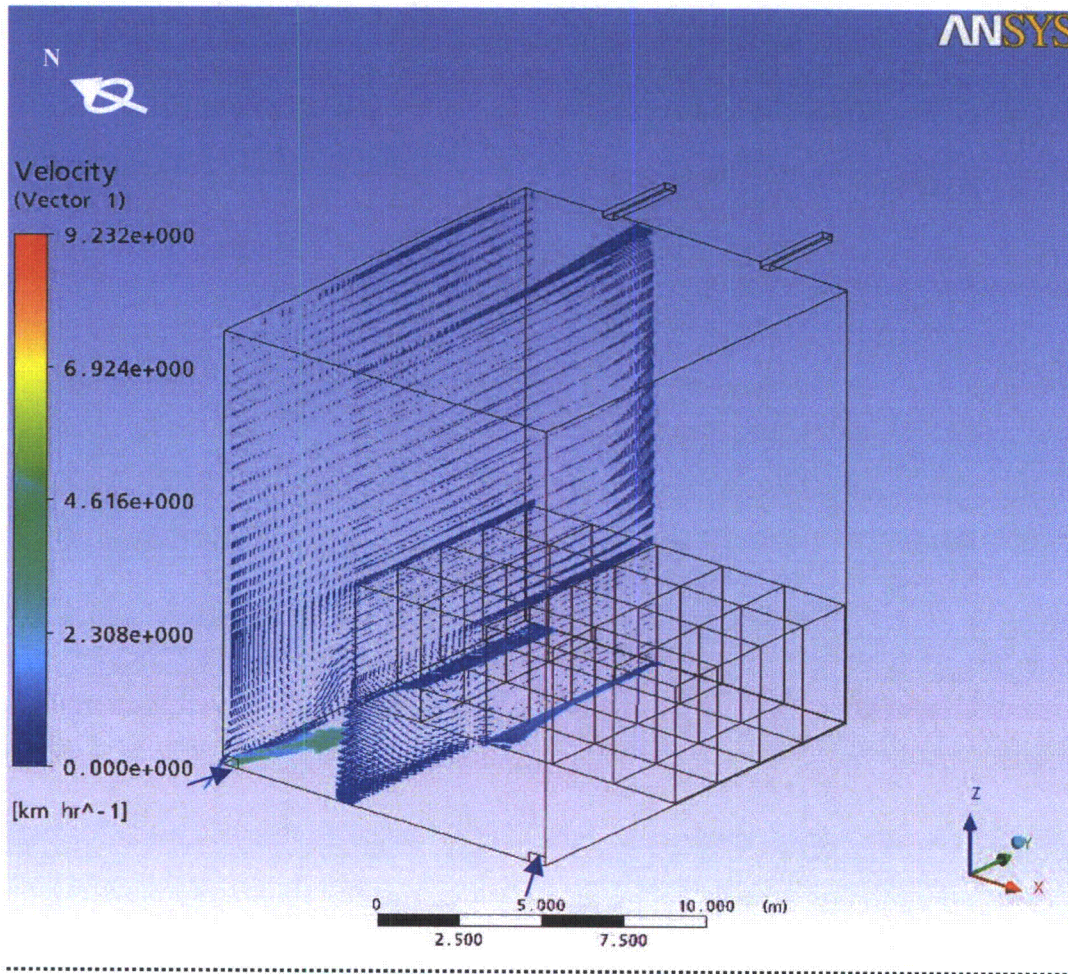


Figure 5–11. Velocity under the Abnormal Conditions Case (y,z)

Figure 5-11 shows the velocity distribution in the SFP under the abnormal conditions case. For this figure, vertical planes (y,z) have been selected.

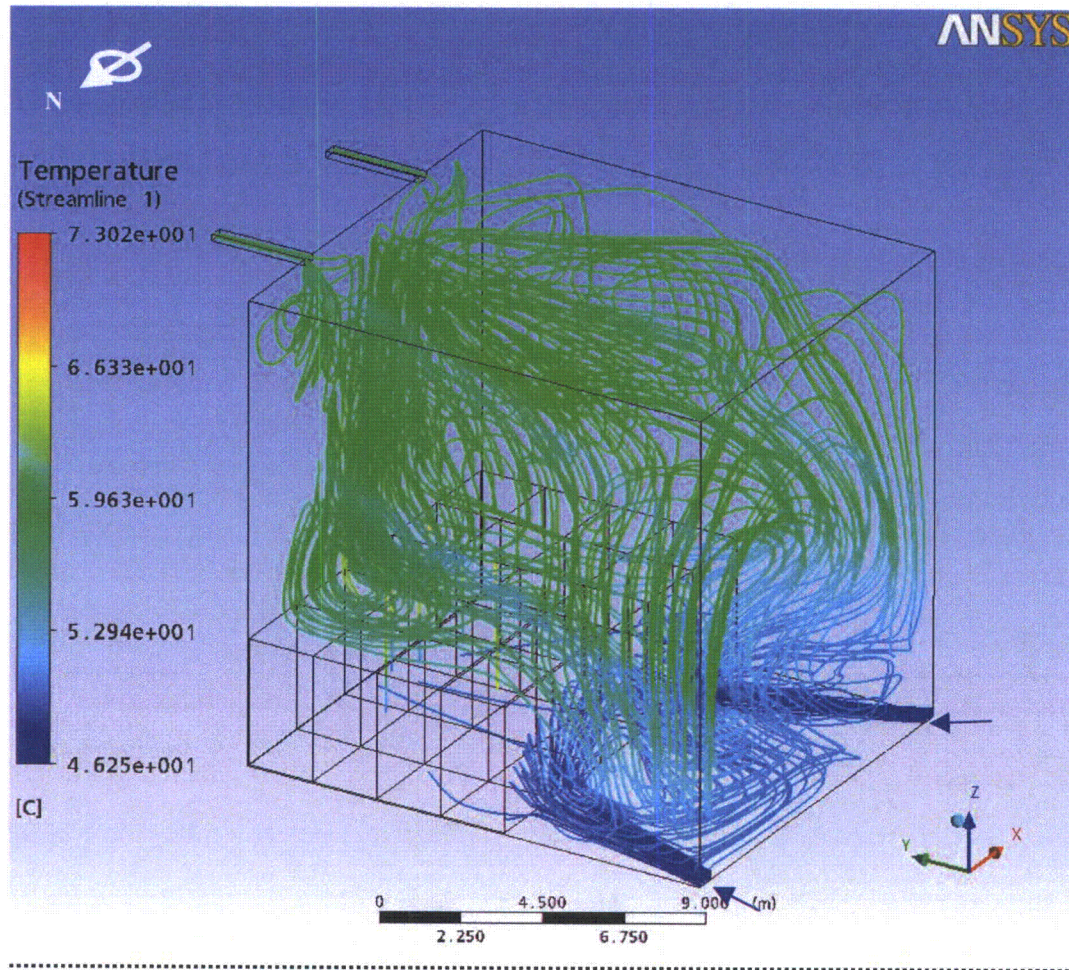


Figure 5–12. Streamlines from Inlets and to Outlets under the Abnormal Conditions Case

Figure 5-12 shows streamlines from the inlets and streamlines to the outlets in the SFP under the abnormal conditions case. The color of the streamline represents the temperature for each point. As each rack is modeled as an individual domain, and is independent of the fluid domain that is in the pool, flow through the rack is obscured from view in this streamline diagram. Evidence of water temperature increasing as it flows through the rack, from bottom to top, is seen in Figure 5-6.

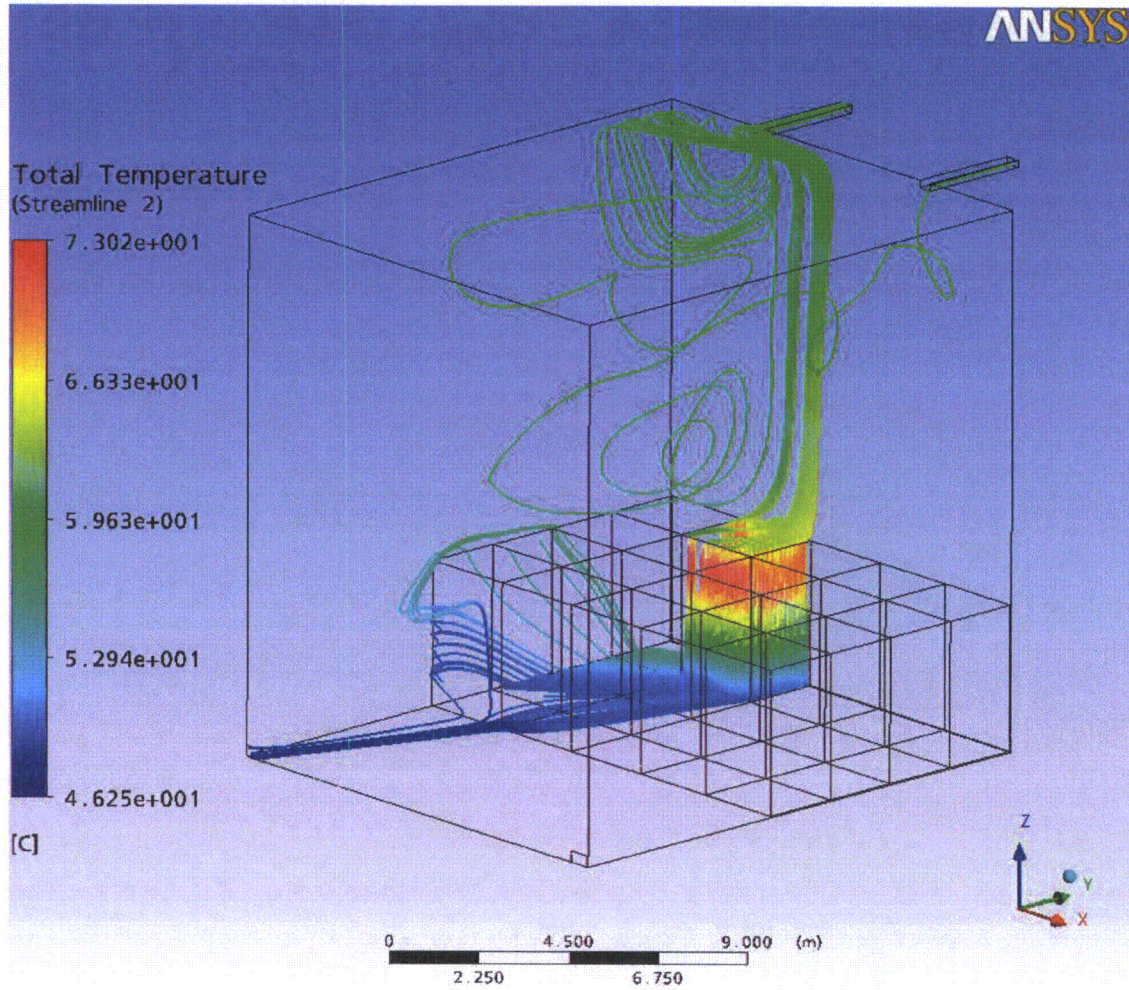


Figure 5-12a. Stream Lines From Inlet #1 Through Rack #5

Figure 5-12a shows a demonstration of the stream line flow when one of the rack domains is enabled in the model to show flow through the rack.

5.3.5 Maximum Cladding Temperature

In order to calculate the maximum fuel cladding temperature in the racks, the following assumptions are made:

- The worst case is assumed to be the case where higher temperatures are reached. This is the abnormal conditions case.
- The fuel rod heat emission rate includes a radial peaking factor value of 1.4.
- The axial power shape is assumed to be a cosine curve, as the axial heat dissipation in the rod is known to reach a maximum in the central region, and taper off at the two extremities.
- A safety factor of 1.2 is considered for the bundle heat load.

Making use of the conservation of energy for a differential piece of rod, an analytical model for the water and cladding temperature is produced. This highly conservative model leads to simple algebraic equations which directly give the maximum local cladding temperature. For added conservatism a foulant layer (crud deposit) is assumed on the cladding surface. Thermal resistance equal to 5673 W/m²°C (1000BTU/h ft²°F) (Reference 7) is assumed. Input data for this calculation is given in the table below.

| Parameter | Value |
|---------------------------------------------------------------|----------------------------|
| Bundle generated heat (W) | 1.2 x 8545.93W = 10255.12W |
| Radial peaking factor | 1.4 |
| No rods per bundle | 92 (*) |
| Rod length (m) | 3.3762m (*) |
| Water temperature at rod's inlet (°C) | 56.38°C (**) |
| Cladding outside diameter (m) | 10.26mm (*) |
| Pellet diameter (m) | 8.76mm (*) |
| Zr-2 Conductivity (W/m°C) | 23W / m°C @ 25°C |
| | 19W / m°C @ 300°C |
| Foulant layer heat transfer coefficient (W/m ² °C) | 5673.4W/m ² °C |
| Total flow rate through the rack (15x12 bundle array) | 13.87Kg/s (**) |

(*) Data taken from (Reference 6).

(**) The inlet temperature and the total flow rate through the rack are taken from the CFD model solution for the worst case and the worst rack, where the maximum temperature is reached.

The governing equations are derived as follows. The volumetric heat generation in a rod is:

$$\int q^m(z) A_c dz = \frac{q(W)}{N_B}$$

$$q^m(z) = q_c^m \cdot \cos\left(\frac{\pi z}{H_e}\right)$$

$$q_c^m = \frac{\frac{q}{N_B}}{\int_{-H_e/2}^{H_e/2} \cos\left(\frac{\pi z}{H_e}\right) A_c dz} = \frac{\frac{q}{N_B}}{2A_c \frac{H_e}{\pi}}$$

$$\frac{q_c^m A_c H_e}{\pi} = \frac{1}{2} \frac{q}{N_B}$$

Where:

N_B : Number of rods in each bundle (FA)

q : Volumetric heat generation rate per bundle (FA)

q_c^m : Volumetric heat generation rate per fuel rod

$A_c = \pi R^2$: Pellet cross section (m²)

R : Pellet radio (m)

H_e : Rod length (m)

$$\frac{q_c^m A_c H_e}{\pi} = \frac{1}{2} \frac{q}{N_B} = \frac{1}{2} \frac{10255.1}{92} = 55.73W$$

$$q_c^m = \frac{\pi \cdot 55.73 \cdot 4}{\pi \cdot 0.00876^2 \cdot 3.3762} = 860489.73 \frac{W}{m^3}$$

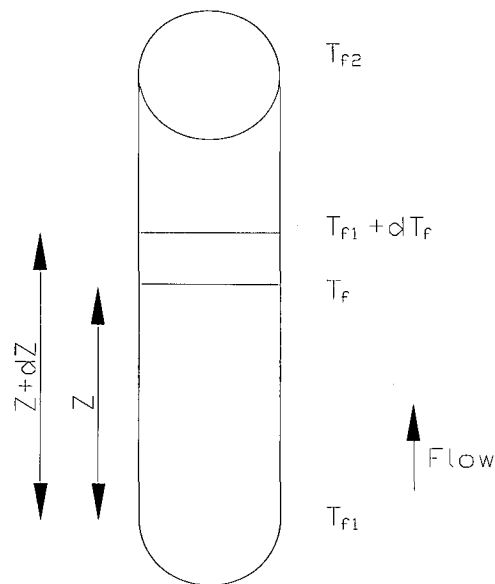


Figure 5-13. Rod Heat Balance

Applying the conservatism of energy between the fuel rod and the coolant, the following equation is obtained for the local fluid temperature.

$$m_{barra} C_p dT = q^m(z) A_c dz$$

$$T_f(z) = T_{f1} + \frac{q_c^m A_c}{m_{barra} C_p} \frac{H_e}{\pi} \left[\sin \frac{\pi z}{H_e} + \sin \frac{\pi}{2} \right] = T_{f1} + \frac{1}{2} \frac{\frac{q}{N_B}}{m_{barra} C_p} \left[\sin \frac{\pi z}{H_e} + \sin \frac{\pi}{2} \right]$$

$$T_{c0}(z) = T_{f1} + \frac{q_c^m A_c}{m_{barra} C_p} \frac{H_e}{\pi} \left[\sin \frac{\pi z}{H_e} + \sin \frac{\pi}{2} \right] + \frac{q_c^m \cos \frac{\pi z}{H_e} A_c}{h \cdot 2\pi(R+c)}$$

For added conservatism a foulant layer (crud deposit) is assumed on the cladding surface. This is equivalent to two thermal resistances in series, so the equation that gives the outside cladding temperature is:

$$T_{c0}(z) = T_{f1} + \frac{q_c^m A_c}{m_{barra} C_p} \frac{H_e}{\pi} \left[\sin \frac{\pi z}{H_e} + \sin \frac{\pi}{2} \right] + \frac{q_c^m \cos \frac{\pi z}{H_e} A_c}{\left(\frac{h_{dep} h}{h_{dep} + h} \right) 2\pi(R+c)}$$

For the value of the inlet temperature (T_{f1}), the maximum temperature of the inlet temperature to the worst rack in the worst case is selected. For the value of the coolant flow per rod, the average flow will be conservatively assumed.

Nomenclature used in preceding equations is:

$$m_{barra} = \frac{m_{rack}}{N_{EC} \cdot N_B} : \text{Coolant (water) flow rate per rod}$$

m_{rack} : Coolant (water) flow rate in the rack

N_{EC} : Number of bundles in the rack

$$C_p = 4182 \frac{J}{KgK} \text{ Coolant (water) specific heat}$$

$T_f(z)$: Local fluid temperature

h : Heat Transfer coefficient

h_{dep} : Foulant layer heat transfer coefficient

c : cladding thickness

T_{c0} : Outside cladding temperature

The minimum heat transfer coefficient from the following table is used (water, heating):

Table 5-1
Approximate Range of Values hm Ordinarily Encountered

| | Btu/(hr) (Sq ft) (Deg F) | |
|-------------------------------|--------------------------|--------|
| Steam, dropwise condensation | 5,000 | 20,000 |
| Steam, film-type condensation | 1,000 | 3,000 |
| Water boiling | 300 | 9,000 |
| Organic vapors condensing | 200 | 400 |
| Water, heating | 50 | 3,000 |
| Steam, superheating | 5 | 20 |
| Air, heating or cooling | 0.2 | 10 |

(*) Table taken from reference (Reference 7).

$$h = 50 \frac{BTU}{hr \cdot ft^2 \cdot F} = 283.9 \frac{W}{m^2 K}$$

$$T_{c,0}(z) = 56.38 + \frac{55.73}{4182 \cdot \frac{13.87}{180 \cdot 92}} \left[\sin \frac{\pi z}{3.3762} + 1 \right] + \frac{860489.73 \cos \frac{\pi z}{3.3762} \pi \frac{0.00876^2}{4}}{\left(\frac{5673.4 \cdot 283.9}{5673.4 + 283.9} \right) 2\pi \left(\frac{0.01026}{2} \right)}$$

The maximum value calculated from this function is at z=1.3m, as measured from the center of the rod. The maximum peak temperature is:

$$T_{c,0}(z) = 89.2^\circ C$$

5.3.6 Maximum Fluid Temperature Under 80% Blockage of Rack Outlet

Due to the different acceptance criteria for the two different cases, a calculation will be performed for each case.

5.3.6.1 Under Normal Conditions Case

For this analysis the assumption is that the rack outlet is 80% blocked. Conservatively, the holes in the rack between bundles are not considered. A bundle in the hottest rack is considered for this case. The maximum temperature at the inlet of the hottest rack will be conservatively assumed. The flow for this bundle will be considered to be the average flow per bundle on this rack:

$$\dot{m}_{FA} = \frac{\dot{m}_{rack}}{N_{FA}} = \frac{27.867}{180} = 0.154816 \frac{Kg}{s}$$

Where:

\dot{m}_{rack} = Total flow at the hottest rack inlet

N_{FA} = Number of bundles in the hottest rack

The loss coefficient increment is given by the following equation:

$$\Delta K = \frac{1}{2} \left(\frac{1.5}{\rho \cdot A_B^2} - \frac{1}{\rho \cdot A_{CEL}^2} \right) = \frac{1}{2} \left(\frac{1.5}{1000 \cdot 0.2^2 \cdot (0.1646^2)} - \frac{1}{1000 \cdot (0.1646^2)^2} \right) = 24.862 Kg^{-1} m^{-1}$$

Where:

A_B = Blocked section Area.

A_{CEL} = Non blocked section Area.

ρ = Fluid density.

Assuming the pressures at the inlet and outlet of the rack will be the same as if unblocked:

$$\Delta P = K_C (\dot{m}_{FA})^2 = K_{TAP} (\dot{m}_{FATAP})^2$$

Where:

K_C = Loss coefficient without blockage

K_{TAP} = Loss coefficient with blockage

\dot{m}_{FA} = Flow through bundle without blockage

\dot{m}_{FATAP} = Flow through bundle with blockage

The loss coefficient without blockage ($K_C = 269.55 \text{Kg}^{-1}\text{m}^{-1}$) is equal to the value calculated in Section 5.2.3.1 of this report. The loss coefficient without blockage will be this value plus the loss coefficient due to the blockage. Therefore:

$$K_{TAP} = K_C + \Delta K = 269.55 + 24.862 = 294.41 \text{Kg}^{-1}\text{m}^{-1}$$

The flow through the blocked bundle can be obtained from the previous equations:

$$\dot{m}_{FABlock} = \dot{m}_{FA} \sqrt{\frac{K}{K + \Delta K}} = \frac{27.867}{15 \cdot 12} \sqrt{\frac{269.55}{294.41}} = 0.14813 \frac{\text{Kg}}{\text{s}}$$

The temperature that will be reached at the outlet of the bundle is:

$$T_{Block} = T_{f1} + \Delta T = T_{f1} + \frac{q}{\dot{m}_{FABlock} \cdot C_p} = 45.91 + \frac{16021 \cdot 1.2}{0.14813 \cdot 4182} = 76.94^\circ\text{C}$$

5.3.6.2 Under Abnormal Conditions Case

For this analysis, the assumption is that the rack outlet is 80% blocked. Conservatively, the holes in the rack between bundles are not considered. A bundle in the hottest rack is considered for this case. The maximum temperature at the inlet of the hottest rack will be conservatively assumed. The flow for this bundle will be considered to be the average flow per bundle on this rack:

$$\dot{m}_{FA} = \frac{\dot{m}_{rack}}{N_{FA}} = \frac{13.87}{180} = 0.077055 \frac{\text{Kg}}{\text{s}}$$

Where:

\dot{m}_{rack} = Total flow at the hottest rack inlet

N_{FA} = Number of bundles in the hottest rack

The loss coefficient increment is given by the following equation:

$$\Delta K = \frac{1}{2} \left(\frac{1.5}{\rho \cdot A_B^2} - \frac{1}{\rho \cdot A_{CEL}^2} \right) = \frac{1}{2} \left(\frac{1.5}{1000 \cdot 0.2^2 \cdot (0.1646^2)} - \frac{1}{1000 \cdot (0.1646^2)^2} \right) = 24.862 \text{Kg}^{-1} \text{m}^{-1}$$

Where:

A_B = Blocked section Area.

A_{CEL} = Non blocked section Area.

ρ = Fluid density.

Assuming the pressures at the inlet and outlet of the rack will be the same as if it unblocked:

$$\Delta P = K_C (\dot{m}_{FA})^2 = K_{TAP} (\dot{m}_{FATAP})^2$$

Where:

K_C = Loss coefficient without blockage

K_{TAP} = Loss coefficient with blockage

\dot{m}_{FA} = Flow through bundle without blockage

\dot{m}_{FATAP} = Flow through bundle with blockage

The loss coefficient without blockage ($K_C = 269.55 \text{Kg}^{-1} \text{m}^{-1}$) is equal as the value calculated in Section 5.2.3.1 of this report. The loss coefficient without blockage will be this value plus the loss coefficient due to the blockage. Therefore:

$$K_{TAP} = K_C + \Delta K = 269.55 + 24.862 = 294.41 \text{Kg}^{-1} \text{m}^{-1}$$

The flow through the blocked bundle can be obtained from the previous equations:

$$\dot{m}_{FABlk} = \dot{m}_{FA} \sqrt{\frac{K}{K + \Delta K}} = \frac{13.87}{15 \cdot 12} \sqrt{\frac{269.55}{294.41}} = 0.073730 \frac{\text{Kg}}{\text{s}}$$

The temperature that will be reached at the outlet of the bundle is:

$$T_{Blck} = T_{f1} + \Delta T = T_{f1} + \frac{q}{\dot{m}_{FABlk} \cdot C_p} = 56.38 + \frac{8545.93 \cdot 1.2}{0.07373 \cdot 4182} = 89.63^\circ \text{C}$$

5.4 REACTOR BUFFER POOL

The calculation methodology for this analysis is similar to that performed for the SFP.

The only time spent fuel can be stored in the buffer pool is during a refuelling outage. During an outage, one train of the fuel pool cooling system has the capacity to cool the entire SFP and is dedicated to that purpose. The redundant train provides cooling to the buffer pool.

The bulk temperature of the buffer pool is maintained below the same maximum value as the SFP (48.9 C, 120 F). The heat load in the buffer pool is 2.5 MW (Reference 10), compared to a heat load of 7.626 MW in the SFP. Each redundant train of the fuel pool cooling system is capable of removing 8.3 MW (Reference 1), therefore, the system is capable of maintaining buffer pool temperature below the maximum bulk temperature.

Since the inlet pipe is routed to the bottom of the racks in the deep pit of the buffer pool, the general configuration is similar to that in spent fuel pool. Therefore, with the cooling capacities being the same between the pools, the maximum temperature that would be reached at the exit of the spent fuel storage racks in the reactor buffer pool is calculated based on the ratio of the average per bundle heat load in the buffer pool to that of the SFP. The calculation below determines the temperature of fluid exiting the spent fuel storage racks in the buffer pool.

The heat per bundle in this pool would be:

$$\frac{2.5 \cdot 10^6 W}{2 \cdot 11.7 FA} = 16223.8 \frac{W}{FA}$$

That is similar to the heat per bundle in normal conditions case = $16021 \frac{W}{FA_{new}}$

It is conservatively assumed that the flow for each bundle would be the same as the value used in the normal conditions case. The flow rate will actually be higher because cooling capacity for the racks in the reactor buffer pool is greater. Also, the heat load is higher; therefore, natural convection flow would be greater.

Because the temperature increment is proportional to the heat, the bulk temperature in the SFP and buffer pool is the same (48.9°C), and the coolant flow is the same, the exit temperature can be calculated as follows:

$$\frac{\Delta T_{RBP}}{\Delta T_{NCC}} = \frac{16223.8}{16021} = 1.01266$$

$$Rack_Exit_Temp = 65.83C \cdot 1.01266 = 66.7C$$

5.5 CONCLUSIONS

The results calculated in the previous sections show that the maximum local coolant temperature reached at the top of the racks in the SFP is 65.03°C under the normal conditions case. This is lower than 121°C, which is the maximum allowable temperature for this case. The maximum peak temperature reached is 73.03°C under the abnormal conditions case. This is lower than 121°C, which is the maximum allowable temperature for this case.

The results also show that the maximum peak cladding temperature that will be reached is 89.2°C.

In the event of 80% blockage at the outlet of the rack, the temperature reached in the normal conditions case would be 76.94°C. This is lower than 121°C, which is the maximum allowable temperature for this case. The temperature reached in the abnormal conditions case would be 89.63°C. This is lower than 121°C, which is the maximum allowable temperature for this case.

The maximum temperature of fluid exiting the spent fuel storage racks in the buffer pool is 66.7°C, which is below the maximum allowable temperature of 121°C.

In the current GE design for the spent fuel pool, the cold inlet water pipe is routed to the bottom of the pool, therefore, the water that cools the fuel elements can easily enter the bottom part of the racks. This inlet pipe design allows that the introduction of cold water at the bottom part of the racks eliminates the dependency of distances between racks or between racks and pool wall.

Based on the results above, there is no condition where water boils within the fuel storage racks, By extension, if convection boiling does not occur within the fuel storage racks, there is no possibility that nucleate boiling can occur.

Considering the variations determined in sensitivity studies, along with the significant margin between analyzed results and acceptance limits, it is concluded that the Spent Fuel Pool Storage Racks in the Spent Fuel Pool and the Reactor Buffer Pool are suitable for the intended duty under the conditions shown previously.

5.6 REFERENCES

1. "Fuel Storage Rack Design Specification" Document No 26A7032 Rev 04 GE Nuclear Energy.
2. ANSYS CFX Computer Program Release 11.0, ANSYS Inc., South Point, 275 Technology Dr., Canonsberg, PA 15317.
3. ESBWR Spent Fuel Pool Decay Heat Part II GE-NE-0000-0040-6730-R0-DRAFT Rev 0. GE Proprietary Information.
4. ESBWR Spent Fuel Pool Boil-off, eDRF 0000-0038-9391/neDRFSection 0000-0038-9392 Rev 02.
5. "Rack Layout at Spent Fuel Building" ENSA 5926.D100 Rev 01.
6. Design Study Summary GE14E, ESBWR Fuel Assembly, DRF Section 41-8790, Global Nuclear Fuel (GNF).
7. "Heat Transmission" William H. McAdams. McGraw-Hill Book Company.
8. "Fuel Storage Requirements" Doc. No 22A5866 Rev 08, GE Nuclear Energy.
9. "Rack Layout at Spent Fuel Building" ENSA 5926.D100 Rev 02.
10. ESBWR Buffer Pool Boil-Off and Makeup Capacity, eDRF Section 0000-0076-3483.
11. ESBWR Spent Fuel Pool Boil-off, eDRF Section 0000-0038-9392, Rev. 6.

APPENDIX G – DISCUSSION OF ABNORMAL CONDITION HEAT LOAD AT 19.0 MW

1.0 DETERMINATION OF ABNORMAL CONDITION HEAT LOAD

The abnormal heat load of 17.3 MW, used in Section 5 of this report, represents the decay heat from the following:

- a) spent fuel from 10 years (5 cycles) of reactor operation, 36 days into the sixth cycle of plant operation and 5 days after shutdown, and
- b) offload of all fuel from the core to the spent fuel pool after 36 days of full power operation and 5 days after shutdown.

This heat load was determined not to be bounding, therefore, re-evaluation of the abnormal condition at a higher heat load is necessary.

An abnormal condition heat load of 19.0 MW is bounding, and is based on the following:

- a) spent fuel from 10 years (5 cycles) of reactor operation at the end of the sixth cycle (1.3 MW) and 5 days after shutdown*,
- b) offload of all fuel from the core to the spent fuel pool at the end of the sixth cycle (16.8 MW) and 5 days after shutdown*, and
- c) margin (0.9 MW).

* This is conservative since SRP 9.1.3, Rev.1, specifies 150 hours (6.25 days).

An extremely conservative abnormal heat load case of 29 MW was analyzed with results presented in Appendix H. This analysis was based on the following:

- a) spent fuel from 10 years (5 cycles) of reactor operation at 80000 seconds (0.93 days) after reactor shutdown, and
- b) offload of all fuel from the core to the spent fuel pool at 80000 seconds (0.93 days) after reactor shutdown.

2.0 DISCUSSION OF ABNORMAL CONDITION HEAT LOAD OF 19.0 MW

The CFD model has not been modified and analysis has not been performed considering an abnormal condition heat load of 19.0 MW. However, given the results of analyses that have been performed at 17.3 MW and 29 MW, a case can be made that an abnormal condition heat load of 19.0 MW is bounded and fuel rack integrity is maintained. The impact on calculations using 19.0 MW is discussed below.

2.1 *Maximum Pool Inlet Temperature*

In section 5.2.2.2 of this report, the maximum pool inlet temperature is calculated to be 46.3°C for the 17.3 MW case. For the 29 MW case, the maximum pool inlet temperature is calculated to be 37.0°C.

Using 19.0 MW as an input with the same methodology used in the previous calculations, the maximum pool inlet temperature is calculated to be 45.0°C. This is an increase of 21.6% as compared to the 29 MW case.

Considering the model sensitivity presented in section 5.2.5 of this report, a 10% decrease in the maximum allowable pool inlet temperature corresponds with no greater than a 6% increase in rack exit temperature. An increase in the maximum allowable pool inlet temperature corresponds with a reduction in the calculated rack exit temperature. As the calculated pool inlet temperature for the 19.0 MW case is an increase over the pool inlet temperature for the 29 MW case, the rack exit temperature for the 19.0 MW case as compared with the 29 MW case will be reduced.

2.2 *Rack Exit Temperature*

The rack exit temperature acceptability limit is 121°C. In both the 17.3 MW and 29 MW cases, maximum rack exit temperatures are seen in the 15x12 racks filled with newly discharged fuel from the core; specifically rack R-9. The maximum rack exit temperature determined in the 29 MW case is 80.9°C.

For the 29 MW case, the heat load in each 15x12 rack filled with newly discharged fuel is calculated to be 3398692.58 W. Using 19.0 MW as an input with the same methodology used in the previous calculations, the heat load for each 15x12 rack filled with newly discharged fuel is calculated to be 2814480.0 W. As this heat load is less than the heat load from the 29 MW case, the conclusion can be made that the rack exit temperature for the 19.0 MW case is less than that for the 29 MW case.

2.3 *Maximum Cladding Temperature*

Per the summary tables in Section 5.3.5 of Section 5 and Appendix H, the input values for water temperature at rod inlet and rack flow rate used to calculate peak cladding temperature are outputs of the ANSYS analyses. As analysis for the 19.0 MW case was not performed, those values are not available to calculate an actual peak cladding temperature. It is anticipated that an actual peak cladding temperature for the 19.0 MW case will be less than that of the 29 MW case as the heat load per bundle and rod inlet temperature is less. However, in order to evaluate the peak cladding temperature for the 19.0 MW case, the conservative highlighted values in the following table are considered:

| Heat Load Case | 17.3 MW | 29 MW |
|-----------------------------------|----------------|--------------|
| Rod (Rack) Inlet Temperature (°C) | 56.38 | 60.39 |
| Total Rack Flow Rate (Kg/s) | 13.87 | 20.789 |
| Peak Cladding Temperature (°C) | 89.2 | 97.12 |

The same methodology was used to calculate the peak cladding temperatures for the 19.0 MW case as was used to calculate the values in the table. To determine a worst-case value for the 19.0 MW case, the 29 MW case rod inlet temperature and 17.3 MW case rack flow rate was used. This evaluation is considered worst-case as the maximum rod inlet temperature is used in combination with the minimum flow rate to produce the result.

Even though the rack exit temperature may be higher for the 19.0 MW case (and as was modeled for the 29 MW case) as described in section 3.0, this effect will not adversely influence the rack inlet temperatures since the bulk pool temperature is maintained at or below 60°C (DCD, Tier 2, Table 9.1-8). This is supported by Figures 5-6, 5-12, 5-12a, H5-6, and H5-12, which clearly show that the water exiting the racks has little, if any, influence on the pool inlet water as it enters the inlet to the racks. The heated water from the racks, being more buoyant, rises to the pool surface and the outlets. The cooler return water enters at the pool bottom, and being the least buoyant, enters the rack inlet plenum with limited mixing with the warmer bulk water, which again is maintained below 60°C. These observations provide assurance that the rod inlet temperature for the 29 MW case is bounding and the actual temperature for the 19.0 MW case is expected to fall below the value of 60.39°C that is used to calculate the bounding peak cladding temperature.

The resulting peak cladding temperature for the 19.0 MW case was calculated to be 101.0°C. As this value is below the boiling temperature of water at the depth of the top of the fuel racks (119°C), conventional boiling does not occur. Therefore, nucleate boiling is prevented.

3.0 CONCLUSIONS

Analyses for the 17.3 MW and 29 MW cases were performed using the same methodology and the same modeling software (ANSYS CFX 11.0). As can be seen in the summary tables in Section 5.2.4 of Section 5 and Appendix H, the inputs are the same, with the exceptions listed below:

- 1) Heat loads – 17.3 MW vs. 29 MW,
- 2) Parameters that were determined using the heat loads – The maximum pool inlet temperatures (Section 5.2.2 of Section 5 and Appendix H) were calculated using the normal and abnormal pool heat loads (see Section 2.1 above). Additionally, the heat load per fuel assembly and per fuel storage rack (Section 5.2.3.2 of Section 5 and Appendix H) was calculated using the normal and abnormal heat loads (see Section 2.2 above), and

- 3) Loss coefficient – The loss coefficient is calculated in Section 5.2.3.1 of Section 5 and Appendix H. For the 29 MW case (Appendix H), the loss coefficient was calculated to be 42.25668/m. For the 17.3 MW case, the loss coefficient was calculated to be 60.13/m.
- 4) Pool inlet locations and orientation – In Section 5.2.3 of Section 5 and Appendix H, the inlet locations are described. For the 17.3 MW case, the inlet locations are modeled at the bottom of each corner of the west wall with a 20° offset towards the middle. For the 29 MW case, the inlet locations are modeled at the bottom of each corner of the west wall with no offset. The explanation is also provided in each section that the actual inlet locations will be inboard from the corners, equally spaced between the pool walls. These modelling differences have negligible impact on analysis results, therefore, neither model was modified to reflect actual inlet locations and no adjustments to results are required in order to compare these cases with the 19.0 MW case.

Using the sensitivity information presented in Section 5.2.5 of this report, the rack exit temperature of 80.9°C for the 29 MW case will be considered for impact of differences in maximum pool inlet temperature and loss coefficient to be consistent with the 17.3 MW case. This adjustment will also be directly comparable to the 19 MW case.

An adjustment is required for the difference in the 29 MW vs. 17.3 MW case loss coefficients. The 29 MW case loss coefficient was calculated using area and length characteristics for fuel other than GE14E. This difference was non-conservative and was corrected for the 17.3 MW case, as the correct fuel length and cross-sectional area values for GE14E fuel were used. Considering loss coefficient sensitivity, an evaluation of the error in the 29 MW case shows that the temperature at the rack outlet would increase by 12.6%, from 80.9°C to 91.1°C. The basis for this value is the sensitivity discussion in Section 5.2.5, where a 20% increase in loss coefficient equates to no more than a 6% increase in rack exit temperature. The change in loss coefficient from 42.25668/m to 60.13/m is an increase of 42%, which represents a total temperature increase of 12.6%, or 10.2°C.

As there is an 8°C difference in the inlet temperatures between the 19.0 MW and 29 MW cases, a conservative and corresponding 8°C increase is considered for the rack exit temperature for the 29 MW case. When added to the adjusted temperature of 91.1°C calculated in the previous paragraph, the adjusted rack exit temperature for the 29 MW case is 99.1°C.

The 17.3 MW and 29 MW analyses are consistent in approach and adjustments were incorporated to reconcile any differences. Therefore, their use in evaluation of the 19.0 MW case is justified and the results are directly comparable.

Based on the results of the previous evaluations, it is concluded that an abnormal condition heat load of 19.0 MW in the spent fuel pool produces a rack exit temperature less than the adjusted rack exit temperature of 99.1°C determined for the 29.0 MW case. Therefore, the rack exit temperature acceptability limit of 121°C will not be exceeded, and significant margin still exists.

As no condition exists within the fuel assembly that causes conventional boiling, nucleate boiling is prevented.

APPENDIX H – ANALYSIS AT A HEAT LOAD OF 29 MW

For the purpose of comparison with the 19.0 MW heat load evaluation, the analysis at a total spent fuel pool heat load of 29 MW is being included in this report. This information serves as a bounding case for the 19.0 MW evaluation.

The FAPCS will be designed for an abnormal heat load of 20.1 MW, which represents 20 years of spent fuel and a full core offload five days after reactor shutdown. This exceeds the 19.0 MW abnormal heat load for fuel rack evaluation, which represents 10 years of spent fuel and a full core offload five days after reactor shutdown.

5. THERMAL-HYDRAULIC ANALYSIS (29 MW CASE)

5.1 INTRODUCTION

The purpose of this analysis is to determine the maximum peak temperatures that will be reached at the exit of the spent fuel racks in the spent fuel pool and the buffer pool in the ESBWR nuclear power station. Also analysis shall demonstrate that these fuel storage racks are designed such that nucleate boiling is prevented.

A Computational Fluid Dynamics (CFD) based method will be used for the spent fuel pool analysis. This will allow analysis of the behavior of the water within the pool and the temperatures that the water will reach.

5.1.1 Inputs/Assumptions

1. There are two postulated scenarios to be evaluated for the spent fuel pool (SFP):
 - a. Normal Conditions
 - Heat Load = 10-year spent fuel accumulation = 7.626 MW (Ref. 1)
 - Maximum Pool Bulk Temperature = 48.9°C (120°F) (Ref.1)
 - Pool Cooling Rated Flow Rate = 545.1 m³/hr = 150.96 Kg/s (Ref. 1)
 - b. Abnormal Conditions:
 - Heat Load = 10-year spent fuel accumulation + full core offload = 29 MW (Ref. 1)
 - Maximum Pool Bulk Temperature = 60°C (Ref. 1)
 - Pool Cooling Rated Flow Rate = 1090.2 m³/hr = 301.92 Kg/s (Ref. 1)

2. For the purpose of this analysis, it is assumed that the FAPCS maintains the pool at a steady bulk temperature and always removes heat at the rate it is produced. This assumption simplifies the model into a steady-state analysis by avoiding bulk temperature transients.

5.2 CALCULATION METHODOLOGY

5.2.1 General Description

The calculation methodology for this analysis consists of two phases.

5.2.1.1 Pool Inlet Temperature Determination

In order to model the fluid dynamics of the pool, it is necessary to determine the temperature of the cooled water being returned to the pool from the FAPCS. The pool inlet temperature will be back-calculated from the assumptions described in 5.1.1. Because this analysis assumes a steady-state condition where the pool bulk temperature is “locked in” at its maximum value, the temperature of the pool inlet water does not necessarily reflect the realistic capabilities of the FAPCS. To determine the maximum inlet temperature of the water in each of the cases, the following values are used: the maximum bulk temperature (also equivalent to the pool outlet temperature), the heat generated by the fuel elements, and the flow rate provided by the FAPCS. Although the calculated pool inlet temperature is not a realistic design parameter, it is conservative in the context of this analysis due to the higher-than-normal bulk pool temperature.

5.2.1.2 Calculation of the Velocities and Temperatures within the Spent Fuel Pool (SFP)

Once the model inputs have been determined, the calculation of the velocities and temperatures are performed using a CFD (Computational Fluid Dynamics) based method, in order to evaluate the bounding temperature profile within the SFP.

5.2.2 Pool Inlet Temperature Determination

In this section, the maximum pool inlet temperatures are calculated for the normal and abnormal conditions.

The normal condition analyzes the spent fuel from 10 years of plant operation, which is limited by the capacity of the initial configuration of fuel racks in the spent fuel pool. The abnormal condition analyzes the spent fuel from 10 years of plant operation plus a full core offload, which is also limited by the capacity of the initial configuration of rule racks in the spent fuel pool.

5.2.2.1 Normal Conditions Case

The heat generated under normal conditions is 7.626 MW [Reference 3].

In the normal conditions case, the flow rate is $545.1\text{m}^3/\text{h}=150.96\text{Kg/s}$ [Reference 1].

$$\Delta T = \frac{\text{Heat}}{C_p \cdot \text{Flow}} = \frac{7.626 \cdot 10^6 \text{ W}}{4182 \frac{\text{J}}{\text{Kg} \cdot \text{K}} \cdot 150.96 \frac{\text{Kg}}{\text{s}}} = 12.08 \text{ K}$$

Maximum Inlet Temperature

$$T_m = 48.9 - 12.08 = 36.8^\circ \text{ C}$$

Therefore, the maximum inlet temperature is 36.8°C for the normal conditions case.

5.2.2.2 Abnormal Conditions Case

The heat generated under abnormal conditions is 29 MW [Reference 4]. This is a very conservative assumption.

In the abnormal conditions case, the flow rate is $1090.2\text{m}^3/\text{h}=301.92\text{Kg/s}$ [Reference 1].

$$\Delta T = \frac{\text{Heat}}{C_p \cdot \text{Flow}} = \frac{29 \cdot 10^6 \text{ W}}{4182 \frac{\text{J}}{\text{Kg} \cdot \text{K}} \cdot 301.92 \frac{\text{Kg}}{\text{s}}} = 22.97 \text{ K}$$

Maximum Inlet Temperature

$$T_m = 60 - 22.97 = 37.03^\circ \text{ C}$$

Therefore, the maximum inlet temperature is 37°C for the abnormal conditions case.

5.2.3 Calculation of the Velocities and Temperatures within the Spent Fuel Pool (SFP)

The calculation of the velocities and temperatures are performed using a CFD (Computational Fluid Dynamics) based method, ANSYS CFX 11.0 [Reference 2].

The Spent Fuel Pool (SFP) water has been modeled and the racks located in the SFP have been modeled as subdomains. In these subdomains a volumetric heat generation and a directional loss coefficient have been imposed (the heat generation for each rack is calculated in Sections 5.2.3.2 and 5.2.3.3 the directional loss coefficient is calculated in Section 5.2.3.1).

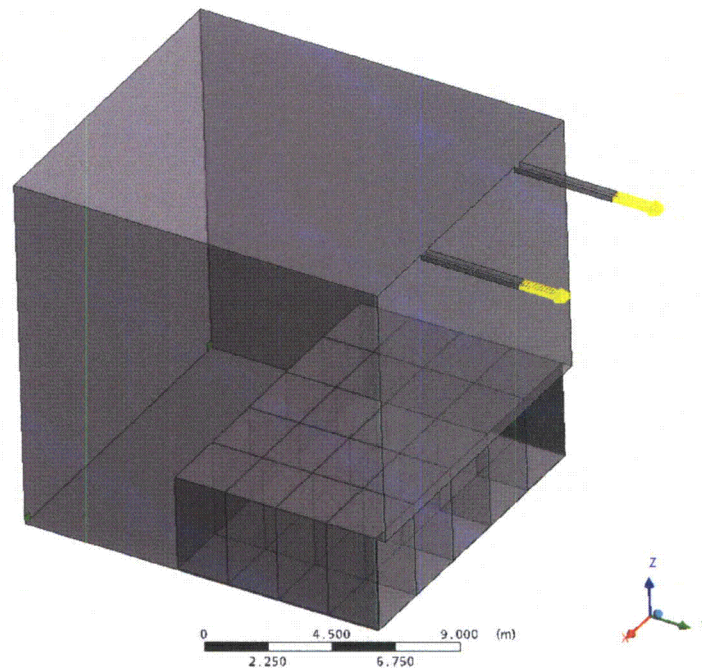


Figure H5-1. SFP Model

The rack layout modeled in Figure H5-1 represents the 10-year configuration [Reference 5]. Each of the 20 racks has an array of 15x12, for a total of 3600 storage spaces.

Two outlets have been modeled at the top of the SFP. Two inlet areas have been modeled at the bottom of the SFP in the corners opposite the racks. The actual inlet locations are inboard from the corners, equally spaced between the pool walls. As this difference from the modelled locations is considered to have negligible impact on results, the model was not modified to reflect the actual inlet locations.

A 42 mm gap between the racks and the northern and southern pool walls has been included in the model. No gap has been considered between the racks and the eastern pool wall. Nor was any gap considered between the racks. The gaps used in the model are conservative relative to actual design values.

5.2.3.1 Loss Coefficient Calculation

Figure H5-2 [Reference 8] shows the loss coefficient in the vertical direction inside the racks. This curve is mathematically fit using the following parabolic expression:

$$y = ax^2 + bx + c$$

Where:

y is the pressure drop (psi)

x is the mass flow rate (lbm/hr)

Since there is no pressure drop when the mass flow rate is zero, $c = 0$. From the parabolic fitting, the coefficients values are:

$$b = 0$$

$$a = 6.2 \cdot 10^{-10} \text{ PSI} \frac{\text{hr}^2}{\text{LBM}^2} = 269.55 \frac{1}{\text{kg} \cdot \text{m}}$$

Thus, pressure loss can be represented by the following formula:

$$\Delta P = K \cdot (m)^2$$

From this figure loss coefficient K can be obtained:

$$K = 269.55 \text{ Kg}^{-1} \cdot \text{m}^{-1}$$

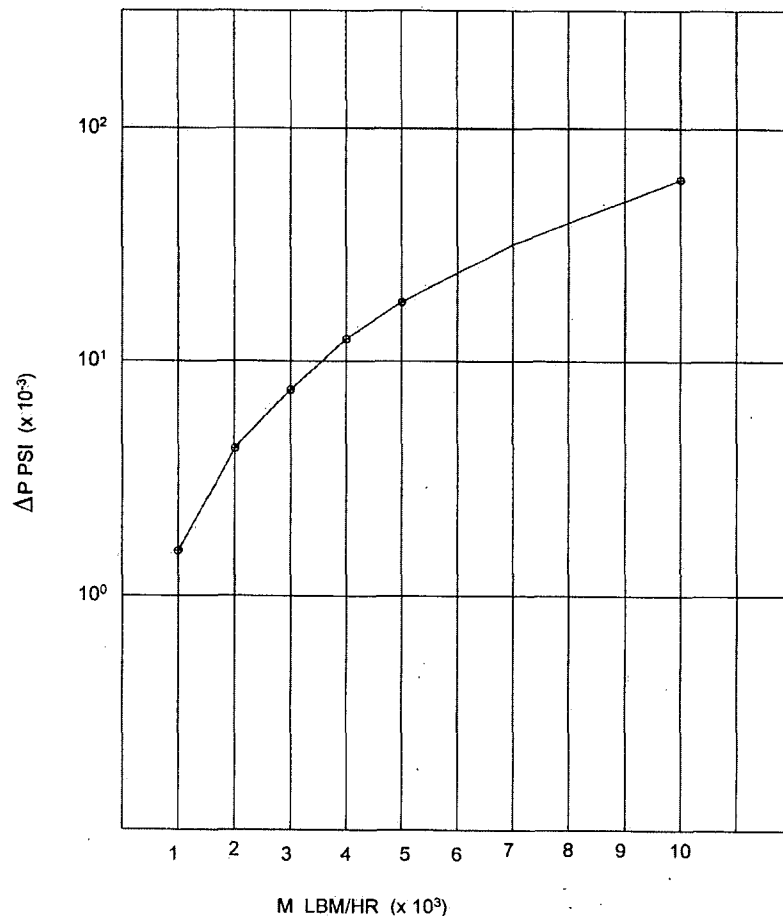


Figure H5-2. Loss coefficient in Racks

The CFD code requires that this loss coefficient be input as a function of velocity. Therefore, an additional calculation using the formula must be performed. An 8% safety factor has been applied to the loss coefficient obtained previously ($K=269.55\text{Kg}^{-1}\cdot\text{m}^{-1}$).

$$K_N \cdot \rho \cdot L \cdot V^2 = K \cdot (m)^2$$

$$m = \rho \cdot V \cdot A$$

$$K_N = K \cdot \rho \cdot \frac{A^2}{L} = 269.55 \cdot 1.08 \cdot 1000 \cdot \frac{(0.1606)^2}{4.583} = 42.25668\text{m}^{-1}$$

This is the value used for all the racks in the model. To model vertical-only water movement inside the racks, the loss coefficient applied in the two horizontal directions (x, y) is assumed to be 10^6 times greater than in the vertical direction.

To simulate the heat generation produced by the Fuel Assemblies (FA) inside the racks, a volumetric heat generation has been applied to the subdomains. For conservatism, it has been assumed that all the new FA (the most active FA) are located together. The temperature reached with this configuration is greater than the temperature that would be reached if the new FA were distributed uniformly between all the racks in the SFP.

Next, the heat generation in each rack will be calculated for each case.

5.2.3.2 Heat Generation Calculation in Each Rack Under the Normal Conditions Case

The heat generated by the FA under the normal conditions case is = 7.626MW. For conservatism, it is assumed that all the heat is generated by the new FA.

$$\frac{7.626 \cdot 10^6 \text{ W}}{476 FA_{new}} = 16021 \frac{\text{ W}}{FA_{new}}$$

In reference to the FA distribution between the racks, the worst-case configuration has the new FA located in the racks farthest from the SFP inlet. The new FA will be located in the racks 5, 9 and 13.

$$\text{Heat generated in rack 5: } 180 FA_{New} \cdot 16021 \frac{\text{ W}}{FA_{New}} = 2883780\text{ W}$$

$$\text{Heat generated in rack 9: } 180 FA_{New} \cdot 16021 \frac{\text{ W}}{FA_{New}} = 2883780\text{ W}$$

$$\text{Heat generated in rack 13: } 7.626 \cdot 10^6 \text{ W} - 2883780\text{ W} - 2883780\text{ W} = 1858440\text{ W}$$

The rest of the racks do not have any heat generation applied.

5.2.3.3 Heat Generation Calculation in Each Rack Under the Abnormal Conditions Case

The heat generated by the FA under the abnormal conditions case is = 29MW. Of the 29MW considered, 7.626MW is attributed to the accumulation of 10-years of spent fuel. The remainder is attributed to a full core offload.

$$\frac{(29 - 7.626) \cdot 10^6 W}{1132 FA_{new}} = 18881.6 \frac{W}{FA_{new}}$$

Fuel from a full core offload requires 6 complete racks and 52 storage spaces in a 7th rack. The heat generated by the accumulation of 10 years of spent fuel is divided among the remainder of storage capacity.

The hottest fuel assemblies are conservatively assumed to be located in the area receiving the least amount of cooling. These racks are 5, 6, 9, 10, 13, and 14.

$$\text{Heat generated in racks 5, 6, 9, 10, 13, and 14: } 180 FA_{new} \cdot 18881.6 \frac{W}{FA_{new}} = 3398692.58W$$

$$\text{Heat generated in racks not completed by new FA: } \frac{7.626 \cdot 10^6}{14} = 544714.3W$$

$$\text{Heat generated in rack 11: } (29 - 7.626) \cdot 10^6 W - 6 \cdot 3398692.58W + 544714.3W = 1526558.8W$$

5.2.4 Summary Tables

The following tables show a summary of the model characteristics and the modeled fluid properties used.

Model Characteristics

| | |
|---------------------------|----------------------------------------------|
| Solver | CFX Serial Standard |
| Solver Advection Scheme | High Resolution |
| Simulation Type | Steady State |
| Bouyancy Option | Bouyant |
| Gavity direction | <0, 0, -9.81m/s2> |
| Bouyancy Ref. Temperature | 60°C |
| Heat Transfer Option | Total Energy |
| Turbulence Option | k-Epsilon |
| Fluid | Liquid Water |
| | Density = 997 Kg/m3 |
| | Dynamic Viscosity = 0.0008899 Kg/m s |
| | Specific Heat Capacity Cp = 4181.7 J/Kg°C |
| | Thermal Conductivity = 0.6069 W/m K |
| | Linear Variation of Density with Temperature |

Boundary Conditions

| Normal Conditions | Abnormal Conditions |
|---------------------------------------------------------|---------------------------------------------------------|
| In Flow Rate = 150.96 Kg/s 75.48 Kg/s (each inlet) | In Flow Rate = 301.92 Kg/s 150.96 Kg/s (each inlet) |
| Inlet Flow Direction = No offset upon entering the pool | Inlet Flow Direction = No offset upon entering the pool |
| Turbulence Intensity = 1% | Turbulence Intensity = 1% |
| Inlet Temperature = 36.8°C | Inlet Temperature = 37°C |
| Adiabatic Walls | Adiabatic Walls |
| Outlet Flow Rate 150.96 Kg/s (total of both outlets) | Outlet Flow Rate 301.92 Kg/s (total of both outlets) |
| Loss coeff = 42.2567/m | Loss coeff = 42.2567/m |
| Transverse Loss Coeff. Multiplier = 1000000 | Transverse Loss Coeff. Multiplier = 1000000 |
| Heat Generation as Section 5.2.3.2 | Heat Generation as Section 5.2.3.3 |

5.2.5 CFD Model Sensitivity

CFD analysis methodology has been used in the past for other spent fuel pool thermal-hydraulic studies. The effect of hypothesis and assumptions, and also the modelling methodology (turbulence model selection, buoyancy treatment or mesh density) has been evaluated by sensitivity studies, according to the best practice guidelines for the use of CFD in nuclear reactor safety applications.

The sensitivity studies are presented in two parts: sensitivity to the numerical method and sensitivity to the mesh density.

Considering the numerical method, many parameters have been evaluated as shown below:

- Inlet mass flow rate increased by 10%
- Inlet temperature reduced by 10%
- Loss coefficient increased by 20%
- Turbulence model validated by a different model (k-ε model vs. SST-k-ω model)
- Reference temperature for buoyancy model reduced by 10%
- Turbulence intensity at the inlets increased by 9% (maximum allowed by the code)

The shape of the temperature distribution throughout the pool remains constant, with temperature variations (peak and bulk) of ≈ 1.5%. For variations of inlet mass flow rate, loss coefficient, and inlet temperature, the temperature variations (peak and bulk) are ≈ 4% to 6%. Inlet temperature refers to the maximum allowable pool inlet temperature. This value is dependent on the heat load in the pool, as the abnormal flow rate (301.92 Kg/s) and maximum bulk pool temperature (60°C) are analyzed as constant. As the heat load in the pool is increased, the corresponding rack exit temperature increases and the maximum allowable pool inlet temperature must decrease to maintain the bulk pool temperature. Conversely, as the heat load in the pool is decreased, the corresponding rack exit temperature decreases and the maximum allowable pool inlet temperature can increase to maintain the bulk pool temperature.

With regard to the sensitivity of mesh density, typically three cases are used for comparison: the original mesh density, a 50% increase over the original mesh density, and a 100% increase over the original mesh density. Specific examples from a specific thermal-hydraulic analysis of an operating BWR are presented below.

The temperature profiles and values of horizontal slices through the spent fuel pool are analyzed at various elevations for comparison purposes. In comparing the three models, the temperature distributions within the pools were constant and the bulk temperature variance for different locations was less than 2°C.

For the peak temperature value, the original mesh density model produced a result of 101.1°C. The 50% mesh density increase case produced a maximum peak temperature of 105.9°C. The doubled mesh density case produced a maximum peak temperature of 107.0°C. The maximum variation for peak temperature was 5.9°C.

Also a thermal-hydraulic analysis of a representative spent fuel pool has been modelled and solved by two different CFD codes. The shape of the temperature distribution throughout the pool is similar for both models.

The results of these sensitivity studies show that the hypothesis and numerical model to be valid.

5.3 RESULTS

Solving the two cases described previously, the results shown in the following sections are obtained.

5.3.1 Temperature Distribution Under Normal Conditions Case

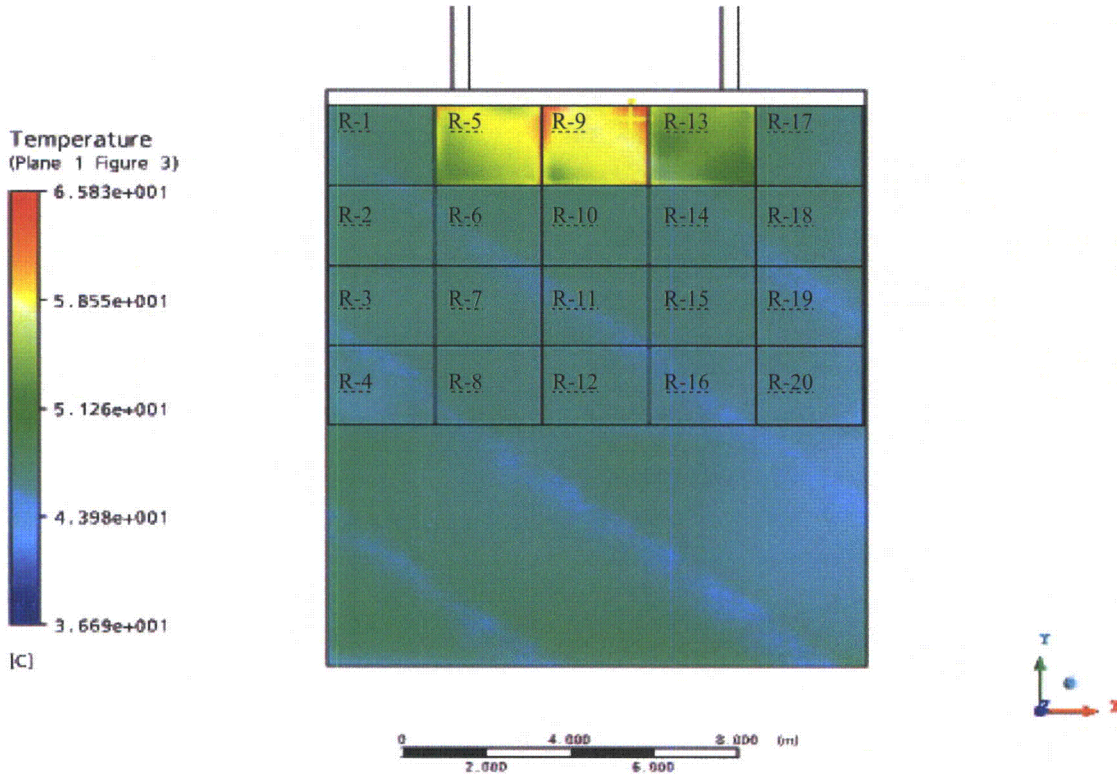


Figure H5-3. Temperature Distribution under the Normal Conditions Case (x,y)

Figure H5-3 shows the temperature distribution in the racks under the normal conditions case. The maximum peak temperature reached in this case is 65.83°C and is reached in the racks where the new FA are located. The maximum is reached at the top of the rack and is significantly less than the maximum allowable temperature of 121°C.

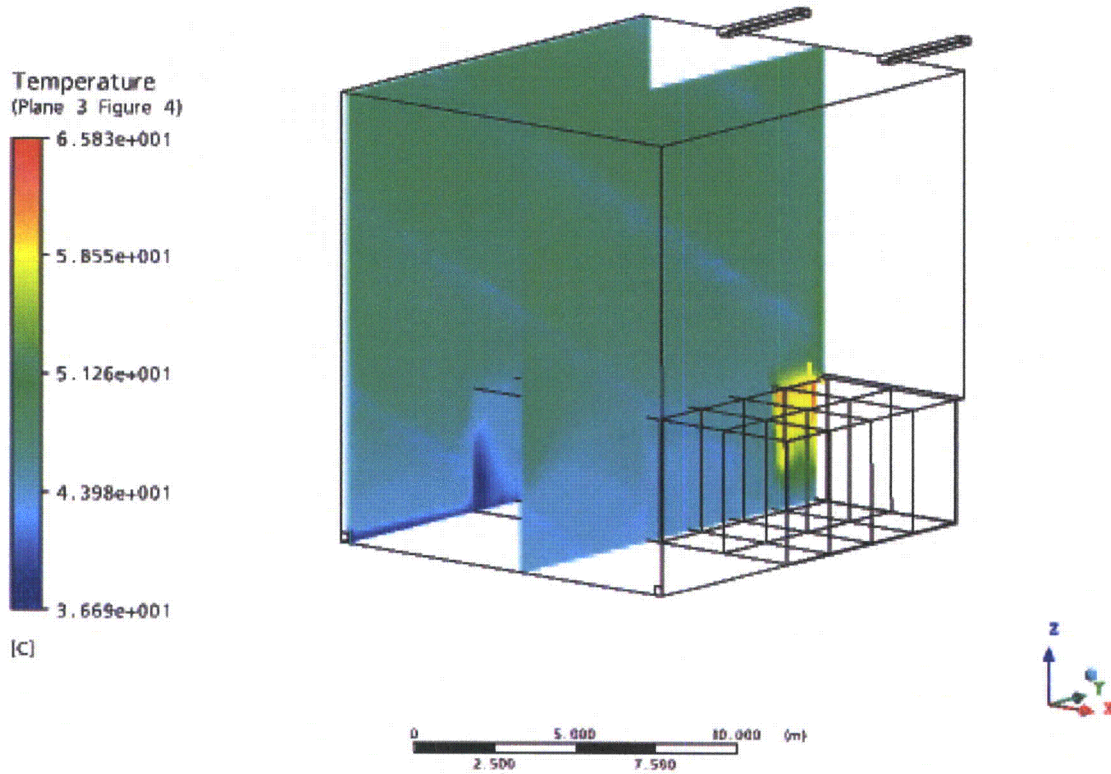


Figure H5-4. Temperature Distribution under the Normal Conditions Case (y,z)

Figure H5-4 shows the temperature distribution in the SFP under the normal conditions case. The temperature scale on the left ranges from the minimum to the maximum temperature on the SFP global. The inlet temperature (minimum temperature) is very close to 36.8°C. The outlet temperature is approximately 48.9°C as calculated in Section 5.2.2 of this analysis. The maximum temperatures are reached at the outlet of the racks where the new FA are located and the fluid temperature decreases as the water rises.

5.3.2 Temperature Distribution Under Abnormal Conditions Case

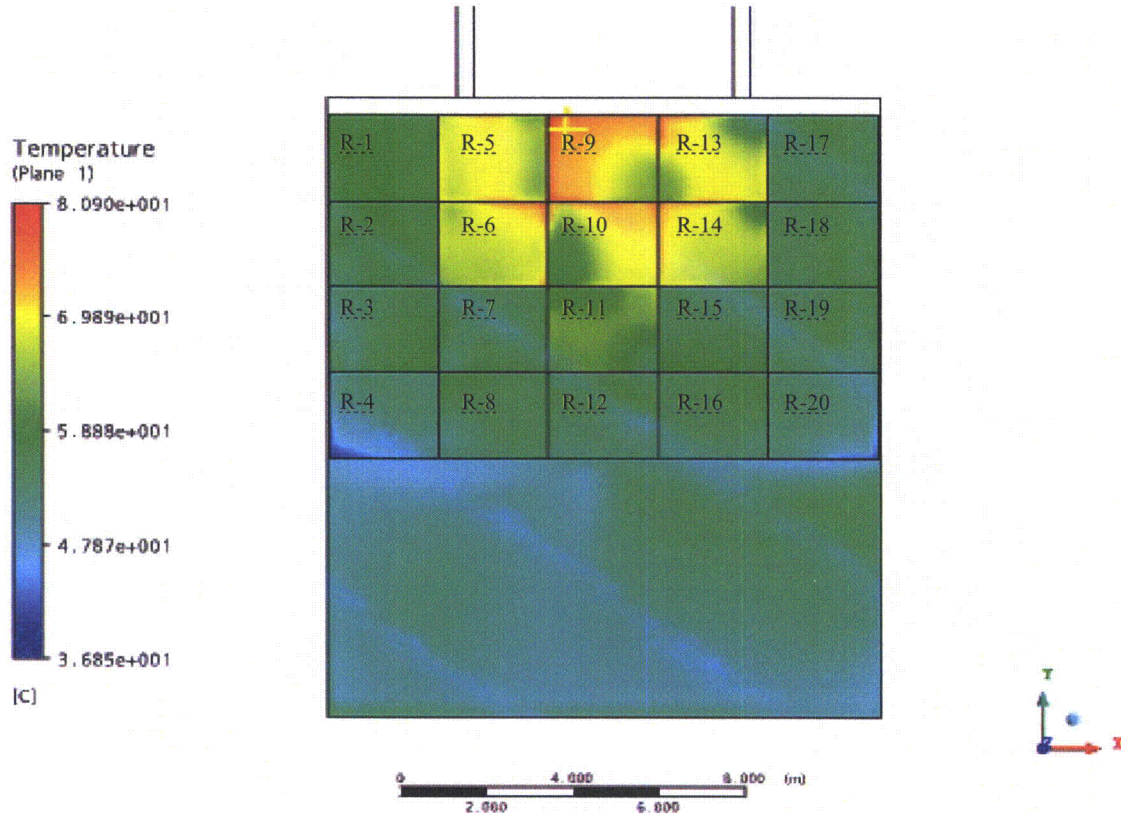


Figure H5-5. Temperature Distribution under the Abnormal Conditions Case (x,y)

Figure H5-5 shows the temperature distribution in the racks under the abnormal conditions case. The maximum peak temperature reached in this case is 80.9°C and is reached in the racks where the new FA are located. The maximum is reached at the top of the rack and is significantly less than the maximum allowable temperature of 121°C.

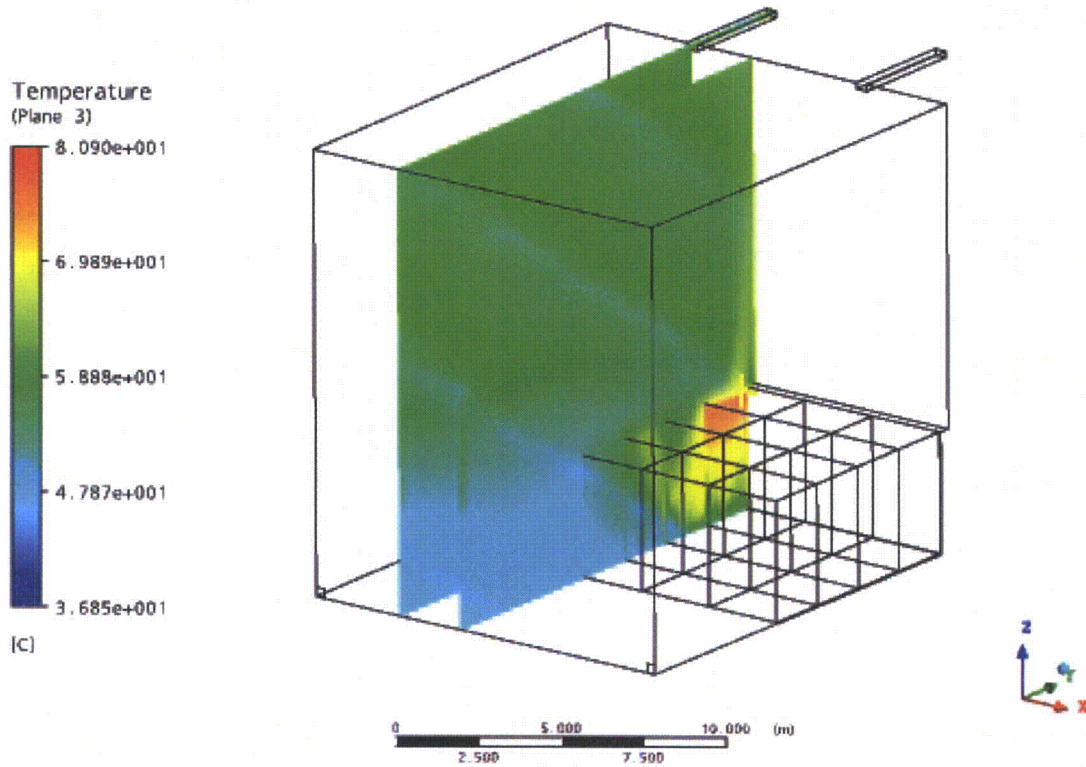


Figure H5-6. Temperature Distribution under the Abnormal Conditions Case (y,z)

Figure H5-6 shows the temperature distribution in the SFP under the abnormal conditions case. The temperature scale on the left ranges from the minimum to the maximum temperature on the SFP global. The inlet temperature (minimum temperature) is very close to 37°C. The outlet temperature is approximately 60°C as calculated in Section 5.2.2 of this analysis. The maximum temperatures are reached at the outlet of the racks where the new FA are located and the fluid temperature decreases as the water rises.

5.3.3 Velocity Distribution Under Normal Conditions Case

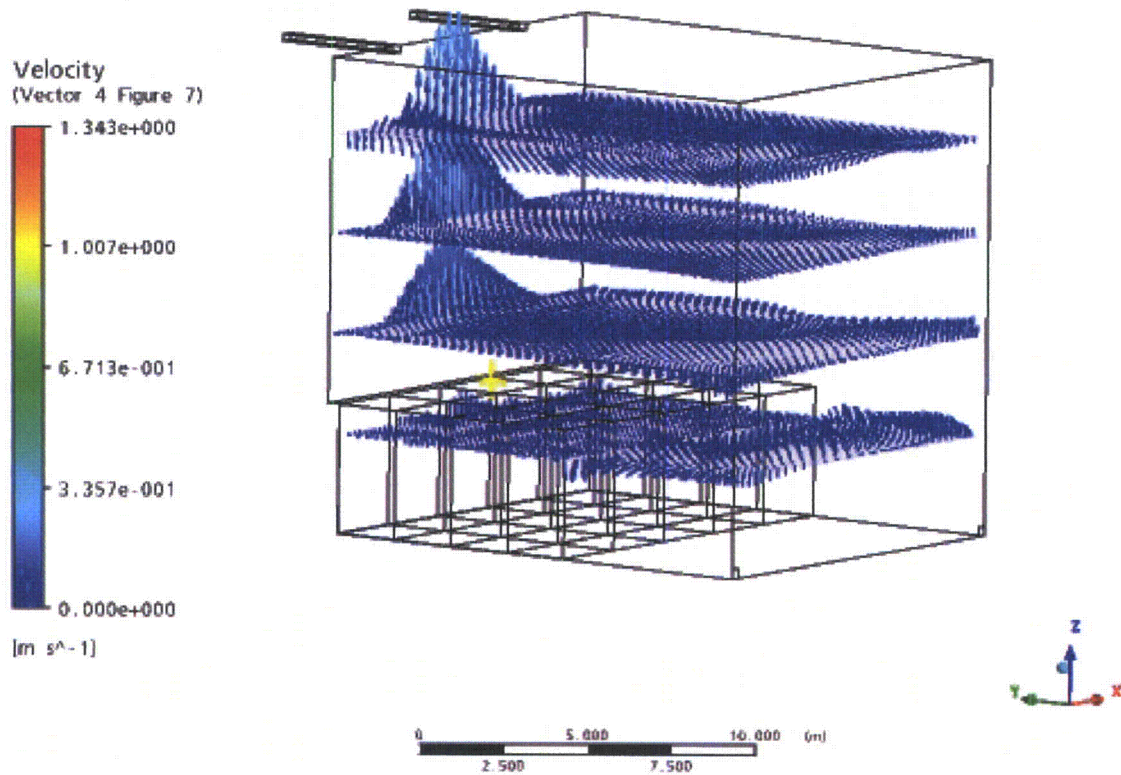


Figure H5-7. Velocity under the Normal Conditions Case (x,y)

Figure H5-7 shows the velocity distribution in the SFP under the normal conditions case. Velocities for horizontal planes at 3, 6, 9, 12 & 14 metres high are shown. Natural convection is forcing a vertical flow from the most loaded racks.

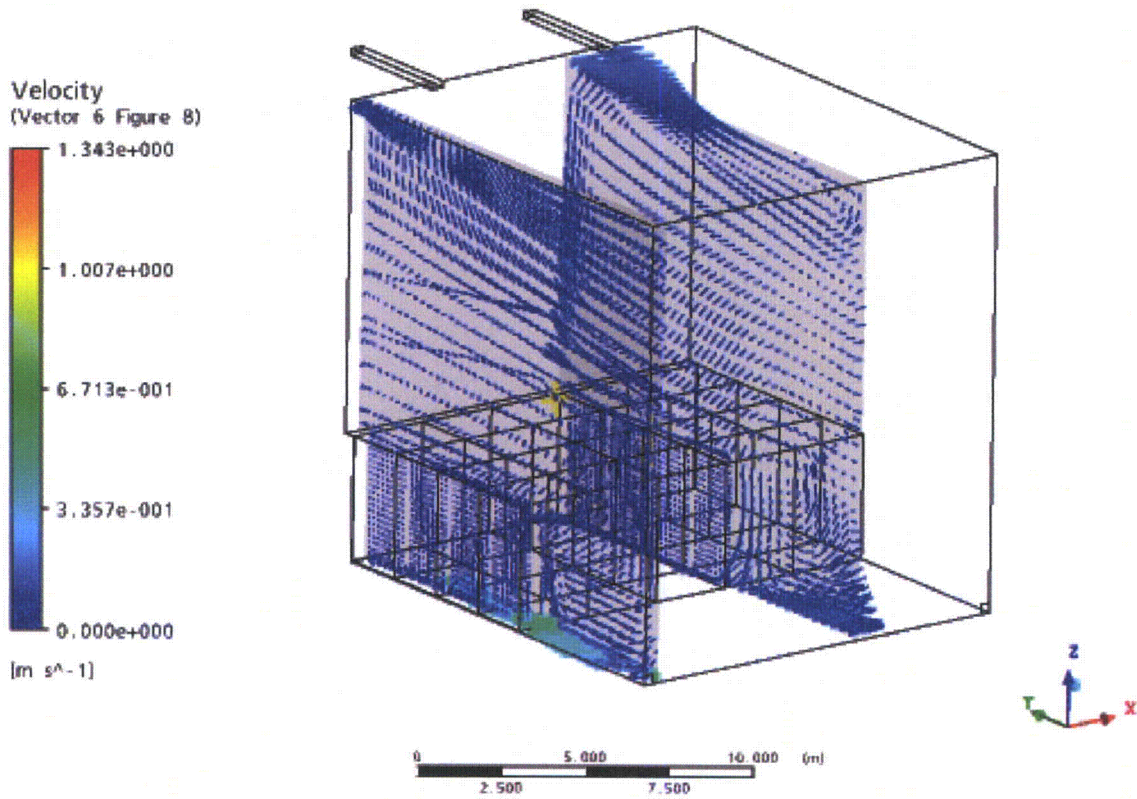


Figure H5-8. Velocity under the Normal Conditions Case (y,z)

Figure H5-8 shows the velocity distribution in the SFP under the normal conditions case. For this figure vertical planes (y,z) have been selected.

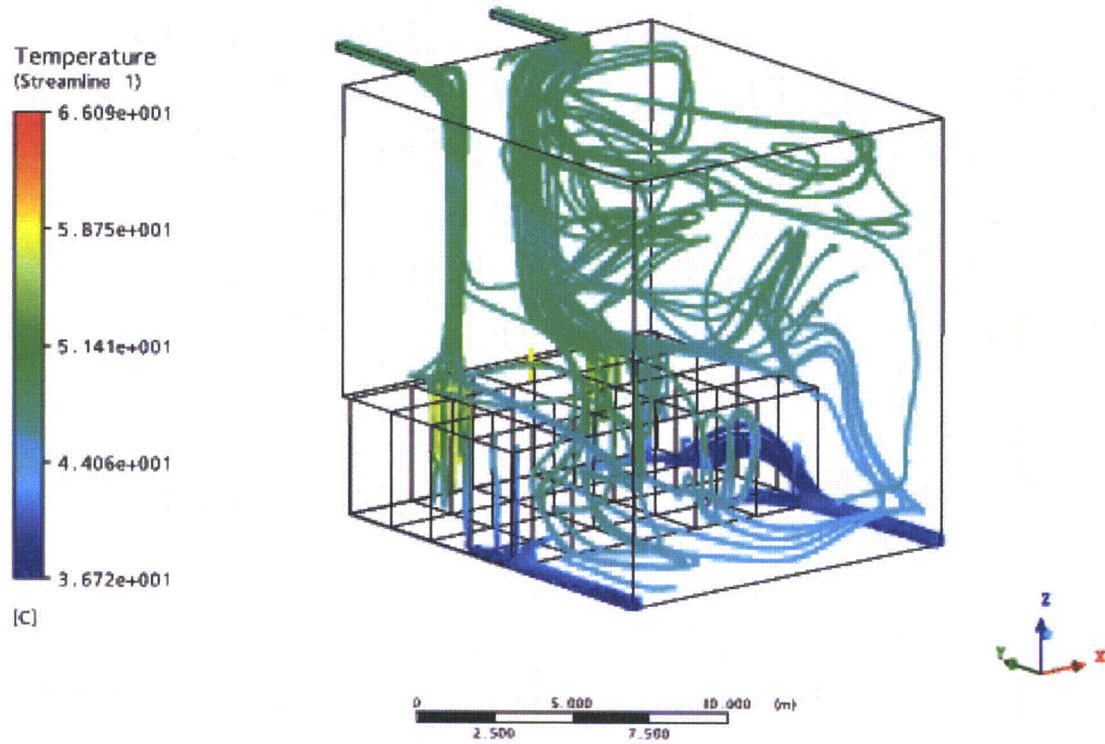


Figure H5-9. Streamlines from Inlets and to Outlets under the Normal Conditions Case

Figure H5-9 shows streamlines from the inlets and streamlines to the outlets in the SFP under the normal conditions case. The color of the streamline represents the temperature for each point.

5.3.4 Velocity Distribution Under Abnormal Conditions Case

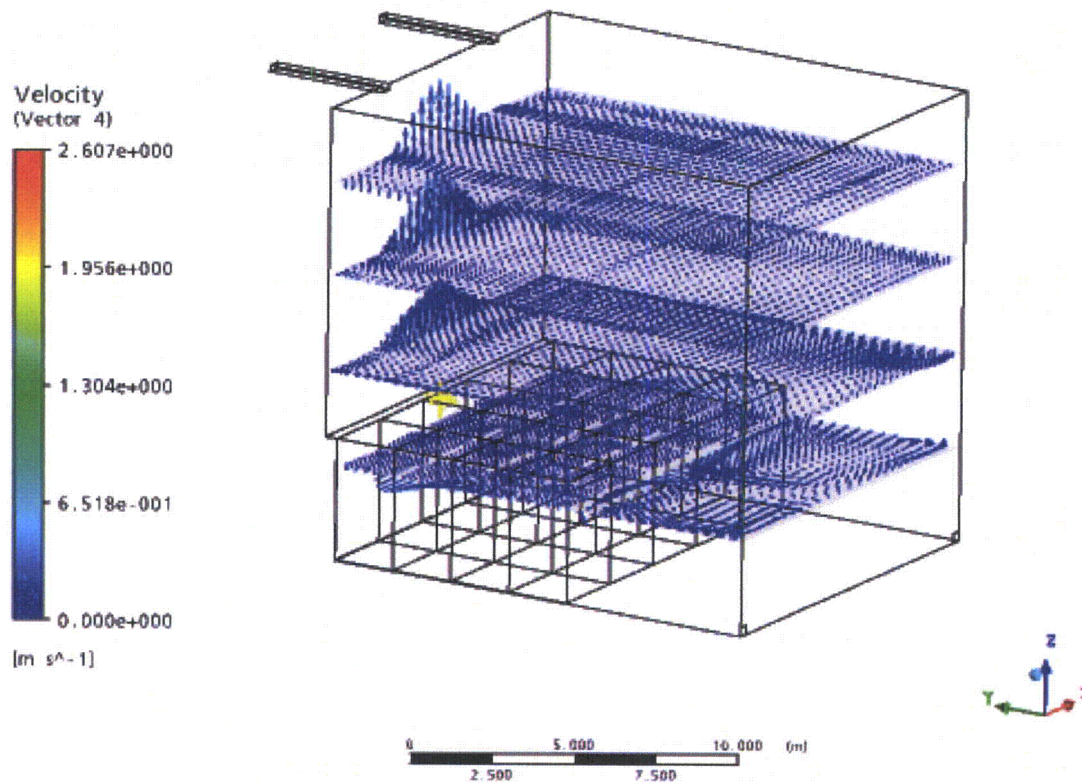


Figure H5-10. Velocity under the Abnormal Conditions Case (x,y)

Figure H5-10 shows the velocity distribution in the SFP under the abnormal conditions case. Velocities for horizontal planes at 3, 6, 9, 12 & 14 metres high are shown. Natural convection is forcing a vertical flow from the most loaded racks.



Figure H5-11. Velocity under the Abnormal Conditions Case (y,z)

Figure H5-11 shows the velocity distribution in the SFP under the abnormal conditions case. For this figure, vertical planes (y,z) have been selected.

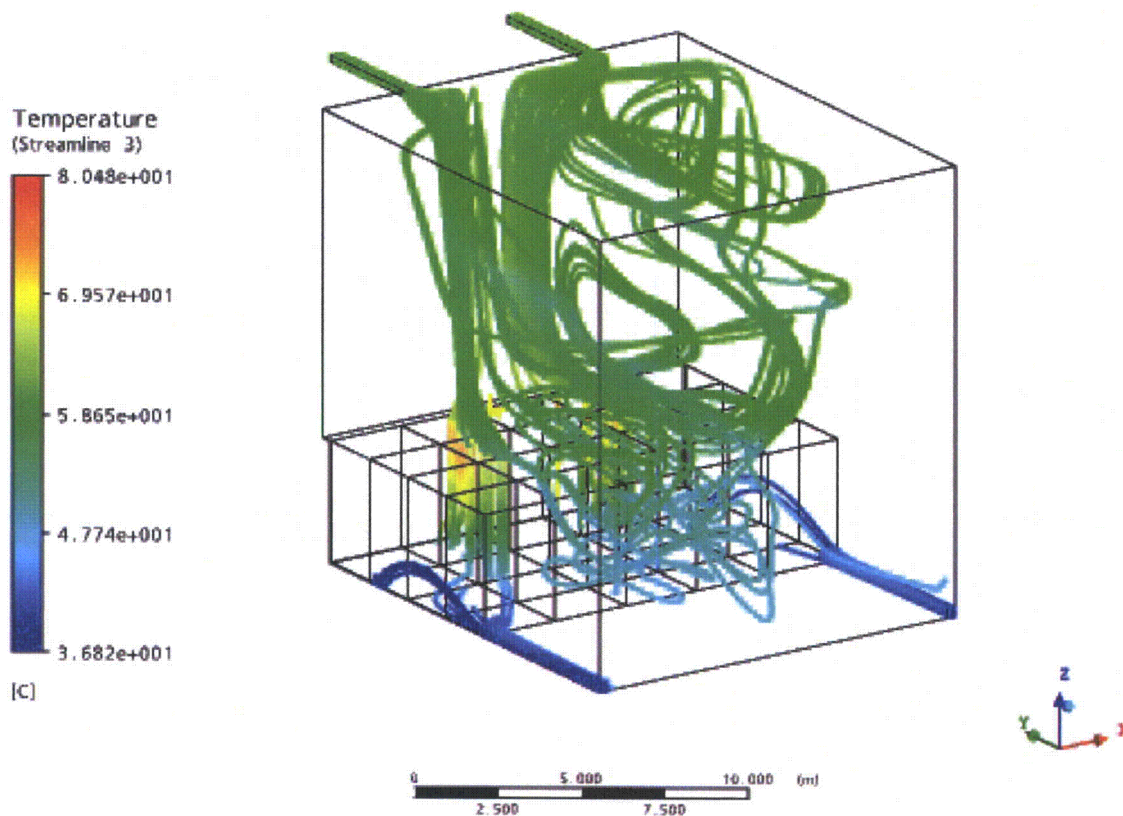


Figure H5-12. Streamlines from Inlets and to Outlets under the Abnormal Conditions Case

Figure H5-12 shows streamlines from the inlets and streamlines to the outlets in the SFP under the abnormal conditions case. The color of the streamline represents the temperature for each point.

5.3.5 Maximum Cladding Temperature

In order to calculate the maximum fuel cladding temperature in the racks, the following assumptions are made:

- The worst case is assumed to be the case where higher temperatures are reached. This is the abnormal conditions case.
- The fuel rod heat emission rate includes a radial peaking factor value of 1.4.
- The axial power shape is assumed to be a cosine curve, as the axial heat dissipation in the rod is known to reach a maximum in the central region, and taper off at the two extremities.
- A safety factor of 1.2 is considered for the bundle heat load.

Making use of the conservation of energy for a differential piece of rod, an analytical model for the water and cladding temperature is produced. This highly conservative model leads to simple algebraic equations which directly give the maximum local cladding temperature. For added conservatism a foulant layer (crud deposit) is assumed on the cladding surface. Thermal resistance equal to 5673 W/m²°C (1000BTU/h ft²°F) [Reference 7] is assumed. Input data for this calculation is given in the table below.

| Parameter | Value |
|---------------------------------------------------------------|---------------------------------------|
| Bundle generated heat (W) | 1.2 x 18881.6W = 22657.92W |
| Radial peaking factor | 1.4 |
| No rods per bundle | 92 (*) |
| Rod length (m) | 3.3762m (*) |
| Water temperature at rod's inlet (°C) | 60.39°C (**) |
| Cladding outside diameter (m) | 10.26mm (*) |
| Pellet diameter (m) | 8.76mm (*) |
| Zr-2 Conductivity (W/m°C) | 23W / m°C a 25°C 19W / m°C a 300°C |
| Foulant layer heat transfer coefficient (W/m ² °C) | 5673.4W / m ² °C |
| Total flow rate through the rack (15x12 bundle) | 20.789Kg/s (**) |

(*) Data taken from [Reference 6].

(**) The inlet temperature and the total flow rate through the rack are taken from the CFD model solution for the worst case and the worst rack, where the maximum temperature is reached.

The governing equations are derived as follows. The volumetric heat generation in a rod is:

$$\int q^m(z) A_c dz = \frac{q(W)}{N_B}$$

$$q^m(z) = q_c^m \cdot \cos\left(\frac{\pi z}{H_e}\right)$$

$$q_c^m = \frac{\frac{q}{N_B}}{\int_{-H_e/2}^{H_e/2} \cos\left(\frac{\pi z}{H_e}\right) A_c dz} = \frac{\frac{q}{N_B}}{2A_c \frac{H_e}{\pi}}$$

$$\frac{q_c^m A_c H_e}{\pi} = \frac{1}{2} \frac{q}{N_B}$$

Where:

N_B : Number of rods in each bundle (FA)

q : Volumetric heat generation rate per bundle (FA)

q_c^m : Volumetric heat generation rate per fuel rod

$A_c = \pi R^2$: Pellet cross section (m²)

R: Pellet radio (m)

H_e : Rod length (m)

$$\frac{q_c^m A_c H_e}{\pi} = \frac{1}{2} \frac{q}{N_B} = \frac{1}{2} \frac{22657.92}{92} = 123.14W$$

$$q_c^m = \frac{\pi \cdot 123.14 \cdot 3.3762}{\pi \cdot 0.00876^2} = 1901191.35 \frac{W}{m^3}$$

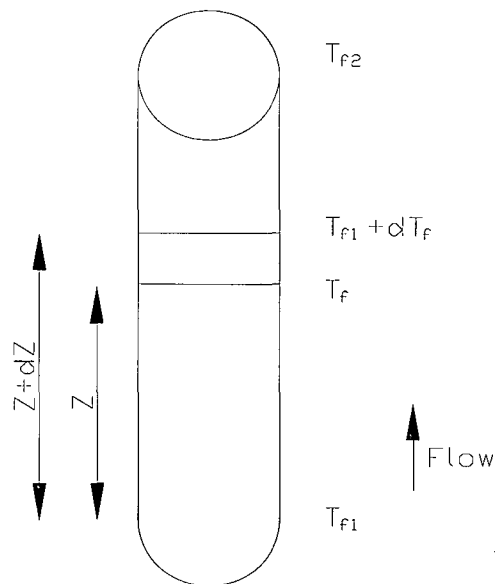


Figure H5-13. Rod Heat Balance

Applying the conservatism of energy between the fuel rod and the coolant, the following equation is obtained for the local fluid temperature.

$$m_{barra} C_p dT = q^m(z) A_c dz$$

$$T_f(z) = T_{f1} + \frac{q_c^m A_c}{m_{barra} C_p} \frac{H_e}{\pi} \left[\sin \frac{\pi z}{H_e} + \sin \frac{\pi}{2} \right] = T_{f1} + \frac{1}{2} \frac{N_B}{m_{barra} C_p} \left[\sin \frac{\pi z}{H_e} + \sin \frac{\pi}{2} \right]$$

$$T_{co}(z) = T_{f1} + \frac{q_c^m A_c}{m_{barra} C_p} \frac{H_e}{\pi} \left[\sin \frac{\pi z}{H_e} + \sin \frac{\pi}{2} \right] + \frac{q_c^m \cos \frac{\pi z}{H_e} A_c}{h \cdot 2\pi (R+c)}$$

For added conservatism a foulant layer (crud deposit) is assumed on the cladding surface. This is equivalent to two thermal resistances in series, so the equation that gives the outside cladding temperature is:

$$T_{co}(z) = T_{f1} + \frac{q_c^m A_c}{m_{barra} C_p} \frac{H_e}{\pi} \left[\sin \frac{\pi z}{H_e} + \sin \frac{\pi}{2} \right] + \frac{q_c^m \cos \frac{\pi z}{H_e} A_c}{\left(\frac{h_{dep} h}{h_{dep} + h} \right) \cdot 2\pi (R+c)}$$

For the value of the inlet temperature (T_{f1}), the maximum temperature of the inlet temperature to the worst rack in the worst case is selected. For the value of the coolant flow per rod, the average flow will be conservatively assumed.

Nomenclature used in preceding equations is:

$$m_{barra} = \frac{m_{rack}}{N_{EC} \cdot N_B} : \text{Coolant (water) flow rate per rod}$$

m_{rack} : Coolant (water) flow rate in the rack

N_{EC} : Number of bundles in the rack

$$C_p = 4182 \frac{J}{KgK} \text{ Coolant (water) specific heat}$$

$T_f(z)$: Local fluid temperature

h : Heat Transfer coefficient

h_{dep} : Foulant layer heat transfer coefficient

c : cladding thickness

T_{co} : Outside cladding temperature

The minimum heat transfer coefficient from the following table is used (water, heating):

Table H5-1
Approximate Range of Values hm Ordinarily Encountered

| | [[Btu/(hr) (Sq ft) (Deg F) | |
|-------------------------------|----------------------------|--------|
| Steam, dropwise condensation | 5,000 | 20,000 |
| Steam, film-type condensation | 1,000 | 3,000 |
| Water boiling | 300 | 9,000 |
| Organic vapors condensing | 200 | 400 |
| Water, heating | 50 | 3,000 |
| Steam, superheating | 5 | 20 |
| Air, heating or cooling | 0.2 | 10 |

(*) Table taken from reference [Reference 7].

$$h = 50 \frac{BTU}{hr \cdot ft^2 \cdot F} = 283.9 \frac{W}{m^2 K}$$

$$T_{c,0}(z) = 60.3 + \frac{123.14}{4182 \cdot \frac{20.789}{180 \cdot 92}} \left[\sin \frac{\pi z}{3.3762} + 1 \right] + \frac{1901191.35 \cos \frac{\pi z}{3.3762} \pi \frac{0.00876^2}{4}}{\left(\frac{5673.4 + 283.9}{5673.4 + 283.9} \right) 2\pi \left(\frac{0.01026}{2} \right)}$$

The maximum value calculated from this function is at z=0.949m, as measured from the center of the rod. The maximum peak temperature is:

$$T_{c,0}(z) = 97.12^\circ C$$

5.3.6 Maximum Fluid Temperature Under 80% Blockage of Rack Outlet

Due to the different acceptance criteria for the two different cases, a calculation will be performed for each case.

5.3.6.1 Under Normal Conditions Case

For this analysis the assumption is that the rack outlet is 80% blocked. Conservatively, the holes in the rack between bundles are not considered. A bundle in the hottest rack is considered for this case. The maximum temperature at the inlet of the hottest rack will be conservatively assumed. The flow for this bundle will be considered to be the average flow per bundle on this rack:

$$\dot{m}_{FA} = \frac{\dot{m}_{rack}}{N_{FA}} = \frac{51.8178}{180} = 0.28787 \frac{Kg}{s}$$

Where:

\dot{m}_{rack} = Total flow at the hottest rack inlet

N_{FA} = Number of bundles in the hottest rack

The loss coefficient increment is given by the following equation:

$$\Delta K = \frac{1}{2} \left(\frac{1.5}{\rho \cdot A_B^2} - \frac{1}{\rho \cdot A_{CEL}^2} \right) = \frac{1}{2} \left(\frac{1.5}{1000 \cdot 0.2^2 \cdot (0.1646^2)^2} - \frac{1}{1000 \cdot (0.1646^2)^2} \right) = 24.862 Kg^{-1} m^{-1}$$

Where:

A_B = Blocked section Area.

A_{CEL} = Non blocked section Area.

ρ = Fluid density.

Assuming the pressures at the inlet and outlet of the rack will be the same as if unblocked:

$$\Delta P = K_C (\dot{m}_{FA})^2 = K_{TAP} (\dot{m}_{FATAP})^2$$

Where:

K_C = Loss coefficient without blockage

K_{TAP} = Loss coefficient with blockage

\dot{m}_{FA} = Flow through bundle without blockage

\dot{m}_{FATAP} = Flow through bundle with blockage

The loss coefficient without blockage ($K_C = 269.55 \text{Kg}^{-1}\text{m}^{-1}$) is equal to the value calculated in Section 5.2.3.1 of this report. The loss coefficient without blockage will be this value plus the loss coefficient due to the blockage. Therefore:

$$K_{TAP} = K_C + \Delta K = 269.55 + 24.862 = 294.41 \text{Kg}^{-1}\text{m}^{-1}$$

The flow through the blocked bundle can be obtained from the previous equations:

$$\dot{m}_{FABlock} = \dot{m}_{FA} \sqrt{\frac{K}{K + \Delta K}} = \frac{518178}{15 \cdot 12} \sqrt{\frac{269.55}{294.41}} = 0.27545 \frac{\text{Kg}}{\text{s}}$$

The temperature that will be reached at the outlet of the bundle is:

$$T_{Block} = T_{f1} + \Delta T = T_{f1} + \frac{q}{\dot{m}_{FABlock} \cdot C_p} = 48.17 + \frac{16021 \cdot 1.2}{0.27545 \cdot 4182} = 64.86^\circ\text{C}$$

5.3.6.2 Under Abnormal Conditions Case

For this analysis, the assumption is that the rack outlet is 80% blocked. Conservatively, the holes in the rack between bundles are not considered. A bundle in the hottest rack is considered for this case. The maximum temperature at the inlet of the hottest rack will be conservatively assumed. The flow for this bundle will be considered to be the average flow per bundle on this rack:

$$\dot{m}_{FA} = \frac{\dot{m}_{rack}}{N_{FA}} = \frac{30.452}{180} = 0.169178 \frac{\text{Kg}}{\text{s}}$$

Where:

\dot{m}_{rack} = Total flow at the hottest rack inlet

N_{FA} = Number of bundles in the hottest rack

The loss coefficient increment is given by the following equation:

$$\Delta K = \frac{1}{2} \left(\frac{1.5}{\rho \cdot A_B^2} - \frac{1}{\rho \cdot A_{CEL}^2} \right) = \frac{1}{2} \left(\frac{1.5}{1000 \cdot 0.2^2 \cdot (0.1646^2)^2} - \frac{1}{1000 \cdot (0.1646^2)^2} \right) = 24.862 \text{Kg}^{-1}\text{m}^{-1}$$

Where:

A_B = Blocked section Area.

A_{CEL} = Non blocked section Area.

ρ = Fluid density.

Assuming the pressures at the inlet and outlet of the rack will be the same as if it unblocked:

$$\Delta P = K_C (\dot{m}_{FA})^2 = K_{TAP} (\dot{m}_{FATAP})^2$$

Where:

K_C = Loss coefficient without blockage

K_{TAP} = Loss coefficient with blockage

\dot{m}_{FA} = Flow through bundle without blockage

\dot{m}_{FATAP} = Flow through bundle with blockage

The loss coefficient without blockage ($K_C = 269.55 \text{Kg}^{-1} \text{m}^{-1}$) is equal as the value calculated in Section 5.2.3.1 of this report. The loss coefficient without blockage will be this value plus the loss coefficient due to the blockage. Therefore:

$$K_{TAP} = K_C + \Delta K = 269.55 + 24.862 = 294.41 \text{Kg}^{-1} \text{m}^{-1}$$

The flow through the blocked bundle can be obtained from the previous equations:

$$\dot{m}_{FABlock} = \dot{m}_{FA} \sqrt{\frac{K}{K + \Delta K}} = \frac{30.452}{15 \cdot 12} \sqrt{\frac{269.55}{294.41}} = 0.1618776 \frac{\text{Kg}}{\text{s}}$$

The temperature that will be reached at the outlet of the bundle is:

$$T_{Block} = T_{f1} + \Delta T = T_{f1} + \frac{q}{\dot{m}_{FABlock} \cdot C_p} = 60.39 + \frac{18881.6 \cdot 1.2}{0.1618776 \cdot 4182} = 93.86^\circ \text{C}$$

5.4 REACTOR BUFFER POOL

The calculation methodology for this analysis is similar to that performed for the SFP.

The only time spent fuel can be stored in the buffer pool is during a refuelling outage. During an outage, one train of the fuel pool cooling system has the capacity to cool the entire SFP and is dedicated to that purpose. The redundant train provides cooling to the buffer pool.

The bulk temperature of the buffer pool is maintained below the same maximum value as the SFP (48.9°C, 120°F). The heat load in the buffer pool is 2.5 MW [Reference 10], compared to a heat load of 7.626 MW in the SFP. Each redundant train of the fuel pool cooling system is capable of removing 8.3 MW [Reference 1], therefore, the system is capable of maintaining buffer pool temperature below the maximum bulk temperature.

Since the inlet pipe is routed to the bottom of the racks in the deep pit of the buffer pool, the general configuration is similar to that in spent fuel pool. Therefore, with the cooling capacities being the same between the pools, the maximum temperature that would be reached at the exit of the spent fuel storage racks in the reactor buffer pool is calculated based on the ratio of the

average per bundle heat load in the buffer pool to that of the SFP. The calculation below determines the temperature of fluid exiting the spent fuel storage racks in the buffer pool.

The heat per bundle in this pool would be:

$$\frac{2.5 \cdot 10^6 W}{2 \cdot 11.7 FA} = 16223.8 \frac{W}{FA}$$

That is similar to the heat per bundle in normal conditions case = $16021 \frac{W}{FA_{new}}$

It is conservatively assumed that the flow for each bundle would be the same as the value used in the normal conditions case. The flow rate will actually be higher because cooling capacity for the racks in the reactor buffer pool is greater. Also, the heat load is higher; therefore, natural convection flow would be greater.

Because the temperature increment is proportional to the heat, the bulk temperature in the SFP and buffer pool is the same (48.9°C), and the coolant flow is the same, the exit temperature can be calculated as follows:

$$\frac{\Delta T_{RBP}}{\Delta T_{NCC}} = \frac{16223.8}{16021} = 1.01266$$

$$Rack_Exit_Temp = 65.83C \cdot 1.01266 = 66.7C$$

5.5 SUMMARY OF RESULTS

The results calculated in the previous sections show that the maximum local coolant temperature reached at the top of the racks in the SFP is 65.83°C under the normal conditions case using a calculated maximum pool inlet temperature of 36.8°C. The maximum peak temperature reached is 80.9°C under the abnormal conditions case using a calculated maximum pool inlet temperature of 37.0°C.

The results also show that the maximum peak cladding temperature that will be reached is 97.12°C.

In the event of 80% blockage at the outlet of the rack, the temperature reached in the normal conditions case would be 64.86°C. The temperature reached in the abnormal conditions case would be 93.86°C.

The maximum temperature of fluid exiting the spent fuel storage racks in the buffer pool is 66.7°C.

In the current GE design for the spent fuel pool, the cold inlet water pipe is routed to the bottom of the pool, therefore, the water that cools the fuel elements can easily enter the bottom part of the racks. This inlet pipe design allows that the introduction of cold water at the bottom part of the racks eliminates the dependency of distances between racks or between racks and pool wall.

5.6 REFERENCES

- 1) "Fuel Storage Rack Design Specification" Document No 26A7032 Rev 02 GE Nuclear Energy.
- 2) ANSYS CFX Computer Program Release 11.0, ANSYS Inc., South Point, 275 Technology Dr., Canonsberg, PA 15317.
- 3) ESBWR Spent Fuel Pool Decay Heat Part II GE-NE-0000-0040-6730-R0-DRAFT Rev 0. GE Proprietary Information.
- 4) ESBWR Spent Fuel Pool Boil-off. NeDRF 0000-0038-9391/neDRFSection 0000-0038-9392 Rev 02.
- 5) "Rack Layout at Spent Fuel Building" ENSA 5926.D100 Rev 01.
- 6) Design Study Summary GE14E, ESBWR Fuel Assembly, DRF Section 41-8790, Global Nuclear Fuel (GNF).
- 7) "Heat Transmission" William H. McAdams. McGraw-Hill Book Company.
- 8) "Fuel Storage Requirements" Doc. No 22A5866 Rev 08, GE Nuclear Energy.
- 9) "Rack Layout at Spent Fuel Building" ENSA 5926.D100 Rev 02.
- 10) ESBWR Buffer Pool Boil-Off and Makeup Capacity, eDRF Section 0000-0076-3483.

NEDO-33373-A, Revision 5

Attachment 1

**Final Safety Evaluation For
GE Hitachi Nuclear Energy
Licensing Topical Report NEDO-33373, Revision 5**

**"Dynamic, Load-Drop and Thermal-Hydraulic Analyses
for ESBWR Fuel Racks"**

October 20, 2010

Mr. Jerald G. Head
Senior Vice President, Regulatory Affairs
GE Hitachi Nuclear Energy
3901 Castle Hayne Road MC A-18
Wilmington, NC 28401

SUBJECT: FINAL SAFETY EVALUATION FOR GE HITACHI NUCLEAR ENERGY
LICENSING TOPICAL REPORT NEDO-33373, REVISION 5, "DYNAMIC,
LOAD-DROP AND THERMAL-HYDRAULIC ANALYSES FOR ESBWR FUEL
RACKS"

Dear Mr. Head:

On August 24, 2005, GE Hitachi (GEH) Nuclear Energy submitted the Economic Simplified Boiling Water Reactor (ESBWR) design certification application to the staff of the U.S. Nuclear Regulatory Commission (NRC). Subsequently, in support of the design certification, GEH submitted the license topical report (LTR) NEDO-33373, Revision 5, "Dynamic, Load-Drop and Thermal-Hydraulic Analyses for ESBWR Fuel Racks." The staff has now completed its review of NEDO-33373, Revision 5.

The staff finds NEDO-33373, Revision 5, "Dynamic, Load-Drop and Thermal-Hydraulic Analyses for ESBWR Fuel Racks," acceptable for referencing for the ESBWR design certification to the extent specified and under the limitations delineated in the LTRs and in the associated safety evaluation (SE). The SE, which is enclosed, defines the basis for acceptance of the LTR.

The staff requests that GEH publish the revised version of the LTR listed above within 1 month of receipt of this letter. The accepted version of the LTR shall incorporate this letter and the enclosed SER and add an "-A" (designated accepted) following the report identification number.

If NRC's criteria or regulations change, so that its conclusion that the LTR is acceptable is invalidated, GEH and/or the applicant referencing the LTR will be expected to revise and resubmit its respective documentation, or submit justification for continued applicability of the LTR without revision of the respective documentation.

The staff concludes that the enclosed SE does not contain any information for which exemption from public disclosure has been sought or approved. However, the NRC will withhold the enclosed SE from public disclosure for 10 calendar days to allow GEH the opportunity to verify the staff's conclusion that the enclosed SE contains no such exempt information.

Document transmitted herewith contains sensitive unclassified information. When separated from the enclosures, this document is "DECONTROLLED."

J. Head

- 2 -

The Advisory Committee on Reactor Safeguards (ACRS) subcommittee, having reviewed the subject LTR and supporting documentation, agreed with the staff's recommendation for approval following the September 23, 2010 ACRS subcommittee meeting.

Sincerely,

/RA Frank Akstulewicz for:/

David B. Matthews, Director
Division of New Reactor Licensing
Office of New Reactors

Docket No. 52-010

Enclosure:

1. Safety Evaluation

cc: See next page

J. Head

- 2 -

The Advisory Committee on Reactor Safeguards (ACRS) subcommittee, having reviewed the subject LTR and supporting documentation, agreed with the staff's recommendation for approval following the September 23, 2010 ACRS subcommittee meeting.

Sincerely,

/RA Frank Akstulewicz for:/

David B. Matthews, Director
Division of New Reactor Licensing
Office of New Reactors

Docket No. 52-010

Enclosure:

1. Safety Evaluation

cc: See next page

Distribution:

Hard Copy:

NGE1 R/F

ACubbage

DGalvin

Email:

RidsNroDnrlNge1

NGE 1/2 Group

RidsAcrsAcnwMailCenter

RidsNroDsraSrsb

RidsNroDeSeb2

RidsOgcMailCenter

JDonoghue

KHawkins

ACubbage

DGalvin

ADAMS ACCESSION NO.: ML102700448-Package

NRO-002

| | | | | |
|--------|----------|------------------|-----------|-----------|
| OFFICE | BWR:PM | BWR:LA | BC:SRSB | SC: SEB2 |
| NAME | DGalvin | Sgreen (BHA for) | JDonoghue | KHawkins |
| DATE | 10/18/10 | 10/13/10 | 10/18/10 | 10/12/10 |
| OFFICE | BWR:LPM | BWR:BC | OGC/NLO | DNRL:D |
| NAME | ACubbage | MTonacci | SLiaw | DMatthews |
| DATE | 10/15/10 | 10/15/10 | 10/15/10 | 10/20/10 |

OFFICIAL RECORD COPY

DC GEH - ESBWR Mailing List

(Revised 08/11/2010)

cc:

Ms. Michele Boyd
Legislative Director
Energy Program
Public Citizens Critical Mass Energy
and Environmental Program
215 Pennsylvania Avenue, SE
Washington, DC 20003

Mr. Tom Sliva
7207 IBM Drive
Charlotte, NC 28262

DC GEH - ESBWR Mailing List

Email

aec@nrc.gov (Amy Cabbage)
APH@NEI.org (Adrian Heymer)
awc@nei.org (Anne W. Cottingham)
bevans@enercon.com (Bob Evans)
bgattoni@roe.com (William (Bill) Gattoni))
BrinkmCB@westinghouse.com (Charles Brinkman)
cberger@energetics.com (Carl Berger)
charles.bagnal@ge.com
charles@blackburncarter.com (Charles Irvine)
chris.maslak@ge.com (Chris Maslak)
CumminWE@Westinghouse.com (Edward W. Cummins)
cwaltman@roe.com (C. Waltman)
Daniel.Chalk@nuclear.energy.gov (Daniel Chalk)
david.hinds@ge.com (David Hinds)
david.lewis@pillsburylaw.com (David Lewis)
David.piepmeyer@ge.com (David Piepmeyer)
donaldf.taylor@ge.com (Don Taylor)
erg-xl@cox.net (Eddie R. Grant)
gcesare@enercon.com (Guy Cesare)
GEH-NRC@hse.gsi.gov.uk (Geoff Grint)
GovePA@BV.com (Patrick Gove)
gzinke@entergy.com (George Alan Zinke)
hickste@earthlink.net (Thomas Hicks)
hugh.upton@ge.com (Hugh Upton)
james.beard@gene.ge.com (James Beard)
jerald.head@ge.com (Jerald G. Head)
Jerold.Marks@ge.com (Jerold Marks)
jgutierrez@morganlewis.com (Jay M. Gutierrez)
Jim.Kinsey@inl.gov (James Kinsey)
jim.riccio@wdc.greenpeace.org (James Riccio)
joel.Friday@ge.com (Joel Friday)
Joseph_Hegner@dom.com (Joseph Hegner)
junichi_uchiyama@mnes-us.com (Junichi Uchiyama)
kimberly.milchuck@ge.com (Kimberly Milchuck)
KSutton@morganlewis.com (Kathryn M. Sutton)
kwaugh@impact-net.org (Kenneth O. Waugh)
lchandler@morganlewis.com (Lawrence J. Chandler)
lee.dougherty@ge.com
Marc.Brooks@dhs.gov (Marc Brooks)
maria.webb@pillsburylaw.com (Maria Webb)
mark.beaumont@wsms.com (Mark Beaumont)
matias.travieso-diaz@pillsburylaw.com (Matias Travieso-Diaz)
media@nei.org (Scott Peterson)
mike_moran@fpl.com (Mike Moran)

DC GEH - ESBWR Mailing List

MSF@nei.org (Marvin Fertel)
mwetterhahn@winston.com (M. Wetterhahn)
nirsnet@nirs.org (Michael Mariotte)
Nuclaw@mindspring.com (Robert Temple)
patricia.l.campbell@ge.com (Patricia L. Campbell)
Paul@beyondnuclear.org (Paul Gunter)
peter.yandow@ge.com (Peter Yandow)
pshastings@duke-energy.com (Peter Hastings)
rick.kingston@ge.com (Rick Kingston)
RJB@NEI.org (Russell Bell)
Russell.Wells@Areva.com (Russell Wells)
sabinski@suddenlink.net (Steve A. Bennett)
sandra.sloan@areva.com (Sandra Sloan)
sara.andersen@ge.com (Sara Anderson)
sfrantz@morganlewis.com (Stephen P. Frantz)
stephan.moen@ge.com (Stephan Moen)
steven.hucik@ge.com (Steven Hucik)
strambgb@westinghouse.com (George Stramback)
tdurkin@energetics.com (Tim Durkin)
timothy1.enfinger@ge.com (Tim Enfinger)
tom.miller@hq.doe.gov (Tom Miller)
trsmith@winston.com (Tyson Smith)
Vanessa.quinn@dhs.gov (Vanessa Quinn)
Wanda.K.Marshall@dom.com (Wanda K. Marshall)
wayne.marquino@ge.com (Wayne Marquino)
whorin@winston.com (W. Horin)

**Safety Evaluation Report on General Electric Hitachi Nuclear Energy
Topical Report NEDO-33373:
“Dynamic, Load-Drop and Thermal-Hydraulic Analyses for ESBWR Fuel Racks”**

1.0 Introduction

GE Hitachi Nuclear Energy (GEH) issued Revision 5 of Topical Report NEDO-33373, “Dynamic, Load-Drop and Thermal-Hydraulic Analyses for ESBWR Fuel Racks,” in October 2010 (Ref. 1). (Unless otherwise noted, references to NEDO-33373 refer to Revision 5.) NEDO-33373 documents the results of the structural and thermal-hydraulic analyses for the design of spent fuel racks located in the spent fuel pool and buffer pool, as well as new fuel racks in the buffer pool. Section 2 of this safety evaluation report (SER) discusses the U.S. Nuclear Regulatory Commission (NRC) staff’s evaluation of the technical adequacy of GEH’s structural analyses to determine the capability of the fuel racks to protect the housed fuel assemblies, as documented in Sections 1, 2, 3, and 4 of NEDO-33373. (Structural evaluation of the pools and stored fuel assemblies is not within the scope of NEDO-33373.)

Section 3 of this SER discusses the staff’s evaluation of the technical adequacy of the applicant’s thermal-hydraulic analysis on decay heat removal from the spent fuel assemblies during all anticipated operating and accident conditions, documented in Section 5 of NEDO-33373. Section 3 also discusses the staff evaluation of the technical adequacy of the applicant’s thermal-hydraulic analysis on adequate natural circulation of the coolant during all anticipated operating conditions, including full-core offloads during refueling, to prevent nucleate boiling for all fuel assemblies.

2.0 Dynamic Load and Load-Drop Analyses

2.1 Regulatory Criteria

The staff reviewed the economic simplified boiling-water reactor (ESBWR) dynamic load and load-drop analyses of the new and spent fuel storage racks in accordance with NUREG-0800, “Standard Review Plan for the Review of Safety Analysis Reports for Nuclear Power Plants: LWR Edition” (hereafter referred to as the SRP), Section 3.8.4, “Other Seismic Category I Structures,” Appendix D, “Guidance on Spent Fuel Pool Racks,” Revision 2, issued March 2007 (Ref. 2). The staff’s acceptance of the dynamic load and load-drop analyses of the new and spent fuel storage racks is based on applicant compliance with the following requirements:

- Title 10 of the *Code of Federal Regulations* (10 CFR) Part 50, “Domestic Licensing of Production and Utilization Facilities,” (Ref. 3) specifically, 10 CFR 50.55a, “Codes and Standards,” as they relate to codes and standards
- General Design Criterion (GDC) 1, “Quality Standards and Records,” of Appendix A, “General Design Criteria for Nuclear Power Plants,” to 10 CFR Part 50, as it relates to structures, systems and components being designed, fabricated, erected, constructed, and tested to quality standards commensurate with the importance of the safety function to be performed
- GDC 2, “Design Bases for Protection against Natural Phenomena,” as it relates to structures, systems, and components important to safety being designed to withstand

appropriate combinations of the effects of normal and accident conditions with the effects of earthquakes.

- GDC 4, "Environmental and Dynamic Effects Design Bases," as it relates to structures, systems and components important to safety being appropriately protected against the dynamic effects of discharging fluids.
- Appendix B, "Quality Assurance Criteria for Nuclear Power Plants and Fuel Reprocessing Plants," to 10 CFR Part 50, as it relates to design control.

2.2 Summary of Technical Information

Sections 1, 2, and 3 of NEDO-33373 supply the dynamic analyses used for the design of the spent fuel racks located in the spent fuel pool and buffer pool, as well as new fuel racks in the buffer pool. Section 4 of NEDO-33373 gives a load-drop analysis to demonstrate that the functionality of the spent fuel racks and the new fuel racks is not affected by the postulated accidental drops. The subsections below give a summary description of each of these analyses. (The respective sections of NEDO-33373 provide detailed descriptions of these analyses.)

Dynamic Load Analysis for Spent Fuel Racks in the Spent Fuel Pool

Section 1 of NEDO-33373 describes the dynamic load analysis for spent fuel racks in the spent fuel pool, which is located in the fuel building. The spent fuel racks give structural support to and protection of the stored spent fuel assemblies, and are designed by analysis in accordance with the requirements for American Society of Mechanical Engineers (ASME) Boiler and Pressure Vessel (B&PV) Code Class 3 plate and shell type supports (Ref. 4). The racks are plate-type structures constructed using stainless steels and borated stainless steels. These racks are permanently submerged in the pool water but are not structurally fastened to the pool walls or base. The fuel assemblies are inserted and removed through the access at the top of the racks. NEDO-33373, Section 1.4, gives the detailed layout and dimensions of the racks.

Section 1.4 of NEDO-33373 also describes the dynamic load analysis for the spent fuel racks in the spent fuel pool. The description includes (1) the dead weight plus buoyancy load, (2) fuel handling loads (upward force by postulated stuck fuel assembly), (3) the thermal effect, (4) the safe-shutdown earthquake (SSE), (5) the safety relief valve discharge (SRVD) load, and (6) the loss-of-coolant accident (LOCA) load. These loads were combined in accordance with the service limits given in Table 1 of Appendix D to SRP Section 3.8.4. The stress limits were based on ASME B&PV Code (2001 edition with 2003 addenda), Section III, Division I, Subsection NF and Appendix F, (Ref. 4) for Class 3 plate and shell type supports.

The applicant performed a response spectrum analysis to calculate the dynamic response of the spent fuel racks to SSE, SRVD, and LOCA loads. A finite element model for an individual rack was developed, with the hydrodynamic coupling between adjacent racks and between racks and the walls through water around them conservatively disregarded. Section 1.5 of NEDO-33373 describes the details of the finite element modeling and also documents the analysis results, including maximum deformations in critical locations and stress checks in the critical sections of the different plates and welds of the rack against the stress limits in accordance with ASME B&PV Code, Section III, Division I, Subsection NF and Appendix F, for Class 3 plate and shell type supports.

Because the spent fuel racks are not structurally connected to the walls and base of the spent fuel pool, the racks could slide against and lift off the pool base. In addition, the fuel assemblies housed in the racks can rattle against the racks. The topical report characterized these dynamic effects through a simplified global coupled fluid structure model. The applicant carried out a transient analysis to determine the dynamic response of the racks subjected to SSE ground motions. NEDO-33373, Section 1.6, gives the details of the fluid structure model, and Sections 1.7 to 1.9 document the analysis results, including maximum deformations in critical locations and stress checks in the critical sections of the different plates and welds of the rack against the stress limits in accordance with ASME B&PV Code, Section III, Division I, Subsection NF and Appendix F, for Class 3 plate and shell type supports.

The applicant concluded in NEDO-33373, Section 1.10 that the design of the spent fuel racks in the spent fuel pool meets the requirements of ASME B&PV Code, Section III, Division I, Subsection NF and Appendix F, for design by analysis of Class 3 plate and shell type supports.

Dynamic Load Analysis for Spent Fuel Racks in the Buffer Pool

Section 2 of NEDO-33373 describes the dynamic load analysis for spent fuel racks in the buffer pool located in the reactor building. The spent fuel racks give structural support to and protection of the stored spent fuel assemblies and are designed by analysis as ASME Code Class 3 plate and shell type supports. The racks are structures fabricated from stainless steel and borated stainless steels plates similar to the spent fuel racks in the spent fuel pool located in the fuel building, except that the spent fuel racks in the buffer pool are designed with different storage capacity and are anchored to the pool structure at the base. The connection of the anchor bolts to the buffer pool base is not within the scope of NEDO-33373. These racks are permanently submerged in the pool water. The fuel assemblies are inserted and removed through the access at the top of the racks. NEDO-33373, Section 2.4, provides the detailed layout and dimensions of the racks.

Section 2.4 of NEDO-33373 describes the dynamic load analysis for the spent fuel racks in the buffer pool. The applicant performed a response spectrum analysis to calculate the dynamic response of the spent fuel racks to SSE, SRVD, and LOCA loads. The load combinations were performed in accordance with the service limits in Table 1 of Appendix D to SRP Section 3.8.4. Section 2.5 of NEDO-33373 describes the stress checks for the critical sections of the plates and welds. The stress limits were based on ASME B&PV Code, Section III, Division I, Subsection NF and Appendix F, for Class 3 plate and shell type supports.

The applicant performed a nonlinear transient analysis to estimate the impact of the fuel assemblies on the racks during an SSE event. On the basis of this dynamic analysis, the applicant checked stresses in the critical sections of the different plates and welds of the racks against the ASME Code stress limits in accordance with ASME B&PV Code, Section III, Division I, Subsection NF and Appendix F, for Class 3 plate and shell type supports. NEDO-33373, Section 2.5.4, provides the detailed analysis and results.

The applicant concluded in NEDO-33373, Section 2.6 that the design of the spent fuel racks in the buffer pool meets the requirements of ASME B&PV Code, Section III, Division I, Subsection NF and Appendix F, for design by analysis of Class 3 plate and shell type supports.

Dynamic Load Analysis for New Fuel Racks in the Buffer Pool

Section 3 of NEDO-33373 describes the dynamic load analysis for new fuel racks in the buffer pool located in the reactor building. The new fuel racks give structural support to and protection of the stored new fuel assemblies. The racks are structures fabricated from stainless steel plates that are anchored to the buffer pool base. These racks are permanently submerged in the pool water, with the fuel assemblies free to be moved in and out of the racks through the lateral entrances. NEDO-33373, Section 3.4 gives detailed layout and dimensions of the racks.

Section 3.4 of NEDO-33373 also describes the dynamic load analysis for the spent fuel racks in the buffer pool. The applicant performed a response spectrum analysis to calculate the dynamic response of the new fuel racks to SSE, SRVD, and LOCA loads. The load combinations were performed in accordance with the service limits in Table 1 of Appendix D to SRP Section 3.8.4. The stress limits were based on ASME B&PV Code, Section III, Division I, Subsection NF and Appendix F, for Class 3 plate and shell type supports.

The analysis results in NEDO-33373, Section 3.5, include maximum deformations in critical locations and stress checks in the critical sections of the different plates and welds of the rack against the stress limits in accordance with ASME B&PV Code, Section III, Division I, Subsection NF and Appendix F, for Class 3 plate and shell type supports.

The applicant performed a nonlinear transient analysis to estimate the impact of the fuel assemblies on the racks during an SSE event. On the basis of this dynamic analysis, the applicant checked stresses in the critical sections of the different plates and welds of the racks against the ASME Code stress limits in accordance with ASME B&PV Code, Section III, Division I, Subsection NF and Appendix F, for Class 3 plate and shell type supports. NEDO-33373, Section 3.5.4, gives a detailed analysis and results.

The applicant concluded in NEDO-33373, Section 3.6 that the design of the new fuel racks in the buffer pool meets the requirements of ASME B&PV Code, Section III, Division I, Subsection NF and Appendix F, for design by analysis of Class 3 plate and shell type supports.

Load-Drop Analysis

Load-drop analysis is required in the design of fuel storage racks for new and spent fuel assemblies. The racks must be capable of withstanding operational and accidental load drops of the fuel assemblies and handling tools. NEDO-33373, Section 4, describes the load-drop analysis for both spent fuel racks and new fuel racks. For the spent fuel racks, the analysis considered two drop scenarios because the fuel assemblies are inserted and removed through the access at the top of the racks: (1) a dropped element may fall through to the bottom of a cell and impact the base plate of the rack, and (2) the dropped element may be arrested at the top of the rack cells. For the new fuel racks that accommodate the fuel operations through lateral entrances, the drop scenarios include the impact of a dropped element on the base plate and the cell walls. NEDO-33373, Section 4.2, describes the geometry and the behavior of the falling fuel elements and the accident drop scenarios associated with the spent fuel racks and new fuel racks.

Sections 4.3 and 4.4 of NEDO-33373 give detailed drop analyses (based on the finite element models of the spent fuel racks) to assess the effects of the postulated drop scenarios on the spent fuel racks. The objectives of these drop analyses were to demonstrate that these postulated drops will not damage the fuel assemblies stored in the rack cells and that the

dropped object would not penetrate through the base plate and thereby damage the pool liner. To achieve these objectives for the drop analyses, the applicant used plastic material properties and the analysis algorithm permitting large deformations to make realistic assessments of the consequences of these postulated accidental drops of fuel elements.

The applicant performed similar drop analyses for the new fuel racks, given in NEDO-33373, Section 4.5.

The applicant concluded in NEDO-33373, Section 4.6 that the drop analyses for both spent fuel racks and new fuel racks demonstrated that the stored fuels and the pool liners were not affected by these postulated drop scenarios.

2.3 Staff Evaluation

The NRC staff reviewed (1) the dynamic analyses of the spent fuel storage racks in the spent fuel pool located in the fuel building and in the buffer pool in the reactor building, and (2) the dynamic analysis of the new fuel storage racks in the buffer pool. The staff also reviewed the drop analyses performed for both spent fuel racks and new fuel racks.

The staff's review included applicable codes and standards for the design of the racks by analysis, material properties, the analysis procedures used to perform the dynamic analyses for the fuel storage racks, load combinations, and structural acceptance criteria for conformance with GDC 1, 2, and 4, as well as other regulatory requirements identified in Section 2.1 of this SER. The staff carried out its technical review of the structural analyses for the fuel storage racks in accordance with Appendix D to SRP Section 3.8.4.

The ESBWR standard design includes facilities for the storage of spent and new fuel. The fuel storage facilities include fuel storage racks that store and protect the fuel, the fuel storage pools that contain the storage racks, and the associated auxiliary components. The scope of this topical report includes the structural dynamic and thermal-hydraulic analyses for the fuel storage racks. This staff evaluation pertains to the technical adequacy of the structural analyses of the ESBWR fuel storage racks.

Fuel storage racks are designed as the storage and structural protection for the spent and new fuel assemblies. The ESBWR fuel storage racks are designed as stainless steel plate type structures. NEDO-33373 designates these racks as ASME Class 3 plate type supports and applies ASME B&PV Code, Section III, Division I, Subsection NF and Appendix F, corresponding to the design by analysis for Class 3 plate and shell type supports. The classification of the fuel storage racks as Class 3 plate and shell type supports and the design of the racks by analysis approach based on the ASME B&PV Code are consistent with 10 CFR 50.55a and with the guidance in Appendix D to SRP Section 3.8.4. On this basis, the staff concludes that the classification and the design-by-analysis approach for the fuel storage racks in NEDO-33373 are acceptable.

According to NEDO-33373, Revision 5, the fuel storage racks are designed and analyzed using stainless steels with material properties consistent with ASME B&PV Code, Section II, Part D (Ref. 5). However, the staff found that the material properties given in NEDO-33373, Revision 0 (Ref. 6) were associated with a temperature that was lower than the accident temperature given in the ESBWR Design Control Document (DCD), Revision 4 (Ref. 7). ESBWR DCD, Revision 4, Tier 2, Section 9.1.2.5, gives the thermal-hydraulic design for the fuel storage racks, which states, "In the event of loss of FAPCS cooling trains, boiling can occur. The structural

acceptance criterion for the fuel storage racks is that the storage rack design does not exceed the allowable stress level given in the ASME B&PV Code, Section III, Subsection NF during boiling." The staff was concerned that the applicant used material properties for the fuel storage racks from below the boiling or accident temperatures. In Request for Additional Information (RAI) 9.1-54 (Ref. 8), the staff asked GEH to justify not using the accident temperature in determining the steel material properties.

In its response dated November 10, 2008 (Ref. 9), the applicant stated the following:

Due to the depths of the spent fuel storage racks in both the Buffer Pool and Spent Fuel Pool, re-analysis of all racks has been performed using ASME code material limits for [121 degrees C] 250° F. Tables 1-3, 2-3, and 3-3 shall be revised to update the material limits to [121 degrees C] 250°F. Sections 1.4.5.3, 2.4.6.3, and 3.4.6.3 of LTR NEDC-33373P, "Dynamic, Load Drop and Thermal-Hydraulic Analysis for ESBWR Fuel Racks," November 2007, shall be revised to reference [121 degrees C] 250° F. In addition, a reference to the ASME Steam Tables shall be added to Sections 1.8, 2.7, and 3.7 as a source for the [121 degrees C] 250°F at the depths of the fuel storage racks.

The staff finds the applicant's response to be acceptable because the applicant has updated the selection of material properties based on the accident temperature of 121 degrees C (250 degrees F), as specified for the buffer pool and spent fuel pool in DCD, Tier 2, Revision 7, Section 9.1.2.5. On this basis, the staff concludes that the material properties used by the applicant for performing dynamic and drop analyses of the fuel storage racks are acceptable. On the basis of the applicant's response, RAI 9.1-54 is resolved.

The applicant used the response spectrum method described in Appendix D to SRP Section 3.8.4 to perform the dynamic analyses of the fuel storage racks under SSE, LOCA, and SRVD loads. Upon reviewing the procedure that the applicant applied to determine the dynamic response of the fuel storage racks based on the response spectrum method, the staff identified a number of technical issues:

- (1) NEDO-33373, Revision 0, described the response spectrum analyses for fuel storage racks under a SSE using a higher damping value than the damping value for welded steel structures given in Table 1 of Regulatory Guide (RG) 1.61, Revision 1, "Damping Values for Seismic Design of Nuclear Power Plants," issued March 2007 (Ref. 10). The fuel storage rack structures are welded steel construction and, according to RG 1.61, the SSE damping should be 4 percent. In RAI 9.1-60 (Ref. 8), the staff asked GEH to justify using a damping value higher than 4 percent in the SSE response analyses.

In its response dated November 10, 2008 (Ref. 9), the applicant stated the following:

Higher damping values are allowed under Regulatory Guide 1.61, Paragraph C.2, and Standard Review Plan Section 3.8.4, Appendix D, Section 3, Paragraph 4, which states that submergence in water can be taken into account. Based on a review of the work by Lawrence Livermore laboratory, "Effective Mass and Damping of Submerged Structures," Report UCRL-52342, by R. G. Dong (1978) [Ref. 11], damping values higher than 4 percent and 6 percent damping were justified for the spent fuel racks located under water with close tolerance fit-up to the fuel assembly. A conservative approach within the industry

showed most racks evaluated with this allowance were using an additional 2 percent damping.

The staff found the applicant's justification inadequate because the study in Lawrence Livermore National Laboratory Report UCRL-52342, "Effective Mass and Damping of Submerged Structures," dated April 1, 1978 (Ref. 11), was based on submerged structures that had different structural configurations from the fuel storage rack structures described in NEDO-33373, Revision 0. Furthermore, the data compiled in Report UCRL-52342 do not support the 6 percent damping value to account for the submergence effect. In RAI 9.1-60 S01 (Ref. 12), the staff asked the applicant to supply adequate and supportable justification for the use of a higher damping value.

In its response to the RAI, dated May 14, 2009 (Ref. 13), GEH agreed to "re-perform the fuel storage rack seismic analysis with a 4 percent damping value as prescribed in Table 1 of RG 1.61." The staff finds the applicant's response acceptable because the applicant redid the seismic analysis of the racks with a damping value consistent with the guidance in Regulatory Guide (RG) 1.61. The staff also reviewed NEDC-33373P¹, Revision 3 (Ref. 14), and confirmed that the applicant has implemented the 4 percent damping value in the seismic analysis of the racks. On the basis of the applicant's response, RAI 9.1-60 is resolved.

- (2) Employing the response spectrum method to determine the dynamic response of fuel racks to SSE, LOCA, and SRVD loads, the applicant stated in NEDC-33373P, Revision 3, Sections 1.5.3, 2.4.8, and 3.4.8, that the modal responses are combined in accordance with the grouping method established in RG 1.92, "Combining Modal Responses and Spatial Components in Seismic Response Analysis." The staff noted that the NRC established the grouping method in RG 1.92, Revision 1, issued February 1976 (Ref. 15) however, the NRC did not include this method in RG 1.92, Revision 2, issued July 2006 (Ref. 16). The staff also noted that in NEDC-33373P, Revision 3, Sections 2 and 3 referred to RG 1.92, Revision 2, while NEDC-33373P, Revision 3, Section 1 did not identify which revision of RG 1.92 was used. In RAI 9.1-148 (Ref. 17), the staff asked the applicant to address this apparent inconsistency.

The staff recognizes that, although RG 1.92, Revision 2, provides some new methods for combining modal responses, the methods established in RG 1.92, Revision 1, are still applicable because they are conservative. However, as described in Sections C.1.4.1 and D of RG 1.92, when applicants use the methods in RG 1.92, Revision 1, they need to include the missing mass contribution, which is particularly important for an adequate estimate of support reactions. The applicant used the 10 percent rule for including the missing mass, which the staff considers nonconservative based on the guidance in RG 1.92, Revision 2. Using the 10 percent rule, the applicant excluded the missing mass effect in NEDC-33373P, Revision 3, Sections 1 and 2, and included the missing mass in NEDC-33373P, Revision 3, Section 3. In RAI 9.1-148, the staff asked the applicant to consider the missing mass effect for modal combinations based on the grouping method in NEDC-33373P, Revision 3, Sections 1 and 2.

¹ Prior to Revision 4, NEDO-33373 was treated by the applicant as a proprietary document and thus designated NEDC-33373P. With Revision 4, the applicant determined that NEDO-33373 did not contain proprietary information, resulting in a new designation.

In its response dated March 11, 2010 (Ref. 18), the applicant revised NEDO-33373, Sections 1.5.3, 1.10, 1.11, 2.4.8, 2.6, 2.7, and 3.7, to assess the effect of the neglected missing masses on the seismic analysis results. The applicant also clarified that it used RG 1.92, Revision 1, in NEDO-33373, Sections 1, 2, and 3, and applicable sections of DCD Tier 2, Chapter 9. According to the applicant's assessment, because of the sizeable design margins in the stress ratios (stress demand to ASME stress allowable) for the fuel storage racks' design, adding the contribution of the neglected missing masses results in a small increase to the stress ratios. However, the resulting stress ratios are still limited to within 1.0, therefore meeting the ASME B&PV Code design requirement. The staff finds that the applicant's response has adequately addressed the missing mass effect and has established that the fuel storage racks design is still adequate when the missing masses are incorporated into the seismic analysis results, which is consistent with the staff position in Sections C.1.4.1 and D of RG 1.92, Revision 2. The staff reviewed NEDO-33373, Revision 4 (Ref. 19), and confirmed that the applicant has supplied detailed descriptions of this assessment. On the basis of the applicant's response, RAI 9.1-148 is resolved.

On the basis of the discussions above, the staff concludes that the response spectrum method used by the applicant for establishing the seismic demands for the fuel storage racks is consistent with RG 1.92, Revision 2, and is therefore acceptable.

In NEDO-33373, Revision 0, the applicant designed the fuel storage racks in the spent fuel pool to be anchored to the pool base. The applicant changed the design in NEDC-33373P, Revision 1 (Ref. 20), so that the fuel storage racks in the spent fuel pool are not structurally fastened to the spent fuel pool, which means that the racks remain freestanding on the base of the pool. To reduce the movement of racks under a SSE, the racks are connected to each other at the bases as well as at the tops. To follow the guidance in Appendix D to SRP Section 3.8.4, the applicant performed a nonlinear transient seismic analysis for the fuel storage racks in the spent fuel pool under SSE ground motions to demonstrate that these racks can withstand sliding and overturning effects associated with the freestanding design. The staff reviewed the nonlinear model that the applicant developed for the nonlinear transient seismic analysis and identified a number of technical issues:

- (1) The applicant developed one nonlinear model in NEDC-33373P, Revision 1, for a north-south (N-S) row of fuel storage rack array and another for an east-west (E-W) row of the rack array. Both models were built with two-dimensional (2-D) beams and point masses. These models are adequate for capturing vibrations in both E-W and N-S directions because the dynamic characteristics of the beam and mass model were developed from the detailed finite element model, which was developed for the response spectrum analysis. However, the staff was concerned that the 2-D models were not able to capture the three-dimensional (3-D) effect of vibrations of the freestanding racks where the racks may be supported at only a corner and pivot about that point. Past studies (NUREG/CR-5912, "Review of the Technical Basis and Verification of Current Analysis Methods Used to Predict Seismic Responses of Spent Fuel Storage Racks," issued October 1992 (Ref. 21)) showed that the pivotal effect may induce large horizontal displacements of the racks. In RAI 9.1-117 (Ref. 12), the staff asked the applicant to either show that the 2-D analyses envelop the pivotal vibration effect or provide an assessment of pivotal effect on the seismic responses.

In its response, dated April 22, 2009 (Ref. 22), GEH agreed to “perform a dynamic analysis of fuel storage rack array. This analysis will include an evaluation of the pivotal effect due to the seismic responses of the fuel storage rack structure using a 3-D model of the racks.” The staff finds the applicant’s response adequate because the applicant performed the nonlinear transient seismic analysis of the racks using a 3-D model of the racks. Furthermore, the staff reviewed NEDC-33373P, Revision 3, and confirmed that the applicant developed a 3-D model based on the dynamic characteristics of the detailed finite element model, which was developed for the response spectrum analysis. On the basis of the applicant’s response, RAI 9.1-117 is resolved.

- (2) Many factors affect the seismic response of the freestanding racks. Among these factors, the friction coefficient between the bearing pads and the pool floor is important in determining whether the racks will be subject to sliding or overturning. NEDC-33373P, Revision 3, Section 1.6.5.1, gives a scenario study of various combinations of factors and establishes a bounding case for the seismic response of racks. The staff noticed that Case C-5 showed that a friction coefficient equal to 0.5 controls the relative displacements of racks with the pool floor at the bottom and the pool wall at the top in the E-W direction. However, the lower bound for the friction coefficient is 0.2. In RAI 9.1-146 (Ref. 23), the staff asked the applicant to demonstrate that the relative horizontal displacements between rack foot and pool floor and fuel storage rack top and pool wall will not exceed the prescribed gaps when Case C-5 is analyzed with a 0.2 friction coefficient.

In its response to RAI 9.1-146 dated March 11, 2010 (Ref. 24), the applicant stated that “[a] new case (Case C-6) will be added.... This new case evaluates the seismic response of the fuel racks assuming a coefficient of friction of 0.2 for the bearing pads on the pool floor....” The staff reviewed the analysis results in NEDC-33373P, Revision 3, Table 1-16, and finds that Case C-6 controls the relative displacements in the E-W direction between the fuel storage racks and the pool liner. In its response to RAI 9.1-144 (Ref. 25) dated March 11, 2010, the applicant changed the design to increase the gap between the fuel storage racks and the pool liner to ensure no impact of fuel storage racks on the liner because of seismic and thermal loads. The staff evaluated the design changes and determined that the large relative displacements induced by Case C-6 are less than the gap between the fuel storage racks and the liner, ensuring no impact of fuel storage racks on the liner. On the basis of the discussion above, the staff concludes that the applicant has adequately considered the seismic load in its nonlinear analysis of fuel storage racks. On the basis of the applicant’s response, RAI 9.1-146 is resolved.

- (3) To determine the global stresses for the freestanding racks, the applicant used a ratio coefficient to scale the fixed-based response spectrum stress results. Because the maximum global bending moments acting at the level of the base plate control the global stresses in plates and welds, the ratio coefficient was determined as the ratio of the maximum bending moment of the freestanding model to the maximum bending moment of the fixed-base response spectrum model. However, the staff noticed that the maximum bending moment of the freestanding model was determined by the SSE motion, while the maximum bending moment of the fixed-base response spectrum model was calculated based on the SSE plus the LOCA plus the SRVD, resulting in a smaller ratio coefficient than if the calculation were done based on the SSE for both models. Given that some stresses provided in NEDC-33373P, Revision 3, Table 1-19, are very close to the ASME stress limit, in RAI 9.1-147 (Ref. 23), the staff asked the

applicant to demonstrate that the ASME stress limit will not be exceeded if the ratio coefficient is calculated using SSE for both models.

In its response dated December 5, 2009 (Ref. 26), the applicant provided an analysis to justify use of the reduction factor. The staff's evaluation finds that the applicant's justification included a mathematical error and is inadequate. However, the applicant indicated that even if the reduction factor is not used, the resulting stresses are within the allowable limits. The applicant specifically stated that "[i]n reviewing NEDC-33373P, Revision 3, Table 1-19 and assuming an f_M factor of 1.0, the resulting stresses are still less than the allowable...." The factor f_M is the applied reduction factor.

The staff reviewed NEDC-33373P, Revision 3, Table 1-19, which provides the stress results for the fuel storage racks and the corresponding ASME stress limits. The staff has confirmed the applicant's position that, if no credit is taken for the reduction factor (set $f_M = 1.0$), the resulting stress demand in all fuel storage rack components is within the ASME stress allowable limits. On the basis of the applicant's response, RAI 9.1-147 is resolved.

On the basis of the discussions above, the staff concludes that the nonlinear transient seismic analysis of the fuel storage racks in the spent fuel pool under SSE motions is consistent with the guidance of Appendix D to SRP Section 3.8.4 and therefore is acceptable.

The applicant followed Appendix D to SRP Section 3.8.4 for load combinations consistent with ASME B&PV Code, Section III, Division I, Subsection NF and Appendix F, corresponding to the design-by-analysis approach for Class 3 plate and shell type supports. However, the staff's review of the implementation of the load combinations concluded that the applicant did not include the thermal load with the SSE in the ASME Service Level D load combination. The staff estimated that, based on the configuration of the rack arrangement in the spent fuel pool, the rack could expand laterally and impact the pool liner if the applicant had appropriately performed its analysis using the Service Level D load combination and included both the temperature and SSE loads. In RAI 9.1-144 (Ref. 27), the staff asked the applicant to demonstrate that when the Service Level D load combination calculations are performed using both the accident temperature and SSE loads, the racks will not impact the liner and the effect of the thermal gradient will not impact the functionality of the racks in accordance with the guidance in Section 1.4 (in particular, the 3rd sentence of the 1st paragraph) of Appendix D to SRP Section 3.8.4.

In its response, dated March 11, 2010 (Ref. 25), the applicant increased the minimum clearance to the fuel pool wall from 42 mm to 92 mm in the N-S direction as a result of the Service Level D reanalysis to include both the accident temperature and SSE loading. The applicant stated that this increase can be accommodated since the tolerance in the N-S pool dimension has been decreased by 100 mm (the minus tolerance was changed from 300 mm to 200 mm per Table 2.16.7-1 in Tier 1 of DCD Rev. 6). The applicant clarified that in the E-W direction, the racks will be placed with a minimum gap of 60 mm to accommodate seismic and thermal expansion.

The staff evaluated the design changes and concludes that the newly established gaps between the fuel storage racks and the pool liner can adequately accommodate the loads resulting from the Service level D load combination. Therefore, this issue is resolved.

In addition, the applicant considered the worst case temperature differential, which results in the maximum temperature gradient between a full cell and an adjacent empty cell, and performed a structural evaluation to determine the impact of the temperature gradient on the functionality of the racks. The applicant stated that “[t]he result of the calculation is that the decrease in the gap between the fuel bundle and the fuel cell walls is less than 44 percent of the nominal gap (...22 mm nominal gap size). Therefore, the distortion of the fuel racks associated with this thermal gradient would not cause the rack walls to contact the stored fuel bundles....” On the basis of the applicant’s evaluation, the staff finds that the functionality of the racks will not be compromised because there remains a gap between a fuel bundle and the racks under the maximum thermal gradient conditions. This is consistent with the guidance in Section 1.4 of Appendix D to SRP Section 3.8.4, which states that the temperature gradient across the rack structure that results from the differential heating effect between a full and an empty cell should be indicated and incorporated in the design of the rack structure. Therefore, on the basis of the evaluation above and the applicant’s response, RAI 9.1-144 is resolved.

The staff concludes that the load combinations are consistent with the guidance of Appendix D to SRP Section 3.8.4 and ASME B&PV Code, Section III, Division I, Subsection NF and Appendix F, and therefore are acceptable.

The applicant used the structural acceptance criteria in Appendix D to SRP Section 3.8.4 to conform to GDC 1, 2, and 4. The applicant chose the design acceptance limits for the rack designs in accordance with ASME B&PV Code, Section III, Division I, Subsection NF and Appendix F, corresponding to the design-by-analysis approach for Class 3 plate and shell type supports. The staff reviewed the applicant’s implementation of the design checks of the structural demands from various load combinations with the ASME B&PV Code’s specified acceptance limits for the critical plate sections and welds and identified a number of technical issues:

- (1) When the stress limits based on F-1332 of Appendix F to ASME B&PV Code, Section III, Division I, are used for plate type supports, a sizeable contribution from bending stress should be present in the plate in addition to the membrane stresses. Therefore, the stress limits per F-1332.2 for membrane plus bending are characterized as peak stresses (recognizing the effect of bending on stress distribution across the plate section) and are much higher than the membrane stress limits provided per F-1332.1. The applicant stated in NEDC-33373P, Revision 3, Sections 1, 2, and 3, that bending plate stresses are negligible; however, the allowable stresses for Service Level D were chosen from F-1332.2. The staff believes that, if the bending effect is negligible, then the plate stress state should be controlled by the membrane stresses. Therefore, the stress allowable per F-1332.1 should be applied. In RAI 9.1-149 (Ref. 17), the staff asked the applicant to make appropriate corrections to the allowable stresses based on F-1332.1 if the bending stress is determined to be secondary to the membrane stress.

In its response dated March 11, 2010 (Ref. 28), the applicant clarified that when the bending stresses are secondary, they are not included in the stress calculations. However, the primary bending stresses are included in the analysis results, in which case the allowable limits will include both membrane and bending components. The applicant also revised the NEDO-33373, Revision 4 sections that provide the stress results to include this statement:

Bending stresses across the plate thickness are negligible and are classified as secondary stresses; however, other directions of the plate

contain primary bending stresses that are included in the stress analysis results.

Because the bending stresses that are identified to be the primary stress have been included in the stress results consistent with F-1332.2, the staff finds that the applicant has appropriately applied the ASME B&PV Code allowable limits. The staff also confirms that NEDO-33373, Revision 4, has incorporated the above statement in the sections documenting the stress results. On the basis of the applicant's response, RAI 9.1-149 is resolved.

- (2) The applicant stated in NEDC-33373P, Revision 3, that the stress limits for Service Level D were based on F-1332 of Appendix F to ASME B&PV Code, Section III, Division I, and provided the stress limits for various stress conditions. However, the staff's review noted that the requirements for compressive stresses are provided under F-1332.5, which then refers to the rules of F-1331.5(a). The staff also noted that the applicant did not evaluate the racks subject to compressive stresses in accordance with the rules of F-1331.5(a). Without such evaluation, the staff considers the applicant's Service Level D analysis to be incomplete. In RAI 9.1-145 (Ref. 27), the staff asked the applicant to provide an evaluation of the rack plates subjected to compressive loads induced during the Service Level D load combination against the buckling limits per F-1331.5(a) of Appendix F to ASME B&PV Code, Section III, Division I.

In its response dated January 29, 2010 (Ref. 29), the applicant stated that "NEDO-33373 will be revised to include an evaluation of the compressive loads induced during the Service D load combination against ASME Code buckling limits. The evaluations will be contained in Appendices B1 and D of NEDO-33373...." The staff confirms that Appendices B1 and D have been added to NEDO-33373, Revision 4. The staff also evaluated the buckling analysis and finds that the buckling analysis based on detailed finite elements, including potential manufacturing imperfections, is consistent with the requirements per F-1331.5 of Appendix F to ASME B&PV Code, Section III, Division I. The results of the buckling analysis show that the allowable buckling limits are much larger than the membrane stresses, and that the buckling loads do not control the design of the fuel storage racks' plates. On the basis of the applicant's response, RAI 9.1-145 is resolved.

- (3) Sections 2.5.4 and 3.5.4 of NEDC-33373P, Revision 3 analyze fuel assemblies impacting the rack cells. The applicant first used simplified beam mass models to develop impact forces on the rack cells, then applied these forces to detailed finite element models for the racks and performed plastic analyses to determine the stresses in the cell plates. The applicant referred to NF-1342.2, which the staff could not locate in Subsection NF. In RAI 9.1-150 (Ref. 17), the staff asked the applicant to clarify the apparently incorrect reference. The staff also asked the applicant to identify applicable and specific ASME Code requirements that were based on plastic analyses.

In its response dated March 11, 2010 (Ref. 28), the applicant clarified that a typographical error was made and that the correct ASME Code requirements applied for the plastic analysis are included in F-1341.2 of Appendix F to ASME B&PV Code, Section III, Division I. The applicant stated that the plastic analysis results showed a localized plasticity that does not lead to any global plastic deformation, therefore not impacting the functionality of the racks. The applicant also stated that the stress results are much lower than the ASME Code allowable limits. On the basis that the applicant

applied Appendix F, F-1341.2 in performing the plastic analysis, the staff concludes that the applicant meets the ASME Code requirements for using plastic analysis methods. The staff has confirmed that the analysis methods and results are appropriately documented in NEDO-33373, Revision 4. The staff also confirmed that the identified typographical error has been corrected in NEDO-33373, Revision 4. On the basis of the applicant's response, RAI 9.1-150 is resolved.

On the basis of the discussions above, the staff concludes that the applicant has appropriately applied the structural acceptance criteria, consistent with the guidance of Appendix D to SRP Section 3.8.4 and ASME B&PV Code, Section III, Division I, Subsection NF and Appendix F, and therefore is acceptable.

For the load-drop analyses, the applicant followed the guidance in Appendix D to SRP Section 3.8.4 to demonstrate the functional capability of the fuel racks to protect the stored fuel during postulated operational accident drops of fuel assembly and associated tools. The applicant postulated several operational accident scenarios that the staff considered acceptable because the determination of the accident drop scenarios was based on the configuration of fuel storage racks and the lift height of fuel assemblies above the racks during the installation and removal operation of the fuel assemblies. The applicant also used detailed finite element models with fine meshes to capture the localized impact effects. The applicant employed a commercial code with the explicit algorithm that is typically used for assessing structural performance associated with impact phenomena. The applicant also demonstrated that, for the various load-drop scenarios, the impact of the accidental drops does not affect the regions of the fuel storage racks that house the fuel assemblies; therefore, the stored fuel assemblies remain in a safe and stable configuration. The staff's review of the applicant load-drop analyses did not identify any technical issues. On the basis of the above assessment of the applicant's load-drop analyses, the staff finds that the applicant's load-drop analyses are consistent with the guidance in Appendix D to SRP Section 3.8.4 and are acceptable.

2.4 Conclusions

This report gives the NRC staff's review and assessment of the dynamic and drop analyses for the ESBWR fuel storage racks in NEDO-33373, Revision 4. The staff's review included applicable codes for the design of the racks by analysis, material properties, analysis procedures used to perform the dynamic analyses for the fuel storage racks, load combinations, and structural acceptance criteria to conformance with GDC 1, 2, and 4, and other regulatory requirements listed in Section 2.1 of this report.

The staff concludes that the ESBWR fuel storage racks meet the relevant requirements of 10 CFR 50.55a and GDC 1, 2, and 4. This conclusion is based on the following:

- (1) The applicant has met the requirements of 10 CFR 50.55a and GDC 1 to ensure that the fuel storage racks are structurally analyzed and designed to the quality standard commensurate with the safety function of protecting the stored fuel assemblies by meeting the guidelines of Appendix D to SRP Section 3.8.4 and ASME B&PV Code, Section III, Division I, Subsection NF and Appendix F.
- (2) The applicant has met the requirements of GDC 2 by structurally analyzing and designing the fuel storage racks to withstand the most severe earthquake that has been established for the ESBWR certified design, with sufficient margin and combinations of the effects of normal and accident conditions with the effects of earthquake loading.

- (3) The applicant has met the requirements of GDC 4 by ensuring that the structural analysis and design of the fuel storage racks are capable of withstanding the dynamic effects associated with accidental load drops and discharging fluids such as those associated with LOCAs and SRVD.

Therefore, the staff concludes that the dynamic and load-drop analyses, as well as the structural design of the ESBWR fuel storage racks, are acceptable.

3.0 Thermal-Hydraulic Analyses

3.1 Regulatory Criteria

The staff reviewed the ESBWR thermal-hydraulic analyses of the spent fuel storage racks in accordance with SRP Section 9.1.2, Revision 4, "New and Spent Fuel Storage," issued March 2007 (Ref. 30). The staff's acceptance of the spent fuel storage facility is based on compliance with GDC 61, "Fuel Storage and Handling and Radioactivity Control," as it relates to the facility design provisions for safe fuel storage and handling of radioactive materials (1) with a residual heat removal capability having reliability and testability that reflects the importance to safety of decay heat and other residual heat removal, and (2) to prevent significant reduction in fuel storage coolant inventory under accident conditions.

The SRP acceptance criteria are also based on conformance to the guidelines in Regulatory Positions C.9 and C.11 in RG 1.13, Revision 2, "Spent Fuel Storage Facility Design Basis," issued March 2007 (Ref. 31), which provide guidance on pool cooling and fuel cooling, respectively.

3.2 Summary of Technical Information

NEDO-33373 Section 5, Appendix G, and Appendix H describe the thermal-hydraulic analyses for spent fuel cooling in the spent fuel pool in the fuel building. NEDO-33373 does not provide thermal-hydraulic analyses for spent fuel cooling in the buffer pool in the reactor building, stating that it is bounded by the spent fuel pool analyses. NEDO-33373 Section 5, Appendix G, and Appendix H describe the calculation of the peak temperatures at the exit of the fuel racks using a computational fluid dynamics (CFD) methodology to determine the temperature distribution throughout the fuel pool.

NEDO-33373, Revision 5, Section 5.1.1, describes the normal and abnormal conditions evaluated in the thermal-hydraulic analyses. For the normal condition, a configuration with the accumulation of 10 years of spent fuel was modeled. For the abnormal condition, a configuration with the accumulation of 10 years of spent fuel and a full-core offload was modeled. In NEDO-33373, Revision 4 (Ref. 19), the abnormal condition was based on a heat load of 17.3 megawatts (MW). The applicant subsequently determined that an alternative abnormal condition heat load of 19.0 MW was bounding. Instead of performing a new CFD analysis for the 19.0 MW heat load condition, the applicant uses the results from the 17.3 MW CFD analysis in NEDO-33373, Revision 4 (Ref. 19) (which is retained in NEDO-33373, Revision 5, Section 5), a previous CFD analysis of a 29 MW heat load condition (in Appendix H), and application of their results to a 19.0 MW heat load condition (in Appendix G).

NEDO-33373, Appendix G, Section 1.0 describes the bases for the 17.3 MW, 19.0 MW and 29.0 MW heat load. NEDO-33373, Appendix G, Section 2.0 describes the key parameters

considered in the evaluation of the 19.0 MW heat load condition. NEDO-33373, Appendix G, Section 3.0 identifies the differences between the 17.3 MW and 29.0 MW CFD analyses and corresponding adjustments made to the 19.0 MW analysis.

The maximum pool inlet temperature from the fuel and auxiliary pools cooling system (FAPCS), for both normal and abnormal conditions, is computed from the first law of thermodynamics for a steady-state, steady-flow process and is described in NEDO-33373, Section 5.2. During normal conditions, the bulk fuel pool temperature will be maintained below 48.9 degrees C (120 degrees F). During abnormal conditions, the bulk fuel pool temperature will be maintained below 60 degrees C (140 degrees F). The applicant imposed a local coolant temperature limit of 121 degrees C (250 degrees F) to maintain favorable material stress properties used in rack fabrication. NEDO-33373 Sections 5.3 and 5.5 and Appendix H describe the results of the CFD analyses. NEDO-33373 Section 5.5 and Appendix G conclude that adequate margin exists to the local coolant temperature limit for the normal condition (7.626 MW) and the abnormal condition (19.0 MW), respectively. NEDO-33373, Section 5.3.6, also describes the determination of the maximum coolant temperature with an 80 percent blockage of the rack channel outlets.

3.3 Staff Evaluation

The staff verified that the design of the ESBWR spent fuel pool racks complies with the requirements of GDC 61 regarding the decay heat removal of spent fuel in the storage racks. The guidelines in SRP Section 9.1.2, Revision 4, specify that the applicant's thermal-hydraulic analysis of the flow through the spent fuel racks should show that there is adequate decay heat removal from the spent fuel assemblies during all anticipated operating and accident conditions. Furthermore, the analysis should show adequate natural circulation of the coolant during all anticipated operating conditions, including full-core offloads during refueling, to prevent nucleate boiling for all fuel assemblies.

The staff notes that the design basis for spent fuel pool cooling during accident conditions allows for the spent fuel pool water to boil. Spent fuel pool cooling during accident conditions is addressed in the Design Certification Document and is outside the scope of NEDO-33373.

SRP Section 9.1.2 does not prescribe specific areas of review for the thermal-hydraulic analyses. The staff carried out its review consistent with standard engineering calculation practice. The method selected and the assumptions and inputs used in the applicant's analyses were independently evaluated.

The analyses provided by the applicant in NEDO-33373 reference design specifications and drawings that are the bases for the CFD model geometry and boundary conditions input.

The staff conducted an audit at the applicant's Washington, DC, office on February 11–12, 2009 (Ref. 32), to review these documents. The staff finds that the CFD model appropriately represents the spent fuel pool and storage rack geometry, as well as FAPCS flow rates and temperatures. The staff also reviewed supporting design calculations for decay heat load and rack pressure drop as a function of flow rate. The staff finds that the calculations used conservative assumptions and standard engineering practice. The 29.0 MW condition was added to NEDO 33373, Revision 5, Appendix H after the staff conducted its audit. As discussed below, the applicant has made adjustments to the results of the 29.0 MW heat load condition (in NEDO-33373, Appendix G, Section 3.0) to account for FAPCS flow temperatures and loss coefficient assumptions that could not be confirmed.

The staff also reviewed the CFD program documentation during the audit to assess the theoretical development, the inherent assumptions, the solution method, and the qualification of the code predictions by comparison to experimental benchmarks and hand-calculated solutions. The staff finds that the CFD program is consistent with other industry-standard finite element fluid dynamics computer programs in theoretical development, assumptions, and solution technique and is therefore acceptable. The CFD code is appropriate for application to spent fuel pool flow and temperature calculations.

Acceptance Criteria

NEDO-33373, Revision 5, Section 5.1, defines the purpose of the thermal-hydraulic analyses as to determine the maximum peak temperatures at the exit of the fuel racks. Section 5.1 defines the acceptance criteria in the form of maximum bulk pool temperatures under normal (48.9 degrees C, 120 degrees F) and abnormal conditions (60 degrees C, 140 degrees F) as well as the maximum local coolant temperature (121 degrees C, 250 degrees F). The staff finds that these acceptance criteria are acceptable because they are consistent with RG 1.13, Regulatory Position C.9, which states that the spent fuel storage facility should include a system for cooling the pool water in order to maintain a bulk temperature below 60 degrees C (140 degrees F) for all heat load conditions. In NEDC-33373P, Revision 2 (Ref. 33), the applicant changed the maximum pool bulk temperatures from acceptance criteria to input assumptions. The staff finds the applicant's approach acceptable since it still ensures that the bulk temperature of the pool remains below 60 degrees C (140 degrees F) for the conditions analyzed in the thermal-hydraulic analyses consistent with RG 1.13, Regulatory Position C.9.

Section 5.1 of NEDO-33373 includes an acceptance criterion that the design of the racks shall allow adequate natural circulation to prevent nucleate boiling within the fuel assemblies. Section 5.1 also includes an acceptance criterion of 121 degrees C (250 degrees F) for the local coolant temperature exiting the spent fuel storage racks. As discussed in Section 2 of this SER, 121 degrees C (250 degrees F) is used for material properties in the dynamic load and load-drop analyses and therefore is acceptable for these purposes.

The staff evaluated whether the temperature limit of 121 degrees C (250 degrees F) could be used as a criterion for nucleate boiling, because nucleate boiling may occur at temperatures below this value. A higher temperature is nonconservative as a criterion to avoid nucleate boiling.

Using NEDO-33373, Figure 5-1, the staff estimated the depth of the pool as 12.5 meters. Assuming that the top of the heated fuel is 3.5 meters from the bottom of the pool, the depth of the highest part of a fuel rod is 9 meters. For water that is 60 degrees C (140 degrees F), the density is 983 kilograms per cubic meter (kg/m^3) (from the ASME Steam Tables, Ref. 34) and the pressure at the 9-meter depth is 1 atmosphere + (density) x (acceleration due to gravity) x (depth) ($P = 101,325 \text{ pascals (Pa)} + 983 \text{ kg/m}^3 * 9.8 \text{ meters per second squared (m/s}^2) * 9 \text{ meters} = 188,026 \text{ Pa}$) or 1.86 atmospheres. The saturation temperature at this pressure (interpolated from the ASME Steam Tables, Ref. 34) is 117.8 degrees C (244 degrees F). This indicates that boiling could occur for temperatures below the 121 degrees C (250 degrees F) criterion set by the applicant.

Another consideration relates to the bulk fluid flow at the top of the rack and fluid temperatures along the fuel rods. The CFD methods used by the applicant do not compute a thermal boundary layer on a fuel rod because of their simplified modeling assumptions. Only a bulk fluid

temperature is computed. If the bulk fluid temperature at the top of the rack is determined to be 121 degrees C (250 degrees F), the temperature of the flow adjacent to a fuel rod will be slightly higher. The local temperature near the fuel rod, not the bulk temperature, governs nucleate boiling. However, the staff finds the use of the bulk fluid temperature acceptable based on the applicant's approaches for determining the maximum cladding temperature and nucleate boiling. In NEDO-33373, Section 5.3.5, Appendix G, and Appendix H, the applicant uses the bulk fluid temperature and not a boundary layer temperature to determine the maximum cladding temperature. The staff finds the maximum cladding temperature determination acceptable below. In NEDO-33373, Section 5.5 and Appendix G, the applicant considers the maximum cladding temperature in the determination of nucleate boiling so the boundary layer temperature does not need to be considered. Based on the above, the staff finds the use of the bulk temperature acceptable.

In RAI 9.1-120 (Ref. 35), the staff asked the applicant to clarify the basis for the temperature limit of 121 degrees C (250 degrees F) in NEDC-33373P, Revision 1, for the maximum coolant temperature allowable exiting the top of the racks. The staff also asked the applicant to explain (1) what criterion it established to prevent boiling within the bundles, (2) what assumptions it used to determine this value, and (3) how the local conditions at the fuel rod are determined from the bulk flow predictions. In its response dated June 30, 2009 (Ref. 36), the applicant stated that the purpose of the limit of 121 degrees C (250 degrees F) is to maintain consistency with the dynamic analyses within NEDO-33373, not to prevent boiling. For nucleate boiling, the applicant added an acceptance criterion in NEDC-33373P, Revision 2, consistent with RG 1.13, Regulatory Position C.11, Revision 2, to demonstrate that the design of the racks allows adequate natural circulation to prevent nucleate boiling for all fuel assemblies. The applicant further stated that the results show that there is substantial margin to boiling. The staff concludes that the RAI response is acceptable because the temperature limit of 121 degrees C (250 degrees F) is used consistently for the structural and thermal-hydraulic analyses in NEDO-33373. The staff also finds the nucleate boiling criterion acceptable because it is consistent with RG 1.13. The staff confirmed that the changes were incorporated into NEDC-33373P, Revision 2. Accordingly, on the basis of the applicant's response and NEDO-33373 revisions, RAI 9.1-120 is resolved.

On the basis of the discussion above, the staff finds the acceptance criteria for the thermal-hydraulics analysis to be acceptable.

Maximum Pool Inlet Temperature Determination

Section 5.2 of NEDO-33373 describes the calculation of the maximum pool inlet temperature condition, which is computed from the First Law of Thermodynamics for a steady-state, steady-flow process. The staff finds this approach acceptable because it is based on basic thermodynamics. The staff also finds the use of a maximum pool inlet temperature acceptable because it maximizes the outlet temperature calculated by the CFD model. For the normal conditions, the heat load is based on 10 years of spent fuel and is identified as 7.626 MW. The staff finds this value acceptable because it is consistent with the design basis of the FAPCS for the cooling of the 10 years of spent fuel accumulation. For abnormal conditions, NEDC-33373P, Section 5.2, Revision 1, specified the heat load as 29.0 MW. This is higher than the heat removal capability of the FAPCS at design conditions (19.2 MW) discussed in the applicant's response to RAI 9.1-10 S02 (Ref. 37). In addition, the applicant reported that the maximum heat load for the pool with 20 years of fuel and one full-core offload is 18 MW. These numbers are inconsistent.

If the maximum inlet temperature for the abnormal case is computed using 18 MW instead of 29 MW, the maximum inlet temperature will be 45.7 degrees C (an increase of almost 9 degrees C). This increase in the pool temperature would increase the rack inlet temperatures for each rack in the pool.

In RAI 9.1-121 (Ref. 35), the staff asked the applicant to clarify the heat load during abnormal conditions. In its response dated July 1, 2009 (Ref. 38), the applicant stated that it would revise the heat load to be consistent with the design basis of the FAPCS for the cooling of the 10 years of spent fuel plus one full-core offload. The heat load is determined to be 17.3 MW. The staff concludes that the RAI response is acceptable because the revised heat load is consistent with the design basis of the FAPCS. The staff confirmed that the changes were incorporated into NEDC-33373P, Revision 2. On the basis of the applicant's response and NEDO-33373 revision, RAI 9.1-121 is resolved.

The applicant subsequently determined that an alternative abnormal condition heat load of 19.0 MW was bounding in NEDO-33373 Revision 5. With the addition of higher abnormal heat load of 19.0 MW and a bounding heat load condition of 29.0 MW in NEDO Revision 5, the staff is further addressing the concern in RAI 9.1-121. In NEDO-33373, Appendix G, Section 1.0, the applicant describes the basis for the 17.3 MW, 19.0 MW, and 29.0 MW heat load conditions. In addition, NEDO-33373, Appendix H identifies that FAPCS is designed for heat load of 20.1 MW. The FAPCS and the spent fuel racks have different design basis heat loads since FAPCS is designed for twenty years of spent fuel with a full-core offloaded at the end of a fuel cycle with 5 days of decay while the spent fuel racks are analyzed for ten years of spent fuel with a full-core offloaded at the end of a fuel cycle with 5 days of decay.

As discussed in Section 3.2 of this report, the applicant is using the results of the CFD analyses for 17.3 MW and 29.0 MW heat load conditions to bound the fuel rack conditions for a 19.0 MW heat load condition instead of performing a new CFD analysis for the 19.0 MW heat load condition. Since the 29.0 MW heat load condition exceeds the design basis heat load of the FAPCS (20.1 MW heat load condition), the results of the CFD analysis for the 29.0 MW heat load condition cannot be directly compared against the fuel rack acceptance criteria. Accordingly, NEDO-33373, Appendix H treats the 29.0 MW condition as a bounding case and does not compare the results of its CFD analysis against the fuel rack acceptance criteria. As discussed below, the applicant has identified in NEDO-33373, Appendix G, Section 3.0 adjustments made to the results 29.0 MW heat load condition regarding the Maximum Pool Inlet Temperature Determination and the CFD Model Loss Coefficient so that the 29.0 MW heat load condition can serve as a bounding case for the 19.0 MW heat load condition and the adjusted results can be compared against the fuel rack acceptance criteria. Because the applicant has identified (1) the basis for the 17.3 MW, 19.0 MW, and 29.0 MW heat load conditions, (2) the relation of the 17.3 MW, 19.0 MW, and 29.0 MW heat load conditions to the 20.1 MW FAPCS design basis heat load condition, and (3) how the 29.0 MW heat load condition serves as a bounding heat load condition through the use of adjusted results, RAI 9.1-121 remains resolved.

In RAI 9.1-122 (Ref. 35), the staff asked the applicant to justify that the SFP inlet temperatures are consistent with the design of the FAPCS. The staff asked this question because the pool inlet temperatures calculated in NEDO-33373 were marginally higher (2.0 degrees C) than the maximum FAPCS heat exchanger shell inlet temperatures specified in DCD Tier 2, Table 9.1-8. In its response dated July 1, 2009 (Ref. 38), the applicant stated that the FAPCS is operated as necessary to remove the heat load in the spent fuel pool. The applicant's response did not directly address the staff concern. However, using the realistic heat loads discussed in its response to RAI 9.1-121, the applicant in NEDC-33373P, Revision 2, calculated higher

allowable SFP inlet pool temperatures. These higher SFP inlet temperatures result in a temperature difference between the pool inlet temperatures and the maximum FAPCS heat exchanger shell inlet temperatures of at least 11.0 degrees C, which addresses the staff concern. On the basis of the applicant's changes in NEDC-33373P, Revision 2, RAI 9.1-122 is resolved.

With the addition of higher abnormal heat load of 19.0 MW and a bounding heat load condition of 29.0 MW in NEDO-33373, Revision 5, the staff is further addressing the concern in RAI 9.1-122. In its October 4, 2010 submittal (Ref. 39), the applicant revised DCD Tier 2, Table 9.1-8, to add the thermal-hydraulic analysis input assumptions and SFP inlet temperatures to ensure that the design of the FAPCS heat exchangers can support the cooling assumed in NEDO-33373, Revision 5. This includes adding performance data for a 20.1 MW heat load condition with two trains of FAPCS running and adding a maximum allowable heat exchanger outlet temperature. The applicant also added a note to DCD Tier 2, Table 9.1-8 to clarify that the maximum allowable tubeside outlet temperature, or SFP inlet temperature, is the value that the fuel rack thermal hydraulic analysis is based upon. These changes address the concern that FAPCS is designed to support the SFP inlet pool temperatures calculated in NEDO-33373, Revision 5.

NEDO-33373, Appendix G, Section 2.1 states that the maximum SFP inlet temperature is calculated for the 19.0 MW using the same methodology as described in NEDO-33373, Section 5.2.2.2. As discussed above, the staff finds this calculation methodology acceptable. For the 29.0 MW case, the applicant used the same methodology to calculate the maximum inlet pool temperature. However, the 29.0 MW condition is outside the performance data for the FAPCS heat exchangers added to DCD Tier 2, Table 9.1-8 in the October 4, 2010 submittal (Ref. 39). The calculated maximum SFP inlet temperature for the 19.0 MW heat load condition is 45.0 degrees C while the calculated maximum SFP inlet temperature for the 29.0 MW heat load condition is 37.0 degrees C. An increase in the SFP inlet temperature for 29.0 MW heat load condition would result in an increase in the SFP bulk temperature and the peak rack exit temperature, which is an acceptance criteria value.

To address the concern of whether the FAPCS can maintain the SFP inlet temperature and bulk temperature at the values assumed in NEDO-33373, Appendix H, the applicant in NEDO-33373, Appendix G, Section 3.0 adjusted the calculated peak rack exit temperature of the 29.0 MW heat load condition by the difference in the calculated maximum SFP inlet temperatures, or 8 degrees C (45.0 degrees C - 37.0 degrees C). In NEDO-33373, Appendix H, the applicant calculated a peak rack exit temperature of 80.9 degrees C for the 29.0 MW heat load condition. Considering only the adjustment for the maximum inlet pool temperature, this would increase the peak rack exit temperature from 80.9 degrees C to 88.9 degrees C. NEDO-33373 Section 5.2.5 documents the results of sensitivity studies performed by the applicant, which indicate that the peak rack exit temperature changes by 0.4 - 0.6 degrees C for each degree C inlet pool temperature change. This sensitivity is reasonable since some of the bulk water in the pool is expected to mix with the water coming into the pool at the entrance to the fuel racks, thus moderating the effect of the inlet pool temperature. Since the applicant conservatively increased the peak rack exit temperature by a full degree for each degree C change in the inlet pool temperature, the staff finds the adjustment for the lower SFP inlet temperature used in the CFD analysis 29.0 MW heat load condition acceptable. On the basis of the above, RAI 9.1-122 remains resolved.

On the basis of the discussion above, the staff finds the maximum pool inlet temperature determination for the thermal-hydraulics analysis to be acceptable.

Computational Fluid Dynamics Model Calculation of the Temperatures and Velocities within the Spent Fuel Pool

NEDO-33373 Section 5.2 and Appendix H describe generally the CFD methods used in the thermal-hydraulic analyses. The CFD-based methods are a common technique for estimating quantities such as the maximum fuel pool coolant temperatures. The results can give assurance when the margin is significant, because CFD methods are generally used to predict ranges of variables rather than precise results. On the basis of the margin discussed in the results below, the staff finds the use of CFD methods acceptable.

NEDO-33373 Section 5.2 and Appendix H describe the model used to perform the thermal-hydraulic analyses. The same model was used for both the 17.3 MW and 29.0 MW heat load conditions with the exception of the limited variances described in NEDO-33373, Appendix G. The ANSYS CFX CFD program (Ref. 40) is used to calculate temperatures and velocities in the fuel pool and rack regions. ANSYS CFX is a high-performance, general purpose CFD program that has been applied to solve wide-ranging fluid flow problems in many industrial applications for over 20 years. To model the ESBWR storage racks and spent fuel pool, a porous medium approach using no physical rack structures is employed to represent the rack regions. This approach simply defines a region that has a loss coefficient applied to slow down or direct the flow. The fluid volume and flow area of this region is unaffected (i.e., region is wide open), and the wide-open region does not affect the velocity of the fluid as a physical rack structure would. For a given rack mass flow, the velocity in the wide-open region is lower than what would be expected in a rack. In addition, fluid residence time in this region is affected. The heat from the fuel is treated as a uniform source term over this region. This method gives only the bulk temperatures. Details such as local temperatures along a fuel rod are not computed. In the staff discussion of the acceptance criteria above, the staff accepted the use of the bulk temperature approach based upon how the maximum cladding temperature and nucleate boiling are determined. In addition, in the staff discussion of the maximum cladding temperature determination, the staff confirmed that the maximum cladding temperature is below the boiling temperature of water at the level of the racks even if a reduced overall heat transfer coefficient is assumed, which also supports the applicant's use of a bulk temperature.

The staff determined that it needed additional information about the CFD model and geometry as described in NEDC-33373P, Revision 1. In RAI 9.1-124 (Ref. 35), the staff asked the applicant to provide the dimensions of the fuel pool model components, information related to loss coefficients, and the locations of the FAPCS inlets and outlets. In its response dated July 31, 2009 (Ref. 41), the applicant provided information on how the pool and rack geometry, and the pool inlets and outlets are modeled. The response also clarified rack assumptions and loss coefficients. The staff concludes that the applicant's response is acceptable because it clarifies the rack assumptions and loss coefficients and how the CFD model as described in the NEDO-33373, Revision 4 is consistent with the ESBWR spent fuel pool design. On the basis of the applicant's response and NEDO-33373 revisions, RAI 9.1-124 is resolved.

On the basis of the discussion above, the staff finds the CFD model calculation of the temperatures and velocities within the spent fuel pool for the thermal-hydraulics analysis to be acceptable.

CFD Model Loss Coefficient

NEDO-33373, Section 5.2 and Appendix H describe the empirical basis for the loss coefficients in the CFD model and their representation in NEDO-33373, Figure 5.2 (repeated in Figure H5-

2). In RAI 9.1-126 (Ref. 34), the staff asked the applicant to clarify NEDC-33373P, Revision 1, Figure 5.2, which is the plot of loss coefficient in the racks and presents the pressure drop as a function of mass flow. In its response dated July 31, 2009 (Ref. 41), the applicant explained that these data are calculated and that the mass flow refers to a single bundle. The applicant also explained that the pressure drop was bounding, because it was based on fuel for existing reactors rather than the shorter ESBWR fuel. The staff concludes that the response is acceptable because the response clarified the information in NEDO-33373, Figure 5.2, and how it is used in the cooling analysis. Therefore, the staff finds the loss coefficient of the CFD model to be acceptable. On the basis of the applicant's response and NEDO-33373 revisions, RAI 9.1-126 is resolved.

With the addition of higher abnormal heat load of 19.0 MW and a bounding heat load condition of 29.0 MW in NEDO Revision 5, the staff is further addressing the concern in RAI 9.1-126. In NEDO-33373 Revision 5, Appendix G, Section 3.0, the applicant states that different loss coefficients were used for the 17.3 MW and 29.0 MW heat load conditions. Appendix G states that the loss coefficient for the 29.0 MW heat load condition was calculated using area and length characteristics for fuel other than the GE14E fuel modeled in NEDO-33373. Appendix G identifies that the loss coefficient is non-conservative and notes that the loss coefficient for the 17.3 MW heat load condition is based on the fuel characteristics of GE14E fuel. NEDO-33373, Section 5.2.5 describes an analysis of this loss coefficient sensitivity and determined that a 20 percent increase in loss coefficient equates to no more than a 6 percent increase in rack exit temperature. NEDO-33373, Appendix G, Section 3.0 identifies that the loss coefficient used for the 29.0 MW heat load condition should be increased 42 percent (to be consistent with the loss coefficient used for the 17.3 MW heat load condition), which represents a total rack exit temperature increase of 12.6 percent, or 10.2 degrees C. The staff finds this adjustment acceptable since the applicant applied the bounding sensitivity results to determine the rack exit temperature correction. On the basis of the above, RAI 9.1-122 remains resolved.

On the basis of the discussion above, the staff finds the loss coefficient of the CFD model for the thermal-hydraulics analysis to be acceptable.

Key Computational Fluid Dynamics Model Assumptions

NEDO-33373 Section 5.2 and Appendix H give tables of the key assumptions about the model characteristics and boundary conditions used in the CFD models for the 17.3 MW and 29.0 MW heat load conditions. For example, it states that the k-epsilon model is used to model turbulence. The treatment of density and buoyancy are addressed by the use of a constant density with a Boussinesq-type (density gradient) approximation for the buoyancy term. The staff determined that additional information was needed about the basis for the modeling assumptions described in NEDC-33373P, Revision 1.

In RAI 9.1-125 (Ref. 35), the staff asked the applicant to describe what sensitivity studies it performed to support its CFD modeling assumptions. In its response dated July 31, 2009 (Ref. 41), the applicant described a series of related sensitivity studies of the CFD model. NEDC-33373P, Revision 2, included a comparable description of sensitivity studies. The specific mesh density studies cited are for an unspecified model of a boiling-water reactor spent fuel pool and are only considered to be qualitative. The staff concludes that the response is acceptable because the margin in the peak temperature predictions bounds the range of CFD model variability shown in the sensitivity studies. The staff also finds that the sensitivity studies support the use of the applicant's selected model characteristics and boundary conditions. On the basis of the applicant's response and NEDO-33373 revisions, RAI 9.1-125 is resolved.

NEDO-33373, Appendix G, Section 3.0 describes the differences between the CFD models for the 17.3 MW and 29.0 MW heat load conditions. As discussed and evaluated above, different loss coefficients are used for the two heat load conditions. Another difference is the orientation of the SFP inlets, which are described in NEDO-33373, Section 5.2.3 and Appendix H. For the 17.3 MW heat load condition, the inlet locations are modeled at the bottom of each corner of the west wall with a 20° offset towards the middle. For the 29 MW case, the inlet locations are modeled at the bottom of each corner of the west wall with no offset. NEDO-33373, Section 5.2.3 and Appendix H state that the actual inlet locations will be inboard from the corners, equally spaced between the pool walls. The applicant determined that the modelling differences have negligible impact on analysis results; therefore, neither model was modified to reflect actual inlet locations and no adjustments to the results are needed in order to compare these cases with the 19.0 MW heat load condition. The staff finds the applicant's approach acceptable since both models have the SFP inlets at the limits of the SFP and bound the distance to the hottest fuel.

On the basis of the discussion above, the staff finds the key CFD model assumptions for the thermal-hydraulics analysis to be acceptable.

Maximum Cladding Temperature Calculation

NEDO-33373, Section 5.3, Appendix G, and Appendix H describe the maximum cladding temperature calculation, which is computed using an analytical model for the water and cladding temperature. The staff determined that the key assumptions in this model are the heat transfer coefficient and the thermal resistance of the crud layer.

To confirm the validity of the results from this approach, the staff performed a confirmatory calculation based on the applicant's data in NEDC-33373P, Revision 1. This calculation used a peak heat flux and a peak temperature, along with Newton's law of cooling and the GEH-provided heat transfer coefficients. The maximum bulk temperature in the rack computed by the CFD code is 80.9 degrees C (177.6 degrees F). Heat flux is determined from the values provided in the table on page 1,021 of the report. An average heat flux at the fuel surface is found to be 2,263 watts per square meter (W/m^2) (717.367 British Thermal Units per hour per square foot (BTU/hr-ft²)). A peak heat flux is estimated by assuming a simple cosine distribution. A peak value, estimated to be a factor of 1.57 higher than the average, is determined to be 3,555 W/m^2 (1126.93 BTU/hr-ft²). Assuming an overall heat transfer coefficient (U) of 270 watts per square meter-degree Kelvin (W/m^2-K) (47.582 British Thermal Units per hour per square foot per degree F (BTU/hr-ft²-F)) ($1/U = 1/283.9 + 1/5673$), the peak cladding temperature is estimated to be 94 degrees C (201 degrees F). This is close to the value of 97 degrees C (207 degrees F) estimated by GEH.

These results depend on the values of the heat transfer coefficient and the fuel rod heat flux. It is assumed that fuel rod heat flux can be established. Heat transfer coefficients, on the other hand, typically have a high uncertainty. If the overall heat transfer coefficient were half of the value used above ($U = 135 W/m^2-K$), the peak cladding temperature would be estimated to be 107.3 degrees C (225.1 degrees F).

In RAI 9.1-127 (Ref. 34), the staff asked the applicant to clarify the basis for the peak cladding temperature prediction in NEDC-33373P, Revision 1. In its response dated July 31, 2009 (Ref. 41), the applicant cited references validating the selection of the heat transfer coefficient and performed sensitivity studies on the heat transfer coefficient to demonstrate that the value

could be reduced by 75 percent and still maintain temperatures below the limit. The applicant also discussed the flow rates, experimental data, and the crud layer resistance and their impact on the peak cladding temperature prediction. The staff concludes that the response is acceptable because the applicant cited standard references for its data and the staff was able to confirm the crud layer resistance sensitivity reported by the applicant. On the basis of the applicant's response, RAI 9.1-127 is resolved.

As described in NEDO-33373 Section 5.3.5, Appendix G and Appendix H, two values in the maximum cladding temperature calculation depend on the CFD analysis, the water temperature at rod inlet and rack flow rate. Since the applicant has not performed a CFD analysis for the 19.0 MW heat load condition, the applicant has used limiting values from the 17.3 MW heat load condition (rack flow rate) and the 29.0 MW heat condition (water temperature at rod inlet), otherwise using the same methodology to calculate the maximum cladding temperature.

As discussed with the maximum pool inlet temperature determination, the 29.0 MW heat load condition is outside the performance data for the FAPCS heat exchangers added to DCD Tier 2, Table 9.1-8 in the October 4, 2010 submittal (Ref. 39). Therefore, the applicant in NEDO-33373, Appendix G, Section 3.0 adjusted the peak rack exit temperature to account for the lower SFP inlet temperature used in the CFD analysis 29.0 MW heat load condition, as described above. In its October 15, 2010 submittal (Ref. 42), the applicant proposed a modification to be included in the accepted version of NEDO-33373, Appendix G, Section 2.3, to justify not making a corresponding adjustment to the maximum rod inlet water temperature calculated for the 29.0 MW heat condition in NEDO-33373, Appendix H. This justification is based on the heated water exiting the racks having little if any influence on the rod inlet water temperature and maintaining the SFP bulk water temperature below 60 degrees C for the 19.0 MW heat load condition. The applicant states that the heated water exiting the racks has little if any influence on the pool water entering the racks because the heated water from the racks is more buoyant and rises to the SFP surface and the outlets. In addition, the cooler SFP inlet water enters at the SFP bottom, and being the least buoyant, enters the rack inlet plenum with limited mixing with the warmer bulk water, which is maintained below 60 C for 19.0 MW heat load condition. The applicant states that these arguments are supported by the results of the CFD analyses presented in NEDO-33373 Figures 5-6, 5-12, 5-12a, H5-6 and H5-12, which show the temperatures of the water in the SFP and the paths the water travels as it passes through the racks. The applicant concludes that these observations provide assurance that the calculated rod inlet temperature for the 29.0 MW heat load condition is bounding and the actual rod inlet temperature for the 19.0 MW heat load condition is expected to fall below the value of 60.39 degrees C that is used to calculate the bounding peak cladding temperature.

The staff confirmed that NEDO-33373 shows that the rack inlet temperature for the hottest fuel for both the 17.3 MW heat load condition and the 29.0 MW heat load condition are both near the SFP bulk water temperature of 60 degrees C used in these analyses. In addition, the figures identified by the applicant show little interaction between the water exiting the racks and the water entering the racks. Therefore, the staff finds the calculation of the maximum cladding temperature for 19.0 MW heat load condition using the rack inlet temperature calculated for the 29.0 MW heat load condition in NEDO-33373, Appendix H acceptable. The staff also finds proposed modification in the October 15, 2010 submittal (Ref. 42) acceptable for inclusion in the accepted version of NEDO-33373.

On the basis of the discussion above, the staff finds the maximum cladding temperature calculation to be acceptable.

Maximum Fluid Temperature Calculation with 80-Percent Blockage of Rack Outlets

Section 5.3 of NEDO-33373 describes the maximum fluid temperature calculation with 80-percent blockage of rack outlets. However, NEDC-33373P, Revision 1 is not clear about what the 80-percent blockage represents. In RAI 9.1-119 (Ref. 35), the staff asked the applicant to clarify what 80-percent blockage means and how it is represented in the CFD model. The staff noted that this type of analysis is needed only if the spent fuel pool liner is not seismic Category I. In its response dated June 30, 2009 (Ref. 43), the applicant clarified that the spent fuel pool liner is seismic Category I and made corresponding changes to the DCD. The applicant also stated that the 80-percent blockage is modeled by reducing the flow area through the channel of each fuel assembly. All channels would therefore be partially blocked. The staff concludes that the response is acceptable because the designation of the spent fuel pool liner as seismic Category I makes the analysis optional and because the applicant clarified the modeling assumption. On the basis of the applicant's response and DCD and NEDO-33373 revisions, RAI 9.1-119 is resolved.

NEDO-33373, Appendix G does not contain a calculation of the maximum fluid temperature calculation with 80-percent blockage of rack outlets for the 19.0 MW heat load condition. As noted above, this calculation is not needed since the SFP liner is seismic category 1.

On the basis of the discussion above, the staff finds the maximum fluid temperature calculation with 80-percent blockage of rack outlets to be acceptable.

Results

The staff compared the results of the calculations documented in NEDO-33373, Section 5.5 and appendix G, against the acceptance criteria. The maximum local coolant temperature at the rack exit for normal conditions is 65 degrees C (149 degrees F). The maximum rack exit temperature for abnormal conditions (19.0 MW heat load condition discussed in Appendix G) is 99.1 degrees C (163.4 degrees F). The maximum peak cladding temperature is 101.0 degrees C (192.6 degrees F). The maximum local coolant temperature at the rack exit for the reactor building buffer pool is 67 degrees C (153 degrees F). These results indicate that there is substantial margin to boiling at the exit of the racks (boiling temperature was previously calculated to be 117.8 degrees C (244 degrees F) at the depth of the top of the racks) and meets the applicant's materials property criteria of 121 degrees C (250 degrees F). The staff notes that the maximum rack exit temperature includes data adjustments from the 29.0 MW heat load condition and that if an actual CFD analysis were performed, lower results would be expected. The staff further notes that if the maximum peak cladding temperature were adjusted upward by 8.0 degrees C to account for the lower inlet pool temperature used in the 29.0MW heat load condition CFD analysis, the cladding would still remain below the boiling point for water at the depth of the top of the racks. Therefore, the staff finds that the results show that acceptance criteria for temperature are met.

The staff assessed the CFD results for demonstration of natural circulation through the storage racks. In NEDO-33373, Figures 5-9, 5-12, and 5-12a show streamlines from inlets to outlets under normal and abnormal conditions, respectively. The figures show that the pools are well mixed and provide evidence of flow through the racks. This supports the conclusion that there is natural circulation through the racks; therefore, the staff finds that the natural circulation criterion is met.

On the basis of the discussion above, the staff finds that the thermal-hydraulic analysis of the flow through the spent fuel storage racks is appropriate to demonstrate adequate decay heat removal from the spent fuel assemblies during all anticipated operating conditions. Furthermore, the analysis shows that adequate natural circulation of the coolant is provided during all anticipated operating conditions, including full core-offloads during refueling, to prevent nucleate boiling for all fuel assemblies. Therefore, the staff finds that the thermal-hydraulic analyses demonstrate that the spent fuel storage racks meet the requirements of GDC 61 and the guidelines of RG 1.13 for the decay heat removal of spent fuel in the storage racks.

3.4 Conclusions

On the basis of the discussions above, the staff finds that the thermal-hydraulic analyses demonstrate that the spent fuel storage racks meet the requirements of GDC 61 and the guidelines of RG 1.13 for the decay heat removal of spent fuel in the storage racks. Therefore, the staff finds that the thermal-hydraulic design of the ESBWR fuel storage racks is acceptable.

4.0 References

1. Kingston, R.E., GE Hitachi Nuclear Energy, letter to U.S. Nuclear Regulatory Commission, "Transmittal of GEH Licensing Topical Report NEDO-33373, "Dynamic, Load-Drop and Thermal-Hydraulic Analyses for ESBWR Fuel Racks," Revision 5, September 2010," MFN-268, October 2, 2010 (ADAMS Accession No. ML102790418, transmittal letter; ML102790420 and ML102790417, NEDO-33373, Revision 5)
2. U.S. Nuclear Regulatory Commission, "Standard Review Plan for the Review of Safety Analysis Reports for Nuclear Power Plants," NUREG-0800, Section 3.8.4, Appendix D, "Guidance on Spent Fuel Pool Racks," Revision 2, March 2007.
3. U.S. Code of Federal Regulations, Title 10, Energy, Part 50, "Domestic Licensing of Production and Utilization Facilities,"
4. American Society of Mechanical Engineers, *Boiler and Pressure Vessel Code*, 2001 edition with 2003 addenda, Section III, "Rules for Construction of Nuclear Facility Components," Division 1, New York, NY.
5. American Society of Mechanical Engineers, *Boiler and Pressure Vessel Code*, 2001 edition with 2003 addenda, Section II, "Materials," Part D, "Properties," New York, NY.
6. Kinsey, J.C., GE Hitachi Nuclear Energy, letter to U.S. Nuclear Regulatory Commission, Transmittal of Licensing Topical Report NEDC-33373P, Revision 0, "Dynamic, Load-Drop and Thermal-Hydraulic Analysis for ESBWR Fuel Racks," November 2007, MFN 07-607, November 16, 2007. (ADAMS Accession No. ML073250236)
7. Kinsey, J.C., GE Hitachi Nuclear Energy, letter to U.S. Nuclear Regulatory Commission, "GE-Hitachi Nuclear Energy—ESBWR Standard Plant Design—Revision 4 to Design Control Document—Tier 1 and Tier 2," September 28, 2007. (ADAMS Accession No. ML072900510)
8. Galvin, D.J., U.S. Nuclear Regulatory Commission, letter to R.E. Brown, GE Hitachi Nuclear Energy, "Request for Additional Information Letter No. 165 Related To Licensing Topical Report NEDC-33373P, Revision 0, 'Dynamic, Load-Drop and Thermal-Hydraulic Analysis for ESBWR Fuel Racks,'" March 19, 2008. (ADAMS Accession No. ML080770166)
9. Kingston, R.E., GE Hitachi Nuclear Energy, letter to U.S. Nuclear Regulatory Commission, "Response to NRC Request for Additional Information Letter No. 165 Related to Licensing Topical Report NEDC-33373P, Revision 0, 'Dynamic, Load Drop and Thermal-Hydraulic Analysis for ESBWR Fuel Racks,' November 2007 RAI Numbers 9.1-51 through 9.1-76," MFN 08-882, November 10, 2008. (ADAMS Accession No. ML083180147)
10. U.S. Nuclear Regulatory Commission, "Damping Values for Seismic Design of Nuclear Power Plants," Regulatory Guide 1.61, Revision 1, March 2007. (ADAMS Accession No. ML070260029)
11. Dong, R.G., Lawrence Livermore National Laboratory, "Effective Mass and Damping of Submerged Structures," UCRL-52342, Livermore, CA, April 1, 1978.

12. Galvin, D.J., U.S. Nuclear Regulatory Commission, letter to R.E. Brown, GE Hitachi Nuclear Energy, "Request for Additional Information Letter No. 298 Related to ESBWR Design Certification Application," February 11, 2009. (ADAMS Accession No. ML090410164)
13. Kingston, R.E., GE Hitachi Nuclear Energy, letter to U.S. Nuclear Regulatory Commission, "Response to Portion of NRC Request for Additional Information Letter No. 298 Related to ESBWR Design Certification Application—Auxiliary Systems—RAI Number 9.1-60 S01," MFN 09-267, May 14, 2009. (ADAMS Accession No. ML091380167)
14. Kingston, R.E., GE Hitachi Nuclear Energy, letter to U.S. Nuclear Regulatory Commission, "Transmittal of GEH Licensing Topical Report NEDC-33373P, "Dynamic, Load-Drop and Thermal-Hydraulic Analyses for ESBWR Fuel Racks," Revision 3, September 2009," MFN 10-005, January 12, 2010 (ADAMS Accession No. ML100190095, transmittal letter; ML100190097 and ML100190098, NEDC-33373P, Revision 3)
15. U.S. Nuclear Regulatory Commission, "Combining Modal Responses and Spatial Components in Seismic Response Analysis," Regulatory Guide 1.92, Revision 1, February 1976. (ADAMS Accession No. ML003740290)
16. U.S. Nuclear Regulatory Commission, "Combining Modal Responses and Spatial Components in Seismic Response Analysis," Regulatory Guide 1.92, Revision 2, July 2006 (ADAMS Accession No. ML053250475)
17. Galvin, D.J., U.S. Nuclear Regulatory Commission, letter to Jerald G. Head, GE Hitachi Nuclear Energy, "Request for Additional Information Letter No. 398 Related to ESBWR Design Certification Application," December 2, 2009 (ADAMS Accession No. ML093360287)
18. Kingston, R.E., GE Hitachi Nuclear Energy, letter to U.S. Nuclear Regulatory Commission, "Revised Response (Revision 2) to Portion of NRC Request for Additional Information Letter No. 398 Related to ESBWR Design Certification Application—Fuel Racks - RAI Number 9.1-148," MFN 09-790, Revision 2, March 11, 2010. (ADAMS Accession No. ML100700638)
19. Kingston, R.E., GE Hitachi Nuclear Energy, letter to U.S. Nuclear Regulatory Commission, "Transmittal of GEH Licensing Topical Report NEDO-33373, "Dynamic, Load-Drop and Thermal-Hydraulic Analyses for ESBWR Fuel Racks," Revision 4, March 2010," MFN-092, March 18, 2010 (ADAMS Accession No. ML100820351, transmittal letter; ML100820357 and ML100820352, NEDO-33373, Revision 4)
20. Kingston, R.E., GE Hitachi Nuclear Energy, letter to U.S. Nuclear Regulatory Commission, "Transmittal of GEH Licensing Topical Report NEDC-33373P, Revision 1, "Dynamic, Load-Drop and Thermal-Hydraulic Analyses for ESBWR Fuel Racks," November 2008," MFN 08-932, December 2, 2008 (ADAMS Accession No. ML083460455, transmittal letter; ML083460456 and ML083460458, NEDC-33373P, Revision 1)

21. U.S. Nuclear Regulatory Commission, "Review of the Technical Basis and Verification of Current Analysis Methods Used to Predict Seismic Response of Spent Fuel Storage Racks," NUREG/CR-5912, October 1992.
22. Kingston, R.E., GE Hitachi Nuclear Energy, letter to U.S. Nuclear Regulatory Commission, "Response to Portion of NRC Request for Additional Information Letter No. 298 Related to ESBWR Design Certification Application—Auxiliary Systems—RAI Numbers 9.1-117 and 9.1-118," MFN 09-268, April 22, 2009. (ADAMS Accession No. ML091120753)
23. Galvin, D.J., U.S. Nuclear Regulatory Commission, letter to Jerald G. Head, GE Hitachi Nuclear Energy, "Request for Additional Information Letter No. 396 Related to ESBWR Design Certification Application," November 24, 2009. (ADAMS Accession No. ML093280035)
24. Kingston, R.E., GE Hitachi Nuclear Energy, letter to U.S. Nuclear Regulatory Commission, "Revised Response (Revision 2) to Portion of NRC Request for Additional Information Letter No. 396 Related to ESBWR Design Certification Application—Fuel Racks—RAI Number 9.1-146," MFN 09-789, Revision 2, March 11, 2010. (ADAMS Accession No. ML100700632)
25. Kingston, R.E., GE Hitachi Nuclear Energy, letter to U.S. Nuclear Regulatory Commission, "Revised Response (Revision 2) to Portion of NRC Request for Additional Information Letter No. 391 Related to Design Control Document (DCD) Revision 6—Fuel Racks—RAI Number 9.1-144," MFN 09-778, Revision 2, March 11, 2010. (ADAMS Accession No. ML100700622)
26. Kingston, R.E., GE Hitachi Nuclear Energy, letter to U.S. Nuclear Regulatory Commission, "Response to Portion of NRC Request for Additional Information Letter No. 396 Related to ESBWR Design Certification Application—Fuel Racks—RAI Number 9.1-147," MFN 09-765, December 5, 2009. (ADAMS Accession No. ML093410054)
27. Galvin, D.J., U.S. Nuclear Regulatory Commission, letter to Jerald G. Head, GE Hitachi Nuclear Energy, "Request for Additional Information Letter No. 391 Related to Design Control Document (DCD) Revision 6," November 9, 2009. (ADAMS Accession No. ML093130024)
28. Kingston, R.E., GE Hitachi Nuclear Energy, letter to U.S. Nuclear Regulatory Commission, "Revised Response (Revision 2) to Portion of NRC Request for Additional Information Letter No. 398 Related to ESBWR Design Certification Application—Fuel Racks—RAI Numbers 9.1-149 and RAI 9.1-150," MFN 09-773, March 11, 2010. (ADAMS Accession No. ML100740442)
29. Kingston, R.E., GE Hitachi Nuclear Energy, letter to U.S. Nuclear Regulatory Commission, "Revised Response to Portion of NRC Request for Additional Information Letter No. 391 Related to Design Control Document (DCD) Revision 6—Fuel Racks—RAI Number 9.1-145," MFN 09-778, Revision 1, January 29, 2010. (ADAMS Accession No. ML100330388)

30. U.S. Nuclear Regulatory Commission, "Standard Review Plan for the Review of Safety Analysis Reports for Nuclear Power Plants," NUREG-0800, Section 9.1.2, "New and Spent Fuel Storage," Revision 4, March 2007.
31. U.S. Nuclear Regulatory Commission, "Spent Fuel Storage Facility Design Basis," Regulatory Guide 1.13, Revision 2, March 2007. (ADAMS Accession No. ML070310035)
32. Summary of the February 11–12, 2009, and September 29–30, 2009, Regulatory Audits of Supporting Information for Fuel Storage Racks Topical Reports at General Electric Hitachi (GEH) Office in Washington, DC. (ADAMS Accession No. ML101450301)
33. Kingston, R.E., GE Hitachi Nuclear Energy, letter to U.S. Nuclear Regulatory Commission, "Transmittal of GEH Licensing Topical Report NEDC-33373P, "Dynamic, Load-Drop and Thermal-Hydraulic Analyses for ESBWR Fuel Racks," Revision 2, August 2009," MFN 09-543, August 14, 2009. (ADAMS Accession No. ML092300498, transmittal letter; ML092300499 and ML092300500, NEDC-33373P, Revision 2)
34. ASME Steam Tables, "Thermodynamic and Transport Properties of Steam," Sixth Edition, The American Society of Mechanical Engineers, New York, 1993.
35. Galvin, D.J., U.S. Nuclear Regulatory Commission, letter to J.G. Head, GE Hitachi Nuclear Energy, "Request for Additional Information Letter No. 337 Related to Design Control Document (DCD) Revision 5," May 14, 2009. (ADAMS Accession No. ML091280154)
36. Kingston, R.E., GE Hitachi Nuclear Energy, letter to U.S. Nuclear Regulatory Commission, "Response to Portion of NRC Request for Additional Information Letter No. 337 Related to ESBWR Design Certification Application—Auxiliary Systems—RAI Number 9.1-120," MFN 09-411, June 30, 2009 (ADAMS Accession No. ML091830348)
37. Kinsey, J.C., GE Hitachi Nuclear Energy, letter to U.S. Nuclear Regulatory Commission, "Response to Portion of NRC Request for Additional Information Letter No. 111 Related to ESBWR Design Certification Application—Auxiliary Systems—RAI Numbers 9.1-10 S02, 9.1-19 S02, and 9.1-20 S02," MFN 06-309, Supplement 8, December 14, 2007. (ADAMS Accession No. ML073520108)
38. Kingston, R.E., GE Hitachi Nuclear Energy, letter to U.S. Nuclear Regulatory Commission, "Response to Portion of NRC Request for Additional Information Letter No. 337 Related to ESBWR Design Certification Application—Auxiliary Systems—RAI Numbers 9.1-121 and 9.1-122," MFN 09-454, July 1, 2009. (ADAMS Accession No. ML091870119)
39. Kingston, R.E., GE Hitachi Nuclear Energy, letter to U.S. Nuclear Regulatory Commission, "Revised Response (Revision 2) to Audit Open Items from the Summary of the June 3 and 15, 2010 NRC Regulatory Audits of the ESBWR Spent Fuel Pool Required Water Inventory," MFN 10-189, Revision 2, October 4, 2010. (ADAMS Accession No. ML102790159)
40. ANSYS CFX Computer Program Release 11.0, ANSYS Inc., Canonsberg, PA.

41. Kingston, R.E., GE Hitachi Nuclear Energy, letter to U.S. Nuclear Regulatory Commission, "Response to Portion of NRC Request for Additional Information Letter No. 337 Related to Design Control Document (DCD) Revision 5—Spent Fuel Pool—RAI Numbers 9.1-124, 9.1-125, 9.1-126 and 9.1-127," MFN 09-522, July 31, 2009. (ADAMS Accession No. ML092160225)
42. Kingston, R.E., GE Hitachi Nuclear Energy, letter to U.S. Nuclear Regulatory Commission, "Transmittal of Markup for Licensing Topical Report NEDO-33373, Revision 5, "Dynamic, Load-Drop and Thermal-Hydraulic Analyses for ESBWR Fuel Racks"" MFN 10-326, October 15, 2010. (ADAMS Accession No. ML102920379)
43. Kingston, R.E., GE Hitachi Nuclear Energy, letter to U.S. Nuclear Regulatory Commission, "Response to Portion of NRC Request for Additional Information Letter No. 337 Related to ESBWR Design Certification Application—Auxiliary Systems—RAI Number 9.1-119," MFN 09-393, June 30, 2009. (ADAMS Accession No. ML091830346)